Studies on Structural, Transport and Magnetic Properties of Mixed Oxide Perovskites

THESIS

Submitted to

Saurashtra University, Rajkot, India

For the Degree of

Doctor of Philosophy

in Science

in the subject of Physics

By

Rohini N. Parmar

Under the supervision of

Dr. D. G. Kuberkar
Associate Professor
Department of Physics
Saurashtra University
Rajkot, India

December 2006

This thesis is dedicated to

My beloved Parents and Family

Acknowledgements

First of all, I obeisance *Maa Saraswati*, Goddess of knowledge.

It gives me immense pleasure and feeling of satisfaction to express my deep sense of gratitude for all those have been contributed and intended significantly to make this work possible. I am greatly indebted to my Ph.D. supervisor **Dr. Deelip G. Kuberkar** for providing me an opportunity so that I can enter in this novel research field of materials world. It has been a great privilege to work with him. His continuous inspiration, motivation and keen guidance has made me to reach at this stage of writing my Ph.D. thesis.

I am grateful to *Prof. S. K. Malik*, DCMP and MS, TIFR, Mumbai for extending PPMS experimental facility which has helped in shaping of this thesis with good research outcome. I also acknowledge other group members of DCMP and MS, namely, *Mr. J. John, Mr. D. Budhikot, Mr. Vivas Bagwe* and *Mr. N. A. Kulkarni* for their help in carrying out thin film deposition and characterization.

I am thankful to *Dr. Ravi Kumar*, IUAC, New Delhi for his guidance, helpful discussions, timely help and support during my collaborative project work related to SHI studies at IUAC, New Delhi. It has been a nice experience to visit his laboratory for a couple of times and receive useful suggestions. Thanks are due to *Dr. Ram Janay Choudhary*, group members at IUAC for his kind help and friendly cooperation during the beam time experiments at IUAC.

I am gratefully thankful to *Prof. A. K. Raychaudhuri* for permitting me to visit his lab for couple of weeks for learning of CSD method and *Dr(Ms). Baranali Ghosh* for her help in this regard.

I also thank UGC-DAE CSR (formally IUC-DAEF), Mumbai and *Prof. P.S.Goyal,* for providing me financial support in the initial stages of this work. I am thankful to my former project collaborators *Dr. M. Ramnadham, Mr. P. S. R. Krishnan* and *Keka R. Chakraborty* at SSPD, BARC, Mumbai for their invaluable cooperation and help in carrying out neutron diffraction measurements and analysis at Dhruva Reactor, BARC. I am very much thankful UGC-DAE CSR, Indore and *Prof. A. Gupta* for providing the experimental facilities at Indore.

My sincere regards to the Head, Department of Physics, Saurashtra University for providing me the departmental facilities and extend my acknowledgements all the teaching faculties of the department for their moral support. I am sincerely obliged to *Prof. B. J. Mehta, Dr. M. J. Joshi, Dr. J. A. Bhalodia* and *Dr. N. A. Shah* who have been helpful to me at various stages during the course of this work.

I would like to express my sincere thanks and regards to my senior colleagues and friends *Dr. Sudhindra Rayaprol, Dr. Krushna Mavani, Dr. Dhanvir Rana* and *Dr. Chetan M. Thaker* for their continuous cooperation, helpful discussions and careful guidance during the course of this work. Thanks are due to my colleagues *Mr. J. H. Markna, Mr. P. S. Vachhani, Mr. P. S. Solanki, Ms. R. R. Doshi, Mr. B. R. Katariya, Mr. S. M. Dalsaniya, Mr. D. D. Pandya, Ms. P. Chhelavda,* and *Ms. J. Chocha* for their friendly cooperation during this work.

It is moment to remember my friends *Ms. Rashmi* and *Ms. Monadevi* for providing a friendly and relaxing environment during my stay at Rajkot.

Thanks to *Ms. Preeti D. Kuberkar* and *Ms. Madhura D. Kuberkar* for a nice hospitality and homely treatment during the course of this work.

I feel short of words when I put on record the efforts of my family members in supporting me throughout these years with all the hardships they have faced for me. My heartfelt regards to my parents, **Smt. Nirmalaben N. Parmar** and **Shri. Narendrakumar C. Parmar** for their unending blessings and moral support. My sisters *Ms. Manisha, Ms. Hetal* and brother *Mr. Milap* always wanted me to see at the pinnacle and extended all the moral support to accomplish my objectives. At this moment, I remember my grand uncle *Mr. Chandulal C. Parmar*, who has inspired me for the Ph. D. work. My family always spirit up me without whom this day would not have been possible.

Finally, I sincerely acknowledge all my teachers who have laid an educational foundation in my career during early stages of my education.

December, 2006 **Rohini N. Parmar**

I thankfully acknowledge Inter University Accelerator Centre (IUAC), New Delhi, India for providing me financial assistance as Project Assistant during February 2005 – Mrach 2007 under the UFUP Research Project No. UFUP 37311 of Dr. D.G. Kuberkar.

December, 2006 **Rohini N. Parmar**

RAJKOT

STATEMENT UNDER O. Ph.D. 7 OF THE SAURASHTRA UNIVERSITY

This is certified that the work presented in the thesis is my own work, carried out under the supervision of ***Dr. D. G. Kuberkar*** *and leads to some important contributions in Physics supported by necessary references.*

Rohini N. Parmar
(Research Scholar)

This is to certify that the work submitted for Ph.D. degree in Physics to Saurashtra University, Rajkot by ***Ms. Rohini N. Parmar*** *has been the result of more than three years of work under my supervision and is a good contribution in the field of Solid State Physics and Materials Science.*

Dr. D. G. Kuberkar
(Research Guide)
Associate Professor
Department of Physics
Saurashtra University
Rajkot

Preface

Mixed oxide high T_c superconductors and Colossal Magnetoresistive manganites are correlated insulators which exhibit varieties of novel correlations in association with spin, orbital and charge degrees of freedom and continue to attract the attention of scientific community owing to their potential for technological applications such as hybrid HTSC/CMR devices, magnetic memory read heads and temperature and field sensor, etc. The low temperature neutron diffraction studies and structural Bond Valence Sum calculations carried out during the present investigations are important from fundamental understanding of structure-property correlation in mixed oxide superconductors. The structural, electronic and magnetotransport properties of some doped manganites were investigated on thin films synthesized using PLD & CSD techniques. Swift heavy ion irradiation induced suppression of resistivity in LBMO manganite films is the unique feature observed as a result of the present work. All the bulk materials in the present work were synthesized using solid state reaction route and novel chemical solution deposition at Department of Physics, Saurashtra University, Rajkot, India. Most of the experimental work has been performed in collaboration with Tata Institute of Fundamental Research TIFR, BARC, Mumbai, India and IUAC, New Delhi.

Index

Contents *Page No.*

Chapter -3

Temperature dependent Neutron Diffraction studies on mixed oxide $La_{2-x}Dy_xCa_{2x}Ba_2Cu_{4+2x}O_z$ (x = 0.3, 0.5) superconductors

Chapter – 4

Studies on $La_{0.5}Pr_{0.2}Ba_{0.3}MnO_3$ (LPBMO) manganite thin films

Chapter -5

Studies on $La_{0.7}R_{0.3}MnO_3$ (LRMO) (R = Ca, Sr and Ba) thin films grown by CSD method

Chapter - 1

Introduction of High T_c Superconductors and Colossal Magnetoresistance manganites

1.1 Introduction

The perovskites and perovskite related structures exhibit several interesting features of fundamental as well as technological interest. The crystal structure of perovskite family of compounds is similar to that of the mineral perovskite, $CaTiO_3$. The two classes of materials crystallizing in perovskite structure are: ionic materials having the ideal chemical formula ABX_3 (A – larger cation, B – smaller cation and X – anion) and alloys having the general formula M_cXM_f (X – interstitial atom, M_c and M_f - metal atoms). Of these two classes, the ABX_3 type is more important from application point of view. The prerequisite for a stable ABX_3 perovskite is the existence of stable, polar, octahedral-site building blocks which requires that, B-cation to prefer octahedral coordination and an effective charge on it. Since, any A-cation must occupy the relatively large cationic interstice, created by corner-shared octahedra; the second prerequisite is an appropriate size of A-cation. Depending on the size of A-cations, the A-X and B-X bond lengths are optimized leading to a stable ABX_3 perovskite structure. Perovskite structure is very common among compounds comprising minerals, fluorites, oxides and alloys. In addition to the stoichiometric ABO_3 (X = O), perovskite compounds in mixed oxide systems as $A_{1-x}A'_xBO_3$ and $AB_{1-x}B'_xO_3$, it is also possible to form perovskite superstructures of the type $AA'B_2O_6$ or $A_2BB'O_6$ and perovskite intergrowth family $(AA')_{n+1}B_nO_{3n+1}$ of compounds. Further, it is ability of the perovskite to accommodate the cation or oxygen deficiency, and hence the large class of defect perovskite phases is governed in many ionic systems and alloys [1].

1.1.1 General concepts and properties

The ability of the ABO_3 structure, to tolerate/tune wide range of mismatch between the mean equilibrium ⟨A-O⟩ and ⟨B-O⟩ bond lengths, where A-site and/or B-site are occupied by various cations with same or different valency, leads to the existence of large number and variety of stoichiometric perovskites. The general crystal structure of ideal ABO_3 perovskite is a primitive cubic, with the A-cation occupying the center of the cube, B-cation at the corner and the anion, commonly oxygen, at the center of the edges. The octahedrally coordinated B-cation and A cation having twelve coordination stabilizes the structure as shown in fig. 1.1.

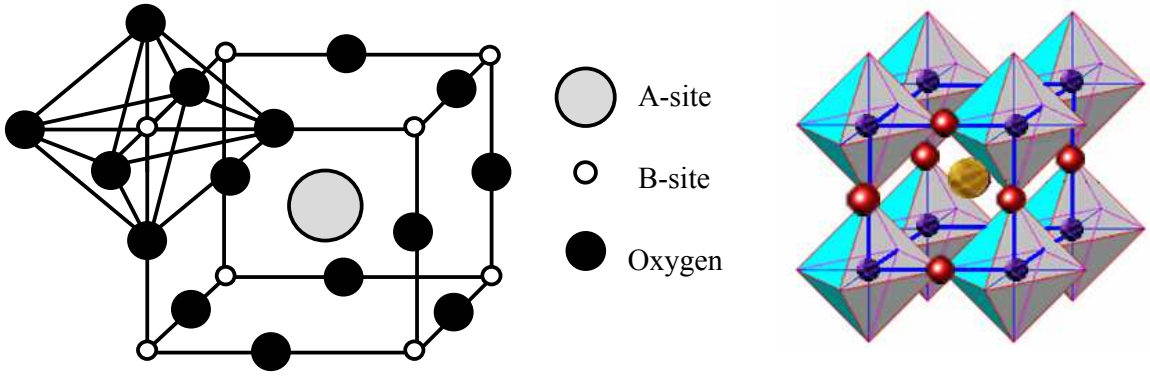

Figure 1.1: Crystal structure of ideal ABO_3 perovskite unit cell. Corner shared $BO_{6/2}$ polyhedra are shown at the corner of the unit cell.

The most striking feature of the ABO_3 perovskite containing the correlated electronic systems is the electronic band structure which is determined by the hybridization of core 3d orbitals with the oxygen (ligand) 2p orbitals. The stoichiometric $A^{3+}B^{3+}O_3$ perovskite structures are mostly correlated insulators: band insulator, Mott-Hubbard or charge transfer insulators depending upon the charge excitations across the gap at the lower (filled) and upper (empty) Hubbard bands as can be seen from fig.1.2, which illustrates the metal-insulator phase diagram for them [2]. It can be observed from fig.1.2, that the perovskite structures, with less than half filled d-shell are Mott-Hubbard insulators whereas the more than half filled d-shell are charge transfer insulators.

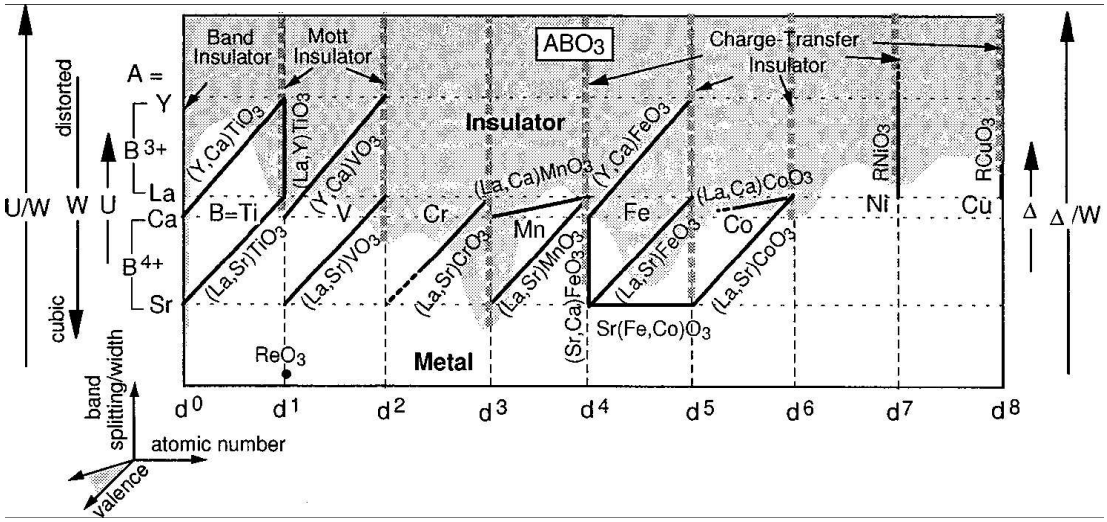

Figure 1.2: Schematic metal-insulator Phase diagram for filling control (FC) and bandwidth control (BC) 3d transition metal oxides with perovskite structure [reproduced from Ref. 2].

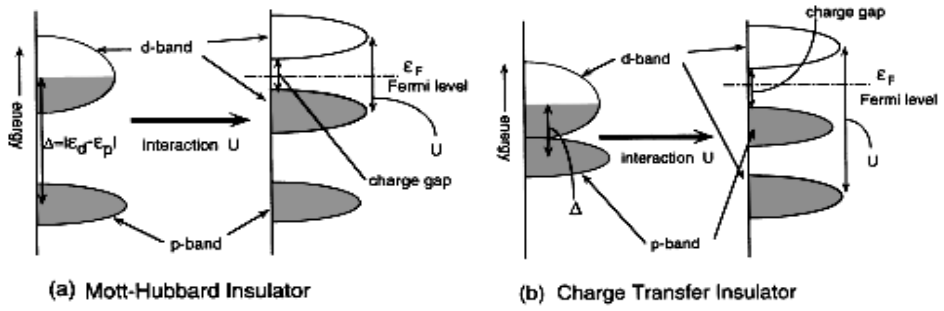

Figure 1.3: Schematic illustration of energy levels for (a) a Mott-Hubbard insulator and (b) a charge-transfer insulator generated by the *d*-site interaction effect.

Figure 1.3 shows the schematic energy level diagram for Mott-Hubbard and charge transfer insulators. Charge transfer gap becomes narrower for the end members of 3d series and hence the $LaNiO_3$ and $LaCuO_3$ have metallic character. However, the situation becomes more complex for the middle 3d members those may be Mott-Hubbard or charge transfer insulators depending on the magnitude of the on site Hund's coupling energy and the dominating pairing energy. Also, it can be noted from fig.1.2 that, YBO_3 shows stronger electron correlation than $LaBO_3$ because of reduced bandwidth (W) due to B-O-B bending in the distorted perovskite structure. Partial substitution of trivalent cation at A-site by a divalent cation results into a composition with a general formula $(A_{1-x}A'_x)BO_3$ (A = La, Pr, Nd, Y, etc; A′ = Ca^{2+}, Sr^{2+}, etc) leads to x amount of fractional B valency which drives the parent insulating system to metallic. However, in certain cases, the compounds remain insulating for large ratio of the on-site Coulombic interactions U and bandwidth (W) [2].

The general electronic structure and physical properties of perovskite related structures are governed by the following key energy terms, namely,

i) On-site (U) and intersite (V) Coulombic interactions,

ii) Hund's coupling energy (J_H) which defines the transfer integral (t_{ij}) which in turn modify one electron bandwidth (W),

iii) Charge transfer energy (Δ) arising due to the crystal field splitting of transition metal 3d orbital in the presence of oxygen ligand 2p orbitals and

iv) Electron-phonon interaction term coming due to the orbital ordering and/or Jahn-Teller (JT) distortion (δ_{JT}) [3].

For U < Δ, charge excitations across that gap are realized by d-d Coulomb interaction (U_{dd}) of the type $(d^n)_i + (d^n)_j \rightarrow (d^{n-1})_i + (d^{n+1})_j$, where i and j denotes the transition metal sites, at a cost energy U_{dd}. While for U > Δ, p-d charge transfer excitations are realized by $p^6(d^n) \rightarrow p^5(d^{n+1})$ at a cost energy (U_{pd}), which is the energy required to transfer an electron from the filled ligand p orbitals to the empty metal d orbitals [4]. For 3d transition metal oxides, the values of U_{dd} and U_{pd} are as large as 4-8 eV [5,6].

The crystal field effects have to be considered while talking about the perovskite structured transition metal oxides, since the transition metal 3d orbitals are degenerate in presence of oxygen ligand 2p orbitals. The octahedral crystal field splits (Δ ~ 10Dq) the five 3d ($3d_{xy}$, $3d_{yz}$, $3d_{zx}$, $3d_{3z^2-r^2}$ and $3d_{x^2-y^2}$) orbitals into three t_{2g} ($3d_{xy}$, $3d_{yz}$, $3d_{zx}$) (directed into the plane) localized and two e_g ($3d_{3z^2-r^2}$ and $3d_{x^2-y^2}$) (directed towards the axes) itinerant orbitals. Figure 1.4 shows the crystal field splitting for cubic and tetragonal symmetry along with the representative interactions of $3d_{3z^2-r^2}$ and $3d_{x^2-y^2}$ orbitals with ligand 2p orbitals forming σ bonding which belongs to e_g symmetry and interactions of $3d_{xy}$ orbital with ligand 2p orbital forming π bonding belonging to t_{2g} symmetry. If the splitting Δ between t_{2g} and e_g is smaller than the Hund's rule coupling ($J_H > 0$), high spin states are realized as in $Mn^{3+}(3d^4)$ and $Fe^{3+}(3d^5)$, while for the opposite case, $\Delta > J_H$, low

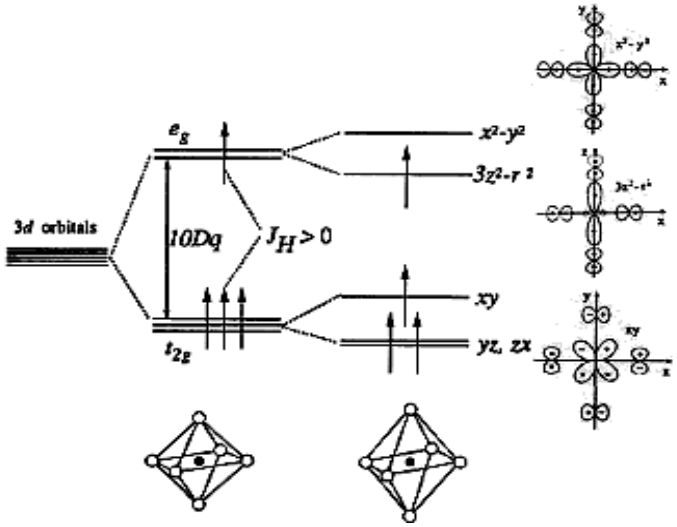

Figure 1.4: Schematic representation of cubic crystal field splitting of 3d transition metal ions with central ion and ligand ion relevant orbitals corresponding to e_g and t_{2g} symmetry.

spin states are enforced as in $Co^{3+}(3d^6)$. From the experiments, the value of octahedral crystal field splitting (Δ), in manganites is ~ 1-2 eV whereas the on site Hund's coupling (J_H) energy lies in the range ~ 2 eV [7,8].

This orbital degeneracy of t_{2g} and e_g is further lifted by Jahn Teller (JT) distortion since a nonlinear molecule with orbitally degenerate electronic states must undergo a distortion to get rid of the degeneracy and to lower the energy and symmetry [8]. It occurs in a metal ion having an odd number of electrons in the e_g level having magnitude ~ 0.5-1.5 eV and the system with such a electronic configuration exhibiting this effect are $Mn^{3+}(3d^4)$ and $Cu^{2+}(3d^9)$. The JT splitting for Cu^{2+}($t_{2g}^{6+}e_g^3$) is shown in fig.1.5, which distorts the octohedral symmetry of the parent compound by creating the four short (in ab-plane) and two long (c-elongation) Cu-O bonds when $3d^2_{3z^2-r^2}$ is fully occupied and $3d^1_{x^2-y^2}$ is half filled.

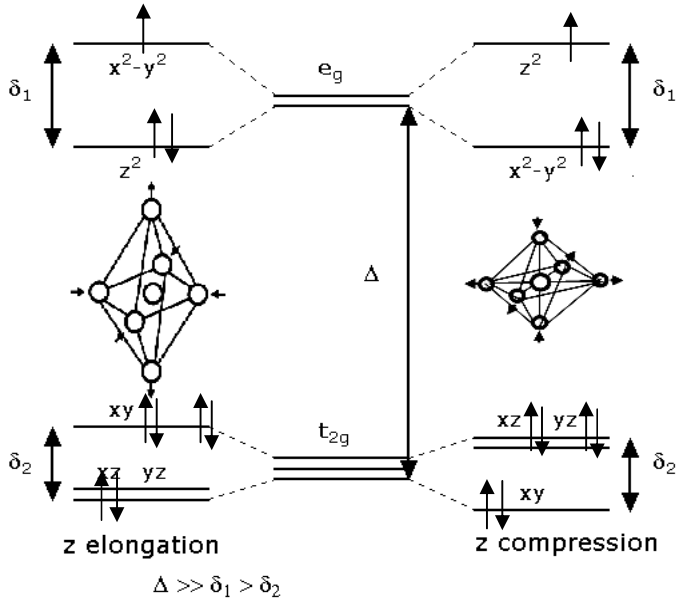

Figure 1.5: Schematic representation of Jahn Teller effect in Cu^{2+} ($3d^9$) system

The JT effect arises because the energy gained due to this splitting of degeneracy, which is linear in distortion and at a cost of lattice elastic energy and by the restriction that if undistorted structure has a centre of symmetry, the distorted structure will also have a centre of symmetry. The phenomenon is termed static if the degeneracy of e_g level is removed by the splitting as in $LaMnO_3$ [9]. The JT effect is termed dynamic when structure oscillates among all tetragonal structure and at any instant its like distorted but on its time average appears undistorted. In Cu^{2+}, JT distortion exclusively assumes four

fold, five fold or six fold coordination whereas in high spin state of Mn^{3+} ($3d^4$), JT distortion reveals in an octahedral geometry.

The ideal perovskite with cubic symmetry is not very common. The distorted perovskite posses reduced symmetry which is important for the exhibition of physical properties such as ferroelectricity, antiferromagnetism, ferromagnetism, superconductivity, thermal conductivity, metal-insulator transition in these compounds having potential applications. The crystallographic distortions can be lifted by five factors namely: i) tolerance factor, ii) average A-site cationic radius, iii) size variance, iv) carrier density/doping and v) Jahn Teller (JT) distortion. Each factor has been described, in brief, in the following section of this chapter. These factors are found to control the structural, electronic and magnetic properties of mixed oxide perovskites and have proved to be efficient handle for optimizing the materials properties for their desired applications.

I. Tolerance factor (*t*)

Goldschimdt tolerance factor is the geometric ratio of the $d\langle$A-O$\rangle$ and $d\langle$B-O$\rangle$ bond distances and can be determined using,

$$t = \frac{(< r_A > + r_O)}{\sqrt{2}(< r_B > + r_O)} = \frac{d\langle A - O\rangle}{\sqrt{2}\, d\langle B - O\rangle}$$

where $<r_A>$, $<r_B>$ and r_O are the average A-site, B-site cation and anion ionic radii (purely ionic bonding is assumed) respectively. Also, it turns out that, the vertex sharing stacking of the cubic perovskite structures are stabilized for the t values between $0.89 < t < 1$, where structure changes to rhomobedral for $0.96 < t < 1$ and orthorhombic for $t < 0.96$ which sets the critical limites of $<r_A>$ and $<r_B>$ cationic radii. For $A^{3+}B^{3+}O_3$ compounds these are $r_A > 0.90$Å and $r_B > 0.51$Å. Figure 1.6 shows the general $<r_A>$-$<r_B>$ phase diagram for $A^{3+}B^{3+}O_3$ compounds based on ionic size consideration [10].

The $\langle$A-O$\rangle$ and $\langle$B-O$\rangle$ are the equilibrium bond lengths between rare earth cations and transition metal cations and oxygens respectively, which have different thermal expansion and compressibilities and hence $t = t$(T, P) is unity for only a single temperature value at a given pressure. The structure is ideally cubic when t is unity with B-O-B bond angle 180°. Accommodation of a $t < 1$ or $t > 1$ makes the system strained and drives it towards the lower symmetry space group, away from its ideal cubic symmetry.

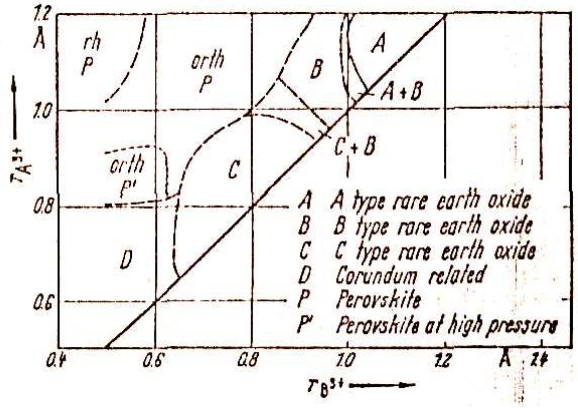

Figure 1.6: The general $<r_A>$-$<r_B>$ phase diagram for $A^{3+}B^{3+}O_3$ compounds based on ionic size consideration. [reproduced from Ref. 10]

For instance, $t < 1$, turns into the ⟨B-O⟩ bond under compression and ⟨A-O⟩ bond under tension, and decreases the space group symmetry from cubic by accompanying a cooperative rotation of the corner-shared $BO_{6/2}$ octahedra so as to reduce the B–O–B bond angle from 180° to (180°−φ). As t is reduced from $t = 1$, rotations about the [001] axis give tetragonal *I*4*/mcm* symmetry; these rotations are followed at smaller t by rotations about [111] to give rhombohedral *R*3*c* symmetry and then about [110] to give orthorhombic *Pbnm* (or *Pnma*) symmetry. The bending angle φ increases with decreasing t, changing discontinuously on going from one cooperative rotation to another as shown in fig.1.7 [11]. For $t > 1$, hexagonal face sharing staking of octahedron is dominated instead of the cubic vertex sharing staking of octahedron which is the case for $t < 1$.

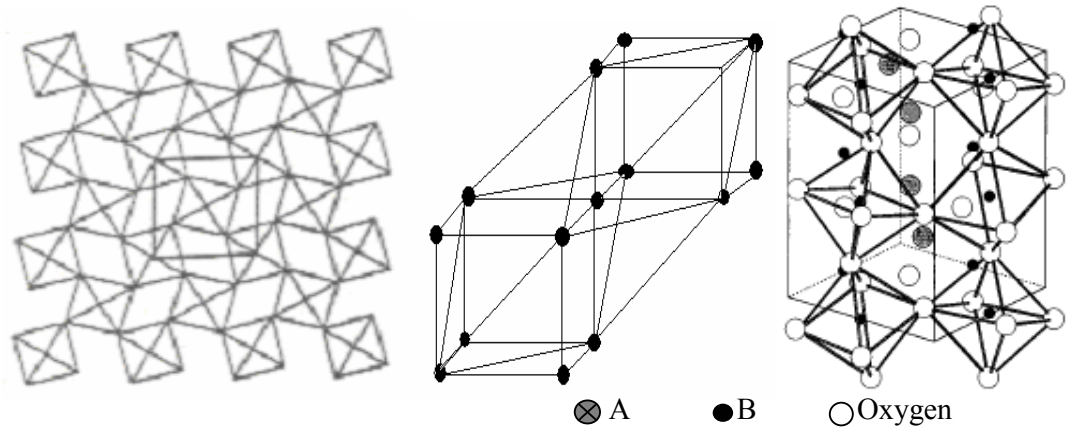

Figure 1.7: Cooperative BO_3 rotations giving (a) tetragonal (projection on (001)) of BO_3 array (b) rhombohedral and (c) orthorhombic (P*bnm* axes) symmetry. Note: P*bnm* axes a, b, c, becomes c, a, b, in P*nma.*

II. Average A-site cationic radius <r_A>

Average A-site cationic radius <r_A> can be determined using the following formula,

$$<r_A> = \sum_i x_i r_i$$

where, r_i is the ionic radii of i^{th} cation. The variation of <r_A> at A-site cation in ABO_3 has a similar effect as an external pressure which enhances the B-O-B transfer integral through a change in B-O-B bond angle and a measure of the degree of radial distortion of the BO_6 octahedra [12]. There is a linear relationship found between T_C and <r_A>, those have an inverse correlation with MR [13]. The quantity, <r_A> is also characterized the one electron bandwidth (w) as,

$$w \cong \frac{\cos 1/2[\pi - (B-O-B)]}{d_{B-O}^{3.5}}.$$

A smaller change in average <r_A>, gives rise to the structural distortion at B-O-B bond angle up to a large extent and hence bending of B-O-B bond angle which in turn tilting the $BO_{6/2}$ octahedra for t <1 and narrowing the e_g electron bandwidth and thereby affecting the matrix elements for the electronic transport [14].

III. Size variance (σ^2)

This factor is related to ionic mismatch due to the doping of divalent alkali, alkaline earth cations or trivalent rare earth cations at A-site, first introduced by Rodriguez-Martinez and P. Attfield and has been described as,

$$\sigma^2 = \sum x_i r_i^2 - < r_A >^2$$

where, x_i is the fractional occupancies of the different i cations of r_i radii. Size variance is attributed to displacements of the oxygen atoms due to the *A* site disorder, as shown by the simple model in fig.1.8 [15]. This shows that σ provides a measure of the oxygen displacements *Q* due to *A* cation size disorder and that (r_A^0 - <r_A>) is the complementary measure of displacements due to <r_A> being less than the ideal value r_A^0 .

The analogous effect of increasing σ^2 have been extensively investigated for $A_{0.7}A'_{0.3}MnO_3$ [A = La^{3+}, Pr^{3+}, Sm^{3+}, Pm^{3+} and Nd^{3+} and A′ = Ca, Sr and Ba] at fixed carrier concentration x = 0.3 and <r_A> which shows the linear reduction in T_P with σ^2 [16].

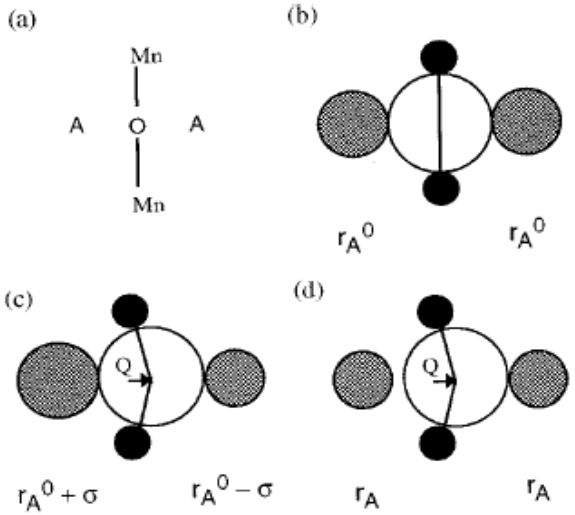

Figure 1.8: Model for local oxygen displacements in AMnO$_3$ perovskites. A fragment of ideal cubic structure with A cations of radii r_A^0 is shown schematically in (a) and as spherical ions in (b). Cation size disorder in (c) gives rise to random oxygen displacements $Q = \sigma$ and a reduction in the A site radius in (d) leads to ordered oxygen displacements $Q = r_A^0 - r_A$.

Recently, similar kind of correlations have been established between superconducting transition T_c and σ^2 for $A_{1.85}A'_{0.15}CuO_4$ (A = La-Eu and A′ = Ca, Sr and Ba) [17]. Increasingly, the structural disorder creates local oxygen displacements and hence the structural fluctuations at B-O-B angle and B-O distance, which results into carrier localization due to the Jahn-Teller distortion of BO_6 octahedra and thereby affecting the electrical transport, T_P and T_c in manganites and HTSC.

IV. Carrier density

Doping determines the carrier concentration and sign of the charge carriers (i.e. positively charged holes or negatively charged electrons) into $(A'O)_m\bullet(ACuO_{3-\delta})_n$ and $A_{1-x}A'_xMnO_3$ (A = Rare earth cation, A′ = divalent or trivalent smaller cation; n = 1, m=1) type of layered cuprates and mixed valent manganite systems respectively. Carrier density decides the fluctuated valence of the transition metal cations i.e. Cu^{1+}/Cu^{2+} or Cu^{2+}/Cu^{3+} in cuprates and Mn^{3+}/Mn^{4+} in manganites which are responsible for charge transfer mechanism in former whereas the ferromagnetic Zener Double Exchange (ZDE) in the later [18,19].

At a fixed amount of doping, perovskite oxide/compounds exhibit very rich phase diagram as a function of temperature, magnetic field, external and internal chemical pressure, etc. which in turn governs their physical properties.

V. Jahn Teller (JT) distortion

This effect is extremely important in modifying the electronic and magnetic transport properties of perovskites, by possible displacements of oxygen anions along the direction of B-O-B bonding in (*001*) basal planes of corner shared B-sites; these sites may be octahedral, square pyramidal or square coplanar. As a result, the electronic properties are strongly anisotropic [20].

Physical properties of the perovskite structures, stoichiometric manganites and layered high T_c cuprates depend to a great extent upon five parameters described above and their effects on structural, transport and magnetotransport properties of La-based HTSC and manganite samples have been discussed in detail in the chapters 3, 4 and 5 of the present work.

1.2 High temperature superconductors

1.2.1 History and developments

The phenomenon of **superconductivity** was discovered by a Dutch physicist Kamerlingh Onnes at Leiden in 1911, in which material undergoes an abrupt transition from normal state of electrical resistivity to zero resistivity as it is cooled below to a certain superconducting transition temperature (T_c) under critical field (H_c) having critical current density (J_c) [21]. Superconductivity occurs in a wide range of materials, including metallic elements of the periodic table, binary and ternary alloys, intermetallics, organic compounds, borocarbides, chalcogenides and heavily-doped semiconductors having low $T_c < 25K$. All these materials are called as classical/conventional superconductors, as the superconductivity in them is caused by a force of attraction between certain conduction electrons arising from the exchange of phonons, which causes the conduction electrons to exhibit a superfluid phase composed of correlated pairs/cooper pairs of electrons which has been explained by the BCS theory of superconductivity [22]. As long as the superconductor is cooled to very low temperatures, the Cooper pairs stay intact, due to the reduced molecular motion. As the superconductor gains heat energy the vibrations in the lattice become more violent and break the pairs and superconductivity vanishes. There

exist another class of unconventional superconductors containing copper oxygen layers and chains, belonging to perovskites, exhibiting quite higher T_c (>77K) as compared to conventional superconductors, known as high temperature superconductors (HTSC). Even after twenty years of the discovery of high temperature superconductivity, there is lack of complete unified recognized theory to understand the quantum mechanical phenomenon of high temperature superconductors and hence remains a novel field of research attraction [23]. Superconductors have strong application potential in transmission lines, power generators and storage, superconducting maglev trains, MRI, SQUID, biomedical, military applications and to develop the superconducting X-ray detectors, cameras and optical devices. Synthesis of superconducting nanoroads and understanding of their properties is a challanging task.

1.2.2 Properties of high T_c cuprates

Discovery of high temperature superconductivity in 1987 by Bednorz and Muller in La-based cuprate $La_{2-x}A_xCuO_4$ (La-214, T_c ~ 40K) superconductor followed by the discovery of $Y_1Ba_2Cu_3O_{7-\delta}$ (Y-123, T_c ~ 90K) (YBCO) by P. Chu and Wu renewed the considerable interest in perovskite related structures exhibiting superconducting transition (T_c) above LN_2 temperature and into the realm of practical applications [24,25]. The T_c increased above 100K in Bi-Ca-Sr-Cu-O (~110K), Tl-Ca-Ba-Cu-O (~125K) and in Hg-Ca-Ba-Cu-O (~138K) systems [26-28]. A considerable interest in the study of these fascinating oxides has been largely attributed to the tunability of properties by elemental substitution for increasing superconducting T_c or J_c or H_c.

The high temperature cuprate superconductors exhibit T_c at the crossover from localized to itinerant electronic behavior as a function of either the *d*-electron bandwidth and/or valence state of the transition-metal ion. It has been argued that the origin of high temperature superconductivity in cuprate superconductors is characterized by the phenomenon of Quantum Critical Point and identified by the electron-phonon hybridization associated with cooperative bond length fluctuations and ordering of correlated pairs into the CuO_2 layer [20]. The cuprates are type-II superconductors where the superconductivity is quenched progressively by an external magnetic field and dose not occur globally at a critical field H_c as in type–I superconductors. Figure 1.9 (a) shows the resistance versus Temperature plots for YBCO whereas its magnetic behavior as a function of temperature and applied magnetic field is shown in fig.1.9(b).

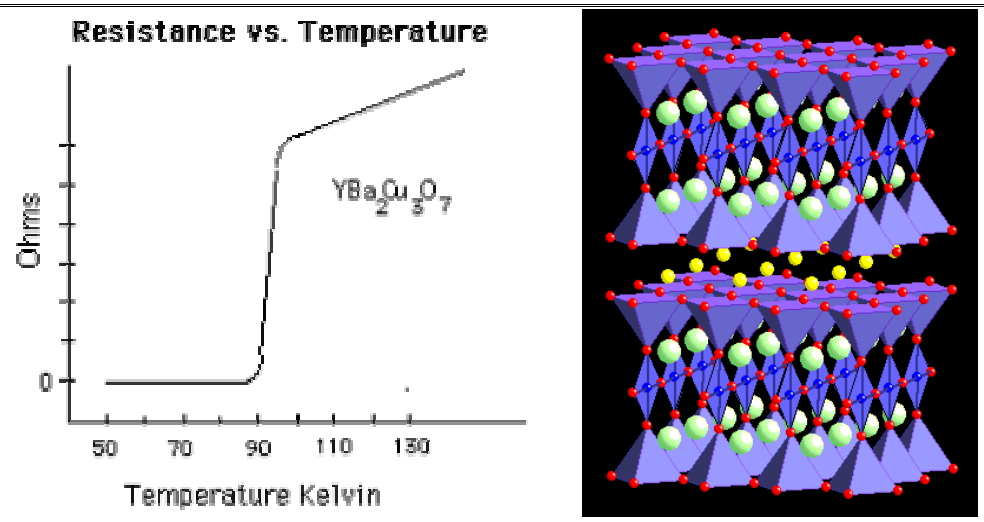

Figure 1.9(a): Resistivity (Ohms) versus Temperature (K) plots for $YBa_2Cu_3O_z$ (Y-123).

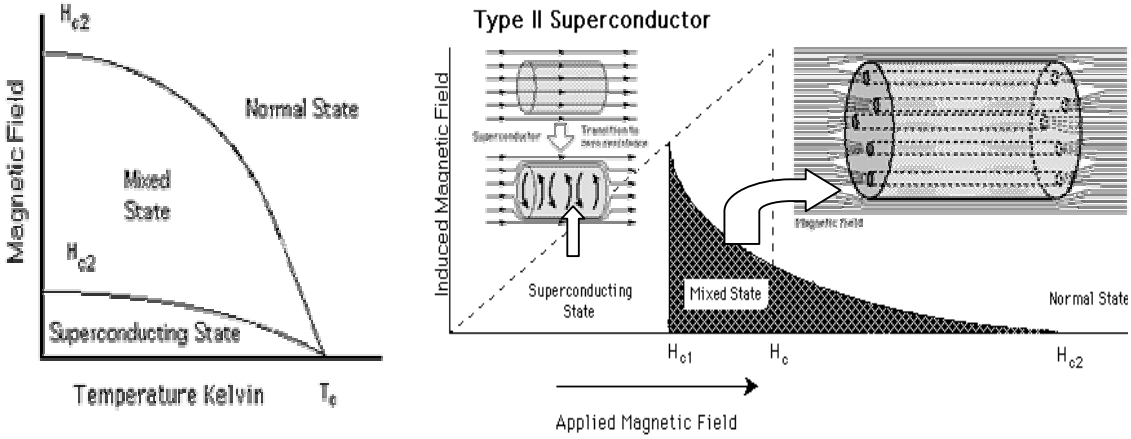

Figure 1.9(b): Magnetic field versus Temperature (K) plots for $YBa_2Cu_3O_z$ (Y-123).

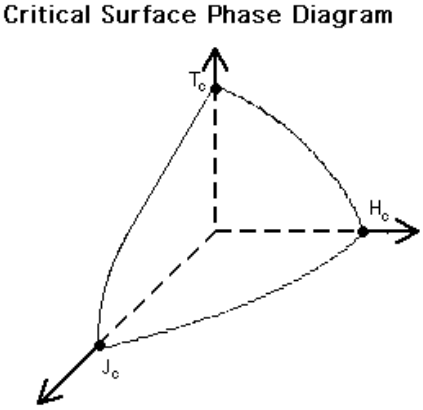

Figure 1.9(c): Phase diagram of critical temperature (T_c), critical field (H_c) and critical current density (J_c) below which high temperature superconductivity exist.

Thus, the superconducting state is defined by three very important factors: critical temperature (T_c), critical field (H_c) and critical current density (J_c). Each of these parameters is very much dependent on the other two properties present. The phase diagram in fig.1.9(c) demonstrates relationship between T_c, H_c, and J_c. Considering all three parameters, the plot represents a critical surface and moving toward the origin, the material is superconducting whereas regions outside this surface the material is normal or in a lossy mixed state. Higher H_c and J_c values depend upon two important parameters which influence energy minimization, penetration depth (λ) and coherence length (ξ). The λ is the characteristic length of the fall off of a magnetic field due to surface currents. Coherence length is a measure of the shortest distance over which superconductivity may be established. In layered cuprates the values of $\xi_{\perp} \sim 3$Å and $\xi_{//} \sim 10$Å whereas in conventional superconductors its value is ~ 1000Å [29].

Tetragonal structure of parent La-214 compound is the simplest example of intergrowth structure of the Ruddlesden-Popper phases $AO{\cdot}(AMO_3)_n$ [Fig.1.10(a)] [30]. However, an orthorhombic distortion about a [110] axis introduced by a cooperative rotation of the CuO_6 for $t_{2D} < 1$ [arrows in Fig. 1.10(a)]. Further, both the high spin Cu(II) and low-spin Cu(III) are also stable in square-pyramidal or square-coplanar sites, which allows the layered copper oxides to accommodate a large family of structures. By accompanying the A-site cation (La^{3+}, Ba^{2+}, Sr^{2+}, Pb^{2+}, etc) with relatively smaller size cations (Y^{3+} or Ca^{2+}) may leave it stable in eight fold coordination, rather an ideal twelve fold coordination causing the loss of oxygen and thus forms A′ layer instead of AO layers when placed between two CuO_2 layers. With this kind of atomic arrangements, CuO_2 layer is in square pyramidal coordination with AO layer at one end and A′ layer at the other; and square coplanar when two adjacent A' layers. It is also possible to place more A′ layers in between two AO layers. A large promising array of p-type superconductors thus can be designated by placing such A′ layers on traversing c-axis and can be presented by,

$$AO \cdot CuO2 \cdot AO \quad (1.2a)$$

$$\Phi \cdot AO \cdot CuO2 \cdot AO \cdot \Phi \quad (1.2b)$$

$$\Phi \cdot AO \cdot CuO2 \cdot A' \cdot CuO2 \cdot AO \cdot \Phi \quad (1.2c)$$

$$\Phi \cdot AO \cdot CuO2 \cdot A' \cdot CuO2 \cdot A' \cdot CuO2 \cdot AO \cdot \Phi \quad (1.2d)$$

$$\Phi \cdot AO \cdot CuO2 \cdot A' \cdot CuO2 \cdot A' \cdot CuO2 \cdot A' \cdot CuO2 \cdot AO \cdot \Phi \quad (1.2e)$$

[Φ is the representative layers between two AO layers]

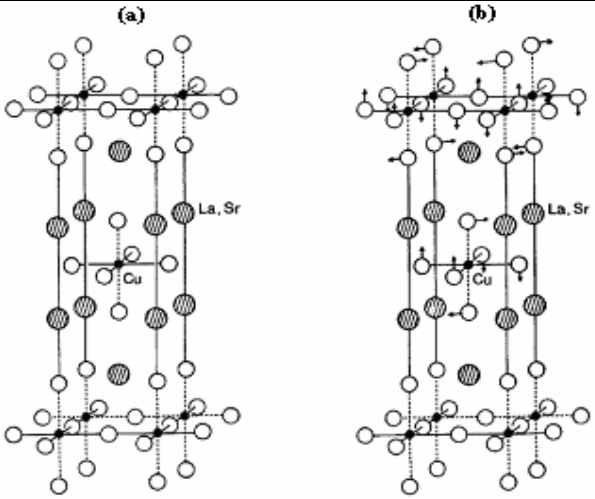

Figure 1.10(a): Structures of (a) tetragonal (T) and (b) orthorhombic (O) La_2CuO_4. The arrows represent the direction of tilting of the CuO_6 octahedra.

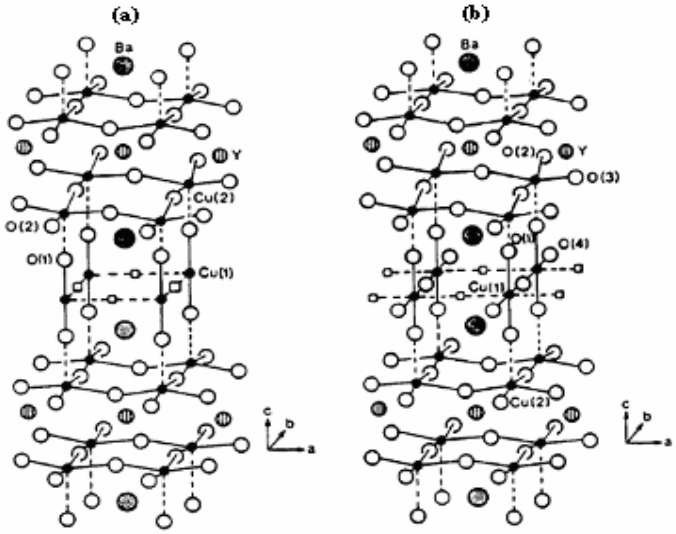

Figure 1.10(b): Structures of (a) tetragonal $YBa_2Cu_3O_6$ and (b) ideal orthorhombic $YBa_2Cu_3O_7$.

In this representative, La-214 is given by (1.2a), Y-123 by (1.2c), Bi-2212 by (1.2c) Tl-21, Tl-2212 and Tl-2223 by [1.2(b) – 1.2(d)] and Hg-1223 by (1.2d) respectively [20].

The $YBa_2Cu_3O_{6+x}$ (YBCO) structure of representation (1.2c) is shown in fig.1.10 (b). The Y^{3+} ions occupy the A′ layer and the Cu(III)/Cu(II) of the CuO_2 sheets are in square pyramidal oxygen coordination. The two BaO layers are bridged by linearly coordinated Cu(I) in the parent tetragonal compound $YBa_2Cu_3O_6$; oxidation occurs by introducing oxygen into the layer of bridging copper to form chains of corner-shared square-coplanar Cu(III)/Cu(II). The Cu(III)/Cu(II) redox band of the $\Phi = CuO_x$ chains

overlap in CuO_2 sheets and the chain segments are, therefore, commonly referred to as a charge-reservoir layer [31].

In summary, the layered copper oxides have been found to exhibit a remarkable ability to oxidize layers containing CuO_2 sheets in a variety of ways without changing the oxygen coordination of the Cu atoms of a sheet even though the Cu atoms of a given sheet may occupy octahedral, square-pyramidal or square-coplanar sites. Where the oxygen coordination or its orientation varies from Cu to Cu in a CuO_2 sheet, superconductivity is suppressed by the resulting perturbation of the two-dimensional (2D) periodic potential. The presence of two different A or A′ cations in adjacent layers perturbs the periodic potential to a lesser extent; it lowers the critical temperature T_c without completely suppressing superconductivity. The superconductivity in the copper oxides occurs in the CuO_2 sheets and appears to be a 2D phenomenon although coupling along the c-axis also occurs. This anisotropic character of the copper oxide superconductor has made processing of these oxides for technical applications a difficult task. The formal number of Cu*(*III*)/*Cu atom (i.e. number of positive charge carriers per Cu atom) in a CuO_2 sheet that gives the highest value of T_c for a given p-type system is always in the range 0.15–0.18; at this state of oxidation, the superconductors all appear to be single phase below T_c. Although a given system may have a large range of oxidation states at higher temperatures, the superconductive phases are all confined to a narrow range of oxidation states of the CuO_2 sheets. The superconductive phase is thus seen to be a thermodynamically distinguishable phase that is stabilized at low temperatures at a crossover from localized to itinerant electronic behavior [32].

1.2.3 Applications

Transportation

Superconductors have variety of applications - the most obvious being as very efficient conductors; if the national grid were made of superconductors rather than aluminium, then the savings would be enormous - there would be no need to transform the electricity to a higher voltage (this lowers the current, which reduces energy loss to heat) and then step it down again. Superconducting magnets are also more efficient in generating electricity than conventional copper wire generators - in fact, a superconducting generator about half the size of a copper wire generator is about 99% efficient; typical generators are around 50% efficient.

Magnetic Levitation

So-called 'MagLev' trains such as the Yamanashi MLX01 train have been under development in Japan for the past two decades - the train floats above the track using superconducting magnets; this eliminates friction and energy loss as heat, allowing the train to reach very high speeds.

Magnetic Resonance Imaging (MRI)

MRI is a technique developed in the 1940s that allows doctors to see what is happening inside the body without directly performing surgery. The development of superconductors has improved the field of MRI as the superconducting magnet can be smaller and more efficient than an equivalent conventional magnet.

Synchrotrons and Cyclotrons (Particle Colliders)

Particle Colliders like CERN's Large Hadron Collider (LHC) are similar to very large running tracks that are used to accelerate particles (i.e. electrons, positrons, hadrons and more) to speeds approaching the speed of light before they collide with one another or other atoms, usually to split them (this was how many sub-nuclear particles such as τ and neutrinos were discovered). By cycling the particles using magnetic fields, continually the speed of the particle is increased. The first project to use superconducting magnets was the proton-antiproton collider at Fermilab.

Superconducting Quantum Interference Devices (SQUID)

Superconducting Quantum Interference Device (SQUID based on the principle of quantum mechanical phenomenon of Josephson Effect, uses the tunneling of correlated electron pairs between superconductors separated by an insulating barrier having thickness ~ 10 to 20Å. By using this device it is possible to detect very small changes in fields with sensitivity ~10^{-14} T. When a flux line penetrates this loop, it generates current in the loop which is lower than J_c and finally produces voltage across the two Josephson junctions which makes it possible to detect the magnetic field. Looking ahead to HTSCs, a SQUID operating at 77 K could be expected but with the noise about 20 times greater.

Fast Electronic Switches

Type II superconductors can be used as very fast electronic switches (as they have no moving parts), due to the way in which a magnetic field can penetrate into the

superconductor - this has allowed Japanese researchers to build a 4-bit computer microchip (compared to today's 32-bit and 64-bit processors) operating at about 500 times the speed of current processors, where heat output is currently a major problem with typical speeds approaching the 1GHz mark.

An article in Superconductor Week focuses upon the efforts of NASA, DARPA and others to build a 'petaflop' (a thousand-trillion floating point operations per second - compared to today's 'teraflop' (1 trillion Flops per sec) using superconductor technology.

Military applications

Superconductors have also found widespread applications in the military. HTSC SQUIDS are being used by the U.S. navy to detect mines and submarines. Significantly smaller motors are being built for military ships using superconducting wire and "tape". American Superconductor unveiled a 5000-horsepower motor made with superconducting wire and expects to deliver an even larger 36.5MW HTS ship propulsion motor.

In addition to reduce power requirement, size and weight, the newest application for HTS cables is in the degaussing of naval vessels which eliminates residual magnetic fields that might otherwise give away a ship's presence.

The size of the low frequency longer antennas can be reduced by employing the use of superconducting tape. The Electronic Materials and Devices Research Group at University of Birmingham (UK) is credited with creating the first superconducting microwave antenna. Applications engineers suggest that superconducting carbon nanotubes might be an ideal nano-antenna for high-gigahertz and terahertz frequencies, once a method of achieving zero "on tube" contact resistance is perfected.

The most ignominious military use of superconductors may come with the deployment of "E-bombs". These are devices that make use of strong, superconductor-derived magnetic fields to create a fast, high-intensity electro-magnetic pulse (EMP) to disable an enemy's electronic equipment.

Other emerging applications

Among emerging technologies is a stabilizing momentum wheel (gyroscope) for earth-orbiting satellites that employs the "flux-pinning" properties of imperfect superconductors to reduce friction to near zero. Superconducting x-ray detectors and ultra-

fast, superconducting light detectors are being developed due to their inherent ability to detect extremely weak amounts of energy. Already Scientists at the European Space Agency (ESA) have developed what's being called the S-Cam, an optical camera of phenomenal sensitivity. And, superconductors may even play a role in Internet communications soon since internet traffic is increasing exponentially, superconductor technology is being called upon to meet this *super* need.

1.3 Colossal Magnetoresistance (CMR) manganites

1.3.1 Introduction

The discovery of negative colossal magnetoresistance (CMR) (~ 99 %) in mixed valent manganites of the type $A_{1-x}A'_xMnO_3$ (A = trivalent rare earth cation, A′ = divalent alkali or alkaline earth cation) initiated the renewed interest of researchers working in the field of perovskite materials. This new class of ABO_3 type compounds posses several interesting and interrelated properties. The magnetic properties of these correlated perovskites are closely related to the electronic ones which are relatively easy to measure. Magnetoresistance (MR) is defined as the change of resistance of the material on the application of external applied field and has been formulated as,

$$MR\% = \frac{\rho_0 - \rho_H}{\rho_0} \times 100$$

where ρ_0 and ρ_H are the resistivities without and with applied field. MR is positive for the metals and metallic alloys having very small value ~ 1% while it is negative for the magnetic and semiconducting multilayers having value ~ 20-50 %, such a large negative MR is termed as “Giant Magnetoresistance” (GMR). Magnetic multilayers of certain kind as Fe/Cr and Cu/Co coupled antiferromagnetically shows such a large GMR which have their strong potential for device fabrication [33-35]. In manganites, negative MR is as large as 100 % and hence termed “Colossal Magnetoresistance” (CMR). The discovery of large negative CMR in $A_{1-x}A'_xMnO_3$ manganites thin films by Von Helmolt *et al* [36], Charara *et al* [37] and Jin *et al* [38] almost simultaneously, renewed a considerable interest of scientific community in these compounds. Owing to the CMR effect, manganites have a strong application potential in magnetic memory read heads, bolometric and magnetic field sensors and in HTSC-CMR hybrid heterostructure devices [39].

Several materials, metals, metallic alloys, semiconductors, magnetic materials and their multilayers exhibit MR properties but the origin of MR effect in these materials phenomenologically differs from one to another. Depending upon its origin, MR can be broadly classified as: Anisotropic Magnetoresistance (AMR), Granular or Tunneling Magnetoresistance (TMR), Giant Magnetoresistance (GMR) and Colossal Magnetoresistance (CMR).

Anisotropic Magnetoresistance (AMR)

Anisotropic magnetoresistance has its origin in the change in resistivity because of the change of direction of applied magnetic field (H) to that of the applied current may be applied in parallel or perpendicular to the direction of current [40]. AMR is a measure of magnetic field induced anisotropy in resistivity of different current vectors (aligned parallel or perpendicular). The resistivity increases when H is parallel to the current whereas the resistivity decreases when H is perpendicular to the direction of current.

Granular and tunneling magnetoresistance (TMR)

The granular magnetoresistance has its origin in spin polarized conduction of carriers at grain boundaries which act as a insulating barriers for charge carriers [41]. The application of magnetic field suppresses this spin dependent scattering process of carriers at insulating grain boundaries and the resulting magnetoresistance is called granular magnetoresistance. This form of MR is also evident in artificially grown magnetic tunnel junctions where the junction boundary act as insulating barrier for carrying the conduction current and resulting MR is tunneling magnetoresistance (TMR) [42].

Giant magnetoresistance (GMR)

Giant Magnetoresistance effect arises from spin dependent transmission of the conduction electrons between two ferromagnetic layers through the thin nonmagnetic spacer layers [33]. The MR effect is obtained in antiferromagnetically coupled magnetic multi layers/superlattices (Fe/Cr, Cu/Co etc.) by aligning the magnetizations of adjacent ferromagnetic layers with an external field. Owing to large amount of MR ~ 20–50 %, name ‘Giant magnetoresistance’ (GMR) was given to emphasize the strength of MR in these materials.

Colossal magnetoresistance (CMR)

The discovery of MR, as large as ~100%, in $La_{2/3}Ba_{1/3}MnO_3$ manganite thin films around room temperature with many interesting inter related phenomena, led the scientists to coin a new term called "colossal magneto resistance (CMR)". Unlike the other forms of MR discussed above, the CMR is an intrinsic phenomenon. The origin of CMR can be attributed to two intrinsic effects: i) reduction in spin disorder at Mn-O-Mn bonds by an externally applied magnetic field and ii) reduction in scattering of charge carriers at grain boundaries. The former dominates around the electronic transition (T_P) whereas the later effects of grain boundaries seem to be dominating at substantially low temperatures (below T_P) [38]. In addition to CMR properties, manganites exhibit several interesting and interrelated structural and physical properties which are extremely important from basic research as well as application point of view.

1.3.2 Properties of CMR manganites

Mixed valent manganites of the type $A_{1-x}A'_xMnO_3$ exhibits varieties of fascinating properties which are governed by the different change transport and hopping mechanisms as discussed in brief in section 1.1.1. In addition to the large negative MR (~ 99%), they exhibit metal-insulator transition (T_P), paramagnetic-ferromagnetic transition (T_C), charge and orbital ordering (CO, OO) etc. Phase diagrams of various CMR manganites have been extensively studied and are found to depend on the doping, temperature, pressure, magnetic field and average cationic radii which modifies the structural, electrical and magnetic phase transitions in these materials (for the detailed review see Ref. 7, 43). In manganites, the metallic conductivity in ferromagnetic region, below T_C and T_P, is governed by the ferromagnetic Zener-Double Exchange (ZDE) mechanism which leads to the hopping of charge carrier from $Mn^{3+}(3d^4)$ to $Mn^{4+}(3d^3)$ via oxygen 2p orbital.

Zener Double Exchange (ZDE)

Double exchange (DE) was proposed by the Zener in order to understand ferromagnetic metallic state in manganites mediated by the spin polarized conduction of charge carriers from one Mn-site to the next [44]. The effective hopping of an electron from one Mn^{3+} ($3d^4$, t_{2g}^3, S = 3/2)-site to central oxygen and simultaneously from oxygen to Mn^{4+} ($3d^3$, $t_{2g}^3e_g^1$, S = 2) is referred to as Zener Double Exchange (ZDE). ZDE mechanism involves the hybridization of ligand oxygen 2p and manganese 3d orbitals

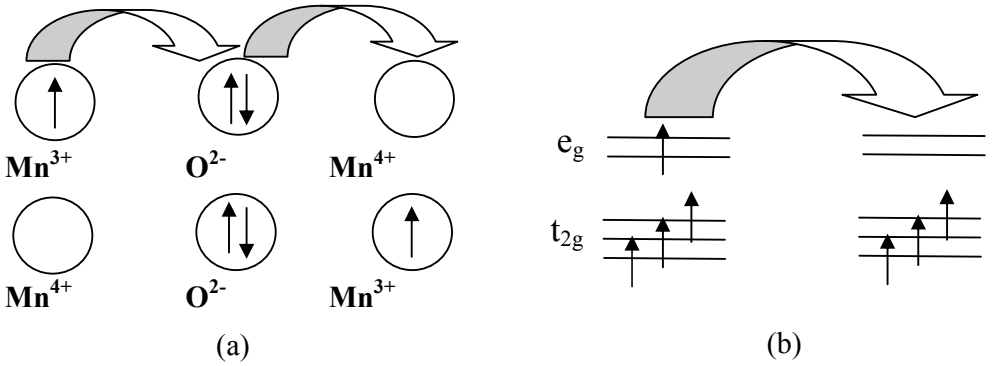

Figure 1.11: (a) Sketch of ZDE mechanism which involves two Mn ions and one O ion.

(b) The mobility of e_g electrons improves if the localized spins are polarized.

and is strongly governed by the on site Hund's rule coupling between t_{2g} and e_g states, which are the lowest energy states when spins of t_{2g} and e_g electrons are aligned parallel and favors hopping of an electron from one Mn site to the next via oxygen. This hopping/transfer process is proportional to the cos(θ/2), where θ being the angle between the nearest neighbor spins and can be given by [45],

$$t_{ij} = t_0 \cos \theta/2$$

When the θ = 0, hopping is maximum while, if θ = 1 corresponds to an antiferromagnetic background and the hopping cancels.

The ZDE mechanism explicitly explains the metallic conductivity and ferromagnetism and thereby the insulator–metal transition and paramagnetic-ferromagnetic phase transitions in manganites. ZDE is strongly affected by the distortion at Mn-O-Mn bond angle and or the Mn-Mn transfer integral and hence the effects of local structural distortion including lattice and electron-lattice interactions have to be considered. However, recent investigations suggest ZDE is not adequate for understanding the novel transport properties of manganites and overall effect can be realized based on the considerations of local symmetry as well as local lattice distortions.

Tolerance factor and Carrier Density

The structural, electronic and magnetotransport properties of manganites further depend upon two major factors, namely, the tolerance factor and the Mn^{3+}/Mn^{4+} ratio (carrier concentration) which have been discussed in detail in section 1.1.1. Depending on

one electron bandwidth, manganites are broadly classified into three categories: i) low bandwidth ii) intermediate bandwidth and iii) large bandwidth system. Figure 1.12 shows the general phase diagram of temperature versus tolerance factor for the fixed carrier density x = 0.3 for divalent doped manganite, $A_{0.7}A'_{0.3}MnO_3$ compounds. The decrease in *t* decreases the hopping integral/amplitude systematically that drives the system from large to low bandwidth system with enhanced MR and lower T_P and T_C [46].

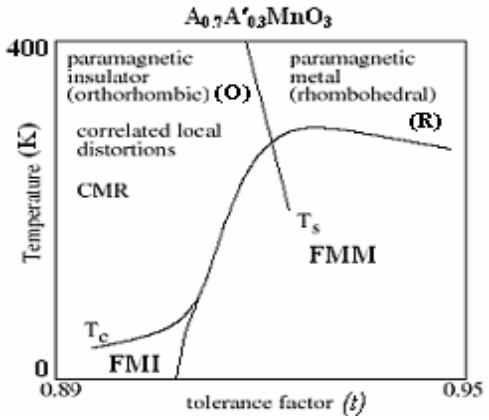

Figure 1.12: Structural and magnetic phase diagram of temperature versus tolerance factor for fixed carried density x = 0.3 for hole-doped CMR manganites $A_{0.7}A'_{0.3}MnO_3$: T_C, Curie temperature; T_s, the O to R transition temperature.

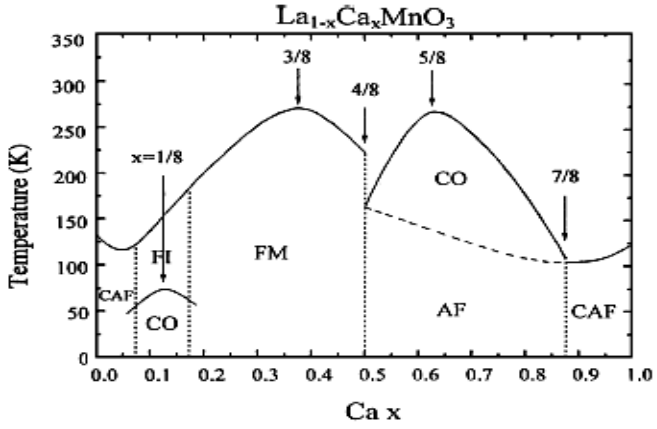

Figure 1.13: A magnetic phase diagram of $La_{1-x}Ca_xMnO_3$ [reproduced from Ref. 47].

A typical magnetic phase diagram of low bandwidth system $La_{1-x}Ca_xMnO_3$ (LCMO), established by Schiffer *et al* [47] is shown in fig. 1.13. The end members of the compounds, $LaMnO_3$ and $CaMnO_3$ are A-type and G-type antiferromagnetic (AFM)

insulators respectively. For $x < 0.18$, the system is canted AFM and FM insulators and becomes FM metallic for doping range of $0.18 < x < 0.5$ for which the compounds exhibit large CMR effect. In $0.48 < x < 0.52$ compositions, the FM metallic state transforms to charge-ordered antiferromagnetic ground state at a certain critical temperature. The AFM state in this range is of CE-type. When $x > 0.52$, a long-range C-type AFM order sets in.

1.3.3 CMR Thin films and applications

Hole doped manganese oxides $La_{0.7}A'_{0.3}MnO_3$ ($A' = Ca^{2+}$, Sr^{2+}, Ba^{2+}, etc) exhibits remarkable variation in resistivity (MR ~ 99%) as a function of applied magnetic field and temperature which makes these compounds as strong candidates for applications in bolometers, magnetic field sensors, magnetoresistive read heads, magnetic memory devices [39], requiring high quality materials in thin film forms. For the development of oxide thin films and heterostructures, basic synthesis plays an important role. The structural, surface morphology, electronic and magnetic properties of mixed oxide manganites are extremely sensitive to the synthesis conditions and method used. Further, the physical and microstructural properties of manganite thin films are considerably affected by two key factors, namely, i) substrate material mismatch (in plane) and ii) thickness induced strain (out of plane) (for detailed review see ref. 48). The details of the manganite thin film synthesis using Pulsed Laser Deposition and Chemical synthesis will be discussed in the chapter 2 of this thesis. Some of applications of manganite thin films are listed below.

Spin Valve and Magnetic recording technology

The nonvolatile magnetic memory heads requires spin polarized read heads which can exhibit MR~20-30% in few hundreds of Oe magnetic field near room temperature (RT). Thin films of $La_{0.7}Sr_{0.3}MnO_3$ (LSMO) and $La_{0.7}Ba_{0.3}MnO_3$ (LBMO) manganite compounds exhibits electronic (T_{IM}) and magnetic transition (T_C) above the RT and optimum CMR effect at these temperature but under high magnetic fields (~ 8 - 9 T) – far higher than the required low field applications. The intrinsic factor has been explored fully and it is unanimously concluded that, the MR decreases with increase in insulator-metal transition (T_{IM}) temperature and near RT the occurrence of low MR at high magnetic fields restricts the application of these materials. However, the effect of extrinsic factor has not been widely explored and there is a tremendous scope to enhance the low field MR

by exploiting grain boundary mechanism. To get low field MR, the GB region can be effectively enhanced by decreasing the grain size or by improved techniques of synthesis such as sol-gel method for bulk synthesis, single crystalline and polycrystalline thin films using CSD, PLD and MBE etc. or by engineering the artificial grain interfaces.

Temperature sensors

In manganites, the temperature coefficient of resistance [TCR % = 1/R ×dR/dT×100] shows remarkable variations with temperature for the wide temperature range, and it is positive and negative in metallic (below T_P) and in semiconducting [above T_P] regions which makes the use of them as temperature bolometric sensors. Commercially available temperature sensors exhibit TCR values ~ 4% whereas the manganites exhibit TCR and values as high as ~ 10-20% but operates at lower temperatures [49].

Magnetic field sensors

Owing to the CMR effect in a film and principle of spin valve structure, manganites can be used as magnetic field sensors. The Field coefficient of Resistance [FCR% = 1/R×dR/dH×100] of the manganites is as high as 10-25% but at relatively higher applied fields.

HTSC and CMR heterostructure Devices

Since the properties of the CMR materials are quite spectacular at reduced temperatures, i.e. below 100 K, there may be some advantages in integrating them with HTS devices. The CMR-HTSC spin injection device is the thought of one such device where the spin polarized electrons from the manganite layers are injected into the HTSC channel layers and the I-V characteristics as a function of gate current are studied.

A CMR-based sensor can be used as a flux to voltage converter owing to the large MR at fields of the order of 0.2 T which can provide a flux to voltage transformer at these temperatures [50].

Electric Field Effect Devices

The double exchange ferromagnetism in manganites can be switched at “room temperature” by an electric field of a “few volts” on the basis of a *p*-*n* junction where control of carrier concentration is easily achieved by designing specific interfacial

electronic band structures. The "band gap engineering" can offer large changes in both electrical and magnetic properties resulting from an electric field of a few volts or exposure to light, which is an advanced concept as compared to the insulative-gate FET. FETs based on CMR channels show some interesting characteristics depending on the dielectric layer on top, as to whether it is a paraelectric layer, such as STO, electron doped STO, or a ferroelectric layer, such as PZT [51].

1.4 Introduction to Swift Heavy Ion (SHI) Irradiation studies

Swift Heavy Ion (SHI) irradiation is an efficient tool for creation of point defects, vacancies, columnar defects and localized strain in the materials (mainly in thin films) which in turn affects their crystallographic, surface and physical properties [52,53]. SHI irradiation on manganite thin films mostly evolves detrimental effects on structural and transport properties; for instance, the irradiation results in enhancement of resistivity, suppression of T_P, etc [54]. Though the deteriorated properties of the irradiated films have adverse effect with respect to their applications as data storage devices, their application possibilities improve as uncooled bolometers, magnetic field sensors, etc. [49,55].

While passing through the material, accelerated energetic charged particles losses their energies mainly by two ways, first by the electronic energy loss [$(S_e)= dE_e/dx$] which is the inelastic collision of charged particles with atomic electrons of the material while the second is nuclear energy loss [$(S_n)= dE_n/dx$] which is the elastic scattering of the charged particles from the atomic nuclei. For the high energetic charge [~ MeV], electronic energy loss is dominated. In the irradiation experiments, the selection of highly energetic ions has been made because of the fact that due to their larger mass these ions can easily pass through the entire thickness of the film and create columnar tracks before striking the substrate. This results in a uniform distribution of strain in the film which is not the case with low energy ion implantation [56]. In manganites, the irradiations studies have two fold interests,

I. The grain boundaries in manganites have a major contribution to MR. SHI with ^{108}Ag, may help in modification of grain interfaces and creation of disorder at Mn-O-Mn bonds for tailoring these materials with large CMR at moderate magnetic fields.

II. The study of modifications in the thickness and lattice mismatch dependent strain in the manganites thin films by the irradiation of swift heavy ions.

Motivation for the present work

The present work coalesce both the aspects of research, basic as well as applied, firstly by the synthesis of ceramic perovskite structured oxides of HTSC and CMR manganites in bulk and thin film forms to understand novel structure-property correlations in them and to evaluate some of them for potential applications. The important part of the work carried out is on the structural understanding of La-2125 type mixed oxide cuprates using highly reliable Neutron diffraction (ND) studies in the temperature range 300-12K. The structural studies have been then parameterized using Rietveld refinement method. The novel idea of Bond Valence Sum (BVS) calculation is applied to correlate the bond lengths, obtained from Rietveld refinement of ND data, to the actual oxidation states of different cations at various crystallographic sites, of particular interest in Cu-I and Cu-II layers, which in turn decides the average oxygen content in these cuprate superconductors and hence can be useful to understand the superconductivity mechanism in theses mixed oxide compounds.

Second aspect of the present work is the study of perovskite structured CMR manganites, particularly in epitaxial thin film forms owing to their strong application potentiality as uncooled bolometers and magnetic field sensors. It has been interesting to study the role of structural disorder at A-site on electrical resistivity and MR behavior in manganite thin films. In addition to this, the present study investigates lattice effects due to the substrate material mismatch and film thickness on structural, morphological and transport properties of manganite thin films. Efforts have been made to carry out the detailed investigations on the thin films prepared by chemical solution deposition and their effects on grain morphology, resistivity and MR behavior.

Finally, the role of swift heavy ion (SHI) irradiation on electrical and magnetotransport properties of the manganite thin films has been studied. SHI irradiation causes considerable suppression in resistivity and enhancement in T_P and MR in the chemically synthesized thin films, properties entirely opposite to the reported resistivity and MR behavior of PLD grown irradiated manganite films. This has been attributed to the irradiation induced enhanced grain morphology and reduction in surface roughness which results into the substantial decrease in low temperature, low field and high field MR.

Chapter-wise details of the all the chapters comprising thesis are given below:

Chapter – 2 describes various experimental characterization tools and techniques employed during the present work for carrying out the structural, morphological and electrical and magnetotransport measurements. The details of various sample synthesis methods used in the present work have been given for bulk and thin films sample preparation. The methods employed for the structural analysis of the ND data namely Rietveld refinement, Bond Valence Sum (BVS) calculation are described in detail.

Chapter – 3 deals with ND studies on mixed oxide $La_{2-x}Dy_xCa_{2x}Ba_2Cu_{4+2x}O_z$ (La-2125) (x =0.3,0.5) superconductors at various temperatures in the ranges 300-12K, carried out during the present work, to investigate the structure of La-2125 superconductors and to evaluate the changes in the unit cell parameters, cell volume, occupancies and bond lengths fluctuations of different cations at different crystallographic sites as a function of temperature, particularly around the superconducting transition T_c. Further, to determine the actual valence/oxidation states of various cations, especially in Cu-I and Cu-II layers, Bond Valence Sum (BVS) calculation has been done, which in turn, determine the actual oxygen content. Finally, comparison has been made on the stoichiometric valence obtained from ND data and global valence from BVS to determine the strain present into the system.

Chapter – 4 presents the studies on $La_{0.5}Pr_{0.2}Ba_{0.3}MnO_3$ (LPBMO) manganite thin films prepared using the Pulsed Laser Deposition (PLD) technique on STO single crystalline substrates. The resistivity vs. temperature behavior of the polycrystalline LPBMO bulk exhibits anomalous low temperature resistivity minimum at ~ 40K in the metallic regime. To verify this, thin films of LPBMO have been grown on single crystalline STO substrates and the studies on thickness dependent strain (bulk effect), lattice effects due to the sample-substrate mismatch on the structural, electrical and magnetotransport have been carried out. The low temperature resistivity minima behavior does not melt on application of magnetic field instead becomes slightly broadened. The origin of such a behavior has been investigated by carrying out detailed SHI irradiation study on LPBMO thin films, and the results are discussed in this chapter.

Chapter – 5 deals with the studies on novel chemical synthesis for $La_{0.7}R_{0.3}MnO_3$ (LRMO) (R = Ca, Sr and Ba) manganites thin films using spin coating unit. The chemical

solution deposition (CSD) technique is relatively simple, cost effective and low temperature synthesis method. The effect of synthesis parameters such as annealing time and annealing temperature on structure, morphology and electrical transport have been studied in detail. Interesting results has been obtained from the SHI irradiation studies of the LRMO thin films. SHI irradiation effects on chemically synthesized thin films are quite different than those reported on PLD grown LRMO films. Irradiation induced enhancement of surface morphology decreases the low temperature MR that leads to resistivity suppression thereby improving the temperature and magnetic field sensitivity of the films.

References

1. J. B. Goodenough, Rep. Prog. Phys. 67, 1915 (2004)
2. M. Imada, A. Fujimori and Y. Tokura, Rev. Mod. Phys. 70, 1093 (1998)
3. E. Dogotto, "Nanoscale Phase Separation and Colossal Magnetoresistance The Physics of Manganites and Related Compounds", Springer (2002)
4. J. Zaanen, G. A. Sawatzky and J. W. Allen, 1985, Phys. Rev. Lett. 55, 418 (1985)
5. J. H. Park, C. T. Chen, S. W. Cheong, W. Bao, G. Meigs, V. Chakarian and Y. U. Idzerda, Phys. Rev. Lett. 76, 4215 (1996)
6. J. E. Mdvedeva, V. I. Anisimov, O. N. Mryasov and A. J. Freeman, Cond-mat/0111038; J. E. Mdvedeva et. al. cond-mat/0104316
7. Y. Tokura, "Fundamental Features of Colossal Magnetoresistive Manganese oxides in Monographs in Condensed Matter Science", Gordon and Breach (1999)
8. Y. Okimoto, T. Katsufuji, T. Ishikawa, A. Urushibara, T. Arima and Y. Tokura, Phys. Rev. Lett. 75, 109 (1995)
9. J. M. D. Coey, M. Viret and S. Von Molnar, "Mixed Valent Manganites", Adv. Phys. 48, 167 (1999)
10. J. B. Goodenough and J. M. Longo, "Crystallographic and Magnetic Properties of Perovskite and Perovskite Related Compounds", Landolt Bornstein Tabellen New Series, Vol III, p126-314, Springer (1970)
11. J. S. Zhou and J. B. Goodenough, Phy. Rev. Lett. 94, 065501 (2005)
12. J. J. Neumeier, M. F. Hundley, J. D. Thompson and R. H. Heffner, Phys. Rev. B, 52, 7006 (1995)
13. H.Y. Hwang, S.W. Cheong, N.P.Ong and B.Batlogg, Phys. Rev. Lett. 75, 914 (1995)
14. P.G. Radaelli, G.Iannone, M.Marezio, H.Y. Hwang, S. W. Cheong, J. D. Jorgensen and D. N. Argyriou, Phy. Rev. B, 56 8265 (1997)
15. L. M. Rodriguez Martinez and J. P. Attfield, Phy. Rev. B, 58, 2426 (1998)
16. L. M. Rodriguez Martinez and J. P. Attfield, Phy. Rev. B, 63, 024424 (2000)
17. J. A. McAllister and J. P. Attfield, Phy. Rev. B, 66, 014514 (2002)

18. R. Cava, B. Batlogg, R. Van Dover, J. Krajewski, J. Waszczak, R. Fleming, W. Peck, L. Rupp, P. Marsh, C. W. P. James and L. F. Schneemeyer, Nature, 345, 602 (1990)

19. P. G. D. Gennes, Phys. Rev. B. 118, 141 (1960)

20. J. B. Goodenough, J. Phys.: Condens. Matter 15**,** 257 (2003)

21. H. K. Onnes, Comm. Phys. Lab. Univ. Leiden 120B, 3 (1911)

22. J. Bardeen, L. N. Cooper and J. R. Schrieffer, Phys. Rev. 108, 1175 (1957)

23. Charles W. Billings, "Superconductivity: From Discovery to Breakthrough", Cobblehill Books (1991)

24. J. G. Bednorz, M. Takashige and K. A. Müller, Europhys. Lett. 3, 379 (1987)

25. T. Kimura, Y. Tomioka, H. Kuwahara, A. Asamitsu, M. Tamura, and Y. Tokura, Science 274, 1698 (1996)

26. M.Maeda, Y.Tanaka, M.Fukutomi and A.Asano, Jpn. J. Appl. Phys. 27, L209 (1988)

27. Z. Z. Sheng, and A. M. Hermann, Nature, 332, 55 (1988)

28. S. N. Putilin, E. V. Antipov, O. Chmaissem and M. Marezio, Nature 362**,** 226 (1993)

29. W. C. Lee, R. A. Klemm and D. C. Johnston, Phys. Rev. Lett., 62**,** 1012 (1989)

30. S. N. Ruddlesden and P. Popper, Acta Crystallogr. 10, 538 (1957); S. N. Ruddlesden and P. Popper Acta Crystallogr. 11, 5 (1958)

31. R. J. Cava, B. Batlogg, C. H. Chen, E. A. Rietman, S. M. Zahurak and D. Werder, Phys. Rev. B, 36**,** 5719 (1987)

32. J. B. Goodenough, J. S. Zhou and J. Chan, Phys. Rev. B, 47, 5275 (1993)

33. M.N. Baibich, J.M. Baroto, A. Fert, F.N. Vandau, F. Petroff, P. Etienne, G. Creuget, A. Freiderich and J. Chagelas, Phys. Rev. Lett. 61, 2472 (1988)

34. A. Fert, A. Barthelemy, P. Etienne, S. Lequiou, R. Loloee, D.K. Lottis, D.H. Mosca, W.P. Pratt and P.A. Schroeder, J. Magn. Magn. Mater. 104, 1712 (1992)

35. G. Binash, P. Grunberg, F. Saurenbath and W. Zinn, Phys. Rev. B 39, 4828 (1989)

36. R. Von Helmolt, J. Wecker, B. Holzapfel, L. Schultz and K. Samwer, Phys. Rev. Lett. 71, 2331 (1993)

37. K. Chahara, T. Ohno, M. Kasai and Y. Kosono, Appl. Phys. Lett. 63, 1990 (1993)

38. S. Jin, T. H. Tiefel, M. McCormack, R. A. Fastnacht, R. Ramesh and L. H. Chen, Science 264, 413 (1994)

39. T. Venkatesan, M. Rajeswari, Z. W. Dong, S. B. Ogale and R. Ramesh, Phil. Trans. Roy. Soc. A 356, 1661 (1998)

40. A. B. Pippard, "Magnetoresistance in Metals", Cambridge University Press (1998)

41. H.Y.Hwang, S.W.Cheong, N.P.Ong and B.Batlogg, Phys. Rev. Lett. 77, 2041 (1996)

42. J.S.Moodera, L.S.Kinder, T.M.Wong and R.Meservey, Phys. Rev. Lett. 74, 3273 (1995)

43. C. N. R. Rao and B. Raveau, "Colossal Magnetoresistance, Charge Ordering and other Related Properties of Rare-Earth Manganates", World Scientific (1998)

44. C. P. Zener, Phys. Rev. 81, 440 (1951); C. P. Zener, Phys. Rev. 82, 403 (1951)

45. P. W. Anderson, H. Hasegawa, Phys. Rev. 100, 675 (1955)

46. A. P. Ramirez, J. Phys: Condens. Matter, 9, 8171 (1999)

47. P. Schiffer, A.P.Ramirez, W. Bao and S.W.Cheong, Phys. Rev. Lett. 75, 3336 (1995)

48. A. M. Haghiri Gosnet and J. P. Renard, J. Phys. D: Appl. Phys. 36, 127 (2003)

49. M. Rajeshwari, A. Goyal, R. Shreekala, S.E. Lofland, S.M. Bhagat, R. Ramesh and T. Venkatesan, Appl. Phys. Lett. (1998)

50. T. Kimura, Y. Yomoika, H. Kuwahara, A. Asamitsu, M. Tamura and T. Tokura, Science 274, 1698 (1996)

51. S. Mathew, R. Ramesh, T. Venkatesan and J. Benedetto, Science 276, 238 (1997)

52. S. B. Ogale, K. Ghosh, J. Y. Gu, R. Shreekala, S. R. Shinde, M. Downes, M. Rajeswari, R. P. Sharma, R. L. Greene, T. Venkatesan, R. Ramesh, Ravi Bathe, S. I. Patil, Ravi Kumar, S.K. Arora, and G. K. Mehta, J. Appl. Phys. 84, 6255 (1998)

53. J. H. Markna, R. N. Parmar, D. G. Kuberkar, Ravi Kumar, D. S. Rana and S. K. Malik, Appl. Phys. Lett. 88, 152503, (2006)

54. B. L. Belevtsev, V. B. Krasovitsky, V.V. Bobkov, D.G. Naugle, K.D. D. Rathnayaka and A. Parasiris, Eur. Phys. J. B. 15, 461 (2001)

55. A. Goyal, M. Rajeshwari, R. Shreekala, S.E. Lofland, S.M. Bhagat, T. Boettcher, C. Kwon, R. Ramesh and T. Venkatesan, Appl. Phys. Lett. 71, 1718 (1998)

56. S. M. Watts, M. Li, S. Wirth, K. H. Dahmen, S. von Molnar, P. Xiong, A. S. Katz and R. C. Dynes, J. Appl. Phys. 85, 4791 (1999)

Chapter - 2

Experimental techniques of Characterization

2.1 Synthesis methods for bulk and thin films

The synthesis of material is the first and foremost important step during the experimental research in condensed matter physics and materials science. The quality of bulk as well as thin films depends to a great extent on the synthesis method used. In addition, the proper selection of synthesis parameters helps to achieve desired properties in the samples to be characterized. There are various methods available for the synthesis of polycrystalline bulk and single crystalline epitaxial thin films of mixed oxide materials. Out of them, Solid State Reaction (SSR) or ceramic method is commonly used for the preparation of bulk samples while Pulsed Laser Deposition (PLD) is an efficient technique for the thin film growth. Also, many chemical methods for the preparation of mixed oxide materials with improved physical properties have been reported such as coprecipitation, sol-gel, alkali-flux, citrate methods, etc. For the synthesis of single crystalline manganite thin films using chemical route, spin-coating method known as Chemical Solution deposition (CSD) is often used which gives good quality manganite thin films on various substrates. During the present work, the polycrystalline bulk samples and epitaxial thin films of high T_c superconductors (HTSC) and Colossal Magnetoresistive (CMR) manganites were prepared using standard solid state reaction, PLD and CSD methods in order to study their physical properties in the bulk as well as single crystalline thin film forms.

2.1.1. Solid State Reaction (SSR) route

All the bulk polycrystalline samples under present study were synthesized using solid state reaction method as per the steps shown in the flowchart [Fig. 2.1]. There are two factors namely, thermodynamic and kinetic factors which are important in solid state reactions, the former determines the possibilities of any chemical reaction to occur by the free energy considerations which are involved while the later determines the rate at which the reaction occurs [1,2]. The atoms diffuse through the material to form a stable compound of minimum free energy. Different compounds or phases might have the lowest free energy at various temperatures or pressures or the composition of the gas atmosphere might affect the reaction. The general steps involved in solid state reaction method for synthesizing high temperature superconductors are described below.

1. All starting materials are high purity powders of carbonates, oxides, nitrides, etc. They are preheated for appropriate time and temperature. Powders are weighed for desired composition.
2. In the solid state reaction, for the reaction to take place homogeneously, it is very important to mix and grind the powders thoroughly for long duration to obtain homogeneous distribution in required proportions of the desired stoichiometric compound.
3. The proper grinding of mixed powders using pestle-mortar decreases the particle size as much as possible. This is necessary for obtaining close contact among the atoms so the right material is formed.
4. This powdered mixture is then heated in air for the first time. During the first calcination, CO_2 is liberated from the mixture.
5. After the first heating, further number of heatings in atmospheric conditions, are required to obtain phase purity and to release the remaining CO_2, if any.
6. Before final sintering of samples, the obtained fine black powder is pressed into cylindrical pellets
7. The pellets are sintered in a furnace in air at certain temperature to obtain the desired structural phase. The furnace is turned off and the samples are left inside to cool down to at least 300° C. After sintering process, the diameter of pellets may decrease.
8. *Annealing:* After sintering the samples have oxygen content slightly less than the required stoichiometry in oxide superconductors. To reach the optimum oxygen content, the samples have to be annealed, preferably in flowing oxygen. Since most of physical properties of oxide superconductors are rather sensitive to oxygen content and ordering, the conditions set during the oxygen annealing are important. For appropriate oxygen content, the sintered pellets are usually kept for oxygen annealing at a certain temperature for a period of time and then cooled down slowly to ambient temperature.

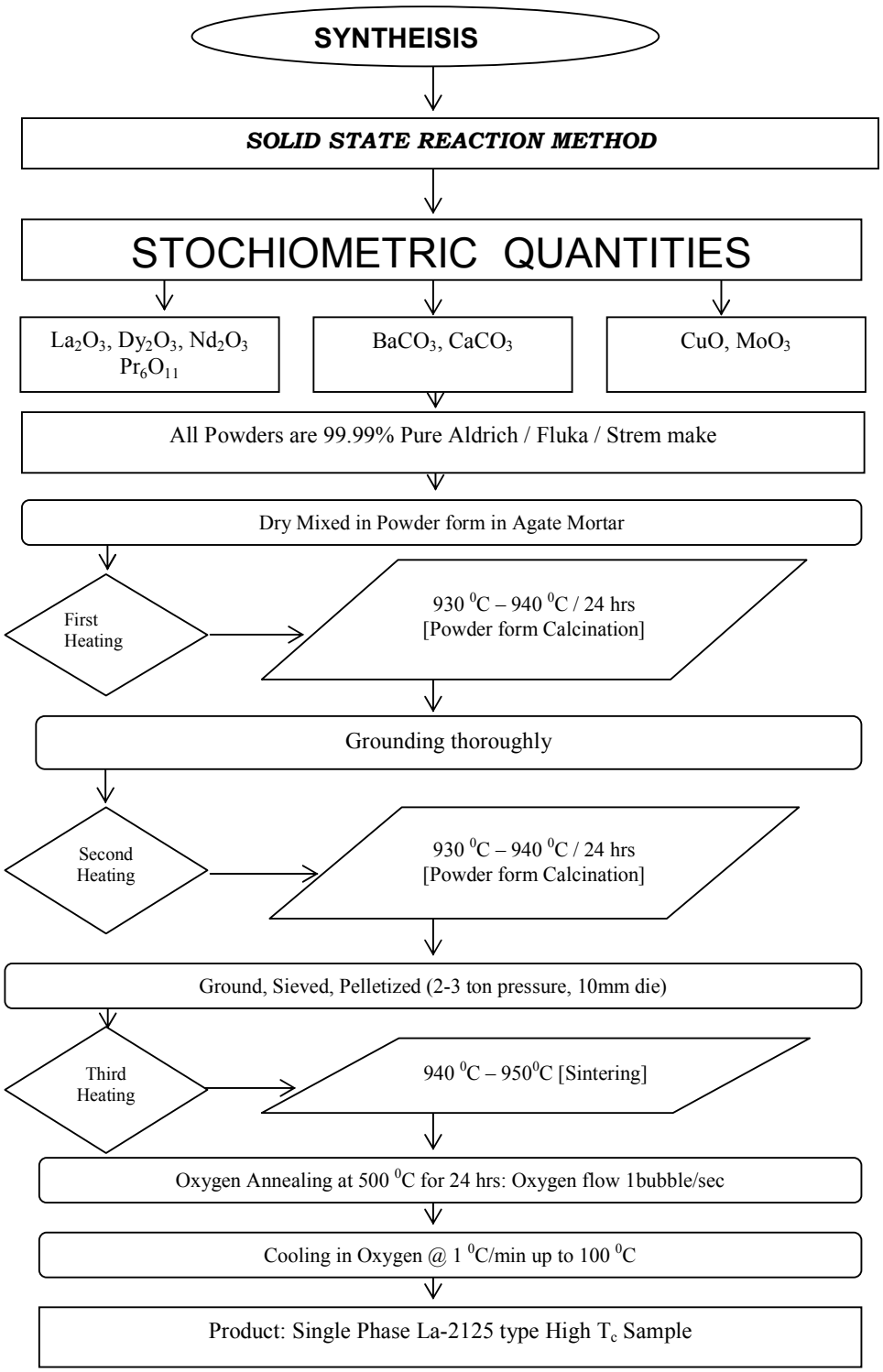

Figure 2.1: Schematic illustration of sample preparation by Solid State Reaction route.

The solid state reaction method has proved to be the most suitable for synthesizing reproducible samples of mixed oxide high temperature superconductors and manganites. The similar steps can be followed for synthesis of manganites by solid state reaction route. Oxygen annealing is not important for manganites as these materials posses good stability of oxygen stoichiometry. However, care must be taken, to control either temperature or atmosphere, if the components have variable oxidation states and certain oxidation state is desired in the product phase.

2.1.2. Pulsed Laser Deposition (PLD)

PLD is an efficient method to synthesize thin films by utilizing the technique of laser ablation. This method for thin film synthesis is applicable to many materials; in particular it is versatile method to ceramic materials [3]. Today, PLD is one of the fastest growing thin-film processes for synthesizing multi-components films. This process transports elements from one location (target material) to another (substrate) by supplying energy to elements from a laser source. Ideally, such a process coats the surface with a pure film of the correct composition.

Principle of PLD

High power pulsed laser beam is focused inside a vacuum chamber to evaporate matter from a target surface such that the stoichiometry of the material is preserved in the interaction. As a result, a dynamic supersonic jet of plasma (plume) is ejected normal to the target surface. The dynamic plasma plume expands away from the target with a strong forward directed velocity distribution of the different particles and is transported over large distances due to quasi free expansion processes and shock wave propagation in the presence of some background gas [4]. The dynamic interactions in the plume can be modelled using a shock wave model that leads to a quantitative scaling law, PD^3 = constant, relating the two prominent parameters, i.e. the pressure P and the target-to-substrate distance D. In the case of oxide films, oxygen is the most common background gas. For pressures in the range of 100–400mTorr, the ablated atoms and ions, which attain high kinetic energies (few 10 eV) in the vicinity of the target, are thermalized due the scattering at a particular target-to-substrate distance that is called the 'plume range' (L) and finally, condensed on the substrate placed opposite to the target. The plume

range, L, defines two distinct regions in the D–P diagram for the morphology and the microstructure and appears as a relevant deposition parameter for the growth of single crystal films with low roughness and large grains by the PLD technique [5]. Further, in most materials, the ultraviolet radiation is absorbed by only the outermost layers of the target up to a depth of ~ 1000 Å. The extremely short laser pulses, each lasting less than 50 ns, cause the temperature of the surface to rise rapidly to thousands of degrees Celsius, but the bottom of the target remains virtually unheated, close to room temperature. Such un-equilibrium heating produces a flash of evaporated elements that deposit on the substrate, producing a film with composition identical to that of the target surface. Rapid deposition of the energetic ablation species helps to raise the substrate surface temperature. In this respect PLD tends to demand a lower substrate temperature for crystalline film growth. Figure 2.2 shows the schematic diagram of PLD apparatus along with target holder, substrate holder, focusing lens, etc, which involves evaporation of a solid target material in an Ultra High Vacuum (UHV) chamber by means of short and high energy laser pulses.

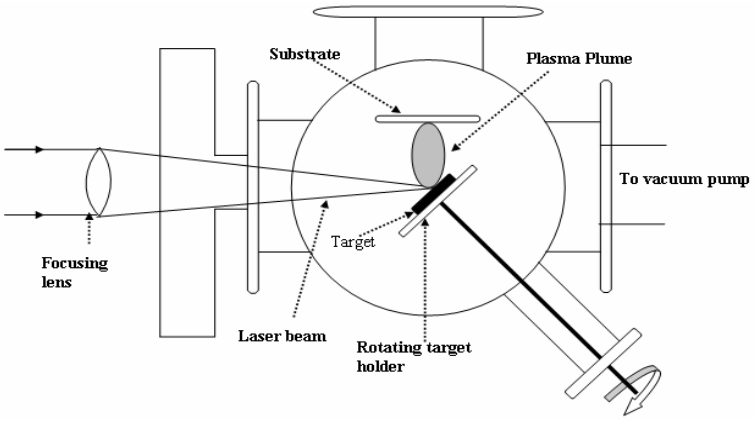

Figure 2.2: A schematic representation of PLD apparatus.

Conventional arrangement for PLD for the synthesis of thin solid films is characterized by the following features:

1 Focused laser beam is directed to the target to ablate the material.

2 The target holder is rotated along an axis or (x, y) - scanned in the focal plane of the laser beam to achieve a stationary ablation rate. The vacuum chamber is made of stainless. Chamber is evacuated down to 10^{-6} bar by using a turbo pump.

3 Well polished substrate located at a typical separation from the target is stationary or rotated for homogenization of the deposited material. To form a film with required stoichiometry, film growth regimes and the temperature of the substrate may be selected between room temperature and 1000^{o} C.

4 A gas supply is often provided to produce desired chemical reactions during film growth.

Each stage in PLD is critical to the formation of thin films with epitaxial crystalline structure, stoichiometry and smooth surface.

The manganite thin films synthesized in the present work were prepared by PLD technique. The details of deposition condition and parameters used for PLD method used are discussed in Chapter 4.

2.1.3. Chemical Solution Deposition (CSD)

The advanced chemical liquid phase synthesis methods consisting of novel coprecipitation and sol-gel processing involves the simultaneous occurrence of nucleation, growth, coarsening and/or agglomeration processes and is the most preferable alternative for the preparation of oxide nanomaterials and thin films. The method offers high degree of homogenization together with the small particle size and thereby speeds up the reaction rate and much lower reaction temperature are sufficient for the reaction to occur. Further, chemical route is relatively simple, cost effective and requires only low synthesis temperature as compared to vacuum deposition techniques. The precipitation of oxides, from both aqueous and nonaqueous solutions can generally be broken into two categories: those which produce an oxide directly and those which produce what is best termed a precursor that must be subjected to further processing (drying, calcination, etc). In either case, monodispersed nanoparticles of oxides, like those of metals, frequently require a capping ligand or other surface bound stabilizer to prevent agglomeration of the particles. In the cases where calcination or annealing of the samples is necessary, some agglomeration will be unavoidable. The products of coprecipitation reactions, particularly those performed at or near room temperature are usually amorphous. It is extremely difficult to experimentally determine whether the as-prepared precursor is a single phase solid solution or a multiphase, nearly-homogeneous mixture of the constituent metal

hydroxides, carbonates and/or oxides that react to form a single phase mixed metal oxide when heated. Figure 2.3 illustrates the general steps involved in sol-gel processing [6].

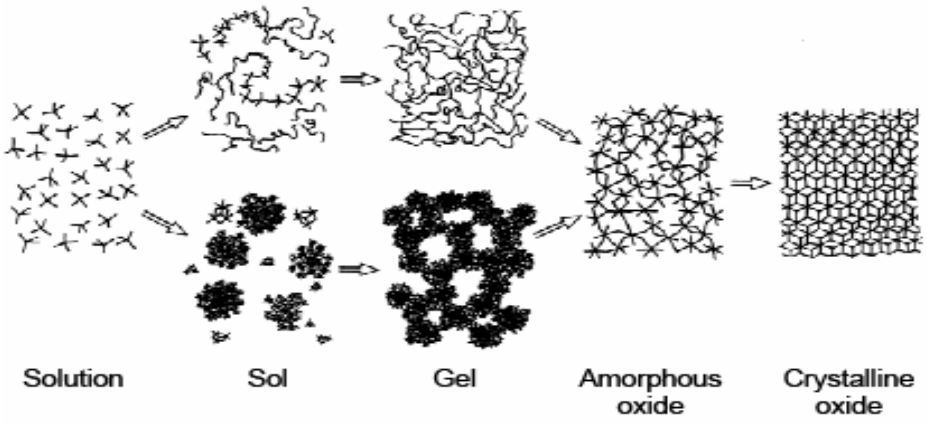

Figure 2.3: Schematic steps involved in the sol-gel synthesis of crystalline.

Chemical Solution Deposition (CSD) technique has been used to prepare $La_{0.7}R_{0.3}MnO_3$ (R = Ca, Sr and Ba) manganite thin films. The mixing, stirring and heating of appropriate stoichiometric quantities of the metal acetates in distilled water and acetic acid resulted in a clear solution of the constituents used for deposition. Deposition of thin films using automated spin coater was then followed by calcination ~ 350°C and annealing at 1000°C in an oxygen environment. The more detailed CSD processing has been given in Chapter 5, section. 5.1.

2.2. Structural

It is very essential to study structural properties of any material in order to verify single phase structure before carrying out further studies on the material. Structural properties are closely related to the chemical characteristics of the atoms in the material and thus form the basics on which detailed physical understanding is built. There are various techniques known to explore the science related to structure of a material. These are used to ascertain single phase samples and detect deviations from the main structure as well as extracting the actual structure. The different techniques have different advantages and disadvantages and thus complement each other. To study the crystalline formation of a material, two techniques are widely used: i) X-Ray diffraction measurements and ii) Neutron diffraction measurements.

2.2.1. X-ray Diffraction (XRD)

X-ray diffraction (XRD) method offers varieties of information concerning the physical and electronic structure of crystalline and noncrystalline materials in a different conditions and environments [7]. The wavelength of x-rays ($\lambda \sim 0.5\text{-}2.5$Å) is of the order of the inter-atomic distances and hence get diffracted when interacts with a crystalline substance (phase). The x-ray diffraction pattern of a pure substance is, therefore, like a fingerprint of the substance. While passing through a crystal, x-rays are diffracted by atoms at specific angles depending on the x-ray wavelength, the crystal orientation and the structure of the crystal. X-rays are predominantly diffracted by electrons and analysis of the diffraction angles produces an electron density map of the crystal. Crystalline materials can be described by their unit cell. This is the smallest unit describing the material. In the material this unit cell is then repeated over and over in all directions. This will result in planes of atoms at certain intervals. The diffraction method is based on this fact of repetition and on Bragg's law which gives a relation between the distance from one atomic plane to the next, d, and the angle, θ, in which constructive interference of a reflected monochromatic beam is seen. The Bragg's law follows the equation given below.

$$2d_{hkl} \times \sin\theta_{hkl} = n\,\lambda, \text{ [Fig. 2.4]}$$

where d = inter planar distance, n = order of reflection (Integer value), λ = wave length of x-rays, θ = angle between incident/reflected beam and particular crystal planes under consideration.

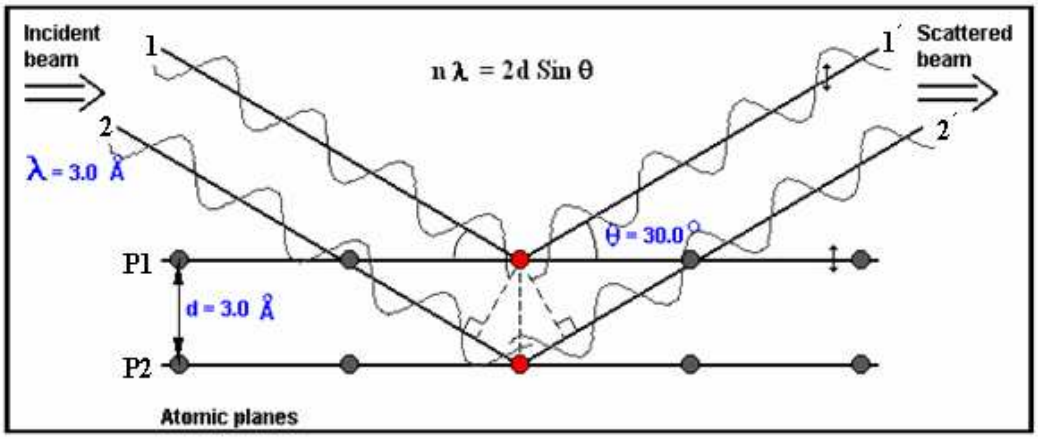

Figure 2.4: Diffraction of X-rays by a crystal planes (Bragg's law).

Bragg law is consequence of the periodicity of the lattice. Reflection (or diffraction) occurs from planes set at angle, θ, with respect to the incident beam and generates a reflected beam at an angle, 2θ, from the incident beam. The possible d-spacing defined by the indices h, k, l are determined by the shape of the unit cell. Therefore the possible 2θ values where we can have reflections are determined by the unit cell dimensions. Notice that the law does not refer to the composition of the basis atoms associated with every lattice point. However, the composition of the basis determines the relative intensities of the various orders of diffraction from a given set of parallel planes. Therefore, the intensities depend on what kind of atoms we have and where in the unit cell they are located. Planes going through areas with high electron density will reflect strongly, planes with low electron density will give weak intensities. A typical powder diffraction spectrum consists of a plot of reflected intensities versus the detector angle 2θ. The detailed description of XRD is given in references [7,8].

Structural characterization of thin films (thickness ~100-1000Å) by XRD requires that the scattered intensity contribution from the bulk substrate be minimized. This is achieved by reducing the angle of incidence [Glancing incidence geometry, Fig. 2.5 (b)] so that the effective distance traversed in the film (t/Sinθ) is enhanced.

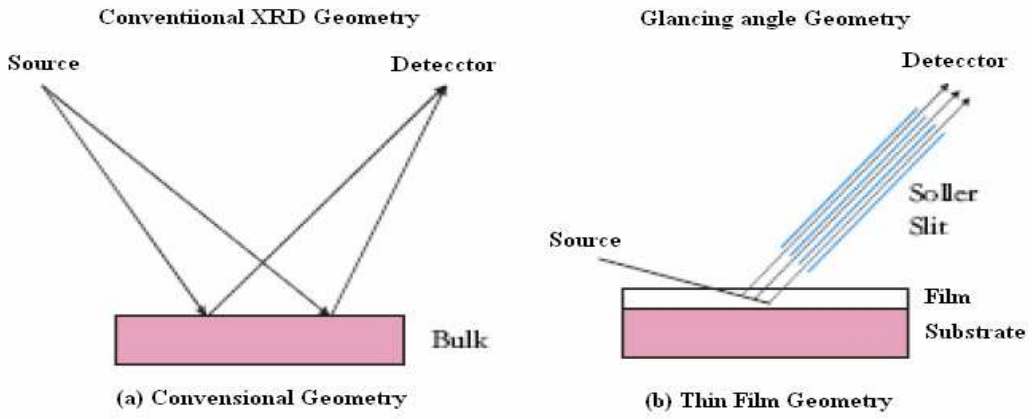

Figure 2.5: Glancing incidence x-rays diffraction geometry for thin films.

The structure and phase purity of bulk as well as thin film samples were examined by the powder x-ray Diffractometer using Cu-K_α x-ray radiation of wavelength 1.5418Å at room temperature (RT). Crystal structure refinements were carried out by performing FULPROOF based Rietveld refinement program.

2.2.2. Neutron Diffraction (ND)

The utility of neutron scattering methods in investigation of atomic scale structure arises from the close match of the wavelengths of this probe to typical interatomic distances (a few Åangstroms) [7]. Neutron powder diffraction (ND) is complementary technique to x-ray diffraction and electron diffraction. The greater penetration depth of neutrons, the fact that the neutron-nucleus interaction is point scattering process implying no variation of nuclear scattering length with scattering angle, the independence of scattering cross-section from number of electrons (Z) of an elements, and therefore the stronger interaction of neutrons with "light" atoms such as hydrogen and oxygen and its isotopes specificity as well as its interaction with magnetic moment of unpaired electrons make neutrons a unique and indispensable probe for condensed matter physics and chemistry. A major drawback of neutron scattering is that it can presently only be done at large facilities (reactors and spallation source), whereas laboratory based x-ray scattering equipment provides same flux much more conveniently. Because the neutron sources are very much weaker than x-ray source, the large sample size is essential.

The neutron powder diffraction measurements on La-based high temperature superconductors were carried out using wave length (λ = 1.249Å) at TT1013 Powder Neutron Diffractometer at Dhruva (100MW), BARC (India). Research reactors are typical source of the neutrons. Neutrons in reactor possess too high energies which are thermalized with a moderator consisting of heavy water. The thermal neutrons have a kinetic energies extending over a considerable range (continuous Maxwellian distribution), but a monochromatic beam of neutrons with a single energy can be obtained by diffraction from a single crystal and this diffracted beam can be used in diffraction experiments [9]. Figure 2.6 shows the schematic illustration of monochromatic neutron beam from the reactor. A layout of typical neutron powder Diffractometer is shown in fig.2.7. The neutrons of wavelength 1.249Å, passing through a Germanium (331) monochromator with flux ~ 5 x 10^5n/cm^2/sec at the sample were focused on the powder sample, kept in vanadium can and cooled to desired temperature using a closed cycle refrigerator (CCR). Diffracted beams were collected by the Position Sensitive Detector (PSD) which can scan 2θ = 3°- 140°. The typical parameters of neutron powder Diffractometer at DHRUVA are summarized in Table 2.1.

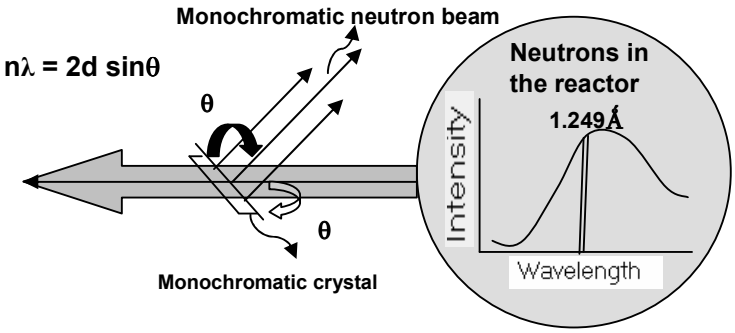

Figure 2.6: Schematic illustration of monochromatic neutron beam from the reactor.

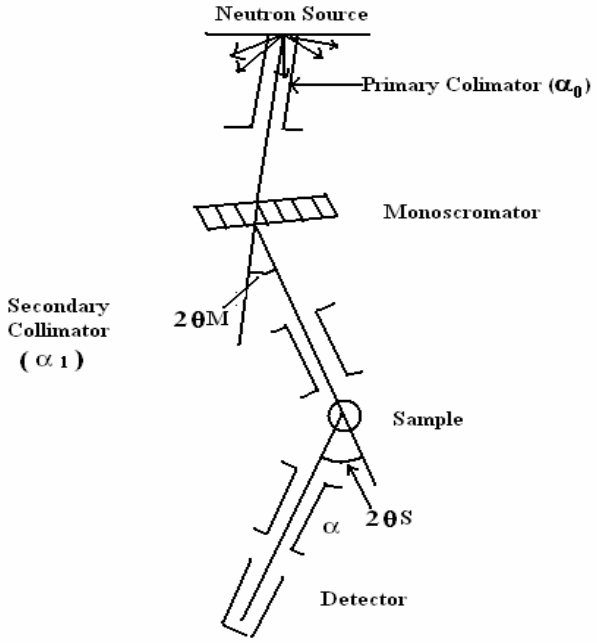

Figure 2.7: Schematic layout of a typical powder diffractometer.

Table 2.1: powder neutron Diffractometer (Instrument parameters) at DHRUVA.

Powder Neutron Diffractometer (Instrument parameters) at DHRUVA	
Beam hole No.	TT1013
Monochromator	Ge (331)
Incident wavelength (λ)	1.249Å
Range of scattering angle (2θ)	$3° < 2\theta < 140°$
Flux at sample	8×10^5 n/cm^2/sec
sinθ / λ	9.45 Å^{-1}
Sample size	10 mm dia, 40 mm high
Detector (1D-PSD)	5 (overlapping)
Resolution (Δd/d)	0.8%

The planes in the polycrystalline sample act as grating to the neutron beams, and diffract them. In order to determine crystal structure, it is necessary to record the full diffraction pattern. The diffracted intensities from the sample are measured by neutron detector (D). Both the sample table and the detector arms are rotated in predetermined step. The sample and the detector move in coupled θ - 2θ mode, in angular steps say ~ 2θ = 0.05°. The span of 2θ scan is over 3° - 140° for the sample studied. Neutron counts were recorded at each step for a fixed amount of monitor counts. Suitable collimation for in-pile before monochromator (α_0), monochromator to sample table (α_1) and sample table to detector d(α) is provided by a mild steel collimators with slits. The collimators used for the present study from the in-pile to the detector end (D) were 0.5°, 0.7°, 0.5° of arc.

Neutrons being a neutral particle, its detection are based on a range of nuclear reactions, which produced energetic charged particles, the most important once are,

$$^{1}n_{0} + {}^{3}He_{2} \rightarrow {}^{3}T_{1} + {}^{1}p_{1} \qquad \text{(a)}$$

$$^{1}n_{0} + {}^{10}B_{5} \rightarrow {}^{7}Li_{3} + {}^{1}p_{1} \qquad \text{(b)}$$

Gas counters are filled with $^{4}_{2}$He gas or BF_3 gas enriched in $^{10}_{5}$B were employed for neutron detection. For the present experimental set-up, the diffracted neutrons are collected by the Position Sensitive Detector (PSD), which is filled with helium gas. For every neutron falling on the PSD, the reaction (a) takes place, and eventually, the intensity is observed. One incoming neutron interacts with the molecule of Helium gas, and breaks it into one tritium and one proton. Protons are charged particles, which ionizes the helium gas thus producing ions. These ions are recorded, as pulses by the "cathode – anode setup" kept under high potential. The whole cathode length is distributed or sliced into 1024 channels in the Dhruva reactor setup. The counts (pulses i.e., the number of ions falling on the cathode) at each channel are recorded. The multi-channel analyzer (MCA) records the data from each channel and using a discriminator separates out the neutron pulses from the background pulses (which occur due to gamma ray etc,). The data from MCA is fed into the computer from where the intensity vs. channel spectrum can be analyzed and recorded. Using appropriate calibration constants, the channels are converted into corresponding angles. The data collected was analyzed using FULLPROF and/or WINPLOTR based Rietveld refinement suites as described below [10].

Rietveld Analysis

There are six factors affecting the relative intensities of the diffraction lines on a powder pattern, namely, i) polarization factor, ii) structure factor, iii) multiplicity factor, iv) Lorentz factor, v) absorption factor and vi) temperature factor. A very important technique for analysis of powder diffraction data is the whole pattern fitting method proposed by Rietveld (1969) [11]. The Rietveld method is an extremely powerful tool for the structural analysis of virtually all types of crystalline materials not available as single crystals. The method makes use of the fact that the peak shapes of Bragg reflections can be described analytically and the variations of their width (FWHM) with the scattering angle 2θ. The analysis can be divided into number of separate steps. While some of these steps rely on the correct completion of the previous one(s), they generally constitute independent task to be completed by experimental and depending on the issue to be addressed by any particular experiment, one, several or all of these tasks will be encountered [12].

The parameters refined in the Rietveld method fall into mainly three classes: *peak-shape function, profile parameters* and *atomic and structural parameters*. The peak shapes observed are function of both the sample (e.g. domain size, stress/train, defects) and the instrument (e.g. radiation source, geometry, slit sizes) and they vary as a function of 2θ. The profile parameters include the lattice parameters and those describing the shape and width of Bragg peaks (changes in FWHM and peak asymmetry as a function of 2θ, 2θ correction, unit cell parameters). In particular, the peak widths are smooth function of the scattering angle 2θ. It uses only five parameters (usually called U, V, W, X and Y) to describe the shape of all peaks in powder pattern. The structural parameters describe the underlying atomic model include the positions, types and occupancies of the atoms in the structural model and isotropic or anisotropic thermal parameters. The changes in the positional parameters cause changes in structure factor magnitudes and therefore in relative peak intensities, whereas atomic displacements (thermal) parameters have the effect of emphasizing the high angle region (smaller thermal parameters) or de-emphasizing it (larger thermal parameters). The scale, the occupancy parameters and the thermal parameters are highly correlated with one another and are more sensitive to the background correction than are the positional parameters. Thermal parameter refinement

with neutron data is more reliable and even anisotropic refinement is sometimes possible. Occupancy parameters are correspondingly difficult to refine and chemical constraints should be applied whenever possible [13].

Once the structure is known and a suitable starting model is found, the Rietveld method allows the least-squares refinement [chi-square (χ^2) minimization] of an atomic model (crystal structure parameters) combined with an appropriate peak shape function, i.e., a simulated powder pattern, directly against the measured powder pattern without extracting structure factor or integrated intensities. With a complete structural model and good starting values of background contribution, the unit cell parameters and the profile parameters, the Rietveld refinement of structural parameters can begin. A refinement of structure of medium complexity can require hundred cycles, while structure of high complexity may easily require several hundreds. The progress of a refinement can be seen from the resultant profile fit and the values of the reliability factors or R-values. The structure should be refined to convergence. All parameters (profile and structural) should be refined simultaneously to obtain correct estimated standard deviations (e.s.d.) can be given numerically in terms of reliability factors or R-values [14].

The weighted –profile R value, R_{wp}, is defined as,

$$R_{wp} = 100\left[\frac{\sum_{i=1,n} w_i \left|y_i - y_{c,i}\right|^2}{\sum_{i=1,n} w_i y_i^2}\right]^{1/2}$$

Ideally, the final R_{wp}, should approach the statistically expected R value, R_{exp},

$$R_{exp} = 100\left[\frac{n-p}{\sum_i w_i y_i^2}\right]^{1/2}$$

where, N is the number of observations and P the number of parameters. R_{exp} reflects the quality of data. Thus, the ratio between the two (goodness of fit),

$$\chi_v^2 = \left[\frac{R_{wp}}{R_{exp}}\right]^2 = S^2$$

An R value is observed and calculated structure factors, F_{hkl}, can also be calculated by distributing the intensities of the overlapping reflections according to the structural model,

$$R_F = 100 \frac{\sum_{\mathbf{h}} \left| \sqrt{F_{obs,k}} - F_{calc,\mathbf{h}} \right|}{\sum_{\mathbf{h}} \left| \sqrt{F_{obs,\mathbf{h}}} \right|}$$

Similarly, the Bragg-intensity R value can be given as,

$$R_B = 100 \frac{\sum_{\mathbf{h}} \left| \sqrt{I_{obs,\mathbf{h}}} - I_{calc,\mathbf{h}} \right|}{\sum_{\mathbf{h}} \left| \sqrt{I_{obs,\mathbf{h}}} \right|}$$

R values are useful indicators for the evalution of refinement, especially in the case of small improvements to the model, but they should not be overinterpreted. The most important criteria for judging the quality of a Rietveld refinement are i) the fit of the calculated pattern to the observed data and ii) the chemical sence of structural model.

2.3. Surface Morphology

Morphological studies are important for understanding the growth and packing density of grains in thin films or polycrystalline bulk materials. There are various techniques known to explore the science related to surface and morphology of a material are, Scanning Electron Microscopy (SEM), Atomic Force Microscopy (AFM) or Scanning Probe microscopy (SPM) [7].

2.3.1. Atomic Force Microscopy (AFM)

The atomic force microscope (AFM) probes a sample with a sharp tip (a couple of microns long and often less than 100 Å in diameter) which is located at the free end of a cantilever (100 to 200 μm long). AFM is operated by measuring the attractive or repulsive forces between a tip and the sample [15]. The force most commonly associated with atomic force microscopy are interatomic force called the Van der Waals force. The three commonly used AFM modes can be described as contact mode (left), non-contact mode (middle) and tapping mode (right) [Fig.2.8] [16].

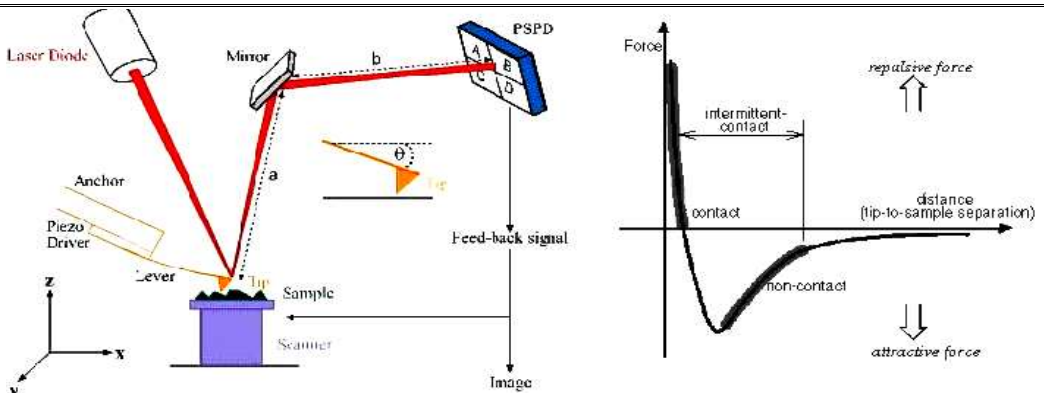

Figure 2.7: Schematic representation of working of AFM and mode of AFM operation in inter-atomic force vs. distance curve.

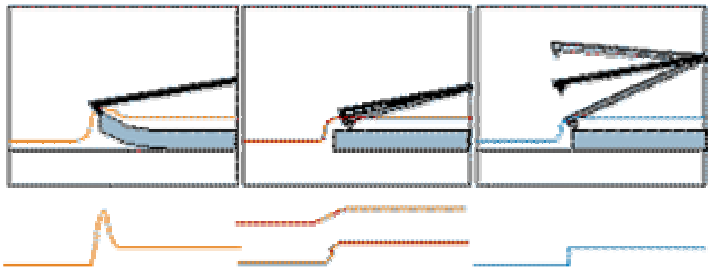

Figure 2.8: Various AFM modes of working: Contact Mode (left), Non-contact Mode (middle) and Tapping Mode (right). (Courtesy of website: http://www.chembio.uoguelph.ca/educmat/chm729/afm/moredet.htm updated on 24.04.1997)

Contact Mode

The contact mode where the tip scans the sample in close contact with the surface is the common mode used in the AFM. The force on the tip is repulsive with a mean value of 10^{-9} N. This force is set by pushing the cantilever against the sample surface with a piezoelectric positioning element. In contact mode AFM, the deflection of the cantilever is sensed and compared in a DC feedback amplifier to certain desired value of deflection. If the measured deflection is different from the desired value, the feedback amplifier applies a voltage to the piezo to raise or lower the sample relative to the cantilever to restore the desired value of deflection. The voltage that the feedback amplifier applies to the piezo is a measure of the height of features on the sample surface. It is displayed as a function of the lateral position of the sample.

Non-contact Mode

A new era in imaging was opened when microscopists introduced a system for implementing the non-contact mode which is used in situations where tip contact might alter the sample in subtle ways. In this mode the tip hovers 50-150Å above the sample surface. Attractive Van der Waals forces acting between the tip and the sample are detected, and topographic images are constructed by scanning the tip above the surface. Unfortunately the attractive forces from the sample are substantially weaker than the forces used by contact mode. Therefore the tip must be given a small oscillation so that AC detection methods can be used to detect the small forces between the tip and the sample by measuring the change in amplitude, phase or frequency of the oscillating cantilever in response to force gradients from the sample. For highest resolution, it is necessary to measure force gradients from Van der Waals forces which may extend only a nanometer from the sample surface.

Tapping Mode

Tapping mode is a key advance in AFM. This potent technique allows high resolution topographic imaging of sample surfaces that are easily damaged, loosely hold to their substrate, or difficult to image by other AFM techniques. With the Tapping Mode technique, very soft and fragile samples can be imaged successfully. Also, incorporated with Phase Imaging, the tapping mode AFM can be used to analyze the components of the membrane. Tapping mode overcomes problems associated with friction, adhesion, electrostatic forces and other difficulties that an plague conventional AFM scanning methods by alternately placing the tip in contact with the surface to provide high resolution and then lifting the tip off the surface to avoid dragging the tip across the surface. Tapping mode imaging is implemented in ambient air by oscillating the cantilever assembly at or near the cantilever's resonant frequency using a piezoelectric crystal. The piezo motion causes the cantilever to oscillate with a high amplitude (typically greater than 20nm) when the tip is not in contact with the surface. When the tip passes over a bump in the surface, the cantilever has less room to oscillate and the amplitude of oscillation decreases. Conversely, when the tip passes over a depression, the cantilever has more room to oscillate and the amplitude increases (approaching the maximum free air amplitude). The oscillation amplitude of the tip is measured by the detector and input to

the controller electronics. The digital feedback loop then adjusts the tip-sample separation to maintain constant amplitude and force on the sample.

Table 2.2: Resolution of AFM/STM.

Technique	Lateral		Vertical		Sample Considerations	Additional Capabilities
	Resolution	Range	Resolution	Range		
AFM/STM	< 0.1 nm	100 um	< 0.1 nm	7 um	Air or Liquid < 25 mm diam. < 10 mm high	Lateral force, nano-scale indentation

2.4. Electrical and magnetotransport

2.4.1. Resistance (RT) & Magnetoresistance (MR) measurements

RT and Magneto RT measurements

Electrical resistance measurements are rather easy and straight forward to be accomplished which provides more useful information about the sample. The normal state of the material is probed and the resistive transition (superconducting transition, T_c in HTSC and Metal-Insulator transition, T_P, in manganites) gives us an easily accessible and accurate value of the critical temperature as well as information of the quality of the sample.

A low contact resistance is desirable due to the small resistance of the samples. To fulfill this requirement, standard four-probe method was used for measuring resistance of the samples [17].

The samples were cut in a rectangular bar shape using a diamond saw. For the electrical contacts silver paint has been used. The silver is applied at the ends for current contacts. Thin copper wires were connected with silver paint as shown in fig.2.9 and the whole assembly was put onto a sample holder where the wires were connected with leads to the measurement instruments.

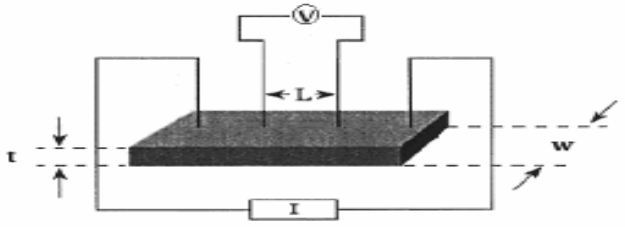

Figure 2.9: Schematic diagram of four probe geometry used for resistivity measurements.

For the purpose of electrical measurements (RT and Magneto RT), rectangular bar shape samples were measured in cryostat by Helium cooler in the temperature range 5-350K and at constant applied fields of 1, 5 and 9T using Quantum Design Physical Property Measurement System (PPMS) [Fig. 2.10]. The resistance versus temperature measurements were recorded by using DC four contact geometry in applied fields in the range 0-9 T.

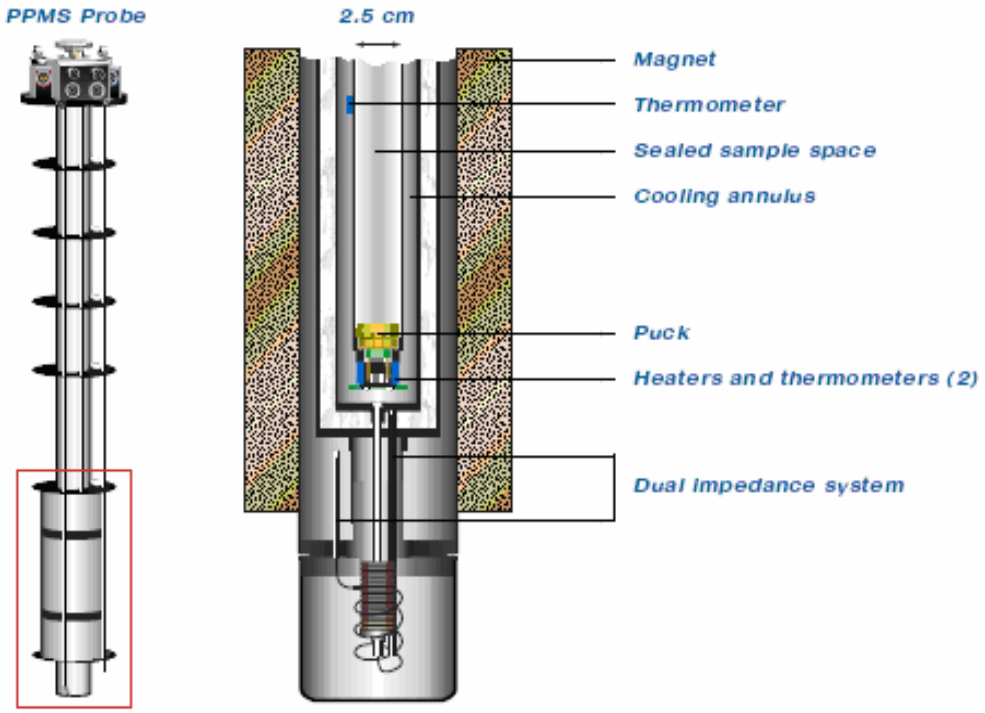

Figure 2.10: PPMS probe and sample chamber geometry (courtesy for Quantum Design).

Magnetoresistance (MR) measurements

To study the magnetoresistive properties of manganite thin films and bulk, magnetoresistance (MR) versus applied magnetic field (H) isotherms of the samples were recorded using the standard four probe method as explained above in the presence of an external magnetic field using PPMS (Quantum Design). At a constant temperature, resistance was measured as a function of applied field (MR vs. H isotherms) in the range of RT to 5K. Mainly, manganite films studied in the present work were characterized by using this technique.

2.4.2. Current vs. Voltage (I-V) characteristics

Current-voltage (I-V) characteristics were studied at zero external field and at various temperatures in (82-300K) are determined by applying dc current and measuring the voltage developed in a four point contact geometry as describe in above section 2.4.1. The applied current (I) vs. voltage (V) plots were measured in current-in-plane (CIP) geometry. The maximum current applied to the film was 1mA. I-V measurements were recorded for forward and reverse applied current.

2.4.3. Thermoelectric power (TEP)

Thermo Electric Power (TEP) for any given sample works on the principle of Seebeck Effect [18]. The potential difference (ΔV) across the two junctions of dissimilar metals governs when two junctions are held at different temperatures as shown in fig.2.11.

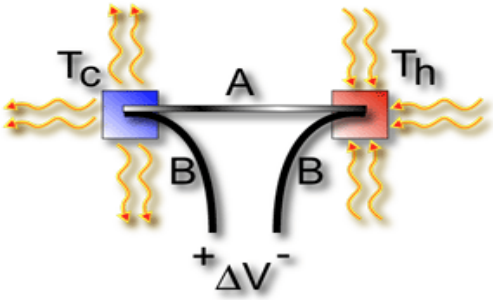

$$V = \int_{T_1}^{T_2} (S_B(T) - S_A(T))\, dT$$

$$V = (S_B - S_A) \cdot (T_2 - T_1)$$

$$S_{AB} = S_B - S_A = \lim_{\Delta T \to 0} \frac{\Delta V}{\Delta T}$$

Figure 2.11: Schematic view of Seebeck effect.

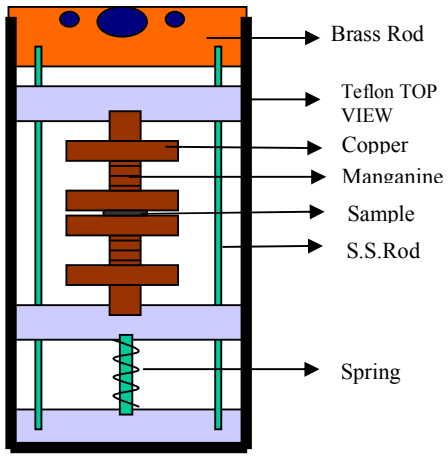

Figure 2.12: Schematic view of Thermo Power (TEP) sample holder.

During the present studies, TEP measurements on the La-2125 mixed oxide superconductors have been carried out under helium atmosphere by differential method at a temperature gradient < 2K, in the temperature range of 45-290K using the sample holder design as shown in fig.2.12. The sample, with a uniform surface, was clamped between two copper blocks that serves as reference samples as well as voltage leads. Si – sensor is used to measure and to control the desired temperature and a copper constantan thermocouple is used to maintain the temperature difference at the end of the sample.

References

1. E. M. Engler, Chem. Technol. 17, 542 (1987)
2. A.R.West, "Solid State Chemistry and its Applications",John Wiley and Sons (1984)
3. H. Karl, B. Stritzker, Phys. Rev. Lett. 69, 2939 (1992)
4. D. B. Geohegan, Thin Solid Films, 220, 138 (1992)
5. M. Strikovski and J. H. Miller, Appl. Phys. Lett. 73, 1733 (1998)
6. B.L.Cushing, V.L. Kolesnichenko and C.J. O'Connor, Chem. Rev. 104, 3893 (2004)
7. E. N. Kaufmann, "Characterization of Materials", John Wiley and Sons (2003)
8. B. D. Culity, "X-Ray Diffraction", Wesly Pub. Co. Inc. (1978)
9. G. E. Beacon, "Neutron Diffraction", Oxford Press (1972)
10. J. Rodriguez-Carvajal (Version 3.5d Oct 98-LLB-JRC) Laboratoire Leon Brillouin (CEA-CNRS)
11. H. M. Rietveld, J. Appl. Cryst. 2, 65 (1969); Acta. Cryst. 22, 151(1967)
12. J. Rodriquez-Carvajal, Physica B, 192, 55 (1993)
13. L. B. McCusker, R. B. Von Dreele, D. E. Cox, D. Louer and P. Scardi, J. Appl. Cryst. 32, 36 (1999)
14. R. A. Young, "The Rietveld Method", Oxford University Press Inc (1993)
15. G. Binning, C. F. Quate, and Ch. Gerber, Phys. Rev. Lett. 56, 930 (1986)
16. http://www.chembio.uoguelph.ca/educmat/chm729/afm/details.htm
17. L. J. Van der Pauw, Philips Res. Repts. 16, 187 (1961)
18. http://en.wikipedia.org/wiki/Peltier-Seebeck_effect#Seebeck_effect

Chapter - 3

Temperature dependent Neutron Diffraction studies on mixed oxide $La_{2-x}Dy_xCa_{2x}Ba_2Cu_{4+2x}O_z$ (x = 0.3, 0.5) superconductors

A major breakthrough in the superconductivity research occured with the advent of superconductivity in mixed oxide compounds having transition temperature (T_c) relatively higher as compared to conventional superconductors. The discovery of superconductivity in $Ln_1Ba_2Cu_3O_z$ (Ln-123) (Ln – rare earth trivalent element except Pm, Tb, Tm and Pr) having $T_c \sim 90K$ accelerated the research efforts in this field owing to the possibility of using these materials in applications at temperatures higher than LN_2 temperature [1]. It is an established fact that, various properties of mixed oxide superconductors, commonly referred as High Temperature Superconductors (HTSC) having copper and oxygen as major constituents, can be tailored successfully for desired applications by using variety of methods such as, cationic substitutions, oxygen content variations, increasing the number of Cu-O layers and chains, etc [2,3]. It is reported that several variants of Ln-123 structure exist, which are derived from different non-superconducting compositions [4].

Our earlier studies in the field of mixed oxide superconductivity have resulted into several interesting structural, transport and magnetic properties of $La_{2-x}R_xCa_yBa_2Cu_{4+y}O_z$ ($0.0 < x < 0.5$; 0.1; and $y = 2x$) (R = Nd, Gd, Pr, Er, Dy, etc) (La-2125) cuprate superconductors. It is well known that, by the simultaneous addition of CaO and CuO to the nonsuperconducting, antiferromagnetic $La_2Ba_2Cu_4O_z$ (La-224) results into a stable tetragonal superconducting phase with the stoichiometric composition $La_{1.5}R_{0.5}Ca_1Ba_2Cu_5O_z$ (R = Nd, Gd, Pr, Er, Dy, etc) having $T_c \sim 78K$ [5]. We have shown that, in these compounds, there exists strong correlation between structure and properties which is dependent on the concentration of the mobile holes in the $Cu\text{-}O_2$ layers which can be varied with the changes in Ca doping concentration. In addition, the detailed neutron diffraction (ND) studies, at room temperature (RT), carried out on series of $La_{2-x}Dy_xCa_yBa_2Cu_{4+y}O_z$ ($0.0< x <0.5$; 0.1 and $y = 2x$) samples by S. Rayaprol *et al* [6] of our group, have shown that with increasing Ca concentration, the occupancy of Ca ions at La-site increases with concomitant displacement of La on to Ba site. This provides the necessary holes for the conduction in Cu-O2 planes. Thus Ca substitution helps in 'turning on' of superconductivity in this system. The presently studied mixed oxide superconducting system $La_{2-x}Dy_xCa_yBa_2Cu_{4+y}O_z$ ($x = 0.3$ and 0.5, $y = 2x$) (La2125) can be normalized to La-123 form using the following relations

$LaBa_2Cu_3O_{7-\delta}$ = $(La_2Ca_1Ba_2Cu_5O_z)$ x (3/5) **(La-2125)**

= $La_{1.2}Ca_{0.6}Ba_{1.2}Cu_5O_{z'}$ (where z' = 3z/5)

= $(La_{0.6}Ca_{0.4})(Ba_{1.2}Ca_{0.2}La_{0.6})Cu_3O_{z'}$ (a)

$LaBa_2Cu_3O_{7-\delta}$ = $(La_{1.7}Dy_{0.3}Ca_{0.6}Ba_2Cu_{4.6}O_z)$ x (3/4.6) **(LD3)**

= $La_{1.11}Dy_{0.2}Ca_{0.4}Ba_{1.3}Cu_3O_{z'}$ (where z' = 3z/4.6)

= $(La_{0.54}Dy_{0.2}Ca_{0.26})(Ba_{1.3}Ca_{0.13}La_{0.57})Cu_3O_{z'}$ (b)

$LaBa_2Cu_3O_{7-\delta}$ = $(La_{1.5}Dy_{0.5}Ca_1Ba_2Cu_5O_z)$ x (3/5) **(LD5)**

= $La_{0.9}Ca_{0.6}Dy_{0.3}Ba_{1.2}Cu_3O_{z'}$ (where z' = 3z/5)

= $(La_{0.3}Dy_{0.3}Ca_{0.4})(Ba_{1.2}Ca_{0.2}La_{0.6})Cu_3O_{z'}$ (c)

During the course of present work, the detailed temperature dependent neutron diffraction studies on LD3 and LD5 compositions were carried out in order to understand the structural phase transition at low temperatures, if any, which can be observed from the variations in different bond lengths in the crystallographic unit cell of $La_{1.7}Dy_{0.3}Ca_{0.6}Ba_2Cu_{4.6}O_z$ **(LD3)** and $La_{1.5}Dy_{0.5}Ca_1Ba_2Cu_5O_z$ **(LD5)** samples under study. The modifications in the interatomic distances, thermal parameters and cell constants as a function of temperature can be determined from neutron diffraction measurements at low temperatures which also help to determine the average Cu valence at different crystallographic sites. Also, the Pauling Bond Valence Sum (BVS) calculations were employed to study the changes in mobile charge density which in turn modifies the average copper valence in these compounds.

3.1. Experimental

Two samples with stoichiometric compositions $La_{1.7}Dy_{0.3}Ca_{0.6}Ba_2Cu_{4.6}O_z$ **(LD3)** and $La_{1.5}Dy_{0.5}Ca_1Ba_2Cu_5O_z$ **(LD5)** were synthesized using standard solid state reaction method. Different steps used during the synthesis are as follows

The high purity starting compounds of La_2O_3, Dy_2O_3, $CaCO_3$, $BaCO_3$ and CuO were initially homogenized by grinding under acetone. These compounds were then

calcined at 920^0C for about one day and then thoroughly reground and palletized before the reaction proceeds. The sintered pellets were reground and heated again at 950^0C for 24 hrs followed by the nitrogen annealing for 12 hrs at 950^0C and then in flowing oxygen for 6-10 hrs. The pellets were slowly cooled to RT at the rate of 1^0C/min. It is observed that starting compounds, particularly La_2O_3, Dy_2O_3 and carbonates, if pre-heated, gives good results. The structural studies using x-ray diffraction (XRD) shows that, samples exhibit single phase tetragonal structure having P4/mmm space group. The temperature dependence of resistivity measurements were performed on LD3 and LD5 samples using d.c. four probe resistivity in order to determine their superconducting transition temperatures.

Neutron Diffraction

The temperature dependent neutron diffraction (ND) was performed on LD3 and LD5 samples weighing ~5g in powder form using the TT1013 Powder Neutron Diffractometer at DHRUVA (100MW) neutron source in BARC, Mumbai (India). The neutrons of wavelength 1.249Å, passing through a Germanium (331) monochromator with flux ~ 5 x 10^5n/cm^2/sec were focused on the powder sample, kept in vanadium can and cooled to desired temperature using a closed cycle refrigerator (CCR). Diffracted neutrons were collected by the Position Sensitive Detector (PSD) in the 2θ range of 3˚- 140˚. The neutron powder diffraction patterns were recorded at 12, 35, 70, 90 and 300K for LD3 and at 12, 40, 70, 90 and 300K for LD5 compositions with step size of 0.05˚. Typical data collection time was 8h per temperature scan of sample. The choice of temperature was such that, we record ND patterns at temperatures below, around and above T_c, so as to see the effect of temperature on the structural modifications in the sample.

The neutron diffraction data were analyzed in tetragonal P4/mmm (space group No. 123) space group using FULLPROF suite employing Rietveld refinement method [7,8]. The background was treated by a polynomial of second order. The peak profiles in all cases were described well by a Gaussian function. The neutron scattering amplitudes used were b(La) = 0.885, b(Dy) = 0.885, b(Ba) = 0.525, b(Ca) = 0.525, b(Cu) = 0.772 and b(O) = 0.580 x 10^{-12} cm. In the final refinement, all structural, lattice and profile parameters were allowed to vary simultaneously until the weighted R factor, R_w, differed

by less than 1 part in a thousand in two successive cycles. In addition, some thermal parameters refined to unreasonably low values, ruled out the possibility of the structure to be noncentrosymmetric. Also, from the careful analysis of thermal and occupancy factors, it was immediately clear that, the neutron data were consistent with the model. Rietveld fitted profiles for tetragonal LD3 and LD5 samples at different temperatures are shown in Figs. 3.1 (a-e) and Figs. 3.2 (a-e). The structural parameters determined from Rietveld refinement along with the goodness of the fit (χ^2) values and R-factors are tabulated in Table 3.1 and Table 3.2 for LD3 and LD5 samples respectively. Figure 3.3 depicts the proposed crystallographic unit cell of La-2125 compound. It can be seen from the figure that, the structure is equivalent to that of the tetragonal Ln-123. Only the ND study could explain the site occupancies of different cations at La and Ba sites. The detailed explanation about the temperature dependent ND patterns obtained for LD3 and LD5 samples along with the discussion about the variations in different derived structural parameters such as, thermal parameter (B), site occupancy (N), variation in position Z, oxygen content, cell parameters, etc has been given in the pages following the figs. 3.1, 3.2 and 3.3 and Table 3.1 and 3.2.

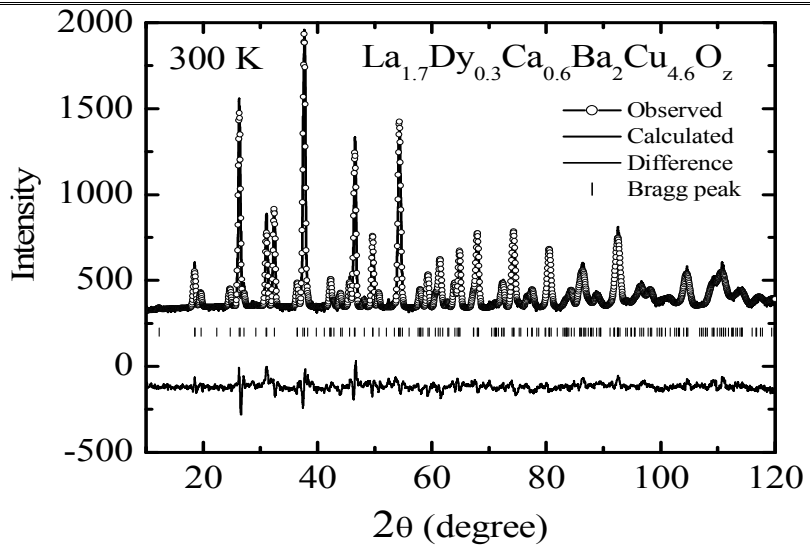

Figure 3.1(a): Rietveld refinement profile showing the observed (o symbol) and calculated (line) neutron powder diffraction data for $La_{1.7}Dy_{0.3}Ba_2Cu_{4.6}O_z$ (LD3) at 300K. Tick mark below the diffraction profile mark the position of allowed Bragg reflections. The difference between the observed and calculated values is given at the bottom.

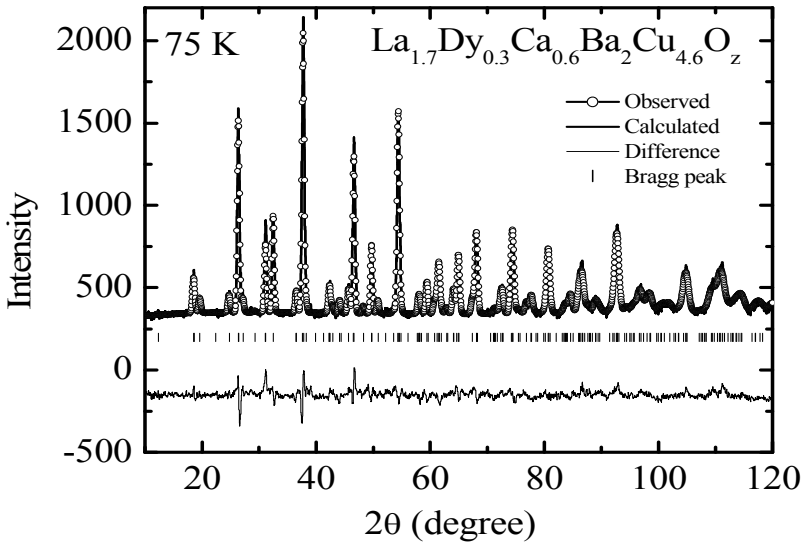

Figure 3.1(b): Rietveld refinement profile showing the observed (o symbol) and calculated (line) neutron powder diffraction data for $La_{1.7}Dy_{0.3}Ba_2Cu_{4.6}O_z$ (LD3) at 75K. Tick mark below the diffraction profile mark the position of allowed Bragg reflections. The difference between the observed and calculated values is given at the bottom.

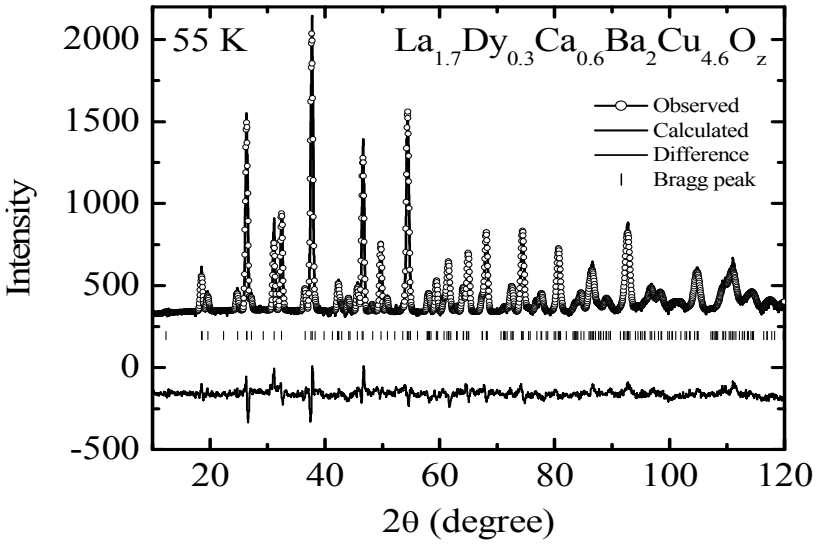

Figure 3.1(c): Rietveld refinement profile showing the observed (o symbol) and calculated (line) neutron powder diffraction data for $La_{1.7}Dy_{0.3}Ba_2Cu_{4.6}O_z$ (LD3) at 55K. Tick mark below the diffraction profile mark the position of allowed Bragg reflections. The difference between the observed and calculated values is given at the bottom.

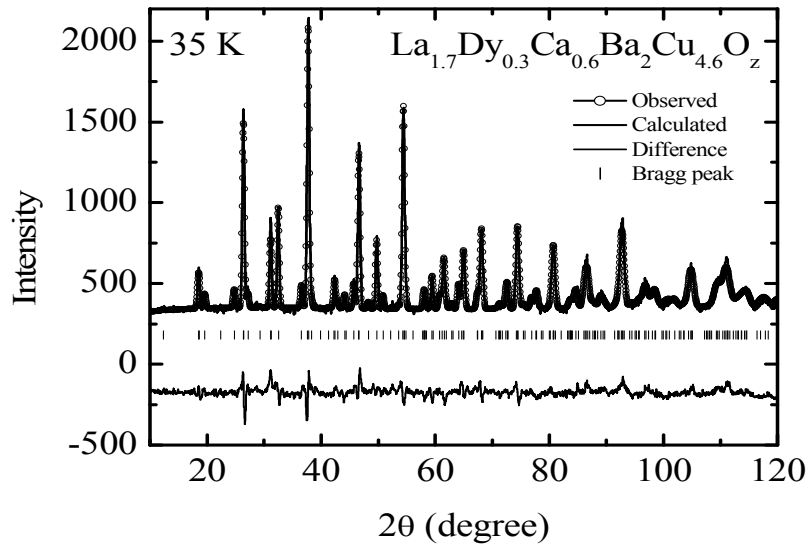

Figure 3.1(d): Rietveld refinement profile showing the observed (o symbol) and calculated (line) neutron powder diffraction data for $La_{1.7}Dy_{0.3}Ba_2Cu_{4.6}O_z$ (LD3) at 35K. Tick mark below the diffraction profile mark the position of allowed Bragg reflections. The difference between the observed and calculated values is given at the bottom.

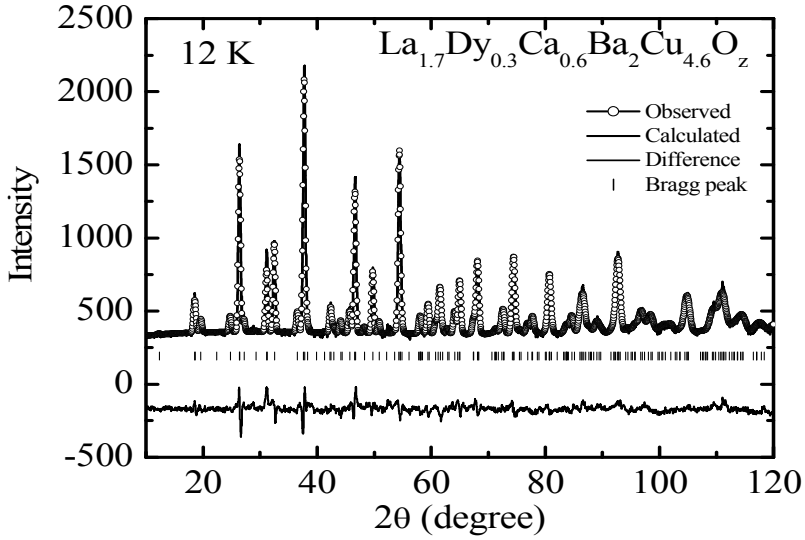

Figure 3.1(e): Rietveld refinement profile showing the observed (o symbol) and calculated (line) neutron powder diffraction data for $La_{1.7}Dy_{0.3}Ba_2Cu_{4.6}O_z$ (LD3) at 12K. Tick mark below the diffraction profile mark the position of allowed Bragg reflections. The difference between the observed and calculated values is given at the bottom.

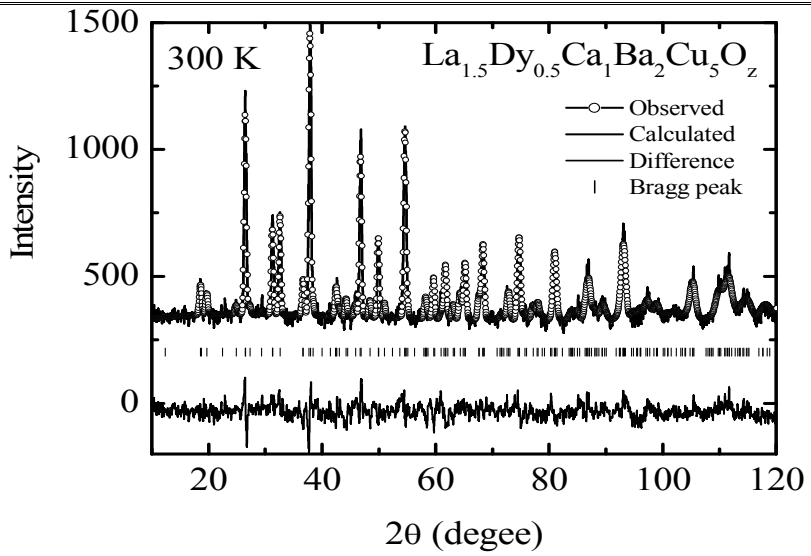

Figure 3.2(a): Rietveld refinement profile showing the observed (o symbol) and calculated (line) neutron powder diffraction data for $La_{1.5}Dy_{0.5}Ba_2Cu_5O_z$ (LD5) at 300K. Tick mark below the diffraction profile mark the position of allowed Bragg reflections. The difference between the observed and calculated values is given at the bottom.

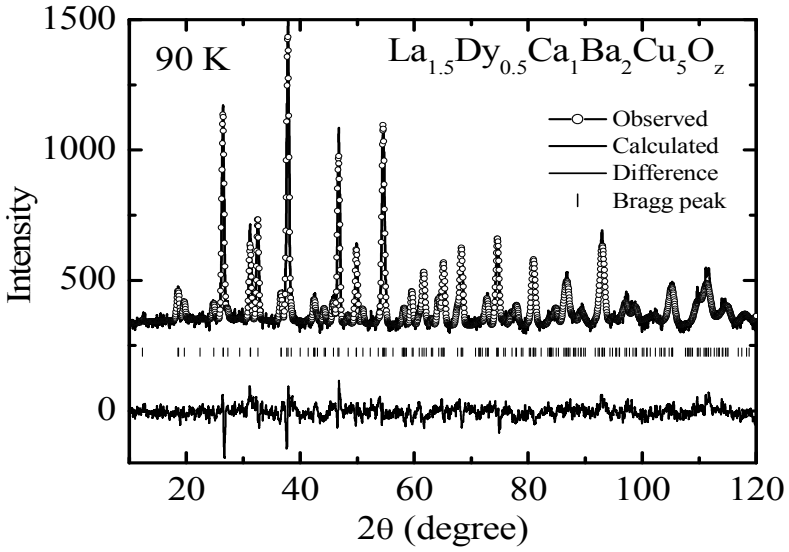

Figure 3.2(b): Rietveld refinement profile showing the observed (o symbol) and calculated (line) neutron powder diffraction data for $La_{1.5}Dy_{0.5}Ba_2Cu_5O_z$ (LD5) at 90K. Tick mark below the diffraction profile mark the position of allowed Bragg reflections. The difference between the observed and calculated values is given at the bottom.

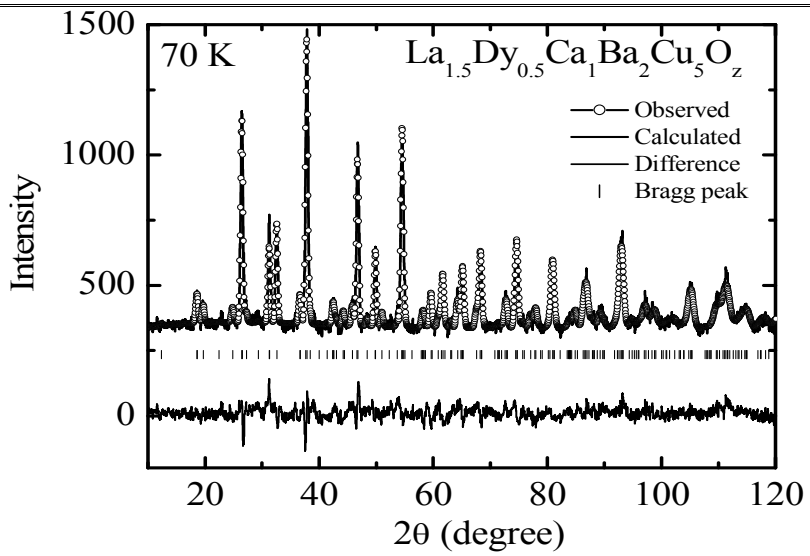

Figure 3.2(c): Rietveld refinement profile showing the observed (o symbol) and calculated (line) neutron powder diffraction data for $La_{1.5}Dy_{0.5}Ba_2Cu_5O_z$ (LD5) at 70K. Tick mark below the diffraction profile mark the position of allowed Bragg reflections. The difference between the observed and calculated values is given at the bottom.

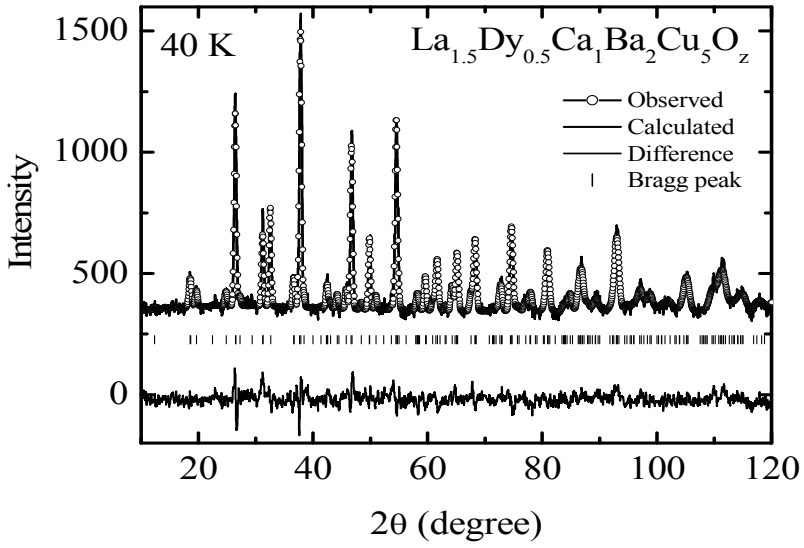

Figure 3.2(d): Rietveld refinement profile showing the observed (o symbol) and calculated (line) neutron powder diffraction data for $La_{1.5}Dy_{0.5}Ba_2Cu_5O_z$ (LD5) at 40K. Tick mark below the diffraction profile mark the position of allowed Bragg reflections. The difference between the observed and calculated values is given at the bottom.

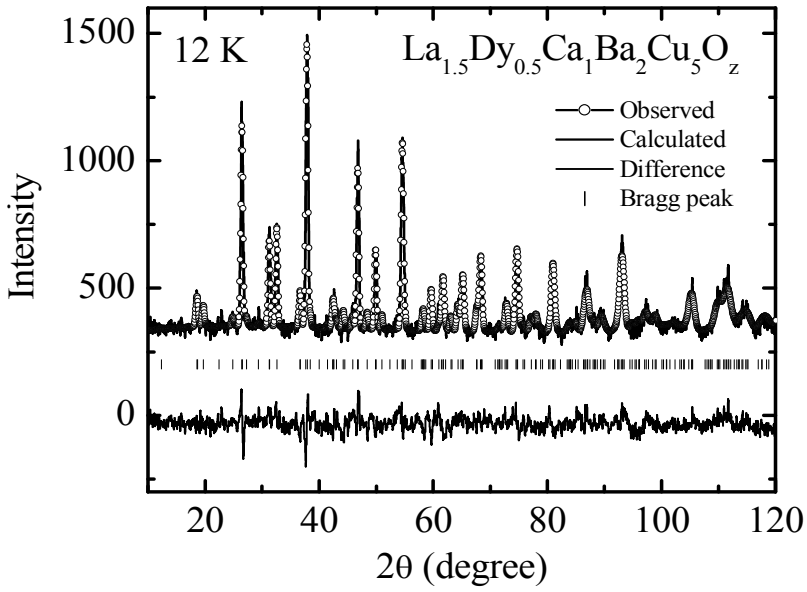

Figure 3.2(e): Rietveld refinement profile showing the observed (o symbol) and calculated (line) neutron powder diffraction data for $La_{1.5}Dy_{0.5}Ba_2Cu_5O_z$ (LD5) at 12K. Tick mark below the diffraction profile mark the position of allowed Bragg reflections. The difference between the observed and calculated values is given at the bottom.

Table 3.1: Structural parameters at various temperatures obtained from Rietveld analysis of Neutron diffraction data for LD3. Numbers in parentheses indicate standard deviation.

Temperature	12 K	35 K	55 K	75 K	300 K
La/Dy/Ca(1d)					
B (Å^2)	0.033(55)	0.033(49)	0.105(55)	0.106(53)	0.292(57)
N_{La}	0.540(3)	0.539(3)	0.540(3)	0.538(3)	0.538(3)
N_{Dy}	0.192(3)	0.195(3)	0.195(3)	0.195(3)	0.196(3)
N_{Ca}	0.256(3)	0.255(3)	0.255(3)	0.247(3)	0.256(3)
Ba/Ca/La (2h)					
B (Å^2)	1.077(85)	1.061(76)	1.033(85)	1.048(87)	0.828(99)
Z (Å)	0.1884(4)	0.1860(4)	0.1875(4)	0.1877(4)	0.1879(4)
N_{Ba}	1.342(6)	1.328(6)	1.337(6)	1.337(6)	1.346(6)
N_{La}	0.592(6)	0.587(6)	0.587(6)	0.587(6)	0.586(6)
N_{Ca}	0.202(6)	0.205(6)	0.205(6)	0.205(6)	0.176(6)
Cu(1) (1a)					
B (Å^2)	0.666(72)	0.806(99)	0.763(89)	0.760(88)	0.948(79)
N	1.000	1.000	1.000	1.000	1.000
Cu(2) (2g)					
B (Å^2)	0.109(53)	0.136(51)	0.181(43)	0.201(45)	0.287(50)
Z (Å)	0.3518(3)	0.3518(3)	0.3519(3)	0.3514(3)	0.3525(3)
N	2.000	2.000	2.000	2.000	2.000
O(1) (2f)					
B (Å^2)	4.874(60)	4.754(55)	4.364(52)	4.588(54)	5.181(61)
N	1.2510(33)	1.2550(35)	1.2310(33)	1.2380(33)	1.2960(46)
O(2) (2g)					
B (Å^2)	2.602(52)	2.690(63)	2.521(62)	2.425(55)	2.963(66)
Z (Å)	0.1535(7)	0.1537(7)	0.1545(7)	0.1543(7)	0.1528(7)
N	1.8580(36)	1.8110(38)	1.8740(37)	1.8690(36)	1.7690(34)
O(4) (4i)					
B(Å^2)	0.302(32)	0.502(35)	0.379(31)	0.396(33)	0.624(36)
Z (Å)	0.3675(4)	0.3667(2)	0.3673(2)	0.3674(2)	0.3675(2)
N	4.2890(34)	4.3310(38)	4.2830(35)	4.2740(36)	4.2770(35)
a = b (Å)	3.8573(2)	3.8577(7)	3.8583(6)	3.8586(3)	3.8644(2)
c (Å)	11.6382(9)	11.6405(5)	11.6406(3)	11.6438(4)	11.6706(4)
Volume(Å^3)	173.163(16)	173.230(22)	173.285(20)	173.357(18)	174.275(22)
Total Oxygen					
(z' – in 123)	7.397	7.395	7.388	7.381	7.342
(z – in 2125)	12.1867	12.1917	12.18	12.185	12.1034
R – factors					
χ^2	1.18	1.34	1.17	1.19	1.01
R_p	4.10	4.40	4.17	4.15	3.83
R_{wp}	5.26	5.63	5.28	5.31	4.93
R_{exp}	4.83	4.87	4.88	4.87	4.90
Bragg –R	9.89	11.4	12.0	10.7	10.3
R_f - factor	7.67	9.74	11.1	9.18	8.54

Table 3.2: Structural parameters at various temperatures obtained from Rietveld analysis of Neutron diffraction data for LD5. Numbers in parentheses indicate standard deviation.

Temperature	12 K	40 K	70 K	90 K	300 K
La/Dy/Ca(1d)					
B (Å^2)	0.026(44)	0.083(47)	0.068(44)	0.392(43)	0.212(45)
N_{La}	0.304(3)	0.304(3)	0.304(3)	0.310(3)	0.310(3)
N_{Dy}	0.304(3)	0.304(3)	0.304(3)	0.310(3)	0.310(3)
N_{Ca}	0.404(3)	0.404(3)	0.404(3)	0.410(3)	0.410(3)
Ba/Ca/La (2h)					
B (Å^2)	0.903(81)	0.825(82)	1.215(88)	0.824(78)	0.674(85)
Z (Å)	0.1904(4)	0.1909(61)	0.1916(4)	0.1912(63)	0.1913(4)
N_{Ba}	1.231(6)	1.220(6)	1.220(6)	1.220(6)	1.220(6)
N_{La}	0.631(6)	0.620(6)	0.620(6)	0.620(6)	0.620(6)
N_{Ca}	0.231(6)	0.220(6)	0.220(6)	0.220(6)	0.220(6)
Cu(1) (1a)					
B (Å^2)	0.804(72)	0.591(78)	1.034(81)	0.486(77)	0.623(79)
N	1.000	1.000	1.000	1.000	1.000
Cu(2) (2g)					
B (Å^2)	0.116(56)	0.089(55)	0.195(51)	0.231(50)	0.242(52)
Z (Å)	0.3533(4)	0.3531(4)	0.3527(3)	0.3528(3)	0.3533 (3)
N	2.000	2.000	2.000	2.000	2.000
O(1) (2f)					
B (Å^2)	5.041(60)	4.588(61)	3.711(58)	3.918(62)	6.136(65)
N	1.3730(33)	1.4340(35)	1.3570(33)	1.3070(33)	1.3070(46)
O(2) (2g)					
B (Å^2)	3.744(53)	3.018(54)	2.679(57)	2.442(53)	3.010(55)
Z (Å)	0.1545(70)	0.1551(131)	0.1557(7)	0.1533(7)	0.1538(7)
N	1.7410(36)	1.6010(38)	1.6910(37)	1.777(36)	1.757(34)
O(4) (4i)					
B(Å^2)	0.546(33)	0.445(37)	0.484(36)	0.527(33)	0.622(35)
Z (Å)	0.3675 (4)	0.3692(33)	0.36984(2)	0.36983(2)	0.3695(2)
N	4.2590(34)	4.3060(38)	4.2910(35)	4.246(36)	4.245(35)
a = b (Å)	3.8461(2)	3.8493(7)	3.8502(3)	3.8495(2)	3.8555(3)
c (Å)	11.6083(9)	11.6106(2)	11.6082(2)	11.6101(3)	11.63794(2)
Volume(Å^3)	171.722(16)	172.038(22)	172.084(22)	172.0459(18)	172.998(13)
Total Oxygen					
(z' – in 123)	7.373	7.341	7.339	7.33	7.309
(z – in 2125)	12.115	12.114	12.114	12.084	12.098
R – factors					
χ^2	1.83	1.37	1.34	1.42	1.13
R_p	5.42	4.56	4.59	4.74	4.24
R_{wp}	6.85	5.84	5.81	6.05	5.45
R_{exp}	5.07	4.98	5.03	5.08	5.14
Bragg –R	12.3	9.41	8.69	9.17	8.32
R_f - factor	9.36	5.6	5.39	5.88	5.13

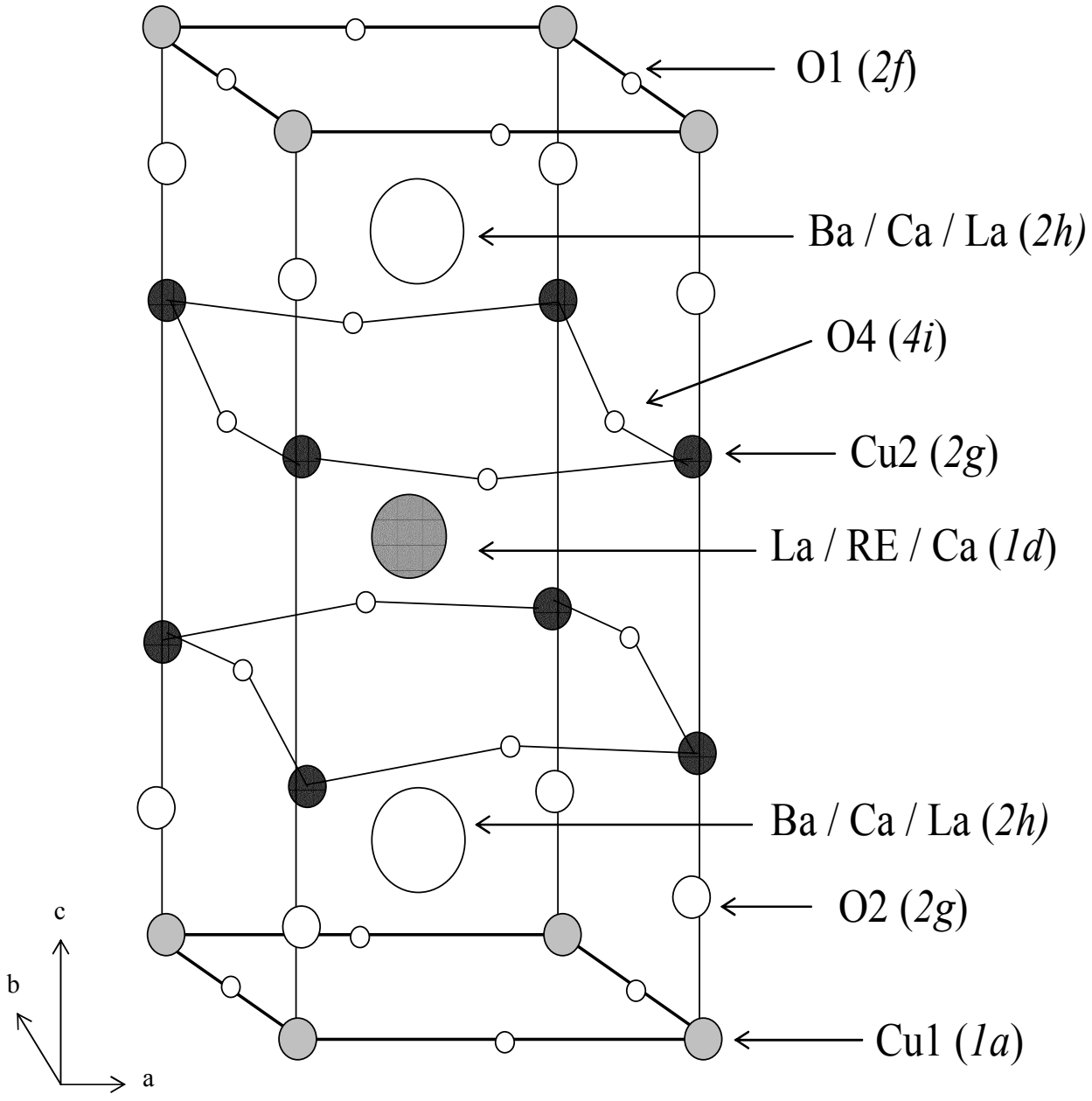

Figure 3.3: Structure of La-2125 unit cell isostructural to tetragonal Ln-123 unit cell.

From the details of the Rietveld refinement of neutron diffraction data of La-2125 (LD3 and LD5) compounds, it turns out that, the structural arrangement of La-2125 is tetragonal (Space group: P4/mmm; Space group No. 123) which is equivalent to that of the tetragonal Ln-123 unit cell as can be seen from fig. 3.3. Due to the difference in the scattering factors of La, Dy and Ca, the site occupancy of Dy and Ca at the La site could be refined in the La-2125 phase. Results shown in Table 3.1 and 3.2, indicate that, the average amount of Dy and Ca in the La site coincide with the nominal composition in La-2125 unit having crystallographic position of *1d* (½, ½, ½) (CN-8). From the analysis of the ND data it is clear that, part of La and Ca occupy the Ba site at *2h* (½, ½, ±z) (CN-10) position. The copper atom occupies two different crystallographic sites and are positioned as Cu1 (CN-6) at *1a* (000) and Cu2 (CN-5) at *2g* (0, 0, ±z) crystallographic positions. In tetragonal geometry of Ln-123, oxygen atoms have three different configurations as O1, O2 and O4 which are positioned at *2f* (0, ½, 0)/(½, 0, 0), *2g* (0, 0, ±z) and *4i* (0,½, ±z)/(½, 0, ±z) respectively. Further, the tetragonal geometry suggests that. there is a presence of Cu1-O1 planes instead of the extended Cu-O chains in the La-2125 compound unlike that of Ln-123 superconductor where the oxygen deficiency ($6.6< z < 7$) in Cu1-O1 layers along the *a* direction leads orthorhombic structure and superconductivity ($T_c \sim 90K$). The site occupancies obtained from Rietveld analysis of ND data at various temperatures for LD3 and LD5 compounds have been tabulated in Table 3.1 and 3.2. There is very close agreement between the site occupancy obtained from the Rietveld refinement of ND data and the values of the fractional occupancies of LD3 and LD5 samples as estimated using Eqns.(b) and (c).

During the procedure of refinements, all possible positional (x, y, z), thermal parameters (B) and occupational (N) parameters were varied in addition to cell parameters, half width parameters, background parameters, zero angle and scale factor. These parameters were varied in separate cycles due to a strong correlation between the thermal and occupancy parameters. The occupancy fractions of Ba and La ions at Ba-sties were refined assuming that no vacancies are present at these sites. The occupancy fractions of La were refined assuming all substituted Dy and Ca ions occupy La-site only (for non-zero values of x and y). As a result of refinement, very good fits were obtained at all the five temperature scans for both the LD3 and LD5 samples [shown in Fig.3.1 and 3.2 (a-e)] on

the basis of standard tetragonal 1-2-3 structural model with the final values of profile R-factors (R_p) converging [Table 3.1 and 3.2]. There is no structural transition observed in both the samples as a function of temperature and the compounds remain tetragonal with space group P4/mmm at all temperatures. With lowering the temperature, the thermal parameters show reasonable values for all the atomic sites refined and remain within the experimentally allowed error. Unit cell parameters at various temperatures determined from the Rietveld refinement of neutron diffraction data of LD3 and LD5 samples are also listed in Table 3.1 and 3.2 and their variation with temperature is plotted in fig. 3.4. For both the compositions, with the decrease in the temperature, the lattice parameters contract leading to the over all decrease in the cell volume. Further, the values of unit cell parameters and volume in LD3 sample are higher as compared to LD5 sample because the LD5 sample is having higher concentration of Ca^{2+} having smaller ionic radius which occupies La and Ba sites simultaneously resulting in the shrinkage of cell dimensions.

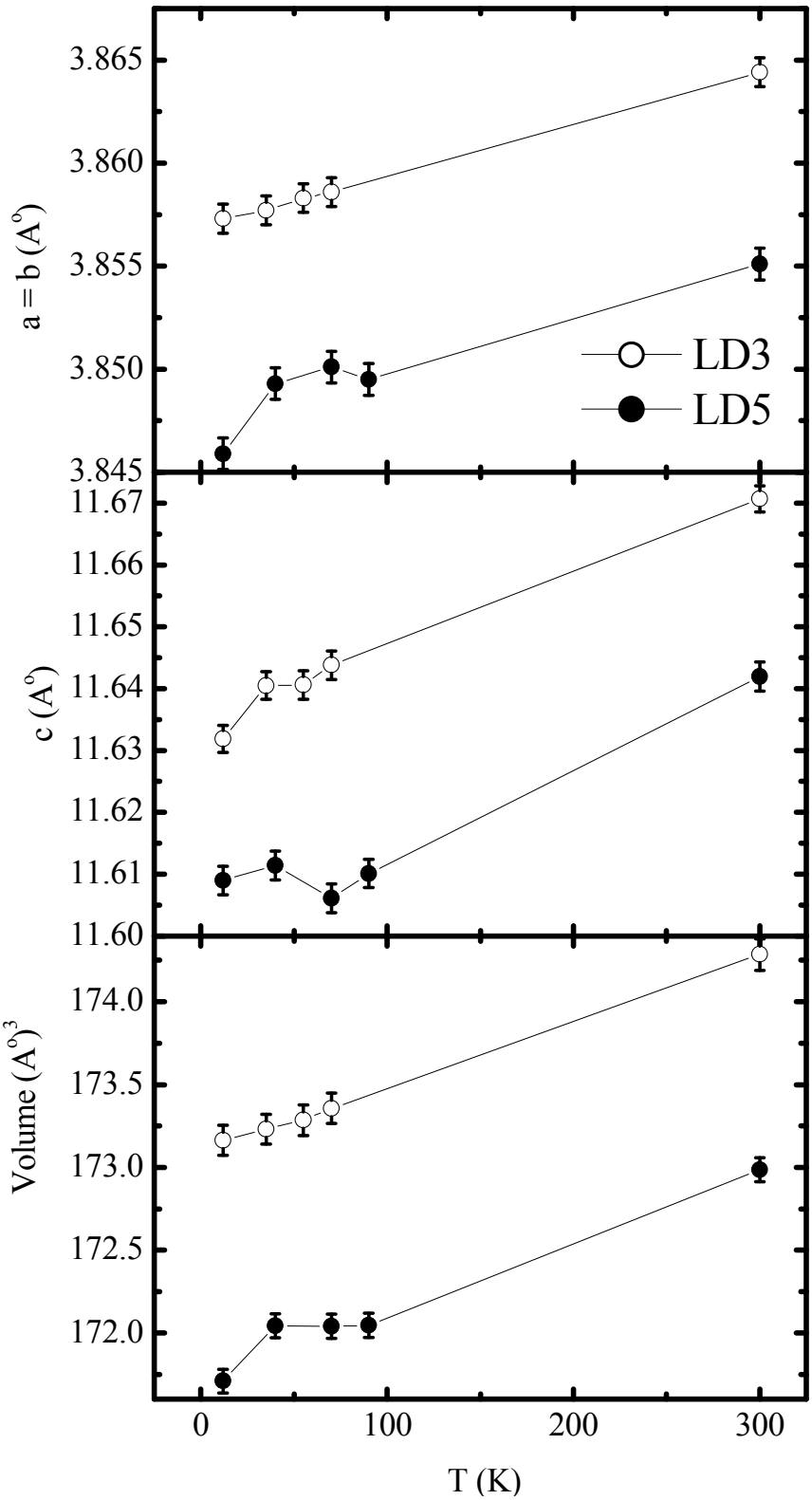

Figure 3.4: Unit cell parameters vs. T (K) for LD3 and LD5 samples.

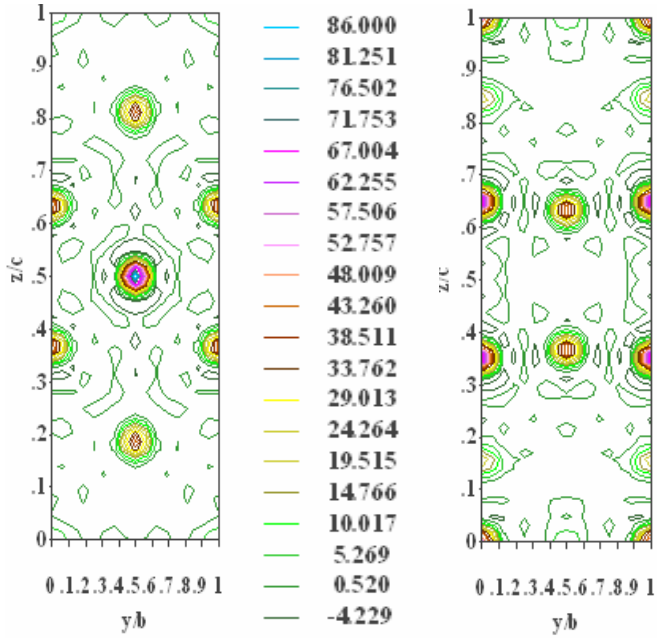

Figure 3.5(a): Difference Fourier map for LD3 at 12K.

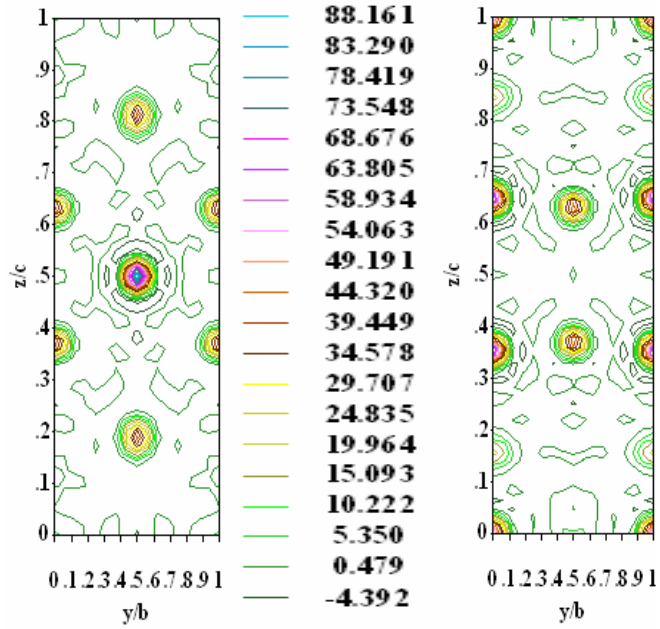

Figure 3.5(b): Difference Fourier map for LD5 at 12K.

Table 3.3(a): Site occupancy (Occ), site multiplicity (Mult), Wyckoff coordination (x/a, y/b, z/c) and atomic densities at 12 for LD3.

Atom	x/a	y/b	z/c	Occ	Mult	Density
La1	0.5000	0.5000	0.5000	0.0625	1	90.7484
Dy	0.5000	0.5000	0.5000	0.0625	1	90.7484
Ca1	0.5000	0.5000	0.5000	0.0625	1	90.7484
Ba	0.5000	0.5000	0.1884	0.1250	2	44.7953
La2	0.5000	0.5000	0.1884	0.1250	2	44.7953
Ca2	0.5000	0.5000	0.1884	0.1250	2	44.7953
Cu1	0.0000	0.0000	0.0000	0.0625	1	57.7008
Cu2	0.0000	0.0000	0.3518	0.1250	2	70.0922
O1	0.0000	0.5000	0.0000	0.1250	2	9.3995
O2	0.0000	0.0000	0.1535	0.1250	2	23.4735
O4	0.5000	0.0000	0.3675	0.2500	4	46.8070

Table 3.3(b): Site occupancy (Occ), site multiplicity (Mult), Wyckoff coordination (x/a, y/b, z/c) and atomic densities at 12 for LD5.

Atom	x/a	y/b	z/c	Occ	Mult	Density
La1	0.5000	0.5000	0.5000	0.0625	1	90.0324
Dy	0.5000	0.5000	0.5000	0.0625	1	90.0324
Ca1	0.5000	0.5000	0.5000	0.0625	1	90.0324
Ba	0.5000	0.5000	0.1904	0.1250	2	46.3625
La2	0.5000	0.5000	0.1904	0.1250	2	46.3625
Ca2	0.5000	0.5000	0.1904	0.1250	2	46.3625
Cu1	0.0000	0.0000	0.0000	0.0625	1	62.0440
Cu2	0.0000	0.0000	0.3533	0.1250	2	69.4829
O1	0.0000	0.5000	0.0000	0.1250	2	5.6948
O2	0.0000	0.0000	0.1545	0.1250	2	22.2865
O4	0.5000	0.0000	0.3675	0.2500	4	48.1759

In order to locate the atoms at particular crystallographic sites, the difference Fourier map was calculated using GFourier program [9] which plots the scattered atomic density contours using the difference between Fast Fourier Transform (FFT) of calculated and observed structure factors. The calculated difference Fourier maps for LD3 and LD5 samples at 12K are shown in figs.3.4(a) and (b). The structural information regarding the site occupancy, site multiplicity, Wyckoff coordination and atomic densities determined from the figs. 3.4(a) and (b) at 12K, are summarized in Table 3.3 (a) and Table 3.3(b) for both the LD3 and LD5 samples. The left part of the fig. 3.4 [(a) and (b)] shows the scattering densities for the central Ln-site, Ba and Cu2 crystallographic sites whereas the right part of the respective figs, show the scattering densities for Cu1, Cu2, O1, O2 and O4 crystallographic sites. The presence of atomic density for O1-site suggests that, there are Cu1-O1 planes instead of extended Cu1-O1 chains in the LD3 and LD5 samples.

Internal strains concerning the bonds with the apical oxygens are important in the doped La-2125 structure derived from La-123 since the apical oxygen site is sensitive to size effects, to the presence of excess oxygen on the basal plane and the La/Ba disorder [10]. These interatomic distances are also sensitive to the occupancy of the O4 sites which may be varied by the La/Ba replacement and the modified values are partially due to the variations in the oxygen doping. In order to have more insight in this regard, interatomic distances obtained from Rietveld analysis of low temperature ND are listed in Tables 3.4 (a) and (b) for LD3 and LD5 samples respectively and are plotted as a function of temperature for various atomic species in figs. 3.6 (a-e).

Table 3.4(a): Interatomic distances (Å) at various temperatures for LD3. Numbers in parentheses indicates standard deviations.

Temperature	12 K	35 K	55 K	75 K	300 K
r(La-O4)	2.4694(2)	2.4707(2)	2.4714(3)	2.4712(2)	2.4745(3)
r(La-Ba)	3.6226(5)	3.6359(7)	3.6368(7)	3.6366(5)	3.6424(2)
r(La-Cu2)	3.2271(2)	3.2271(3)	3.2270(3)	3.2307(2)	3.2294(3)
r(Ba-Cu1)	3.5021(2)	3.4926(4)	3.4944(4)	3.4957(2)	3.5037(3)
r(Ba-Cu2)	3.3243(2)	3.3319(5)	3.3322(5)	3.3285(2)	3.3404(4)
r(Ba-O1)	2.9232(2)	2.9128(5)	2.9122(5)	2.9142(2)	2.9298(3)
r(Ba-O2)	2.7593(2)	2.7536(3)	2.7535(2)	2.7543(1)	2.7631(2)
r(Ba-O4)	2.8371(2)	2.8406(6)	2.8432(6)	2.8434(2)	2.8464(4)
r(Cu1-O1)	1.9287(2)	1.9288(2)	1.9291(3)	1.9293(4)	1.9322(2)
r(Cu1-O2)	1.7861(3)	1.7850(2)	1.7859(1)	1.7849(3)	1.7831(2)
r(Cu1-Cu1)	3.8573(2)	3.8577(7)	3.8583(6)	3.8586(3)	3.8644(2)
r(Cu2-Cu2)	3.4493(5)	3.4488(8)	3.4470(8)	3.4601(4)	3.4424(5)
r(Cu2-O2)	2.3083(3)	2.3068(3)	2.3190(2)	2.3199(3)	2.3310(2)
r(Cu2-O4)	1.9373(2)	1.9374(2)	1.9375(4)	1.9382(1)	1.9401(3)
Cu2-O4-Cu2	169.329(2)	169.731(1)	169.416(2)	169.003(2)	169.632(3)
Buckling Length	0.88244	0.88259	0.88513	0.8738	0.89524

Table 3.4(b): Interatomic distances (Å) at various temperatures for LD5. Numbers in parentheses indicates standard deviations.

Temperature	12 K	40 K	70 K	90 K	300 K
r(La-O4)	2.4593(2)	2.4510(2)	2.4481(3)	2.4495(3)	2.4537(2)
r(La-Ba)	3.5735(5)	3.6044(7)	3.6062(7)	3.6189(5)	3.6147(3)
r(La-Cu2)	3.2098(1)	3.2120(3)	3.2141(3)	3.2169(1)	3.2163(1)
r(Ba-Cu1)	3.5051(2)	3.5111(4)	3.5172(4)	3.5153(2)	3.5198(2)
r(Ba-Cu2)	3.3108(2)	3.3093(5)	3.3043(5)	3.3094(4)	3.3150(3)
r(Ba-O1)	2.9454(1)	2.9240(5)	2.9209(5)	2.9186(2)	2.9320(3)
r(Ba-O2)	2.7578(2)	2.7505(3)	2.7465(2)	2.7462(1)	2.7534(1)
r(Ba-O4)	2.8181(2)	2.8270(6)	2.8261(6)	2.8329(5)	2.8319(5)
r(Cu1-O1)	1.9230(2)	1.9246(3)	1.9251(3)	1.9262(1)	1.9277(3)
r(Cu1-O2)	1.7937(3)	1.7941(1)	1.7952(2)	1.7921(2)	1.7909(2)
r(Cu1-Cu1)	3.8458(2)	3.8492(5)	3.8501(4)	3.8495(3)	3.8551(1)
r(Cu2-Cu2)	3.4096(5)	3.4112(8)	3.4172(8)	3.4223(4)	3.4131(2)
r(Cu2-O2)	2.3056(3)	2.2994(1)	2.2971(1)	2.3189(3)	2.3214(2)
r(Cu2-O4)	1.9307(2)	1.9338(7)	1.9362(8)	1.9363(5)	1.9370(5)
Cu2-O4-Cu2	169.789(2)	168.840(2)	168.290(3)	168.264(2)	168.828(3)
Buckling Length	0.9424	0.9028	0.8994	0.8986	0.9209

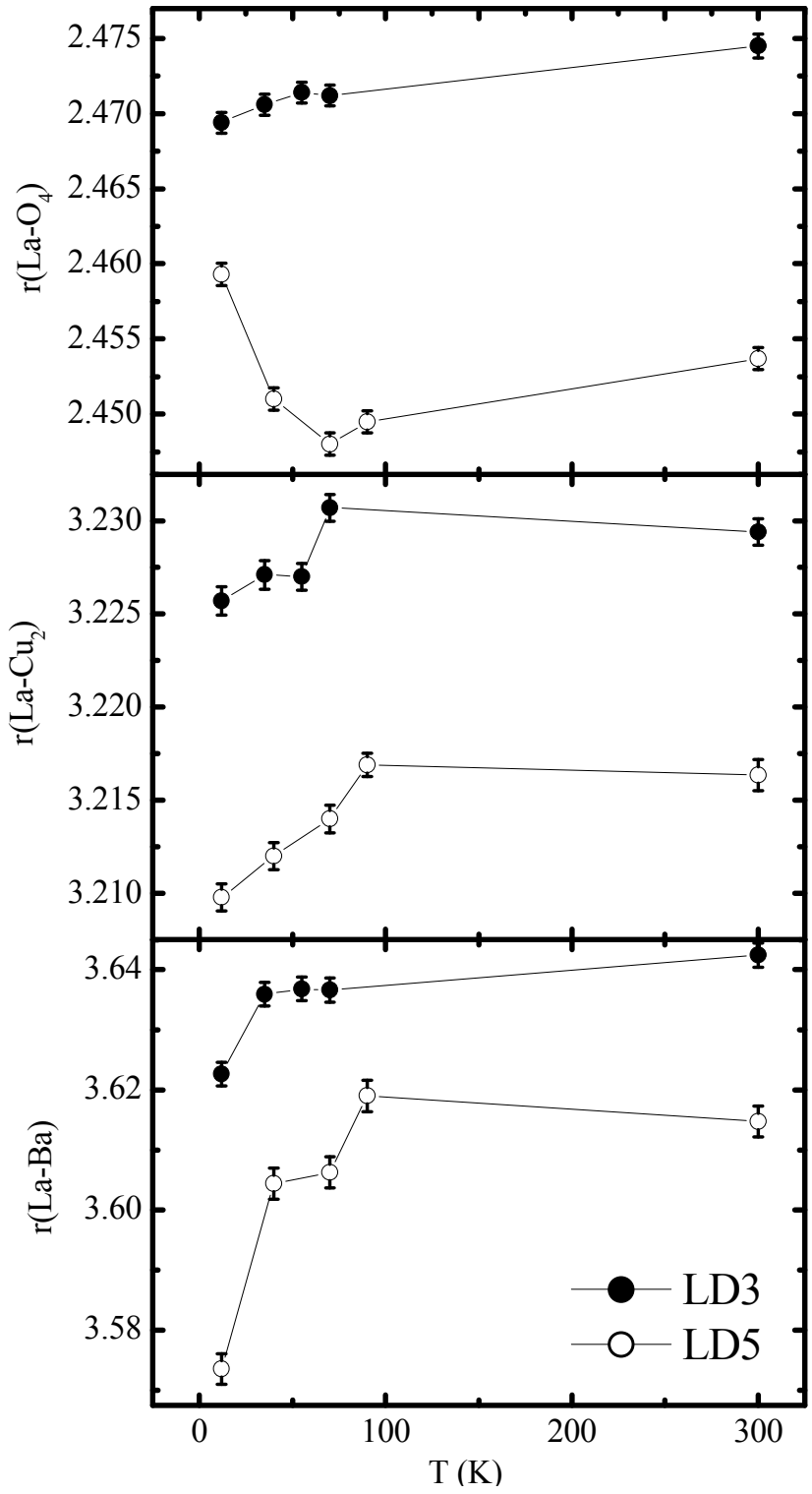

Figure 3.6(a): Interatomic distance between r(La-O4), r(La-Cu2) and r(La-Ba) vs. T (K) for LD3 and LD5 samples.

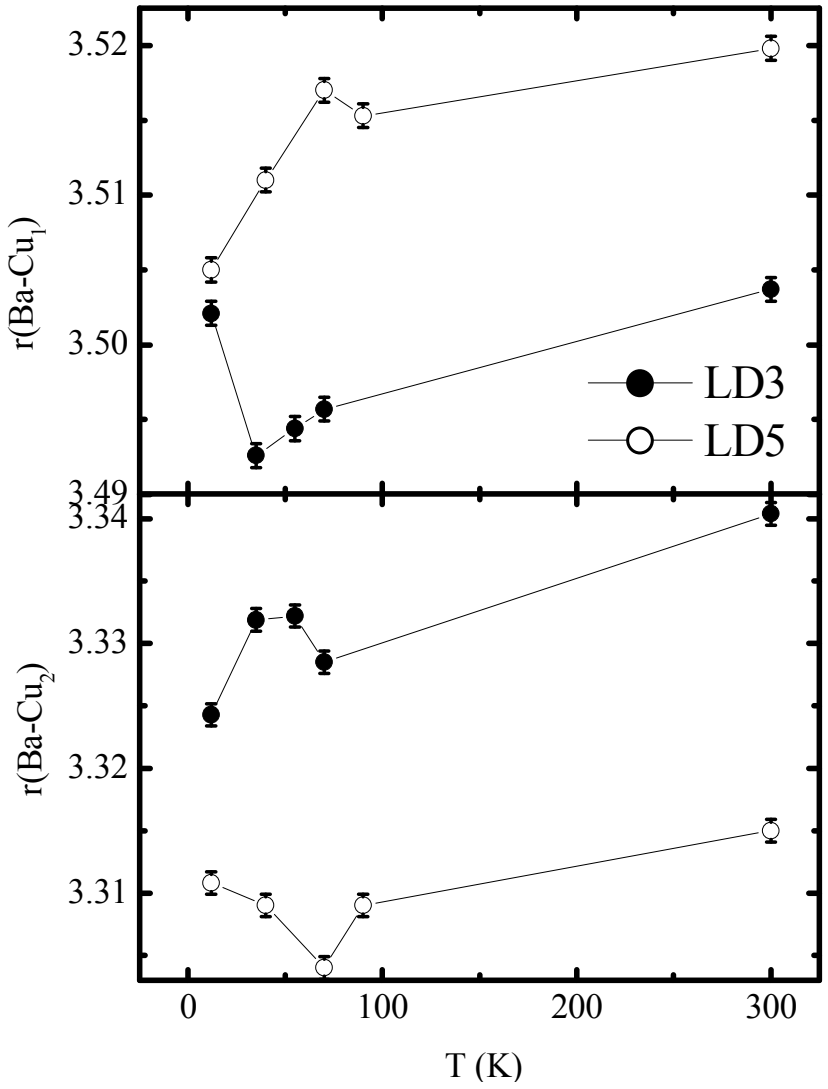

Figure 3.6(b): Interatomic distance between r(Ba-Cu1) and r(Ba-Cu2) vs. T (K) for LD3 and LD5 samples.

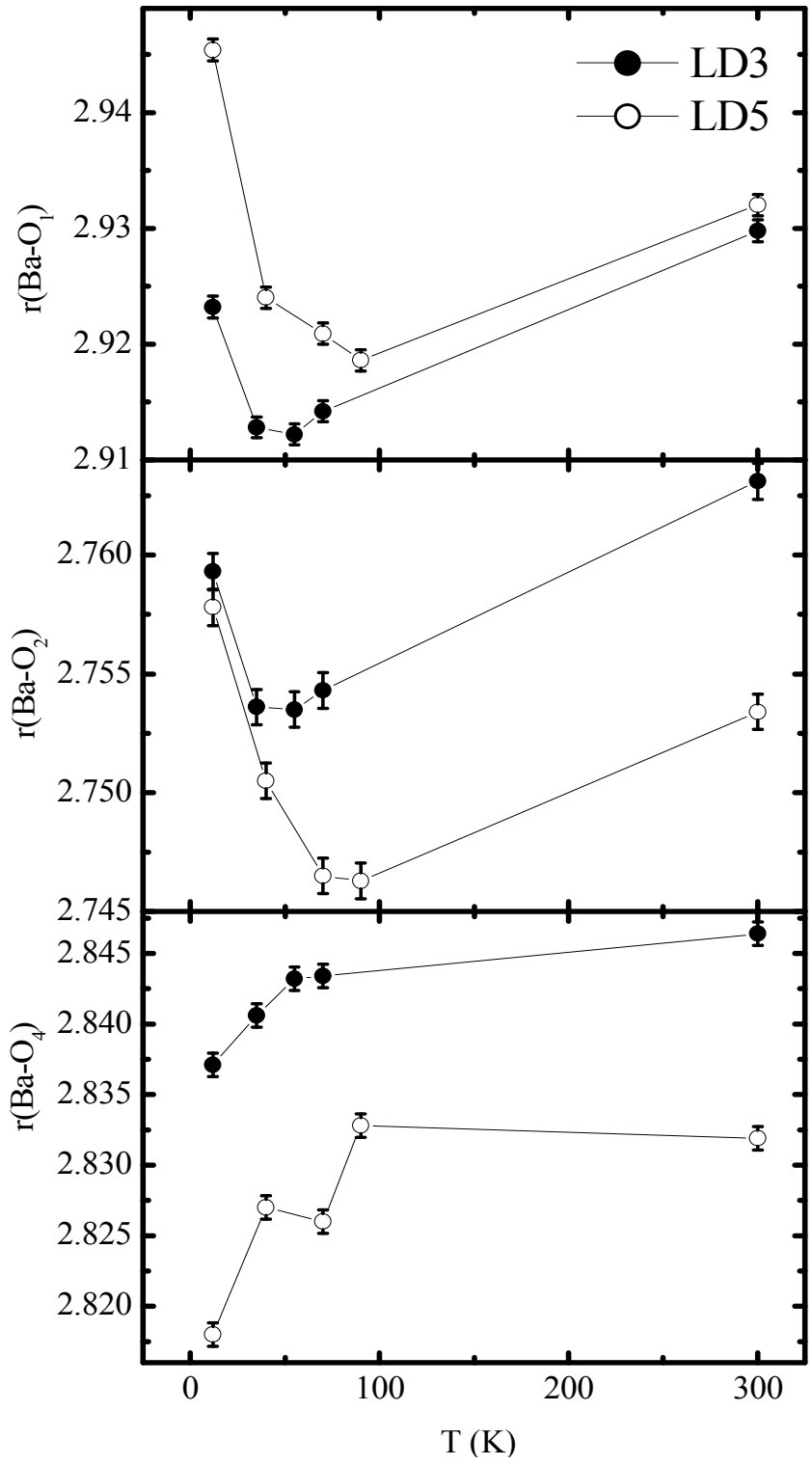

Figure 3.6(c): Interatomic distance between r(Ba-O1), r(Ba-O2) and r(Ba-Cu2) vs. T (K) for LD3 and LD5 samples.

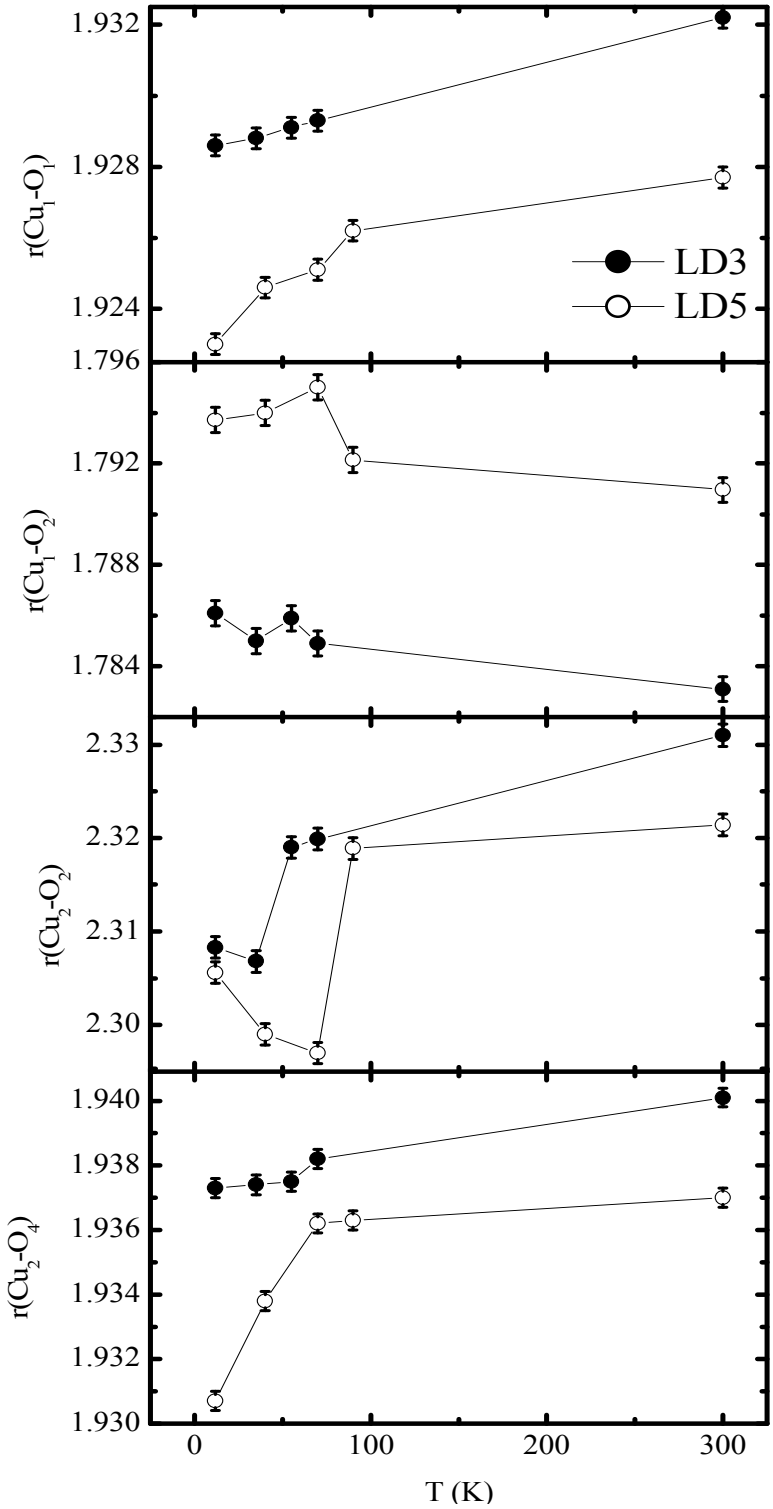

Figure 3.6(d): Interatomic distance between r(Cu1-O1), r(Cu1-O2), r(Cu2-O2) and r(Cu2-Cu4) vs. T (K) for LD3 and LD5 samples.

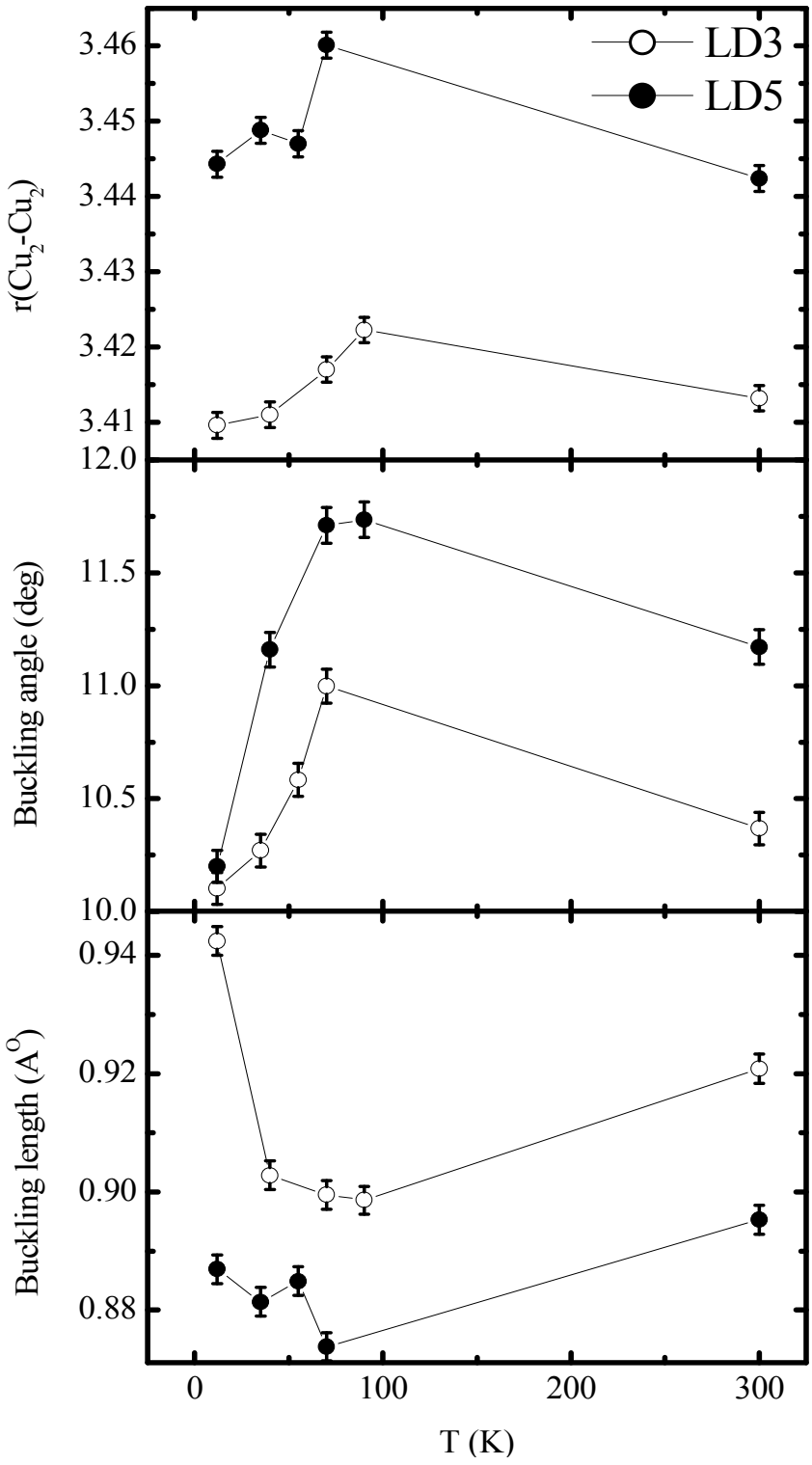

Figure 3.6(e): Bond distance r(Cu2-O2), buckling angle and buckling length vs. T (K) for LD3 and LD5 samples.

The observed variation in the bond length of LD3 and LD5 samples at various temperatures, shown in figs.3.6(a-e) can be explained as follows

It can be seen from fig. 3.6 that, r(La-O4), r(La-Cu2) and r(La-Ba) bond lengths get compressed with the decrease in temperature for both the samples [Fig 3.6(a)] while the r(Ba-O1) and r(Ba-O2) bond lengths decreases first and below T_c shows an increasing trend as compared to their values at RT [Fig.3.6(c)]. The variation in different Cu-O bond lengths has been shown in fig.3.6(d). In Cu1-O1 and Cu2-O4 planes, the r(Cu1-O1) and r(Cu2-O4) bond lengths decreases linearly with temperature. This indicates that, the ionic size effect and shrinkage is more pronounced in the central perovskite block comprising of Cu2-O4-Cu2 in the triple perovskite unit cell. The decrease in the r(Ba-Cu1) and r(Ba-Cu2) bond lengths [Fig 3.6(b)] in the upper and lower perovskite blocks containing central Ba-atom can be attributed to the partial substitution of La and Ca at Ba site. In addition, La-2125 structure, with increasing Dy^{3+} and Ca^{2+} concentration substituting at La-site having 1*h* *(*1/2,1/2,1/2) position in the unit cell, results in the decrease of r(Cu2–Cu2) bond length in LD5 sample as compared to LD3 sample which is accompanied by the suppression in Cu2-O4-Cu2 buckling angle [Fig.3.6(e)]. Hence, the overall effect of this results in the increase in T_c of LD5 sample [$T_c \sim 78K$].

3.2. Bond Valence Sum (BVS) analysis

According to the Pauling's electrostatic valence rule, for an an ionic crystal in a stable ionic structure, the charge on an ion is balanced by the sum of electrostatic bond strengths to the ions in its coordination polyhedron. The Pauling's Bond valence sum (BVS) relates the bond lengths of the cations to be considered with its average valence state using the formula,

$$V_i = \sum_j S_{ij} = \exp\left(\frac{R_0 - R_{ij}}{B}\right) \qquad (1)$$

where r_0 (characteristic value for a given cation-anion pair) and B (0.37Å) are empirical parameters and R_{ij} is the interionic distance, where an ion can exist with several different oxidation states. The value of R_0 will depend on the oxidation state. The idea is that, the sum of these empirical bond valences about a given ion should agree with that of oxidation state of ion. Any significant discrepancy ~ 30% between the BVS and the true oxidation state represents strain in the crystal, and may even indicate that the assumed structure is incorrect. The BVS technique has sometimes proved to be a useful tool in checking crystal structures [11,12]. In layered cuprates, the hole concentration is distributed at two different crystallographic sites of Cu i.e. in CuO_2 planes and Cu-O chains between the inter Ba-planes and can be determined by chemical route, Bond Valence Sum (BVS) analysis, thermo electric power (TEP) and Hall effect studies. The chemical idometric titration gives the values of mobile charge density from the estimation of oxygen content while TEP and Hall effect measurements are direct methods for the determination of hole concentration. The BVS technique provides the information about the explicit distribution of Cu valences in CuO2 planes and Cu-O chains in the mixed oxide superconductors [13].

In the present work, BVS calculations were performed based on the low temperature ND data obtained on LD3 and LD5 samples. Structural BVS analysis for Cu gives the effective Cu valence which is helpful in understanding the role played by holes in inducing superconductivity in these samples. For the sake of clarity and better understanding, the values of average copper valence calculated from BVS studies and those obtained from Rietveld refinement have been compared in the last part of this Chapter.

Bond Valence Sum calculation have been performed to determine average copper valence in Cu-O planes using Eqn.(1) and Ref.[14]. In oxide superconductors, the copper valance varies between 2+/3+ or 2+/1+ and hence it can have fractional value. It is reported that, tetragonal superconductors, such as LD3 and LD5 having total oxygen content ~7.31 and ~7.33 per formula unit, lies in the 'over hole doped' region of high temperature superconductors and hence can possess Cu valence between 2+ and 3+. Let us assume that the fractional value is given by ξ i.e. the content of Cu^{+3}, then (1- ξ) will be Cu^{2+} content. Hence,

$$V_{avg} = 3\xi + 2(1 - \xi) = 2 + \xi \qquad (2)$$

$$\xi = (V^{2+} - 2) / (V^{2+} + 1 - V^{3+}) \qquad (3)$$

where ξ is the mixing parameter. V^{2+} is the BVS for Cu^{2+} and V^{3+} is the BVS for Cu^{3+}. ξ can be determined as follows:

1. Calculate copper valence for Cu_I plane by using $r_0 (Cu^{2+})$ and then $r_0 (Cu^{3+})$ in Eqn.(1) and find out ξ_I using Eqn.(3).
2. Follow the same procedure for Cu_{II} plane and find out ξ_{II}

Global average can be determined by the following equation,

$$V_{avg}^{Global} = (V_{avg}^{CuI} + 2\, V_{avg}^{CuII}) / 3 = (6 + \xi_I + 2\, \xi_{II}) / 3 \qquad (4)$$

while the stoichiometric average copper valence can be determined from the values of oxygen contents and of other stoichiometric ions obtained from ND data using the following formula,

$$V_{Avg}^{Stoichiometry} = \frac{2z - Q}{3};\ Q = [(2 - x)(La) + (x)(Dy) + (2x)(Ca) + 2(Ba)] \times \frac{3}{5} \qquad (5)$$

where $3/5$ is the normalization factor [6].

3.3. Comparative study: Experimental and Theory

Since the relation between valence and bond lengths is inversely proportional [Eqn.(1) and Ref.13], one would expect increase in Cu valence with decreasing bond length. In the present case, the decrease in bond length r(Cu2-O4) with decrease in temperature [Fig.3.6(d)] and consequently increase in average Cu valence with decrease in temperature [Fig.3.7] have been observed in LD3 and LD5 samples. Below T_c, r(Cu2-O4) bond length and average Cu valence remains almost constant in LD3 sample while in LD5 sample, there is a decrease in the bond length and a sharp rise in average Cu valence suggesting that, the concentration of mobile holes in the superconducting region (below T_c) increases appreciably in the LD5 sample. The parameters obtained from BVS analysis using Eqns.(1-5) are listed in Tables 3.6(a) and (b).

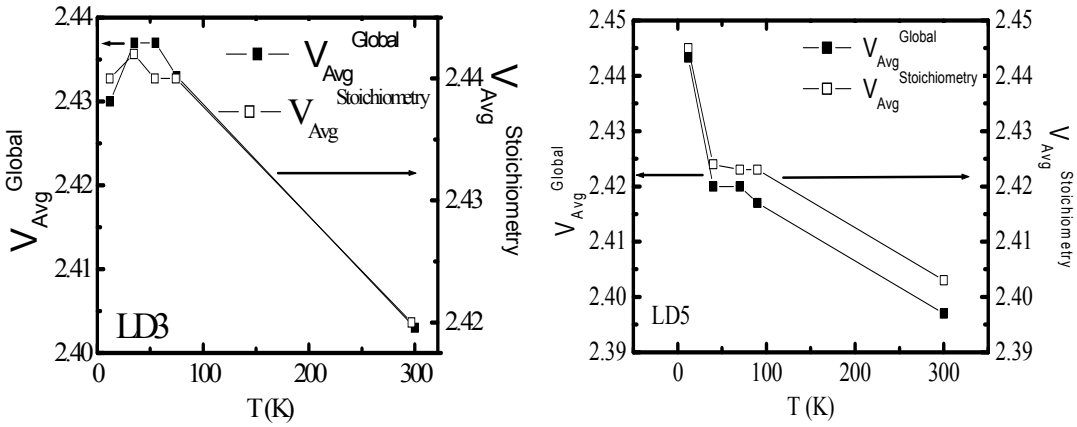

Figure 3.7: Variation of calculated and observed average copper valence with temperature for $La_{2-x}Dy_xCa_{2x}Ba_2Cu_{4+2x}O_z$ (x = 0.3 and 0.5).

It is reported that, the difference between calculated and observed values of average copper valence determines the strain in the lattice [13] and hence this correction must be added in Eqn.1 for determination of global average valence. In the present case this deviation is ~ 0.01 / 2 = 0.005, which is added to V_{avg}^{CuI} and V_{avg}^{CuII} respectively as correction. The r.m.s values of these deviations for every temperature is only ~ 0.05 v.u (i.e. < 0.1 v.u.) which prove the absence of strain on the bonds and also the absence of any structural instabilities in the samples studied.

Table 3.6(a): Values of ξ_I and ξ_{II}, average copper valence obtained from BVS calculation and from stoichiometry at different temperatures for LD3.

Temperature (K)	**12 K**	**35 K**	**55 K**	**75 K**	**300 K**
ξ_I	0.77	0.77	0.78	0.78	0.75
ξ_{II}	0.25	0.25	0.24	0.24	0.21
$V^{Avg}_{Stoichiometry}$	2.431	2.43	2.43	2.421	2.395
V^{Avg}_{Globle}	2.4233	2.423	2.42	2.42	2.39

Table 3.6(b): Values of ξ_I and ξ_{II}, average copper valence obtained from BVS calculation and from stoichiometry at different temperatures for LD5.

Temperature (K)	**12 K**	**40 K**	**70 K**	**90 K**	**300 K**
ξ_I	0.71	0.68	0.72	0.73	0.83
ξ_{II}	0.31	0.29	0.27	0.25	0.18
$V^{Avg}_{Stoichiometry}$	2.445	2.424	2.423	2.423	2.403
V^{Avg}_{Globle}	2.4433	2.42	2.42	2.417	2.397

Conclusions

The structural studies on the $La_{2-x}Dy_xCa_yBa_2Cu_{4+y}O_z$ (x = 0.3 and 0.5, y = 2x) mixed oxide superconductors using temperature dependent neutron powder diffraction measurements and structural Bond Valence Sum (BVS) analysis at various temperatures in the range 12-300 K have been carried out. The important conclusions derived from the above studies are summarized as follows

Temperature dependent ND measurements on LD3 and LD5 samples at various temperatures and the Rietveld refinement of ND data reveals that, there is no structural transition observed in the samples up to 12K. At low temperatures, there is a unit cell contraction in both the samples. The scaling between T_c and r(Cu2-Cu2) bond length and buckling angle has been observed. It can be clearly seen that, near T_c, r(Cu2-Cu2) bond length and buckling angle are maximum which are found to decrease on either side of T_c monotonically.

Structural Bond Valence Sum calculations performed on low temperature ND data at various temperatures on LD3 and LD5 samples show an increase in average Cu valence with the decrease in temperature. The V_{Avg}^{Global} saturates around low temperature indicating an increase in the mobile charge density in the superconducting state. The values of average Cu valence calculated by BVS are slightly different from those of stoichiometric valence which can be attributed to the asymmetrical variation of Cu-O bond length. There is no observation of structural strain or instability at low temperatures in the La-2125 mixed oxide superconductors.

References

1. R. J. Cava, B. Batlogg, R. B. van Dover, D. W. Murphy, S. Sunshine, T. Siegrist, J. P. Remeika, E. A. Rietman, S. Zahurak. and G. P. Espinosa, Phys. Rev. Lett.1987, 58 (1676)
2. Y. Song, J. P. Golben, S. Chittipeddi, S. I. Lee, R. D. McMichael, X. D. Chen, J. R. Gaines, D. L. Cox and A. J. Epstein, Phys. Rev. B, 37, 607 (1988)
3. J. B. Goodenough, Supercond. Sci. Technol. 3, 26 (1990)
4. S. Rayaprol, Krushna Mavani, D. S. Rana, C. M. Thaker. S. Thampi, D. G. Kuberkar Journal of Supercond. 15, 3, 211 (2002)
5. S. Rayaprol, D. C. Kundaliya, C. M. Thaker, D. G. Kuberkar, Keka R. Chakraborty, P. S. R. Krishna and M. Ramanadham, J. Phys.: Condens. Matter, 16, 6551 (2004)
6. S. Rayaprol, Rohini Parmar, D. G. Kuberkar, Keka R. Chakraborty, P. S. R. Krishnan and M. Ramanadham, Pramana J. Phys. 63, 213 (2004)
7. H. M. Rietveld, J. Appl. Cryst. 2, 65 (1969)
8. L. B. McCusker, R. B. Von Dreele, D. E. Cox, D. Louer and P. Scardi, J. Appl. Cryst. 32, 36 (1999)
9. J. Rodriguez-Carvajal (Version 3.5d Oct 98-LLB-JRC) Laboratoire Leon Brillouin (CEA-CNRS)
10. A. Gantis, M. Calamiotou, D. Palles, D. Lampakis and E. Liarokapis, Phys. Rev. B, 68, 064502 (2003)
11. L. J. Pauling, Am. Chem. Soc. 49, 765 (1927)
12. A. Bystrom and K. A. Wilhelmi, Acta. Chem. Scand. 5, 003 (1951)
13. I. D. Brown, A. Dabkowski and A. Mccleary, Acta Cryst. B53, 750 (1997)
14. O. Chmaissem, Y. Eckstein, and C. G. Kuper, Phys. Rev. B, 63, 174510 (2001)

Chapter - 4

Studies on $La_{0.5}Pr_{0.2}Ba_{0.3}MnO_3$ (LPBMO) manganite thin films

Owing to the large CMR effect on the application of external applied field, mixed valent manganites exhibit Metal-Insulator transition (T_P) accompanied by a Ferromagnetic-Paramagnetic transition (T_C) [1,2]. In this Chapter, a detailed study on $La_{0.5}Pr_{0.2}Ba_{0.3}MnO_3$ (LPBMO) manganite thin films synthesized using Pulsed Laser Deposition (PLD) has been made. The study of various physical properties of epitaxial manganite thin films is interesting for understanding the clean physics in the absence of various defects and polycrystalline grain boundaries and leads to their tailoring for device applications. In particular, a negligible low temperature magnetoresistance (MR) observed in epitaxial thin films as compared to the polycrystalline bulk samples has prompted the research community working in the field of manganites to devise ways to enhance low temperature MR in epitaxial thin films. It is well established fact that, the electronic transport and MR properties of manganites are governed by the three key factors, namely, tolerance factor, carrier density and the cationic size disorder (σ^2) [3,4]. Several reports are available on the studies of A-site cationic disorder in modifying the structural, transport and MR properties in manganite bulk and thin films [5-9]. In this regards, our previous studies on the effect of cationic size variance in the polycrystalline LPBMO manganite system, derived from the standard $La_{0.7}Ba_{0.3}MnO_3$ by partial replacement of the larger size La^{3+} by smaller Pr^{3+} resulting into the enhanced A-site cation size-disorder ~0.016Å^2, may be useful to achieve large MR. In addition to this, the investigations on the LPBMO samples have resulted into the observation of characteristic low temperature resistivity minima, a very interesting phenomenon, below 50K. In order to understand the cause of low temperature resistivity minima and get to know more about it, during the present course of work, the studies on epitaxial LPBMO manganite thin films having different thicknesses have been carried out. The variation in grain size acts as a probe to investigate whether, grain boundary is the cause of low temperature electron localization. The structural, morphological, electronic transport and MR properties of epitaxial LPBMO thin films deposited on single crystalline $SrTiO_3$ [STO] (*l00*) substrates using PLD method have been determined. The observation of the low temperature minima feature in the epitaxial LPBMO thin films, further motivates to study the effect of Swift Heavy Ion (SHI) irradiation on the properties of these samples. The results obtained are discussed in

light of the modifications in electronic properties; MR and the changes in low temperature minima are given in the following section of this Chapter.

4.1 Synthesis

Polycrystalline bulk sample of LPBMO was synthesized using conventional solid-state reaction method. Dried powders of La_2O_3, Pr_6O_{11}, $CaCO_3$, $BaCO_3$ and MnO_2 (all > 99.9% pure) were mixed thoroughly in stoichiometric proportions and heated at 950° C for 24 hrs. The obtained powder was then palletized and fired twice at 1100° C and 1200° C for 48 hours each, with intermediate grindings. Finally, the sample was pressed into 15 mm diameter pellet and sintered at 1300°C for 24 hrs and was used for bulk characterization as a target material for PLD of thin film deposition. The LPBMO thin films with the thicknesses of 500Å, 1000Å and 2000Å were deposited on single crystal STO (*100*) substrates using a KrF excimer laser having wave length of 248nm, energy 3 J/cm^2 and deposition rate 25nm/s obtained with laser frequency 25 Hz. The substrate-to-target distance was kept at 4.2cm with substrate heater temperature at 830°C. The oxygen partial pressure was maintained at 400 mTorr. In the deposition chamber, target was typically oriented at 45^0 to the beam so that the ablated species emitted in the plume can fall on to the heated substrate.

The structure of the target and thin film samples was analyzed using x-ray diffraction (XRD) and microstructure was studied using atomic force microscopy (AFM) measurements. Using d.c. four probe resistivity technique, the electrical resistivity of all the films was measured i) as a function of temperature in the range of 5-325K in zero-field and in applied fields of 9T and ii) as a function of magnetic field (up to 9T) at various temperatures (5 – 300K) using RT and magneto RT measurements.

4.2 Structural studies

XRD

Indexing of XRD patterns of the parent LPBMO bulk target sample reveals that, sample crystallizes in a distorted orthorhombic structure (space group: *Pnma*, no. 62) with lattice parameters determined as a=5.512(2) Å, b=7.791(2) Å & c=5.548(2)Å. The XRD patterns of the thin film were indexed using the cell parameters of bulk and are found to be

single phase and (*100*) oriented, with nearly the similar lattice parameters as the bulk. Figure 4.1 shows a typical Rietveld fitted XRD patterns of the LPBMO bulk and thin film samples. The lattice mismatch, δ, along the interface has been calculated using the following formula $\delta\% = \frac{d_{substrate} - d_{thin\ film}}{d_{substrate}} \times 100$ is ~ 0.23%, ~0.26% and ~1.09% for the 500Å, 1000Å and 2000Å films respectively. The positive values of δ-mismatch correspond to the tensile strain present in the films.

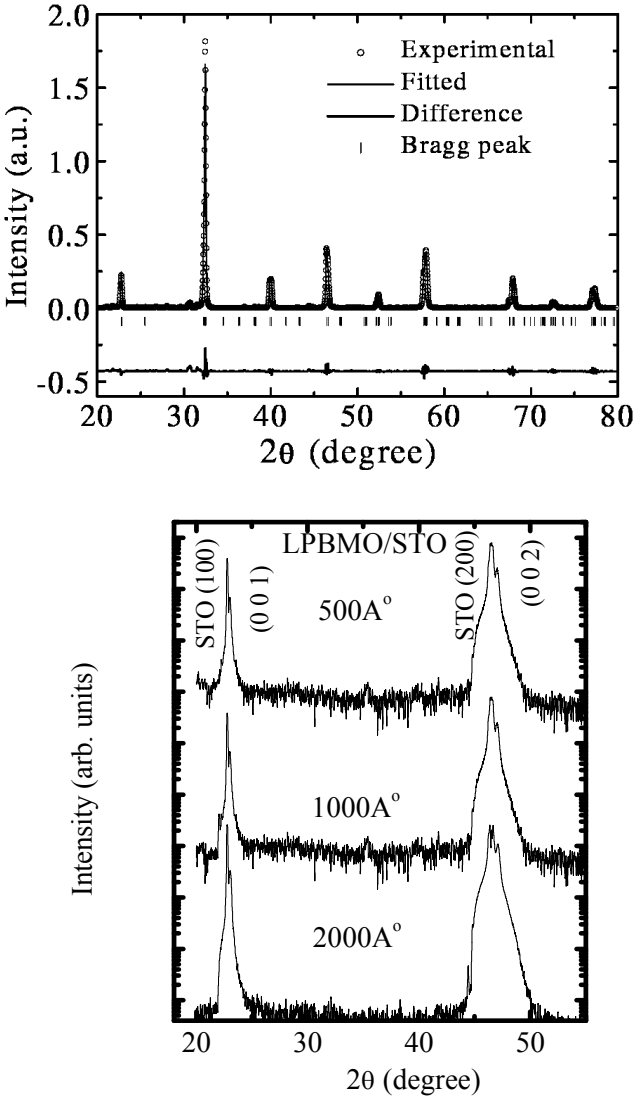

Figure 4.1: A typical Rietveld fitted XRD patterns of LPBMO bulk sample (top) and for 500Å, 1000Å and 2000 Å LPBMO/STO thin films.

Morphology

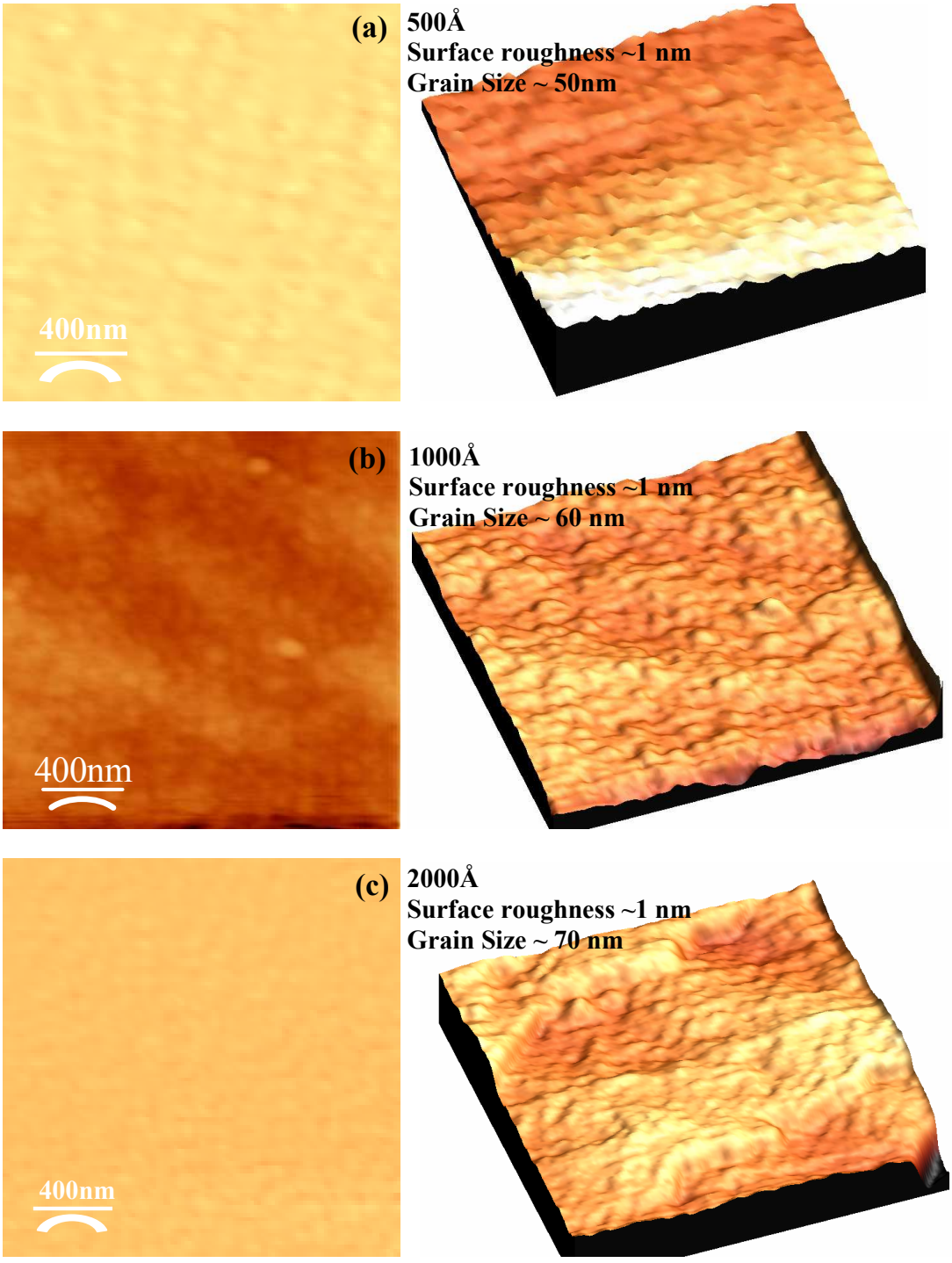

Figure 4.2: 2μ x 2μ AFM images of (a) 500Å (b) 1000Å and (c) 2000Å LPBMO/STO thin films with their respective 3D view.

The AFM micrographs of the LPBMO/STO thin films having film thickness 500Å, 1000Å and 2000Å are shown in fig.4.2. The average surface roughness in all the LPBMO thin films is not more than 1nm. The films are smooth exhibiting average grain size in the range of 50nm - 70nm.

4.3 Resistivity and MR measurements

Figure 4.3(a) shows the electrical resistivity for LPBMO bulk sample as a function of temperature in the range 5-300K in zero field and in an applied field of 1T and 5T respectively. The bulk sample exhibits insulator-metal transition (T_P) at 173 K in 0T. Figure 4.3(b) shows the magnified portion of the resistivity at low temperatures to visualize the resistivity minima. The temperature dependences of the film resistivity have been plotted in fig.4.4(a) –(c) for all the LPBMO thin films. The values of T_P and peak resistivity (ρ_P) are 235K and 6.81 mΩcm for 500Å, 241K and 6.63 mΩcm for 1000Å and 207K and 3.4 mΩcm for 2000Å respectively. T_P values are far higher as compared to their polycrystalline bulk counterparts implying good quality of the films. Another important feature of the ρ-T behavior of LPBMO thin films is the observation of characteristic low temperature resistivity minima around 50K. Figure 4.5 (a)-(c) shows the ρ-T plots in the temperature range 5-100K emphasizing the resistivity anomaly around 50K.

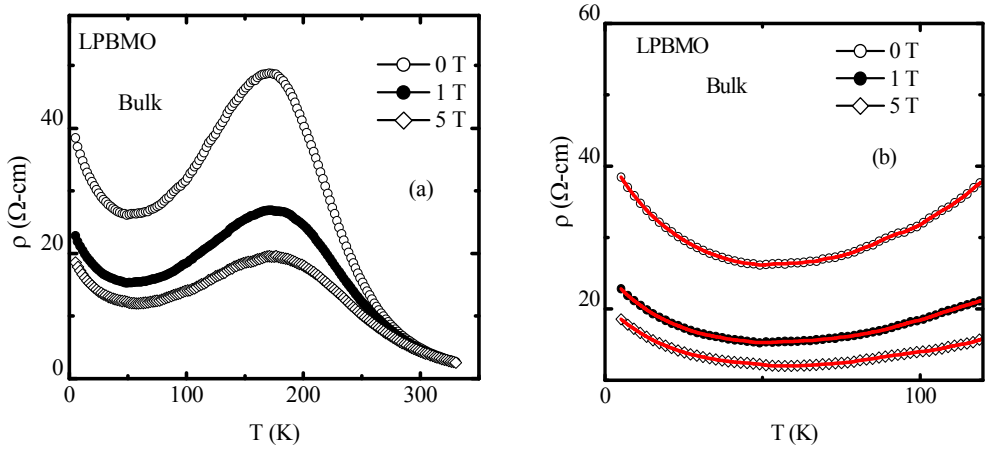

Figure 4.3: (a) Resistivity versus temperature plot for LPBMO bulk sample and

(b) Magnified portion depicting the low temperature resistivity minimum.

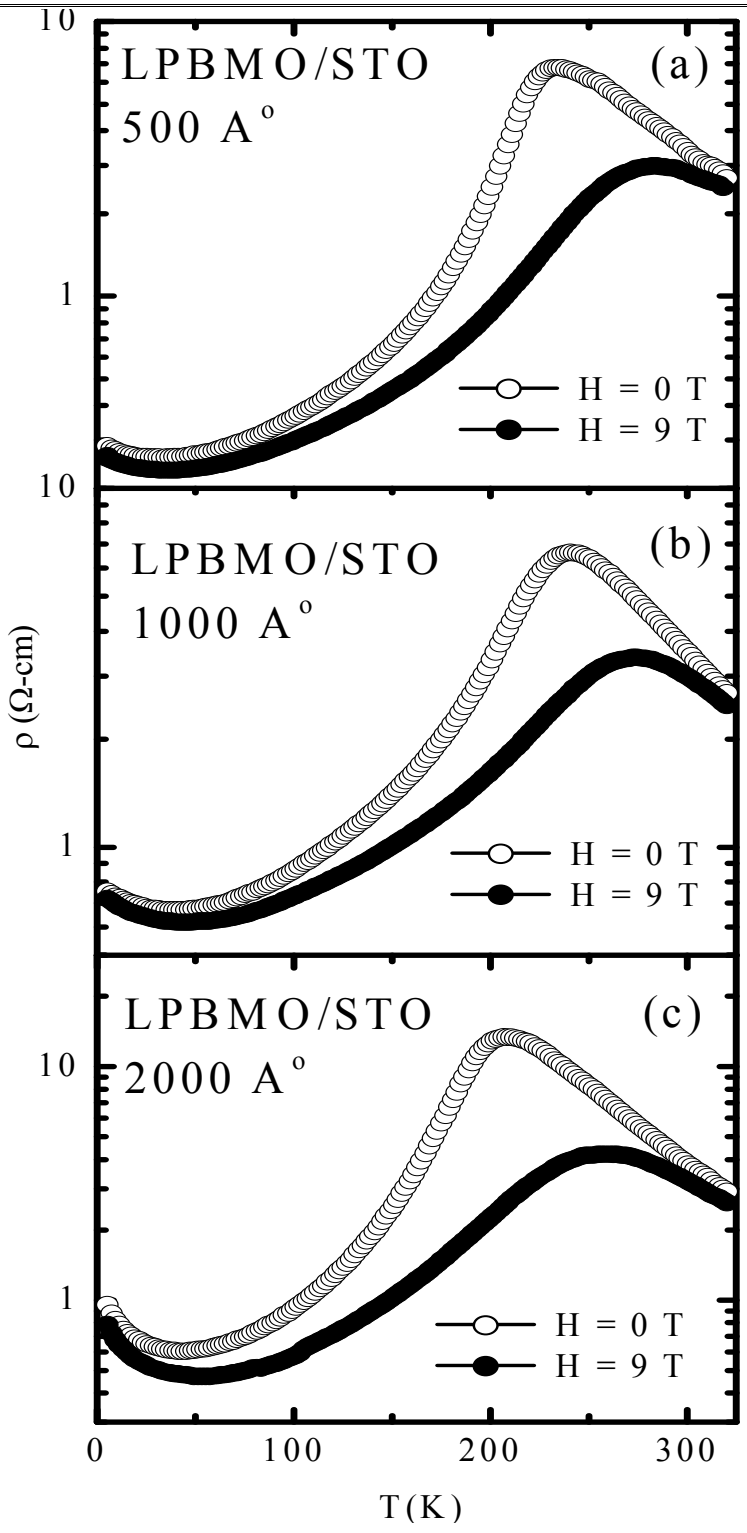

Figure 4.4: ρ – T plots for LPBMO/STO (a) 500Å (b) 1000Å and (c) 2000Å thin films.

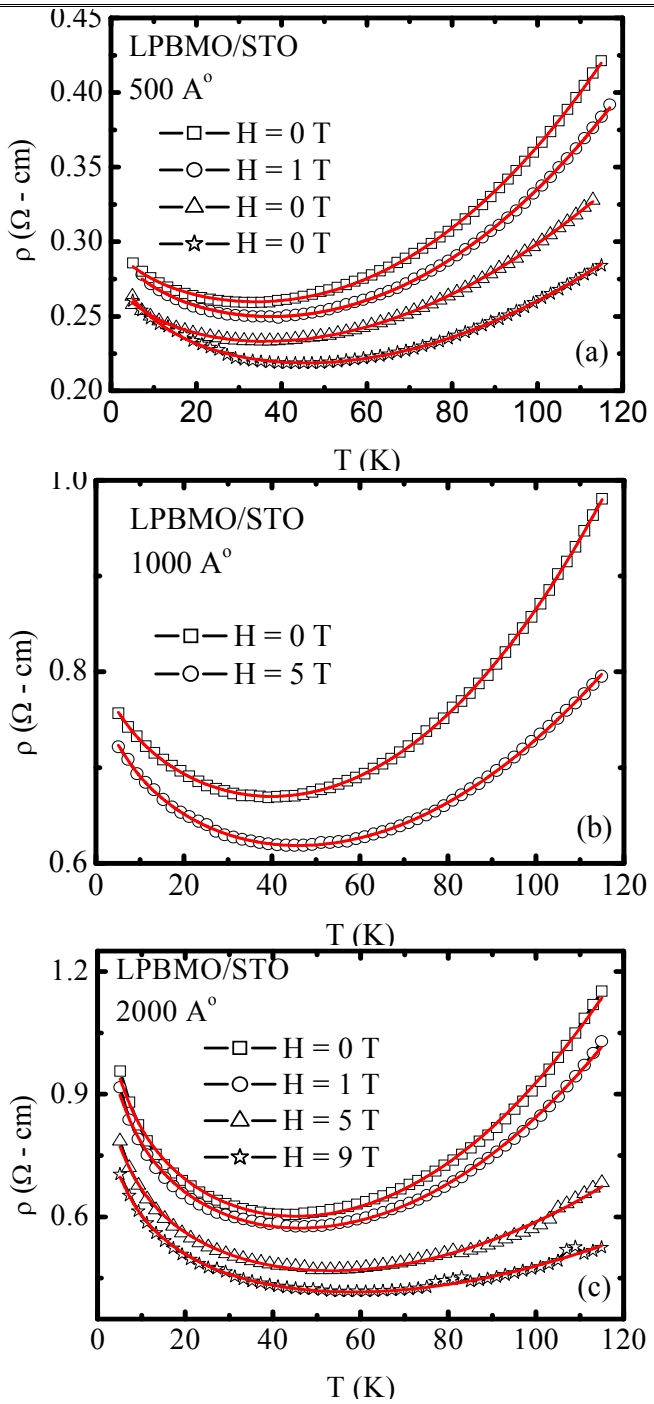

Figure 4.5: Low temperature resistivity fits to $\rho = \frac{1}{\sigma_0 + BT^{1/2}} + \rho_n T^n$ law for (a) 500Å (b) 1000Å and (c) 2000Å LPBMO/STO thin films.

From the figs.4.3(b), 4.4 and 4.5, it is observed that the application of applied magnetic filed can not dissolve the low temperature resistivity minima, however, it shifts to slightly higher temperature (T_m) with the broadening of minima curvature.

This phenomenon of low temperature resistivity minima is not a common feature reported in manganites. However, there are few reports available on the observation of such a behavior in some of the $La_{1-x}R_xMnO_3$ (R=Ca, Sr, Ba) polycrystalline bulk and thin film samples [10-14]. The resistivity upturn is also observed in many systems having larger A-site cation disorder where the structural distortion results into the electron localization [12-14]. The interesting phenomenon investigated in the manganites is, the existence of a quantum critical point (QCP). QCPs are thought to be crucial in the description of certain strongly correlated electron compounds such as non-Fermi liquid metals, high T_C superconductors, the localization problem, etc. In the case of manganites, the possibility of the existence of a QCP has been recently explored theoretically. Such studies have been focused on its relevance in the observation of colossal magnetoresistance effect [15,16] and in the electron localization [17,18].

The low temperature resistivity minimum may have its origin in

1. Grain boundary localization
2. Kondo effect
3. Electron-electron (e-e) scattering due to enhanced columbic interactions and weak localization

The e-e scattering term is responsible for resistivity minimum and is given by

$$\rho = \frac{1}{\sigma_0 + BT^{1/2}} + \rho_n T^n \qquad (1)$$

The above mentioned equation has two terms, first term is the electron-electron (e-e) interaction or Coulombic term which dominates below the resistivity minimum temperature (T_m) where, B signifies the columbic interactions resulting in e-e scattering while the second term is inelastic scattering power law $\rho = \rho_n T^n$ dominating at high temperature (above T_m).

In presently studied single crystalline LPBMO thin films, the possibility of Kondo effect and grain boundary contribution to low temperature resistivity is ruled out because the Kondo effect is observed due to the scattering in nonmagnetic material having magnetic impurity while the grain boundary effect is not present in the thin films and has been discussed later in discussion on MR behavior. Electron localization effect may be the possible cause for the observed resistivity up turn in presently studied LPBMO thin films. In order to check the possibility of e-e scattering, the fitting of the above equation has been carried out on the ρ-T plots in the temperature range 5-120K. The obtained results of this fits are shown in figs.4.3(b) and 4.5 and summarized in Table 4.1 for all the LPBMO bulk and films studied. Very low values of the goodness of fits determined by χ^2 implies that the resistivity due to e-e scattering agrees nicely with the experimental resistivity data.

Table 4.1: Values of T_m and various derived parameters from low temperature resistivity fits for the LPBMO bulk and films.

Sample	Magnetic field (T)	T_m(K)	σ_0 (Ω^{-1} cm^{-1})	B ($\Omega^{0.5}$ cm$^{0.5}$)	ρ_n (Ω cm/K^n)	n	χ^2
500Å	0	33	3.23416	0.13118	1.404 x 10^{-6}	2.5055	6.83 x 10^{-7}
	1	37	3.19871	0.16326	1.636 x 10^{-6}	2.4473	
	5	37	3.46138	0.17666	5.439 x 10^{-6}	2.148	
	9	45	3.26279	0.24733	4.538 x 10^{-6}	2.1387	
1000Å	0	39	1.18324	0.06053	3.278 x 10^{-6}	2.48522	1.19 x 10^{-7}
	5	45	1.21245	0.07525	6.721 x 10^{-6}	2.25808	
2000Å	0	41	0.66149	0.17916	3.198 x 10^{-6}	2.60576	40 x 10^{-6}
	1	45	0.68517	0.18986	4.603 x 10^{-6}	2.49862	
	5	53	0.78259	0.22718	4.681 x 10^{-6}	2.37259	
	9	57	0.86739	0.25093	8.507 x 10^{-6}	2.16702	
Bulk	0	49	8.41	0.0031	5	2.68	7 x 10^{-3}
	3	53	3.06	0.0056	5	2.57	
	5	59	3.67	0.0072	4	2.55	

The above table shows the values of derived fitting parameters for the bulk and all thin films studied. It can be seen that, T_m shifts to higher values in higher applied fields. For instance, in ~500Å thin film, the T_m increases from 33K at 0T to 45K at 9T which may be understood in terms of magnetic field induced suppression of inelastic scattering with increasing temperature. This is also evident from the fact the values of inelastic scattering exponent (n) decrease with increasing applied field which implies suppression of spin fluctuations indicating towards the electron-magnon scattering process. Among the other terms, B increases as the field which signifies the depth of minima [12]. The significance of terms can be understood as the contribution to Columbic interactions [12] given by the equation

$$B = 0.915\frac{e^2}{2\pi^2\hbar}\left(\frac{2}{3}-\frac{3}{4}F_\sigma\right)\sqrt{\frac{k_B}{\hbar D}}$$

where F_σ is the screening constant for the Coulomb interactions and D is the diffusion constant.

Increasing the magnetic field causes the depth of minima to increase which also supports the increase in T_m with magnetic field. This signifies that, at low temperatures, the e-e scattering term is insensitive to magnetic field whereas the exponent of inelastic scattering term suppresses largely with increasing magnetic field. Our results agree quite well with the theoretical predictions of increase in T_m with the applied field. However, there have been some reports on the decreases of B in higher fields which is beyond the scope of this law [13]. We do not observe such anomalous behavior and our experimental and reported theoretical predictions agree very well which justifies that electron-electron scattering is the possible cause of low temperature resistivity minima.

Magnetoresistance

MR vs. H isotherms at various temperatures are shown in fig.4.6 for LPBMO bulk and thin films in order to compare the observed MR behavior of bulk with the epitaxial thin films. It can be seen that, films possess maximum MR ~ 90% in the vicinity of T_P (~200K) which decreases with decreasing temperature. The temperature dependence of MR can be discussed as follows

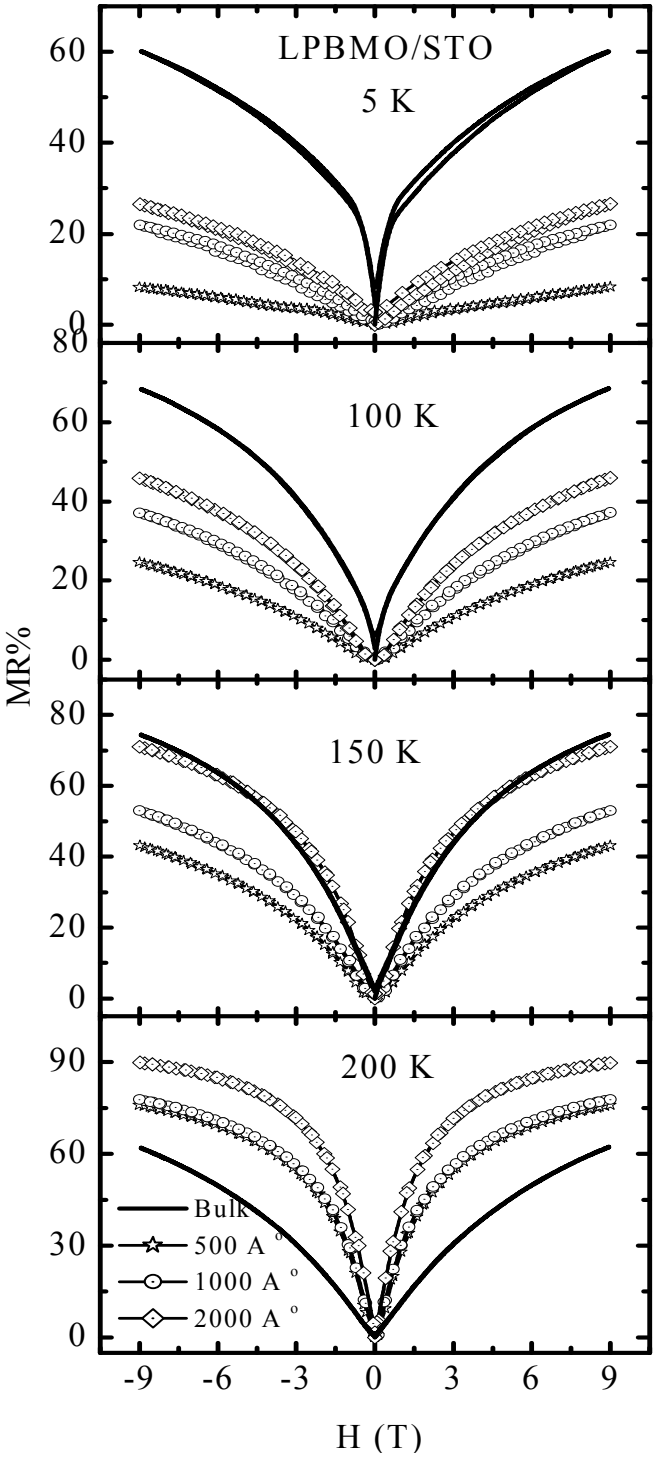

Figure 4.6: A comparison of MR% vs. applied magnetic field for LPBMO thin films of different thicknesses and bulk sample at various temperatures.

At low temperature, 5K, LPBMO bulk exhibits low field MR (LFMR) as high as 30% where as the thin films exhibit almost negligible MR. At this low temperature LFMR is attributed to the grain boundary contribution [19,20]. The negligible LFMR in LPBMO films suggests the absence of grain boundary contribution to MR which further supports our justification that, the low temperature minima does not have its origin at grain boundaries. The LPBMO bulk exhibit high field MR (HFMR) ~ 60% whereas the values of HFMR are ~ 30%, 20% and 10% for the 500Å, 1000Å and 2000Å LPBMO films respectively. At low temperature HFMR is ascribed to the reorientation of disordered spins at grain interface which in turn depends on the connectivity between the grains and on the stiffness of the aligned blocked spins at the grain surface originating due to the poor connectivity between the grains, pinning of Mn spins at the grain surface, etc [21]. At intermediate temperature, in the range 100-150K, MR increases subsequently with field and becomes maximum at T_P owing to the suppression of spin fluctuations at Mn-O-Mn bond. At all temperatures, the observed subsequent rise in MR with the film thickness has been attributed to the lattice mismatch, δ, which increases with thickness.

In summary, our measurements on the series of LPBMO bulk and thin films indicate the existence of electron localization by Ba doping. These results open new perspectives in order to understand better, the electron localization processes in manganites and more in general in the systems having large cationic size disorder.

4.4 SHI irradiation studies on LPBMO films:

A comparative study of Pristine and Irradiated films

To study the Swift Heavy Ion (SHI) irradiation induced modifications in the low temperature resistivity minima in samples studied having varying size-disorder at A-site, detailed SHI studies have been carried on the LPBMO thin films with varying film thickness and SHI irradiation dose. Since the SHI is well known tool for tailoring the material properties by the creation of controlled defects as vacancies, columnar defects and localized strain on to the materials, it is responsible for the modifications in physical properties of materials [22,23].

While passing through the materials, accelerated ions loss their energies by mainly two kinds of interactions, namely, electronic energy loss [$S_e = dE_e/dx$] which dominates at higher ion energies (~MeV) and nuclear energy loss [$S_n = dE_n/dx$] dominating at lower ion energies (~keV). The possible range of the ions in the materials, S_e and S_n, estimated in the present case, using the software Stopping Range of Ion in Matter (SRIM) 2003 programme [24], are ~ 23 μm, 13.3 keV and 36.9 eV respectively. This implies that almost all ions can pass through the film thickness and hence the observed irradiation effects can be analyzed as consequence of ion induced electronic energy transfer. The reported electronic energy threshold, calculated using Szenes thermal spike model, for LCMO is ~6.6 keV/nm [25] which is far lower than the calculated electron energy loss S_e for LPBMO.

SHI irradiation was performed at Inter University Accelerator Centre (IUAC), New Delhi, India, using a 15 UD tandem accelerator using 200 MeV Ag^{+15} ion beam with a beam current ~ 0.3 pnA and in ion doses of 5×10^{10}, 5×10^{11} and 1×10^{12} ions/cm^2. The irradiations were performed at an angle of 5°±1° away from the *c* axis to avoid channeling. The ion beam was focused on to a spot of 1mm×1mm and scanned over an area of 10mm×10mm using magnetic scanner to achieve dose uniformity across the sample area which was typically 2.5mm×2.5mm. The structural and microstructural properties of irradiated LPBMO thin films were studied by XRD and AFM measurements. Using d.c. four probe resistivity technique, the electrical resistivity of all the films was measured i) as a function of temperature in the range of 5-325 K in zero-field and in an applied field of 9 T and ii) as a function of magnetic field (up to 9 Tesla) at various temperatures [PPMS, Quantum Design].

4.4.1 Structure and morphology

Structure

The structure of the pristine and irradiated LPBMO/STO thin films was examined using XRD. Figure 4.7 shows the XRD patterns of the thin films indexed using bulk cell parameters of LPBMO showing an epitaxial (*h00*) growth for the pristine and films

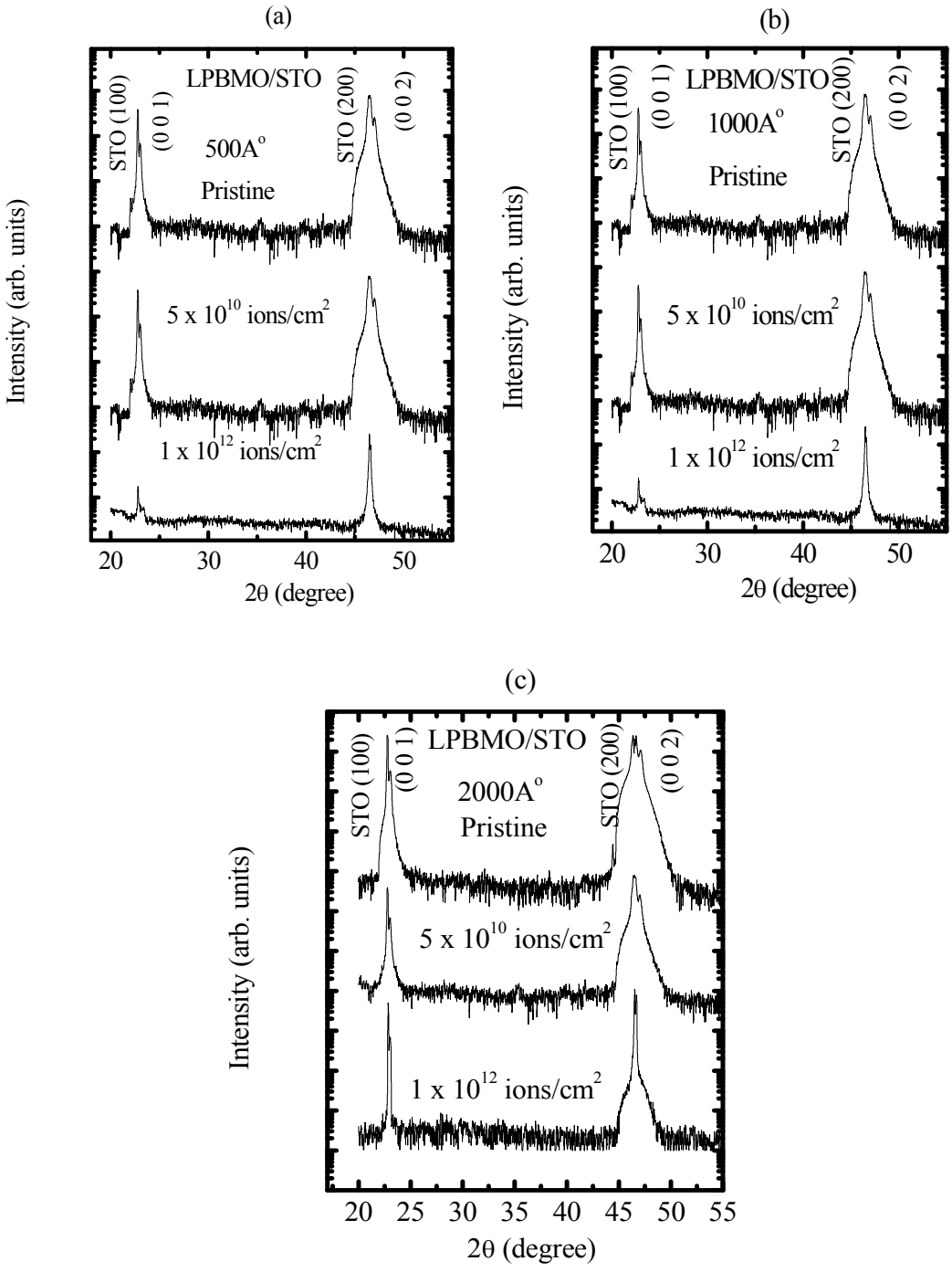

Figure 4.7: XRD patterns for pristine and irradiated LPBMO/STO (a) 500Å (b) 1000Å and (c) 2000 Å thin films.

irradiated with 5 x 10^{10} ions/cm^2 and for 1 x 10^{12} ions/cm^2 Ag ion doses. Irradiation has significant effect on the peak intensity and FWHM of thin films. The peak intensity decreases and FWHM increases with irradiation. In contrast, in 2000Å films, there is an increase in peak intensity and decreasing FWHM with irradiation of 1 x 10^{12} ions/cm^2. The calculated lattice mismatch, δ, along the interface are ~ 0.23%, ~0.26% and ~1.09% for the 500Å, 1000Å and 2000Å pristine films respectively which become ~ 0.30%, 0.29% and 1.25% respectively with 1x 10^{12} ions/cm^2 ion irradiation. The values of lattice mismatch are tabulated in Table 4.2.

The increase of tensile strain along with the suppression in peak intensity and increase of FWHM suggests that, the crystallanity of these films is adversely affected by the SHI irradiation.

Table 4.2: The values of lattice mismatch, δ, for the pristine and irradiated LPBMO/STO thin films.

Sample	**Thickness**	**Irradiation dose**	**Mismatch (δ)**
LPBMO/STO	500Å	Pristine	~ 0.23%
		5×10^{10} ions/cm^2	~ 0.28%
		1×10^{12} ions/cm^2	~ 0.30%
LPBMO/STO	1000Å	Pristine	~ 0.26%
		5×10^{10} ions/cm^2	~0.29%
		1×10^{12} ions/cm^2	~ 0.30%
LPBMO/STO	2000Å	Pristine	~1.09%
		5×10^{10} ions/cm^2	~1.25%
		1×10^{12} ions/cm^2	~ 0.89%

Surface morphology

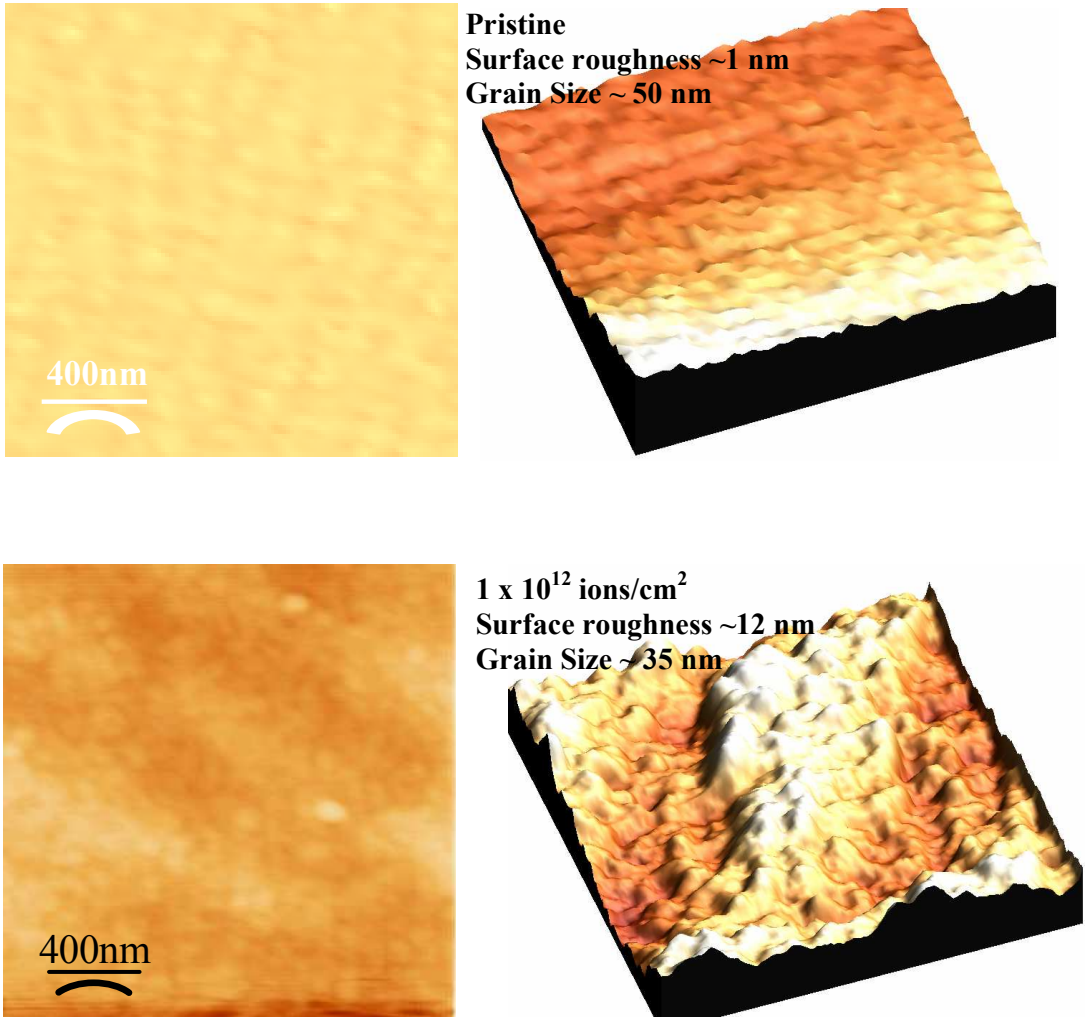

Figure 4.8(a): 2μ x 2μ AFM images of 500Å pristine (top) and 1×10^{12} ions/cm^2 irradiated ((bottom) LPBMO/STO thin films with their respective 3D view.

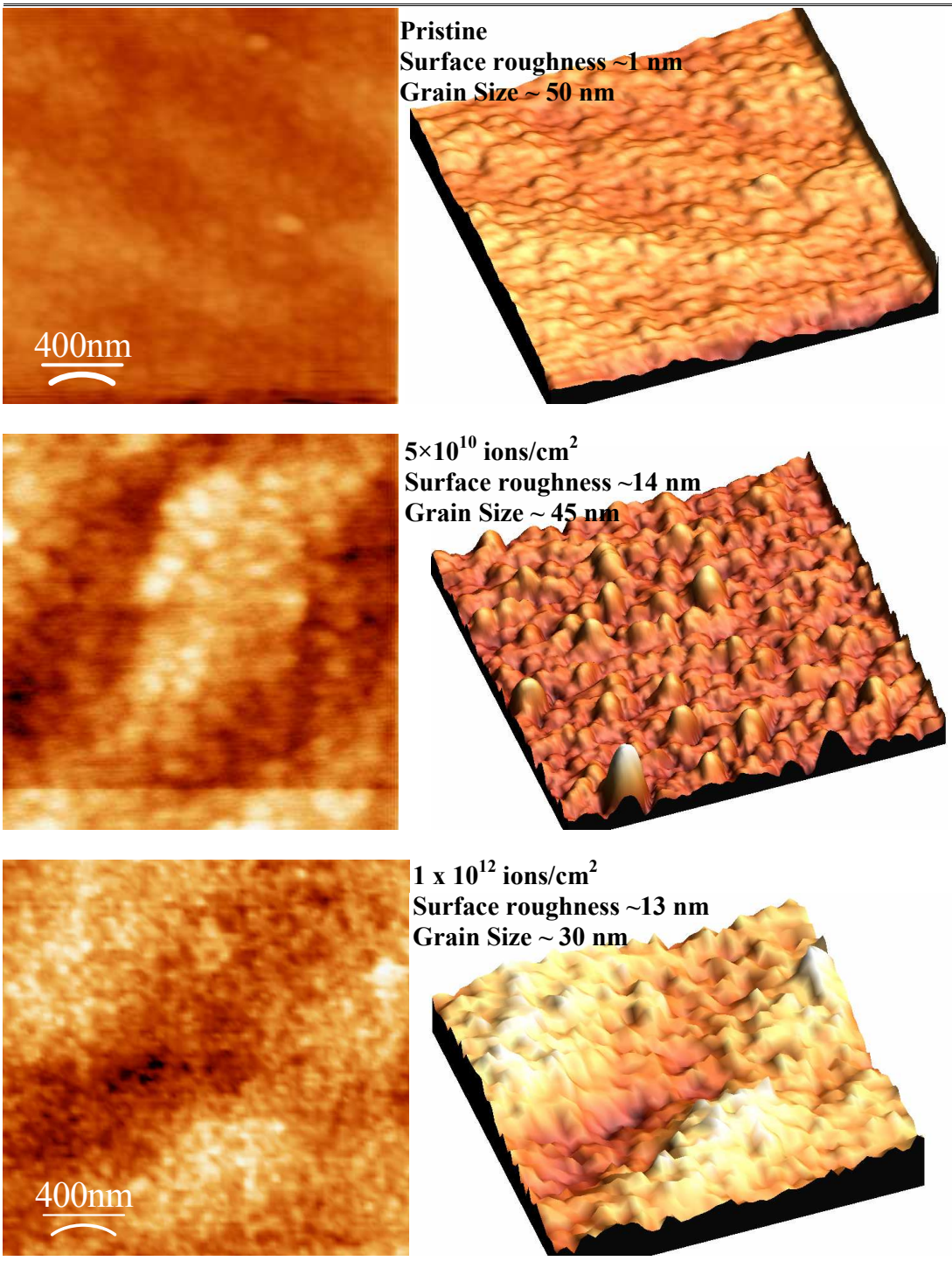

Figure 4.8(b): 2μ x 2μ AFM images of 1000Å pristine (top), 7.5×10^{10} ions/cm^2 irradiated (middle) and 1×10^{12} ions/cm^2 irradiated (bottom) LPBMO/STO thin films with their respective 3D view.

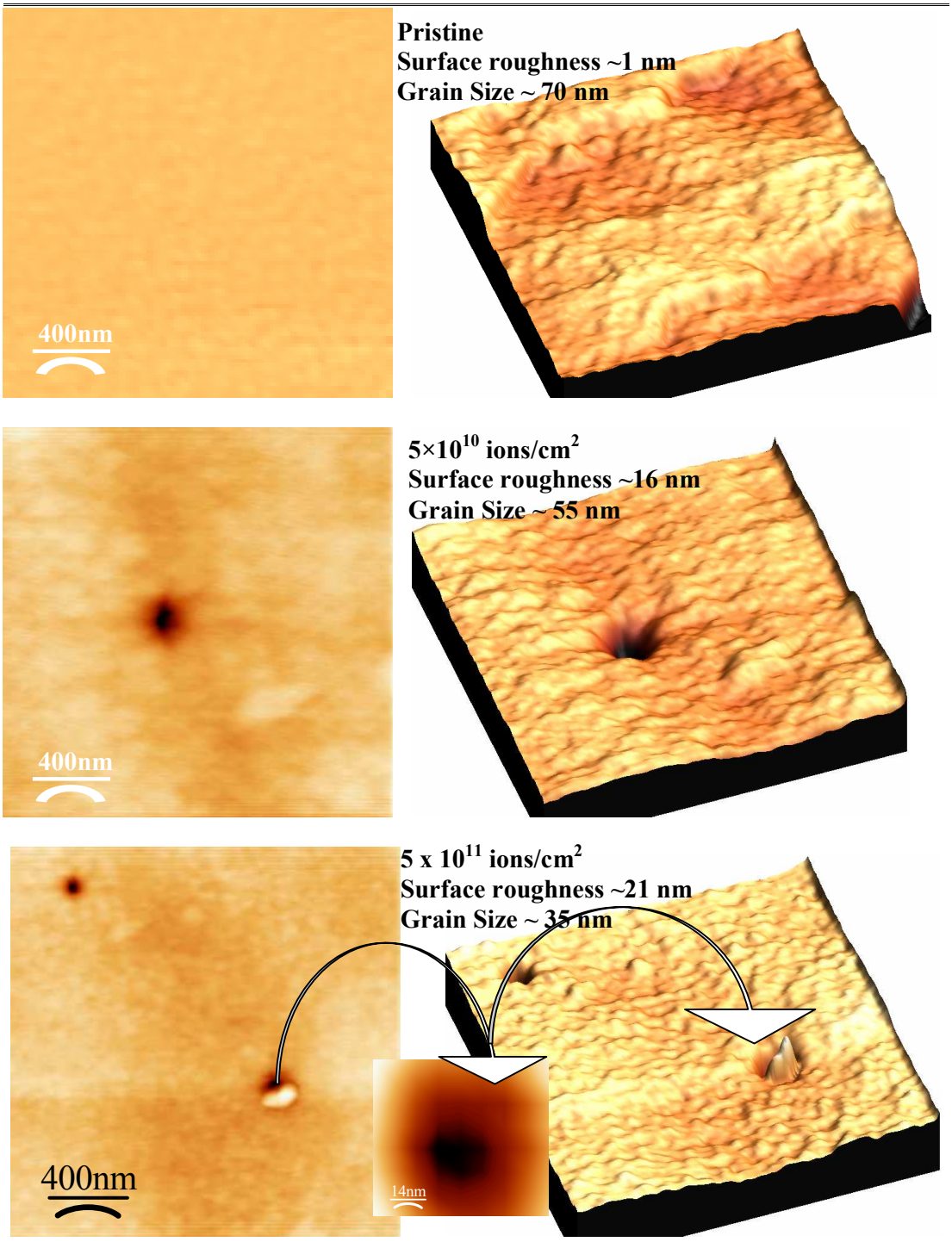

Figure 4.8(c): 2μ x 2μ AFM images of 2000Å pristine (top), 7.5×10^{10} ions/cm^2 irradiated (middle) and 5×10^{11} ions/cm^2 irradiated (bottom) LPBMO/STO thin films with their respective 3D view.

The AFM micrographs of the pristine and irradiated LPBMO thin films are shown in fig.4.8(a)-(c). From the AFM pictures, it can be clearly seen that the surface morphologies of the film deteriorates after the irradiation which has been described as follows

The value of average surface roughness ~ 1 nm in all the pristine LPBMO films becomes ~12nm and 13nm in $1x10^{12}$ ions/cm^2 ion irradiated 500Å, 1000Å and 2000Å films respectively where as the values of average grain size varies marginally in the range 35nm-45nm due to $1x10^{12}$ ions/cm^2 ion irradiation. It is well established fact that, SHI irradiation creates the various types of defects while passing through the material. In the case of present study, we have observed the formation of the columnar track like defects having average column radius ~ 6±1 nm in 2000Å films with irradiation dose of 5×10^{10} ions/cm^2 and 5×10^{11} ions/cm^2, which can be clearly seen from fig.4.8(c). In 500Å and 1000Å thickness films clustering of point defects has been observed [Figs.4.8(a) and (b)]. The arrow in fig.4.8(c) indicates the magnified portion of the columnar region observed in the AFM micrographs. These effects of SHI may affect the electronic and magnetic properties of the thin films studied which in turn may modify the resistivity and decrease T_P and MR in these films after the irradiation [22,23].

4.4.2 Resistivity and MR measurements

The temperature dependent resistivity behavior of pristine and irradiated LPBMO thin films are plotted in fig.4.9 (a), (b), (c) and (d). The values of T_P and peak resistivity determined from these plots are given in Table 4.2. From figs.4.9 and Table 4.3, it can be observed that, T_P decreases while the peak resistivity increases with the increase in film thickness and subsequent increase in irradiation dose. The subsequent drop in T_P along with appreciable rise in resistivity with irradiation can be attributed to the observed increase of tensile lattice strain which indicates that, the irradiation induced defect formation, creates considerable changes in the lattice which accommodates the electronic and magnetic anisotropies and are reflected in physical properties of the films.

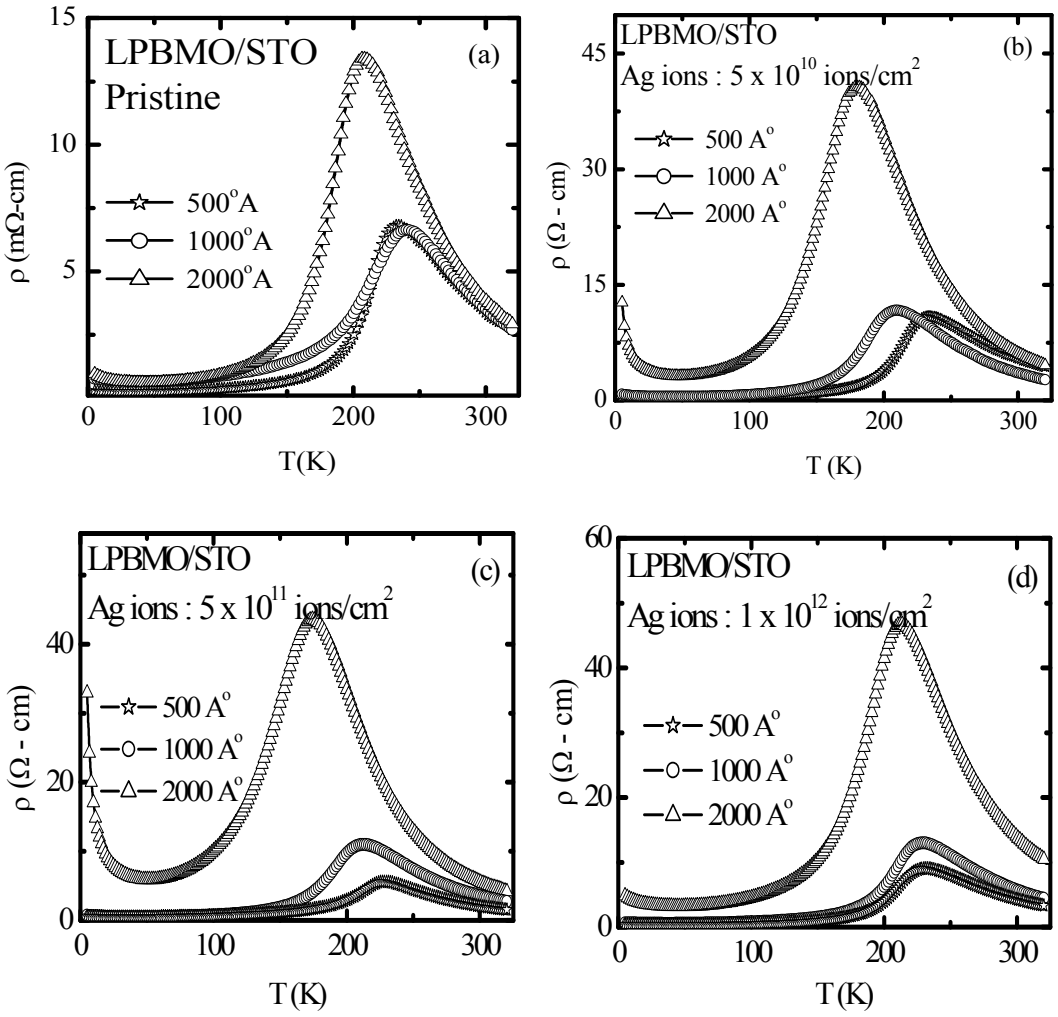

Figure 4.9: ρ – T plots for LPBMO/STO thin films with different thicknesses for irradiation dose of (a) Pristine (b) 5 x 10^{10} ions/cm^2 (c) 5 x 10^{11} and (d) 1 x 10^{12} ions/cm^2 ions/cm^2 at various temperatures.

Table 4.3: The values of T_P and ρ_P for pristine and irradiated LPBMO/STO films.

	Film Thickness (Å)	T_P (K)	ρ_P (mΩcm)
Pristine	500	235	6.8178
	1000	241	6.6325
	2000	207	13.4038
5 x 10^{10} ions/cm^2	500	234	10.89
	1000	209	11.7074
	2000	180	40.6720
5 x 10^{11} ions/cm^2	500	228	5.5899
	1000	212	10.9807
	2000	174	43.5611
1 x 10^{12} ions/cm^2	500	231	9.0534
	1000	228	12.9867
	2000	213	46.6747

A comparison of the resistivity plots in zero applied filed for the 500Å, 1000Å and 2000Å film thickness is given in fig 4.9(a), (b), (c) and (d) for Pristine and 5 x 10^{10} ions/cm^2, 5 x 10^{11} ions/cm^2, 1 x 10^{12} ions/cm^2 films respectively. The T_P and resistivity of 500Å and 1000Å pristine films remain almost same while in 2000Å film, there is an appreciable increase in the peak resistivity.

The irradiation with the ion dose of 5 x 10^{10} ions/cm^2, 5 x 10^{11} ions/cm^2 and 1 x 10^{12} ions/cm^2 results in an increase in the peak resistivity of all the films appreciably but this effect is more prominent in 2000Å film.

The significant increase in the resistivity with the corresponding decrease in T_P, can be understood from the change in structure and grain morphology of these films. In addition, the observed formation of columnar tracks in 2000Å film leads to the amorphization of the grains along the ion path thereby introducing the structural disorder which is more prominent at the periphery of the column. This causes a comparative larger lattice mismatch and leading to the increase of resistivity and drop in T_P.

Further, it can be observed from fig.4.9 that, low temperature resistivity minima becomes more prominent with the increase in irradiation dose. The ρ-T plots depicting resistivity minima along with the fits to Eqn.(1), in the temperature range 5-120K for all the LPBMO films studied are shown in figs.4.10(a),(b) and (c). The parameters obtained from these fits are tabulated in Tables 4.4, 4.5 and 4.6 for the irradiation dose of 5x10^{10} ions/cm^2, 5 x 10^{10} ions/cm^2 and 1 x 10^{12} ions/cm^2 respectively.

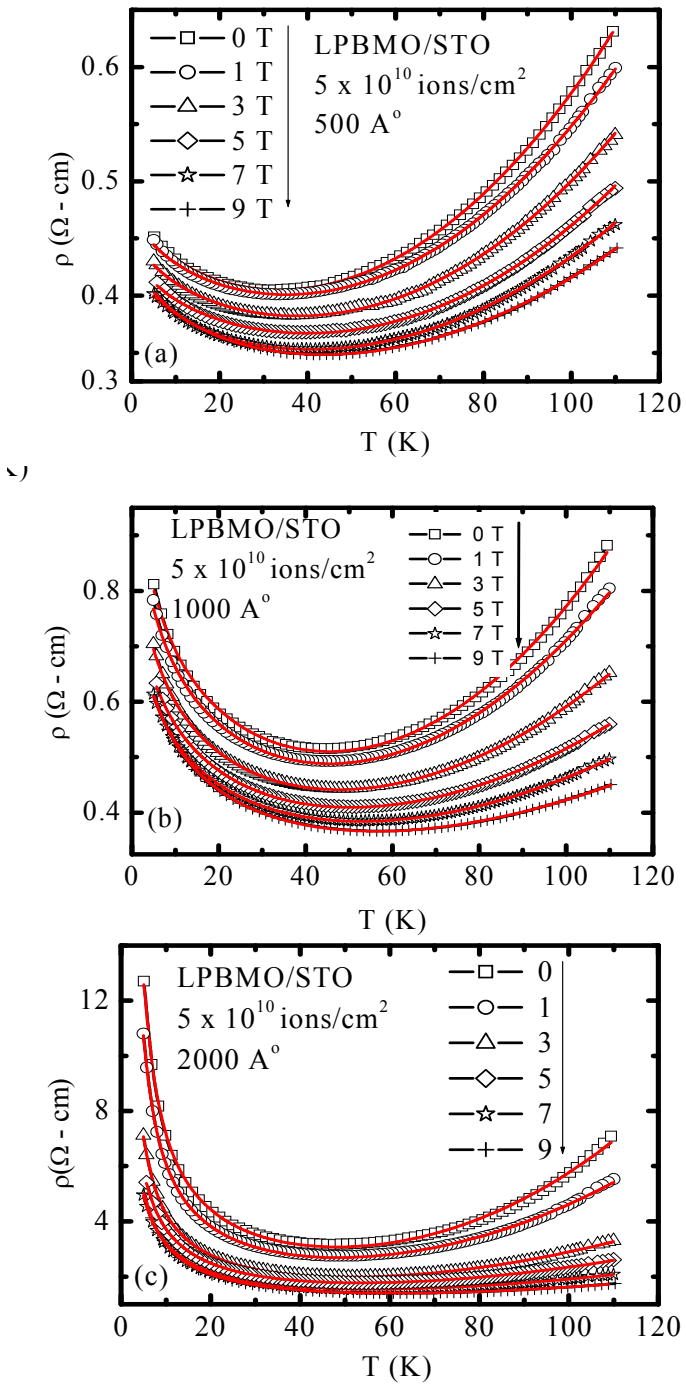

Figure 4.10(a): Low temperature resistivity fits to $\rho = \frac{1}{\sigma_0 + BT^{1/2}} + \rho_n T^n$ law for 5 x 10^{10} ions/cm^2 ion irradiated LPBMO/STO films.

Table 4.4: Values of T_m and various derived parameters from low temperature resistivity fits for the films irradiated with the Ag ion dose: 5 x 10^{10} ions/cm^2

Sample	Magnetic field (T)	T_m(K)	σ_0 (Ω^{-1} cm^{-1})	B ($\Omega^{0.5}$ $cm^{0.5}$)	ρ_n (Ω cm/K^n)	n	χ^2
500Å	0	34	1.99546	0.10269	4.9172 x 10^{-6}	2.3500	5.5393^{-7}
	1	35	2.03168	0.09743	3.5422 x 10^{-6}	2.3923	1.3566^{-6}
	3	36	2.11499	0.1019	2.7974 x 10^{-6}	2.4058	1 x 10^{-6}
	5	39	2.19937	0.10324	2.184 x 10^{-6}	2.4214	7 x 10^{-7}
	7	41	2.23548	0.11864	4.4177 x 10^{-6}	2.2537	3 x 10^{-7}
	9	41.	2.18364	0.13287	6.0126 x 10^{-6}	2.1695	1 x 10^{-7}
1000Å	0	44	0.76451	0.21542	40 x 10^{-6}	2.5116	3 x 10^{-5}
	1	46	0.79295	0.22812	6.9012 x 10^{-6}	2.3735	2 x 10^{-5}
	3	48	0.88393	0.24917	10 x 10^{-6}	2.2071	5 x 10^{-6}
	5	51	0.9782	0.25849	10 x 10^{-6}	2.1444	1 x 10^{-6}
	7	53	1.03263	0.27304	10 x 10^{-6}	2.0660	1 x 10^{-6}
	9	58	0.95323	0.303	20 x 10^{-6}	1.9385	6 x 10^{-7}
2000Å	0	41	-0.07212	0.06716	10 x 10^{-6}	2.7826	
	1	43	-0.07885	0.07695	30 x 10^{-6}	2.5362	
	5	55	-0.0831	0.10047	70 x 10^{-6}	2.2194	14 x 10^{-4}
	7	57	-0.07015	0.10732	110 x 10^{-6}	2.2537	
	9	63	2.18364	0.13287	160 x 10^{-6}	2.1695	

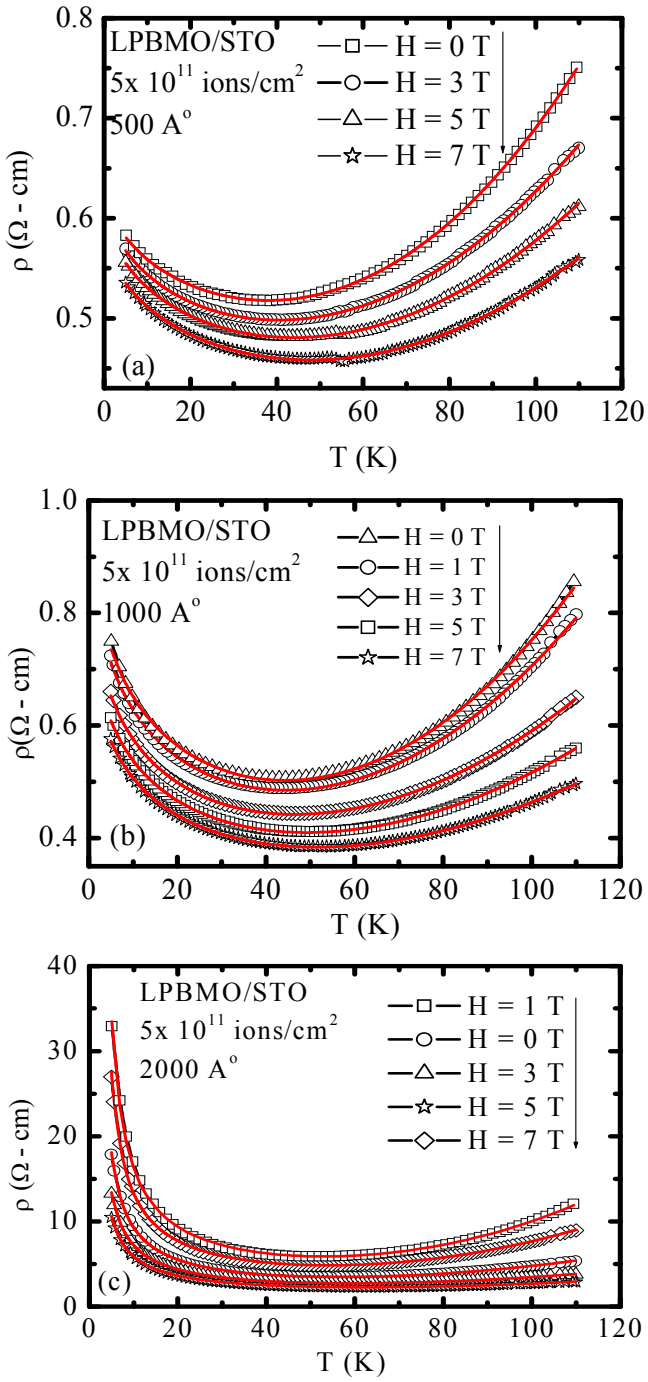

Figure 4.10(b): Low temperature resistivity fits to $\rho = \frac{1}{\sigma_0 + BT^{1/2}} + \rho_n T^n$ law for 5 x 10^{11} ions/cm^2 ion irradiated LPBMO/STO films.

Table 4.5: Values of T_m and various derived parameters from low temperature resistivity fits for the films irradiated with the Ag ion dose: 5 x 10^{11} ions/cm^2

Sample	Magnetic field (T)	T_m(K)	σ_0 (Ω^{-1} cm^{-1})	B ($\Omega^{0.5}$ $cm^{0.5}$)	ρ_n (10^{-5} Ω cm/K^n)	n	χ^2
500Å	0	35	1.55158	0.07611	$2.58x10^{-6}$	2.49957	6.5×10^{-7}
	3	42	1.56872	0.08673	$5.053x10^{-6}$	2.31592	
	5	44	1.59838	0.0915	$4.518x10^{-6}$	2.29998	
	7	46	1.65821	0.09471	$2.99x10^{-6}$	2.34696	
1000Å	0	43	0.9193	0.19578	$3.907x10^{-6}$	2.50753	$6.957x10^{-6}$
	1	45	0.94627	0.20516	$5.7x10^{-6}$	2.407	
	3	47	1.02599	0.22634	$1x10^{-5}$	2.207	
	5	49	1.1128	0.23788	$1x10^{-5}$	2.1423	
	7	55	1.19119	0.24905	$1x10^{-5}$	2.0803	
2000Å	0	52	-0.04893	0.0349	$8.462x10^{-6}$	2.94915	6.04×10^{-3}
	1	53	-0.0576	0.04204	10×10^{-6}	2.78761	
	3	56	-0.07243	0.05705	40×10^{-6}	2.4493	
	5	59	-0.08163	0.06981	50×10^{-6}	2.28203	
	7	63	-0.08813	0.08168	60×10^{-6}	2.16135	

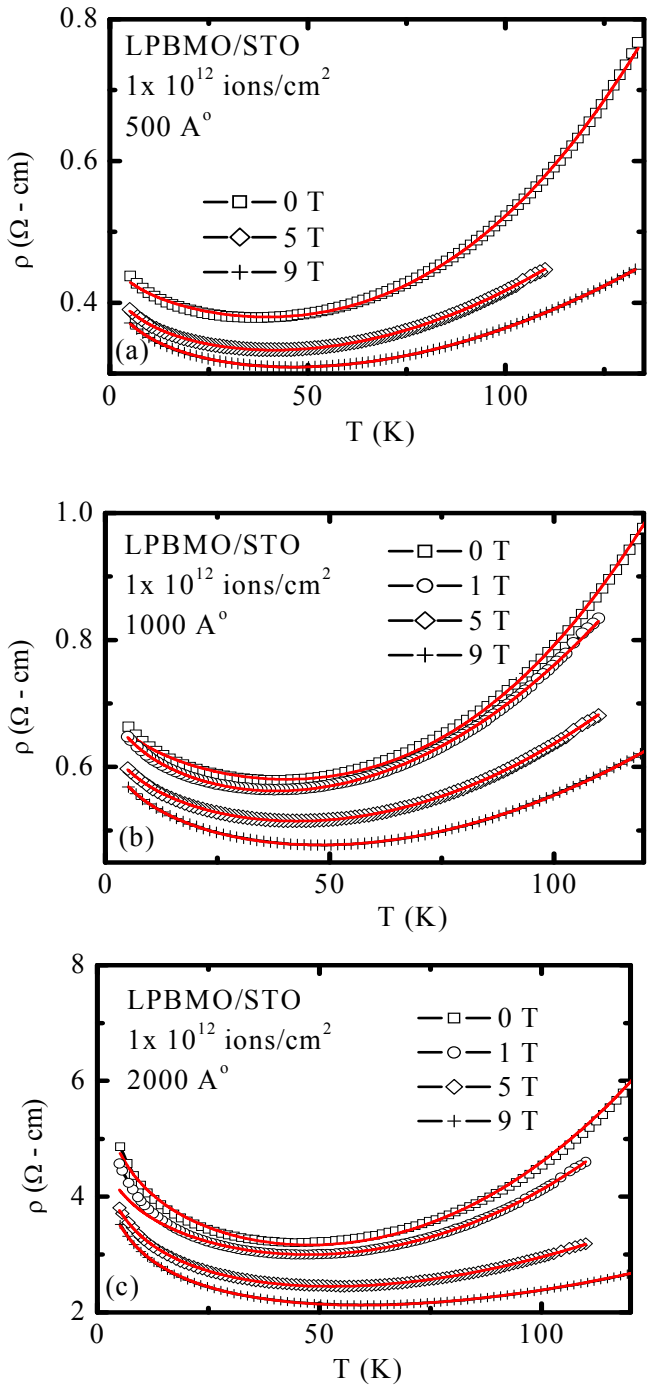

Figure 4.10(c): Low temperature resistivity fits to $\rho = \frac{1}{\sigma_0 + BT^{1/2}} + \rho_n T^n$ law for 1 x 10^{12} ions/cm^2 ion irradiated LPBMO/STO films.

Table 4.6: Values of T_m and various derived parameters from low temperature resistivity fits for the films irradiated with the Ag ion dose: 1 x 10^{12} ions/cm^2

Sample	Magnetic field (T)	T_m(K)	σ_0 (Ω^{-1} cm^{-1})	B ($\Omega^{0.5}$ $cm^{0.5}$)	ρ_n (Ω cm/K^n)	n	χ^2
500Å	0	37	2.10324	0.10117	4.917 x 10^{-7}	2.8062	1 x 10^{-5}
	5	45	2.24367	0.14843	5.054 x 10^{-6}	2.2348	
	9	50	2.30841	0.17363	6.347 x 10^{-6}	2.1332	
1000Å	0	38	1.39106	0.06255	4.957 x 10^{-6}	2.8875	7.4 x 10^{-6}
	1	40	1.38033	0.07828	3.109 x 10^{-7}	2.4918	
	5	48	1.48193	0.0881	4.26 x 10^{-6}	2.3496	
	9	53	1.51817	0.10562	6.191 x 10^{-6}	2.21548	
2000Å	0	47	0.15164	0.0275	3.256 x 10^{-6}	2.9168	1.14 x 10^{-3}
	1	49	0.18495	0.026	7.687 x 10^{-6}	2.6932	
	5	53	0.17612	0.04018	60 x 10^{-6}	2.1451	
	9	57	0.17538	0.0488	90 x 10^{-6}	1.99315	

It is seen that, T_m shifts to higher values with increasing irradiation dose, for e.g. in 2000Å film, the T_m increases from 41K for pristine to 52 K and 47K for the irradiated films [Table 4.1, 4.4, 4.5 and 4.6]. This may be understood in terms of irradiation induced suppression of inelastic scattering ρ_n which decreases with subsequent irradiation doses. Among the other terms, the Coulombic interaction coefficient, B, signifies the depth of resistivity minima which decreases with successive irradiation dose and is reflected in the broadening of the resistivity upturn.

The fitting of the ρ-T data of 2000Å films irradiated with $5x10^{10}$ ions/cm^2 and 5 x 10^{11} ions/cm^2 shows negative σ_0 (Ω^{-1} cm^{-1}) values, the explanation of which needs further investigations.

Magnetoresistance

The magnetotransport behavior of all the LPBMO/STO films has been studied and the MR vs. H isotherms at different temperatures for the 500Å, 1000Å and 2000Å pristine and irradiated films are shown in fig.4.11(a), (b) and (c) respectively. The temperature dependence of MR behavior is discussed in the following paragraph.

The observed maximum values of MR at 195K (~ T_P) for the 500Å, 1000Å and 2000Å are tabulated in Table 4.7. It can be observed from the MR vs. H plots that, there is no remarkable variation in MR with irradiation dose in all the films studied whereas with increasing the film thickness maximum MR is observed for 2000Å film. It has been illustrated from the fig.4.11(a), (b) and (c) that, variation in maximum MR (~T_P) is insensitive to the irradiation but has significant enhancement at low temperatures in 2000Å films. In addition to this, an appreciable MR at low temperature, 5K, is observed in all the films irradiated with 5 x 10^{10} ions/cm^2 and 5 x 10^{11} ions/cm^2 while MR gets suppressed with 1 x 10^{12} ions/cm^2 ion dose.

From the MR vs. H studies, it can be summarized that, the irradiation has no remarkable effect for the low thickness films while in higher thickness film it gets modified appreciably at low temperatures.

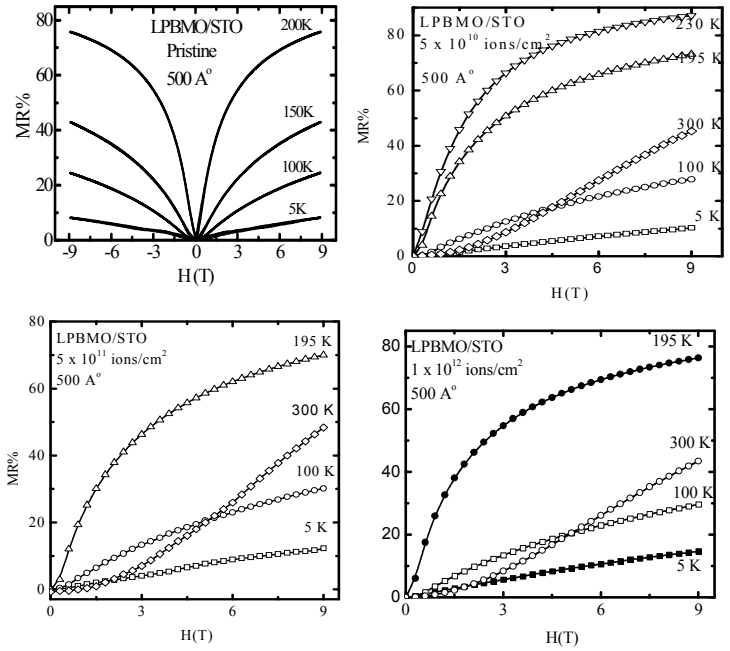

Figure 4.11(a): MR vs. H isotherms at various temperatures for pristine and irradiated 500Å LPBMO/STO thin films.

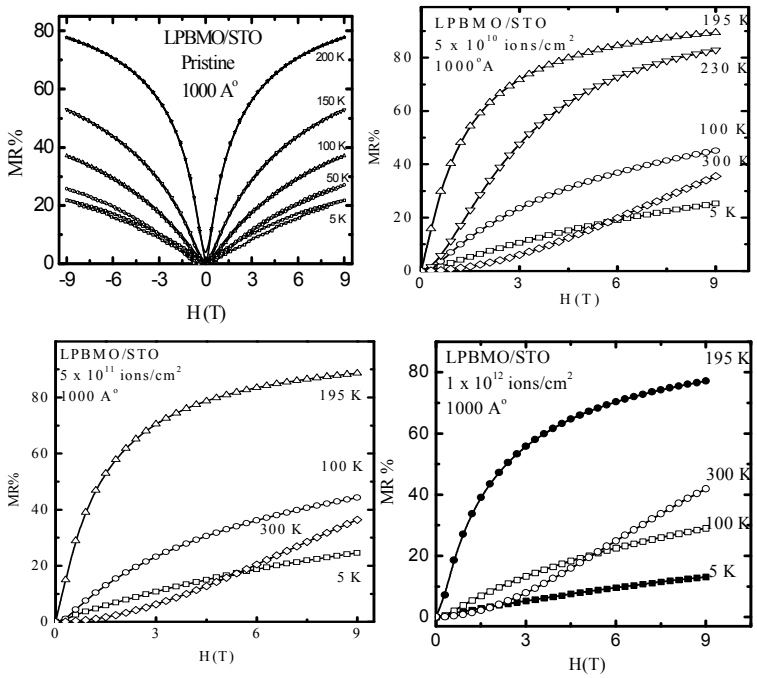

Figure 4.11(b): MR vs. H isotherms at various temperatures for pristine and irradiated 1000Å LPBMO/STO thin films.

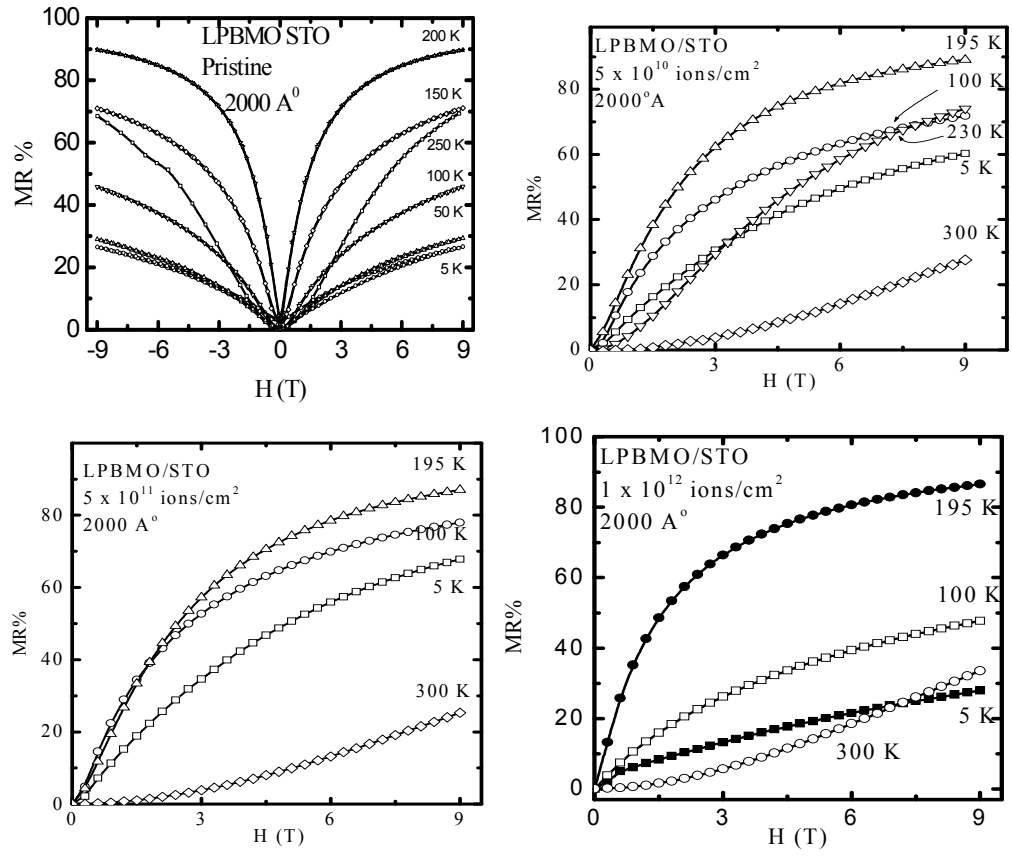

Figure 4.11(c): MR vs. H isotherms at various temperatures for pristine and irradiated 2000Å LPBMO/STO thin films.

Table 4.7: Values of maximum MR (at 9T) observed at 5K, 100K and 195K (~T_P) for pristine and irradiated LPBMO/STO films

Thickness	Temperature (K)	Pristine	$5x10^{10}$ ions/cm^2	$5x10^{11}$ ions/cm^2	$1x10^{12}$ ions/cm^2
500Å	5	9%	10%	12%	16%
	100	25%	29%	30%	30%
	195	77%	75%	70%	78%
1000Å	5	22%	25%	24%	14%
	100	38%	45%	44%	30%
	195	79%	90%	89%	79%
2000Å	5	28%	60%	69%	30%
	100	46%	75%	79%	49%
	195	90%	90%	89%	88%

4.4.3. TCR and FCR studies

For any temperature and field sensing applications, the values of TCR and FCR decide its efficiency and usefulness. For this purpose, we have determined the TCR and FCR values from resistivity and MR plots which are shown in figs.4.12(a) and (b).

The variation of TCR with temperature can be seen from fig.4.12(a) for pristine and irradiated LPBMO films. The values of TCR are maximum in the temperature range of 170-210K. The positive values of maximum TCR are 3%, 2.5% and 1.6% for 500Å, 1000Å and 2000Å pristine films respectively which become 3%, 2.5% and 2% for ion dose of 5 x 10^{10} ions/cm^2, 2%, 2.1% and 1.7% for ion dose of 5 x 10^{11} ions/cm^2 and 3%, 2.5% and 2% for 1 x 10^{12} ions/cm^2 ion dose respectively. At low temperature (<10K), the negative maximum TCR values are ranging between 0 to -1% for all the films except 2000Å ion irradiated films while the negative maximum TCR around 200K is ~ -1-2% for all the films. At very low temperature, 2000Å film exhibits appreciable rise in negative TCR ~ - 4.5% for 5 x 10^{10} ions/cm^2 and 1 x 10^{12} ions/cm^2 whereas, it becomes ~ -12% for the irradiation dose of 5 x 10^{11} ions/cm^2.

The variation in FCR with H at 195K is shown in fig.4.12(b) for all the pristine and irradiated films. The values of maximum FCR are ~ - 1-2% for 500Å pristine and irradiated films. With increment of film thickness from 500Å to 1000Å, the value of FCR increases. The values of FCR varies from -3.5% to -1.5% for 1000Å and -0.05% to -2.25% for 2000Å pristine and irradiated films.

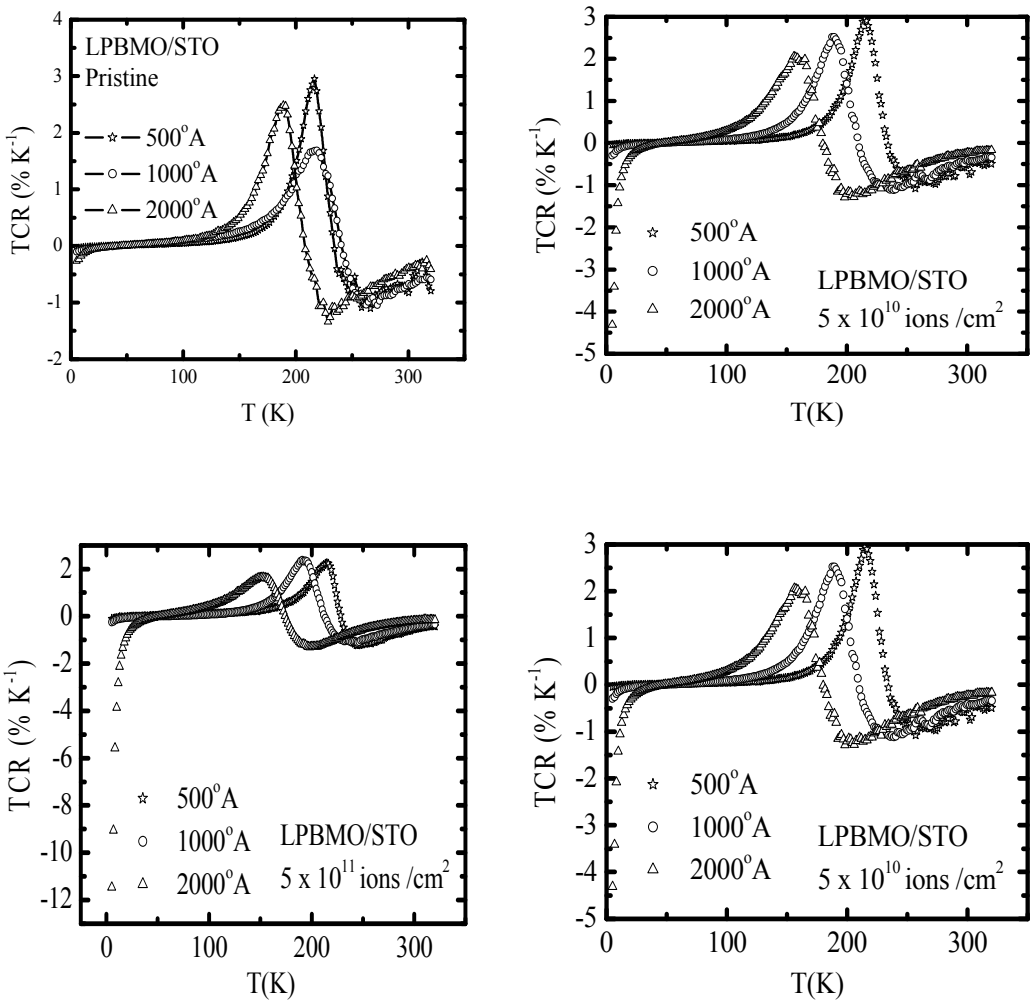

Figure 4.12(a): TCR (%K^{-1}) vs. T(K) plots for pristine and irradiated LPBMO/STO films.

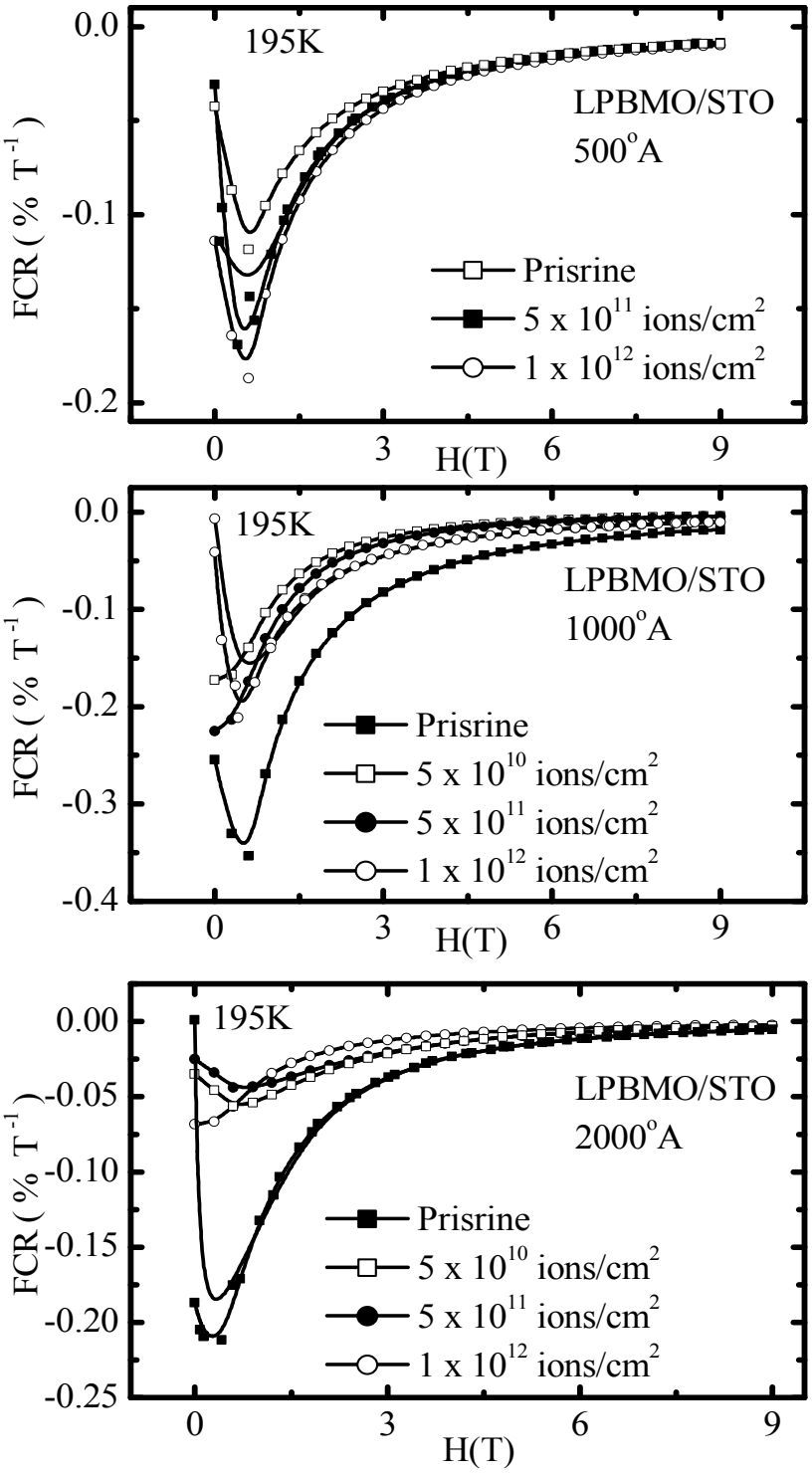

Figure 4.12(b): FCR (%T^{-1}) vs. H(T) plots for pristine and irradiated LPBMO/STO films.

Conclusions

In summary, the studies on $La_{0.5}Pr_{0.2}Ba_{0.3}MnO_3$ (LPBMO) manganite thin films on single crystalline STO (*100*) substrates grown using PLD technique are presented in this chapter. The important conclusions derived from the above studies are summarized as follows

Firstly, the dependence of structural, microstructural, electronic and magnetotransport properties of thickness dependent LPBMO manganite films are discussed. The electronic and MR properties reveals that, the T_P value decreases along with the increase in resistivity with increasing film thickness from 500Å to 2000Å. The investigations on LPBMO/STO films resulted into the observation of low temperature resistivity minima below 50K, similar to that observed in bulk counterpart which is not very common feature in the manganites. Based on our studies, it turns out that, low temperature anomalous resistivity behavior is due to the electron-electron localization. Some implications and parameters derived from electron-electron localization are,

- The application of magnetic field do not dissolve the resistivity minima
- The T_m shifts to slight higher temperature with H with corresponding decrease in resistivity and broadening of the minima

The SHI irradiation with 200 MeV Ag^{15+} ions does not affect the low temperature minima and T_m increases with the increase in irradiation dose. The structural, electronic and magnetotransport properties of all the thin films reveal that, the peak resistivity increases with the decrease in T_P. Also, the effect of irradiation is not very significant on the MR behavior of films studied. Further, below 100K, MR shows significant enhancement in 2000Å films irradiated with an ion dose of 5×10^{11} ions/cm^2 and 5×10^{11} ions/cm^2 which introduces electronic and magnetic anisotropies in these films by the creation of columnar defects. However, higher irradiation dose has some relaxation effect which is clear from the resistivity and MR behavior. In addition to this, it is observed that, irradiation has comparatively less effect on the structure and transport properties of lower thickness films as compared to higher thickness films.

References

1. "Colossal Magnetoresistance, charge ordering and other related properties of rare earth manganites", ed. by C. N. R. Rao and B. Raveau, World Scientifics Publishing Company (1998)
2. R. Von Helmolt, J. Wecker, B. Holzapfel, L. Schultz, K. Samwer, Phys. Rev. Lett. 71, 2331 (1993)
3. S. Zin, T.H. Tiefel, M. McCormack, R.A. Fastnacht, R. Ramesh, L.H. Chen, Science 264, 413 (1994)
4. T. Venktesan, M. Rajeswari, Z. W. Dong, S. B. Ogale, R. Ramesh, Phil. Trans. Roy. Soc. A 356, 1661 (1998)
5. L. M. Rodriguez Martinez and J. P. Attfield, Phy. Rev. B, 58, 2426 (1998)
6. H. Y. Hwang, S. W. Cheong, P.G. Radaelli, M. Marezio, B. Batlogg, Phys. Rev. Lett. 75, 914 (1995)
7. D. S. Rana, K.R. Mavani, Darshan C. Kundaliya, D.G. Kuberkar,and S.K. Malik Physica B, 378, 501 (2006)
8. D. S. Rana, C. M. Thaker, K. R. Mavani, D. G. Kuberkar, Darshan C. Kundaliya and S. K. Malik, J. Appl. Phys. 97, (2005)
9. V. G. Prokhorov, V. S. Flis, G. G. Kaminsky, Y. P. Lee and J. S. Park and V. L. Svetchnikov, Low. Temp. phys., 31, 161 (2005)
10. J. L. Alonso, L. A. Ferna´ndez, F. Guinea, V. Laliena and V. Martin-Mayor, Phys. Rev. B 66, 104430 (2002)
11. D. S. Rana, J. H. Markna, R. N. Parmar, P.Raychaudhuri , J.John, D.G.Kuberkar and S. K. Malik Phys. Rev. B, 71,212404 (2005)
12. D. Kumar, J. Sankar, J. Narayan, Rajiv K. Singh, A.K. Majumdar, Phys. Rev. B 65, 94407 (2002)
13. M. Auslender, A.E. Karkin, E. Rosenberg, G. Gorodetsky, J. Appl. Phys. 89, 6639 (2001)
14. M. T. Mercaldo, J.Ch. Angle´s d'Auriac and F. Iglo´i, cond-mat/ 0502035

15. J. Burgy, M. Mayr, V. Martin-Mayor, A. Moreo and E. Dagotto, Phys. Rev. Lett. 87, 277202 (2001)

16. A. Tiwari, K.P. Rajeev, Solid State Commun. 111, 33(1999)

17. S. L. Sondhi, S. M. Girvin, J. P. Carini, and D. Shahar, Rev. Mod. Phys. 69, 315 (1997); J. M. De Teresa, P. A. Algarabel, C. Ritter, J. Blasco, M. R. Ibarra, L. Morellon, J. I. Espeso and J. C. Go´mez-Sal, Phy. Rev. Lett. 94, 207205 (2005)

18. T. Vojta, Ann. Phys. 9, 403 (2000)

19. H. Y. Hwang, S. W Cheong, N. P. Ong and B. Batlogg, Phys. Rev. Lett. 77, 2041 (1996)

20. A. de Andres, M. Garcia-Hernandez, J. L. Martinez, Phys. Rev. B 60, 7328 (1999)

21. L. Balcells, J. Fontcuberta, B. Martinez, and X. Obradors, Phys. Rev. B, 58, 14697 (1998)

22. S. B. Ogale, K. Ghosh, J. Y. Gu, R. Shreekala, S. R. Shinde, M. Downes, M. Rajeswari, R. P. Sharma, R. L. Greene, T. Venkatesan, R. Ramesh, Ravi Bathe, S.I. Patil, Ravi Kumar, S. K. Arora, and G. K. Mehta, J. Appl. Phys. 84, 6255 (1998)

23. J. H. Markna, R. N. Parmar, D. G. Kuberkar, Ravi Kumar, D. S. Rana and S. K. Malik, Appl. Phys. Lett. 88, 152503 (2006)

24. Program SRIM (2003) by J. F. Ziegler and J. P. Biersack, http://www.srim.org

25. G. Szenes, Phys. Rev. B. 51, 8026 (1995)

Chapter - 5

Studies on $La_{0.7}R_{0.3}MnO_3$ (LRMO) (R = Ca, Sr and Ba) thin films grown by CSD method

In this Chapter, the studies on $La_{0.7}R_{0.3}MnO_3$ (LRMO) (R = Ca, Sr and Ba) manganite thin films synthesized using novel chemical synthesis method have been discussed. Usually high quality epitaxial manganite thin films are grown by vacuum deposition techniques like Pulsed Laser Deposition (PLD) [1,2], RF sputtering [3], Metallorganic Chemical Vapour Deposition (MOCVD) [4] or Molecular Beam Epitaxy (MBE) [5]. The microstructural and physical properties of manganite thin films are different from their bulk counterparts and are found to be dependent on the processing techniques, growth conditions, environment, post-annealing, substrate and film thickness [6,7].

Chemical Solution Deposition (CSD), consisting of novel sol-gel route and coprecipitation methods using metal organic decomposition (MOD), for preparation of homogeneous bulk ceramics and their thin films, has number of advantages over conventional vacuum deposition techniques. CSD method is cost-effective, composition compatible, yields stochiometrically predefined compounds and provides the varieties of alternative precursors to choose, contains wide range of concentration, viscosity and pH, easier to set up and handle. The adhesion of the wet films to the substrate optimizes the thin film properties grown using CSD method. However, the method does not offer particle size control but up to some extent, results in the monodispersed particles. Hence, CSD method becomes an alternative for depositing magnetoresistive manganite thin films. Several reports are available on processing, structural, morphological, electronic transport and magnetoresistance (MR) studies on $La_{0.7}Rn_{0.3}MnO_3$ (Rn = Ca^{2+}, Sr^{2+}, Ba^{2+}) thin films grown using the chemical route [8,9]. However, very few reports are available on the studies on varying synthesizing conditions on the microstructure and MR properties of CSD grown manganite films [10-12]. In this context, during the course of present work, $La_{0.7}Sr_{0.3}MnO_3$ (LSMO) thin films were deposited on $LaAlO_3$ [LAO] (*h00*) single crystal substrates by CSD method and the effect of processing parameters, annealing temperature and time on the microstructure, electrical resistivity and magnetotransport properties of LSMO films were studied. The obtained results on LSMO films, motivated further, to synthesize LRMO (R = Ca and Ba) films using CSD route and to study their structural, microstructural, electronic and magnetotransport studies. Finally, the Swift Heavy Ion (SHI) irradiation studies on all the films have been carried out which manifest the thin film

transport and MR properties for their application possibilities as uncooled bolometers and magnetic field sensors.

5.1 Synthesis

The high purity Lanthanum acetate hydrate [$La(CH_3COO)_3 \cdot xH_2O$], Strontium acetate hydrate [$Sr(CH_3COO)_2 \cdot xH_2O$] and Manganese acetate hydrate [$Mn(CH_3COO)_2 \cdot xH_2O$] [all 99.9% pure] were dissolved stochiometrically (0.7 : 0.3 : 1) in acetic acid and distilled water (1:1 by volume) followed by the stirring at elevated temperature (~80°C, 10 min.) to obtain a clear 0.2-0.6M precursor solution which was used for film deposition. Depositions of LSMO films on highly polished LAO (*h00*) single crystal substrates were done using automated spin coater at 6000 rpm for 20 sec followed by drying and calcination at 120°C and 350°C for 30 min and final annealing in oxygen in the temperature range of 700°C–1000°C. The annealing time was kept as 6h and 12h for the LSMO films annealed at 1000°C. Thickness per coating was ~ 800Å, estimated using DESJECT thickness profilometer. The spin coating process was then repeated once to obtain the films with desirable film thickness ~ 1500Å. Figure 5.1 shows the flow diagram of the CSD method used for the deposition of LSMO films.

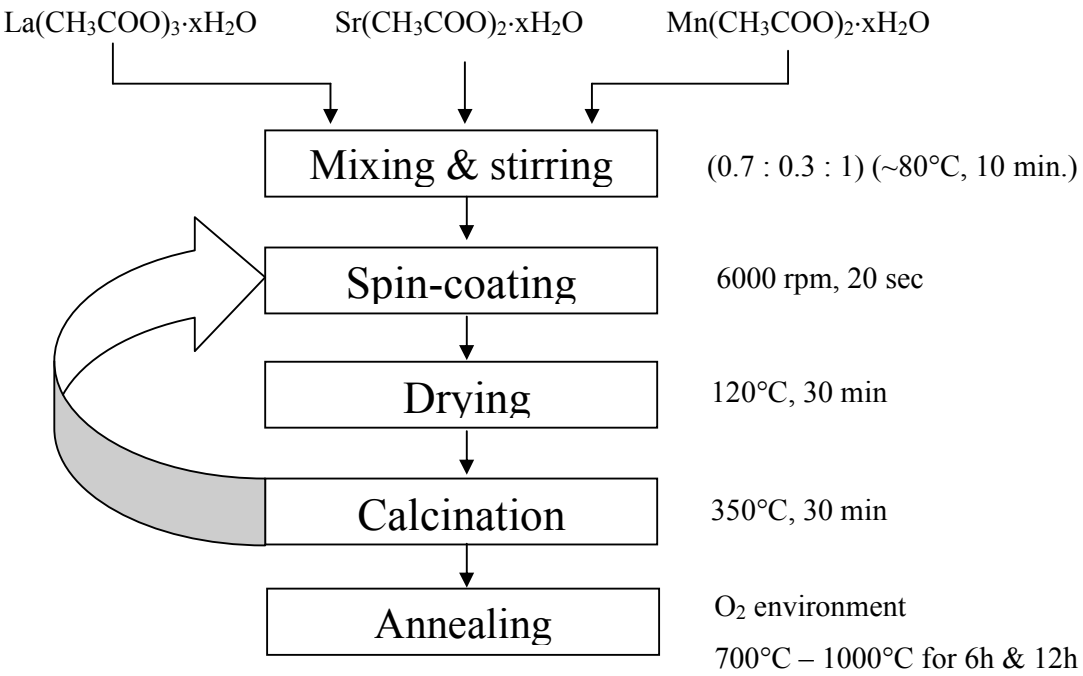

Figure 5.1: Flow diagram of CSD method used for $La_{0.7}Sr_{0.3}MnO_3$ film deposition.

The detailed study on the effect of synthesis parameters on structure, morphology, resistivity and MR properties of LSMO thin films synthesized following the above mentioned route [Fig. 5.1], is given in sections 5.1.1. and 5.1.2.

All the LSMO films were characterized by X-ray diffraction (XRD) and atomic force microscopy (AFM) measurements for their structural and microstructural properties. Using d.c. four probe resistivity technique, the electrical resistivity of all the films was measured i) as a function of temperature in the range of 5-425K in zero-field and in applied fields of 5T and 8T respectively and ii) as a function of magnetic field (up to 9T) at various temperatures (5 – 300K) using RT and magneto RT measurements.

5.1.1 Effect of annealing temperature

Structure

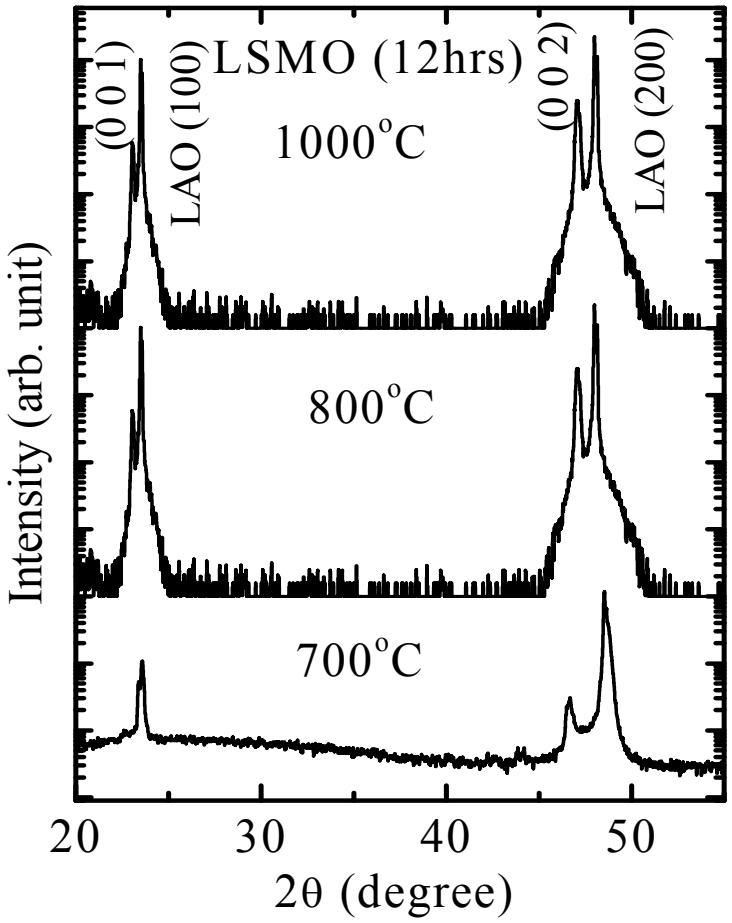

Figure 5.2: XRD patterns of LSMO/LAO films annealed at 700°C, 800ºC and 1000°C.

The typical indexed XRD patterns of LSMO films on LAO (*h00*) single crystal substrates annealed at different temperatures are shown in fig.5.2. All the LSMO films are epitaxially c-axis (*00l*) oriented and indexed using bulk LSMO cell parameters [a = 5.471(1)Å, b = 7.771(2)Å and c = 5.5503(1)Å]. The values of lattice mismatch between the LSMO films and LAO substrates determined using the formula, $\delta\% = \frac{d_{substrate} - d_{thin\ film}}{d_{substrate}} \times 100$ are -2.65%, -1.90 % and -1.89 % for the films annealed at 700°C, 800°C and 1000°C respectively. This suggests a decrease in compressive strain in the films with increasing annealing temperature. The intensity of the diffraction peaks increases while FWHM value decreases with increasing annealing temperature which signifies the considerable improvement in the crystalline structure of the LSMO films with annealing temperature.

Microstructure

The AFM pictures recorded to study the microstructure of LSMO thin films annealed at different temperatures are shown in fig.5.3. The distinct grain structure can be observed for the films annealed at various temperatures which shows domain like growth composed of faceted grains. Annealing temperature manifests the growth and alignment of grains into the domains which can be seen from fig.5.3. In the film annealed at 700°C, grains are in preliminary stage and are partially grown. The growth, alignment and size of the grains and domains become more significant in 800°C and 1000°C annealed films. The observed surface roughness for 700ºC film is ~ 31nm which reduces to 13nm and 16nm for the LSMO films annealed at 800°C and 1000°C respectively. The values of average grain size obtained from AFM pictures are 50nm, 70nm and 90nm for the films annealed at 700°C, 800°C and 1000°C respectively. A significant enhancement in grain size would result in a decreased grain boundary region and, consequently, an improved electronic transport at the grain boundaries which accounts for reduction of resistivity in CSD grown LSMO thin films at higher annealing temperature.

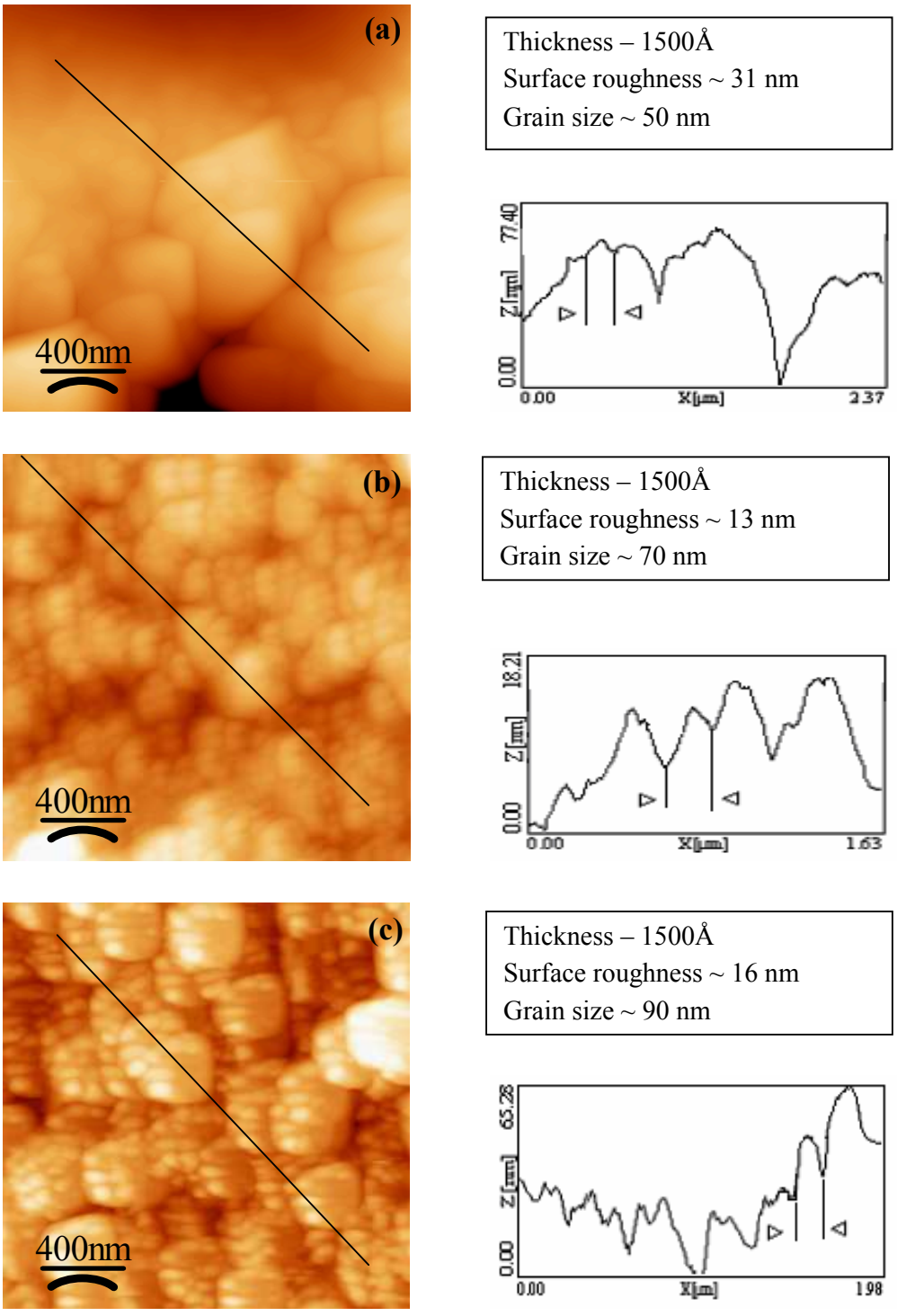

Figure 5.3: 2µm x 2µm AFM image of LSMO/LAO films annealed at (a) 700°C (b) 800°C and (c) 1000°C with their respective surface roughness histogram. The two arrowheads define an atomic step.

RT & Magneto RT

All the LSMO thin film samples were characterized for electrical and magnetotransport behavior in the temperature range 5-425K. Figure 5.4 shows resistivity (ρ) vs. temperature (T) plots for LSMO films in zero-field and in a field of 5T and 8T. All the LSMO films exhibit Insulator-Metal transition (T_P) at the temperatures higher than 340K. The values of processing parameters, resistivity at 5K [ρ_{5K}], peak resistivity [ρ_P] and T_P in zero applied field, for the films annealed at different temperatures are summarized in Table 5.1. Thin films annealed at lower temperatures possess broad I-M transition which sharpens with increasing annealing temperature. The electrical resistivity decreases along with the enhancement in T_P with increasing annealing temperature from 700°C to 1000°C which is in good agreement with the reports available on the effect of annealing temperature on transport properties of manganite thin films [13]. In zero applied magnetic field, the peak resistivity suppresses by a factor of $\sim 10^2$, whereas at 5K resistivity reduction is $\sim 10^3$ as annealing temperature increases from 700°C to 1000°C respectively. Also, it can be seen from the ρ – T curves that, in the temperature range 5-300K, applied field of 5T and 8T do not modify resistivity behavior from that of the zero field resistivity for 1000°C annealed film. Further, the LSMO thin film, annealed at 700°C, exhibits low temperature resistivity minimum below 50K which disappears in the films annealed at 800°C and 1000°C. This low temperature resistivity behavior, in 700°C annealed film, can be attributed to the spin disorder scattering consisting of both spin polarization and grain boundary tunneling [14, 15].

Table 5.1: Values of processing parameters, resistivity at 5K [ρ_{5K}], peak resistivity [ρ_P] and T_P for LSMO/LAO thin films in zero applied field.

Sample	Annealing Temperature	Annealing time	ρ_{5K} (mΩcm)	ρ_P (mΩcm)	T_P (K)
LSMO	700°C	12h	294	1100	341
LSMO	800°C	12h	67	300	353
LSMO	1000°C	12h	0.3	9	377

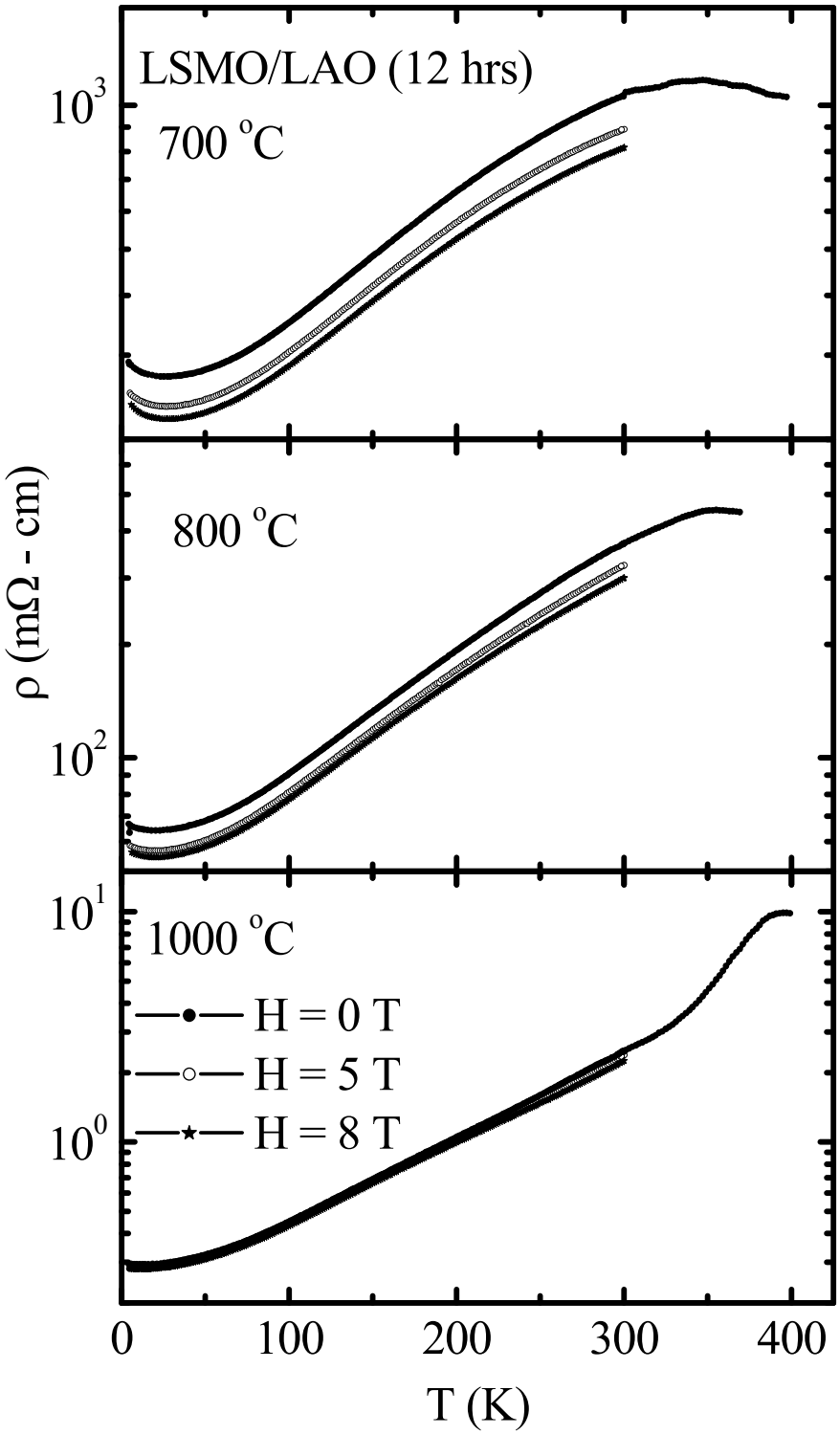

Figure 5.4: ρ – T plots for LSMO/LAO films annealed at 700°C, 800°C and 1000°C in H = 0, 5 and 8T fields.

Magnetoresistance

Figure 5.5 shows MR vs. H isotherms at various temperatures for all the LSMO thin films annealed at various temperatures. From the plots it can be seen that, all the films exhibit maximum MR in the vicinity of T_P which decreases with decreasing temperature. The temperature dependence of MR has been discussed as follows,

i) At low temperature of 5K, the films annealed at 700°C and 800°C exhibit low field MR (LFMR) ~ 5% (in a field of < 1T). This uncharacteristic MR behavior of an oriented film partially resembles the LFMR behavior of polycrystalline samples, the origin of which is attributed to the intergrain spin polarized tunneling (SPT) of charge carriers that depends upon the alignment of the magnetic moments of the ferromagnetic domains [16,17]. It is interesting to note that, at 5K, LFMR of the film annealed at 1000°C is almost zero. Also, the high field MR (HFMR) (in a field >1T) at 5K decreases from ~ 15% for film annealed at 700°C to nearly 5% for the film annealed at 1000°C. This points towards the enhancement in connectivity between the grains, reduction in pinning of Mn-ion spins at grain boundaries, etc [18,19].
ii) At intermediate temperatures in the range 100-240K, the film annealed at 700°C shows LFMR < 3% while the 800°C and 1000°C annealed films show nearly zero MR. The HFMR is nearly 20% for film annealed at 700°C which reduces to 16% and 7%, respectively, for the films annealed at 800°C and 1000°C temperatures.
iii) At room temperature (RT), the LFMR < 3% is observed for all the LSMO films annealed at different temperatures. The HFMR observed for the 700°C and 800°C annealed film is ~23%, while it is ~16% for 1000°C annealed film. Such an enhancement in MR at RT may be attributed to the field induced delocalization of charge carriers due to the structural disorder at grain boundaries and at Mn-O-Mn bond angles [16,19].

The above-mentioned results on MR behavior show suppression in MR at low temperatures and its enhancement at high temperatures around RT, signifying the importance of grain boundary contribution to MR. Such a MR behavior can be understood using the two channel model proposed by the De Andres *et al* [18]. There exists two kinds of conduction channels in the samples and all of them are parallel.

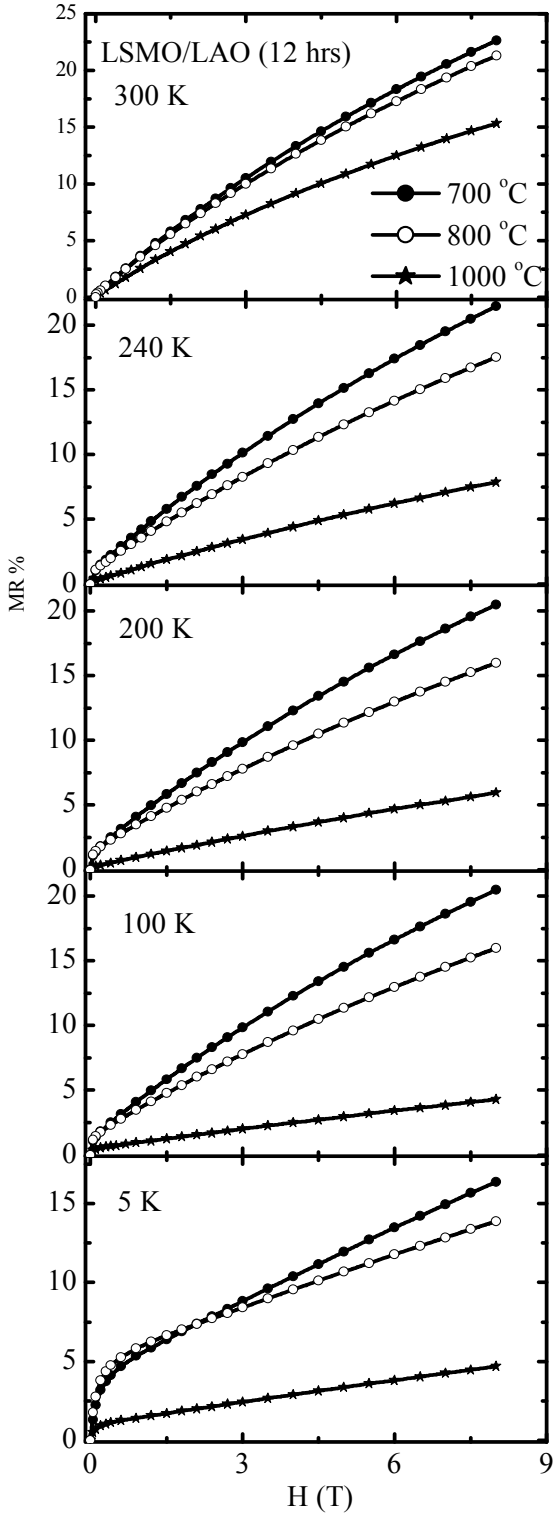

Figure 5.5: MR vs. H isotherms for LSMO/LAO films annealed at 700°C, 800ºC and 1000°C.

One kind is related to the intrinsic transport properties of the system and is achieved through good contacts between grains. The other kind of channels shows energy barriers that inhibit metallic conduction at all temperatures due to poor connectivity, disorder, and/or contamination at the grain surface that inhibit the metallic conduction. The conduction will be effective for the less resistive one because these are parallel channels.

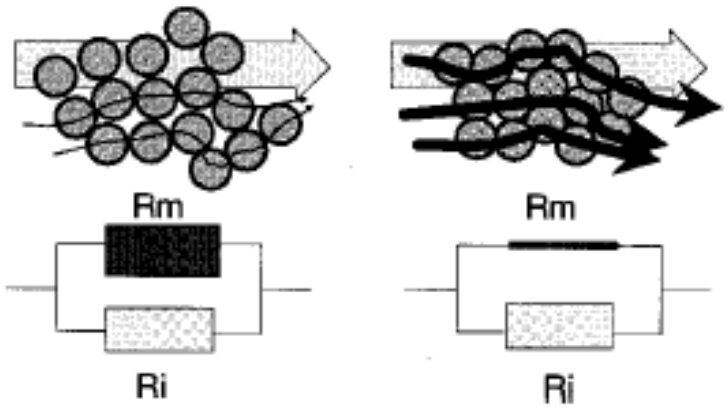

Figure 5.6: Scheme for the conduction in two granular systems with a poor connectivity (left) and a better connectivity (right). Lower part: the equivalent circuits with two resistances in parallel: R_M (for good channels) and R_I (for bad channels). The curved arrows in the upper part are related to good channels.

Moreover, suppression of LFMR indicates further the improvement in crystallographic orientation and parallel alignment of magnetic domains. This inference is supported by increasing line intensity in XRD patterns [Fig. 5.2] and moderate reduction in surface roughness [Fig. 5.3]. Both the observations point towards the better orientation and crystalline order of the films annealed at higher temperatures. At low temperatures, HFMR arises due to poor connectivity between grains, pinning of Mn spin at grain boundaries, etc. [19]. The suppression of HFMR at 5K indicates annealing temperature induced enhancement in grain connectivity. Such granular contribution is also evident from the MR behavior at T_P (> RT). The enhancement in MR at RT with increasing annealing temperature implies the improved magnetic order at the grain boundaries thereby allowing better electronic transport.

5.1.2 Effect of annealing time

Structure

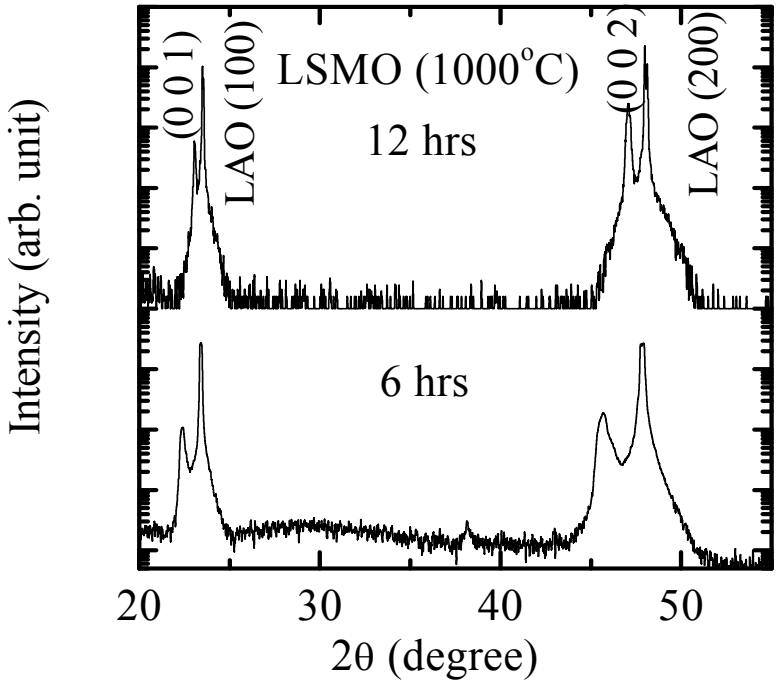

Figure 5.7: XRD patterns for LSMO/LAO films annealed for 6h and 12h.

The XRD patterns of LSMO thin films on single crystalline LAO (*h00*) substrates annealed at 1000ºC for 6 and 12 hrs depicting epitaxially c-axis (*00l*) oriented are shown in fig.5.7. It can be seen from the figure that, intensity of diffraction peaks increases (almost 10 times) and the value of FWHM decreases with the increasing annealing time intervals from 6h to 12h respectively. For instance, the FWHM of (*002*) peak decreases from 0.256º for the film annealed for 6h to 0.121º for the film annealed for 12h. In addition to this, the calculated residual microstrain present into the film due to the mismatch between single crystal substrate and material is found to decrease from -2.41% to -1.89% for the films annealed for 6h and 12h respectively. Thus, there is a substantial decrease in compressive strain along with the increase in peak intensity and decrease of FWHM, clearly suggesting an improvement in the crystalline structure of the film with progressive annealing time intervals.

Microstructure

Figure 5.8 shows the AFM micrographs illustrating the surface morphologies of LSMO thin films annealed for 6h and 12h respectively. The typical grain structure has been observed for the films annealed for different periods. The values of average surface roughness and grain size are 12nm and 80nm respectively for 6h annealed film which become 16nm and 90nm for the film annealed for 12h. Although there is very small change in the values of surface roughness and grain size, the orientation and alignments of the grains and domains improve the connectivity between the grains extensively with annealing time intervals. The arrangements of the grains into the domains and domains themselves become more ordered which is apparent in 12h annealed film as compared to 6h annealed film [Fig.5.8].

RT & Magneto RT

Both the LSMO thin films were characterized for electrical and magnetotransport behavior in the temperature range 5-425K. Figure 5.9 shows ρ-T plots for LSMO films in 0, 5 and 8T fields respectively. The T_P is higher than 350K for both the LSMO thin films. Table 5.2 lists the values of processing parameters, resistivity at 5K [ρ_{5K}], peak resistivity [ρ_P] and T_P for both the films in zero applied field. The electrical resistivity decreases while T_P increases with annealing time. In zero applied magnetic field, the peak resistivity suppresses by the factor of ~10, while at 5K, resistivity reduction is ~10^2 as annealing time increases from 6h to 12h respectively. Also, it can be seen that, under applied magnetic fields of 5 and 8T, the temperature dependence of resistivity is similar to that of the zero field resistivity in the temperature range of 5-200K for both the LSMO thin films.

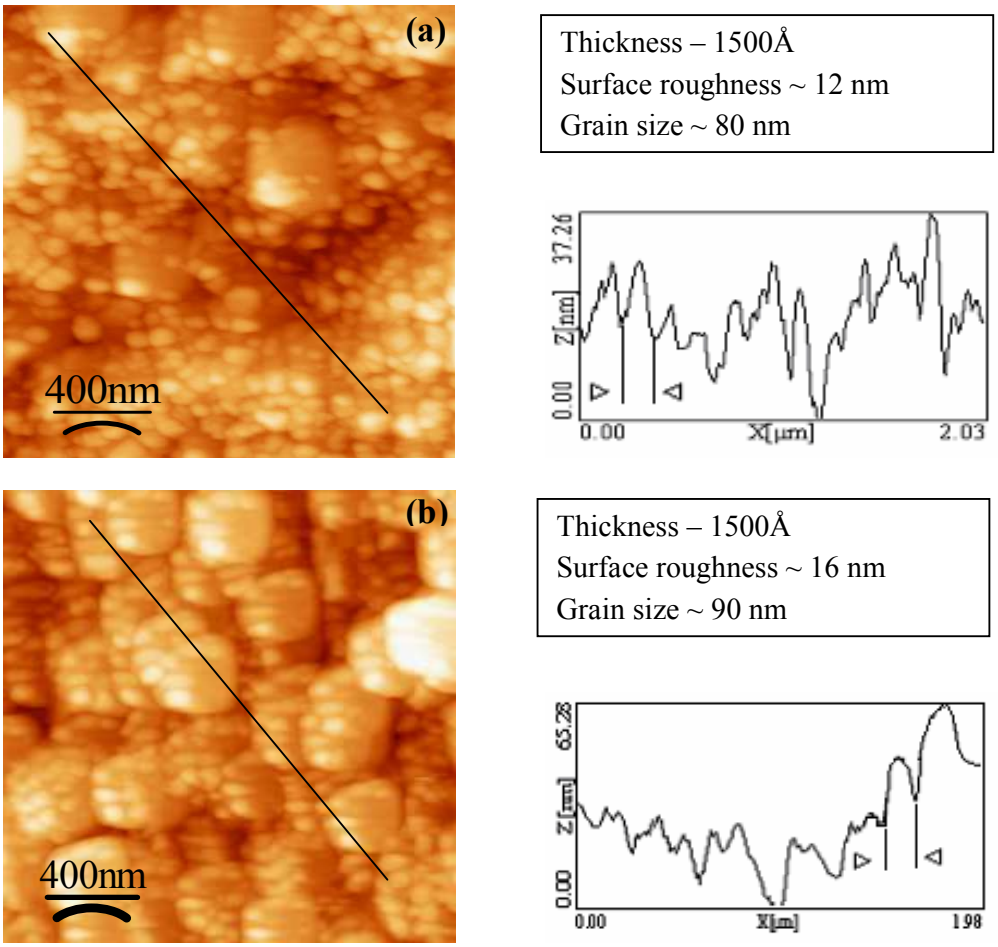

Figure 5.8: 2μ x 2μ AFM image of LSMO/LAO films annealed for (a) 6h and (b) 12h with their respective surface roughness histogram. The two arrowheads define an atomic step.

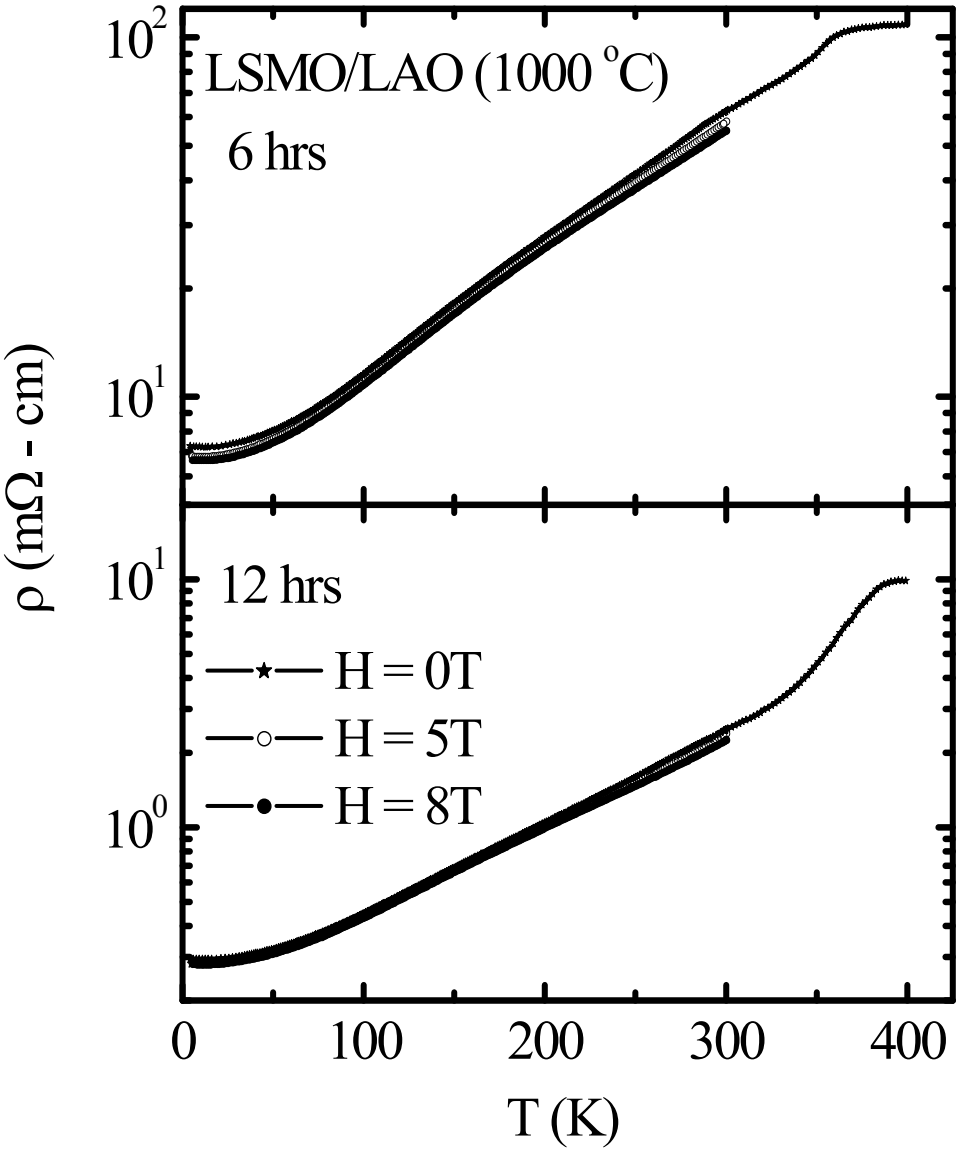

Figure 5.9: ρ – T plots for LSMO/LAO films annealed for 6h and 12h in H = 0, 5 and 8T fields.

Table 5.2: Values of processing parameters, resistivity at 5K [ρ_{5K}], peak resistivity [ρ_p] and T_P for LSMO/LAO thin films in zero applied field.

Sample	Annealing Temperature	Annealing time	ρ_{5K} (mΩcm)	ρ_P (mΩcm)	T_P (K)
LSMO	1000°C	6h	7.1	111	355
LSMO	1000°C	12h	0.3	9	377

Magnetoresistance

MR vs. H isotherms at various temperatures for 6h and 12h annealed LSMO films have been shown in fig.5.10. It can be seen that, films possess maximum MR in the vicinity of T_P which decreases with decreasing temperature. Temperature dependent MR behavior can be discussed as follows,

i) At low temperature (5K), the film annealed for 6h exhibits LFMR ~4% which can be attributed to the intergrain spin polarized tunneling (SPT) [16,17]. LFMR is almost negligible for the film annealed for 12h [Fig. 5.10]. The values of HFMR are ~8% and 4% for the films annealed for 6h and 12h respectively. The reduction in HFMR at low temperatures implies reduction in insulating grain boundary regions and hence the enhanced connectivity between the ferromagnetic metallic grains [19].
ii) At intermediate temperatures (100-240K), both the films exhibit negligible LFMR (< 2%). The observed values of HFMR in this temperature range are ~8-10% for 6h annealed film which reduces to ~ 4-7% for the film annealed for 12h respectively.
iii) At room temperature (RT), the respective values of LFMR and HFMR are negligible and ~15% for the films annealed for 6h and 12h.

These results signify the importance of grain boundary contribution to MR. At low temperatures, the LFMR has its origin in the spin dependent scattering and/or tunneling process of charge carriers at grain boundaries that depends on the angle formed by magnetic moment of the ferromagnetic grains/domains and is the typical feature of the polycrystalline bulk. The reduction of LFMR with increasing annealing time implies the improved crystalline structure of an oriented film which is further confirmed from the increased diffracted peak intensity [Fig. 5.7]. The HFMR is ascribed to the reorientation of disordered spins at grain interface which in turn depends on the connectivity between the grains and on the stiffness of the aligned blocked spins at the grain surface [19]. The connectivity between the grains is decided by the processing conditions, most commonly, annealing temperature and/or time. A significant improvement of the alignment and orientations of the grains [Fig. 5.8] would result in a decreased insulating grain boundary region with increasing annealed time which is responsible for the substantial reduction in HFMR at low temperatures. At RT the enhanced HFMR is attributed to the field induced suppression of spin disorder at Mn-O-Mn bond angles.

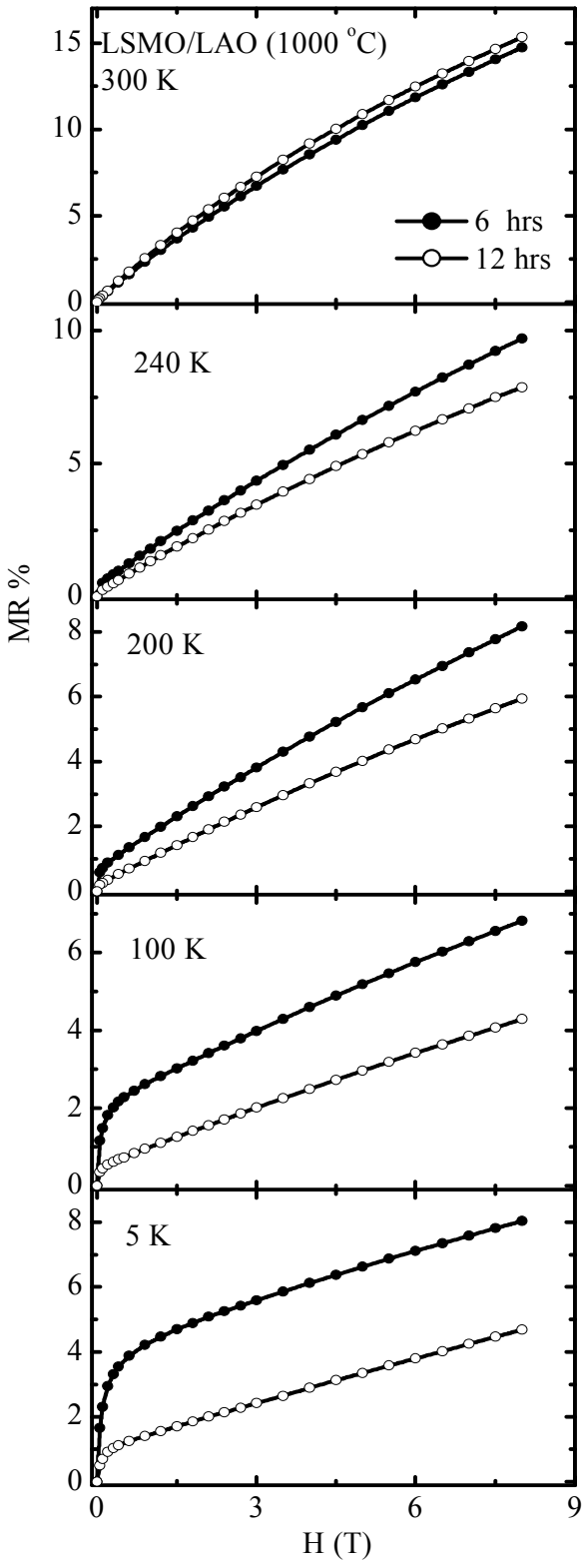

Figure 5.10: MR vs. H isotherms for LSMO/LAO films annealed for 6h and 12h.

In conclusion, the structural, microstructural and magnetotransport properties of LSMO thin films deposited on LAO single crystal substrates annealed at different temperatures and for different time periods have been investigated. It has been observed that, both the synthesis factors modify the microstructure, electronic and magnetotransport properties of the LSMO thin films grown by CSD method. By properly selecting the synthesis conditions, the high quality manganite thin films can be grown with desirable T_P and MR properties. It has been observed that, the grain size scales with annealing temperature and annealing time interval. The film resistivity decreases with the elevation of annealing temperature and time which can be correlated to the increasing orientation, alignment and size of the grains.

5.2 Structural, morphological, transport and magnetotransport studies

In this section, the results obtained from the studies on structural, morphological, electronic and magnetotransport properties of $La_{0.7}R_{0.3}MnO_3$ (LRMO) (R = Ca, Sr, Ba) i.e. $La_{0.7}Ca_{0.3}MnO_3$ (LCMO), $La_{0.7}Sr_{0.3}MnO_3$ (LSMO) and $La_{0.7}Ba_{0.3}MnO_3$ (LBMO) manganite thin films have been given in detail. Various LRMO manganite thin films were deposited on LAO *(h00)* single crystal substrates using CSD route as described in section 5.1. Deposition of thin films using automated spin coater was then followed by heating and annealing at 1000°C in an oxygen environment for 12h.

All the LRMO films possess film thickness ~ 1500Å, determined using DESJECT thickness profilometer. The structural and microstructural properties of LRMO films were studied by XRD and AFM measurements. Using d.c. four probe resistivity technique, the electrical resistivity of all the films was measured i) as a function of temperature in the range of 5-385K in zero field and in an applied field of 9T and ii) as a function of magnetic field (up to 9 Tesla) at various temperatures [PPMS, Quantum Design] at TIFR, Mumbai.

Note: In Sections 5.2 and 5.3, the results on XRD, AFM, ρ - T and MR measurements on LSMO/LAO film annealed at 1000°C (12h), already given in section 5.1, are given again in order to complete the comparative study on LRMO (R = Ca, Sr and Ba) films, grown by PLD and CSD routes.

5.2.1 XRD studies

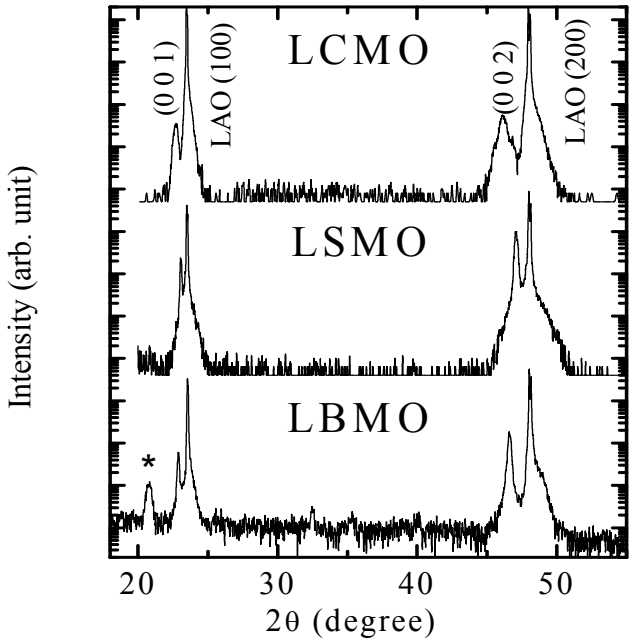

Figure 5.11: XRD patterns for $La_{0.7}R_{0.3}MnO_3$ (LRMO) (R = Ca, Sr and Ba) films on LAO (*h00*) single crystal substrate. The asterisk (*) denotes BaO impurity phase.

The indexed XRD patterns of LRMO (R = Ca, Sr, Ba) thin films on LAO (*h00*) single crystal substrates are shown in fig.5.11. All the LRMO films are epitaxially c-axis (*00l*) oriented and crystallizing as single-phase bulk LCMO, LSMO and LBMO. The cubic lattice parameters for LCMO, LSMO and LBMO films are found to be ~3.8597(3)Å, 3.8779(2)Å and 3.9091(3)Å respectively. A small amount (of ~4-5%) of BaO secondary phase has been detected in LBMO film which is marked by an asterisk in fig.5.11. The calculated values of compressive strain into the films due to the lattice mismatch (δ) between the LRMO films and LAO single crystal substrate are -3.34%, -1.89% and -2.88% for LCMO, LSMO and LBMO films respectively. It can be seen from these values of lattice mismatch that LCMO/LAO film is more strained as compared to LSMO and LBMO films.

5.2.2 AFM studies

The surface morphologies of the nanostructured LRMO thin films have been studied using AFM micrographs. Figure 5.12. shows the topographic images of LCMO,

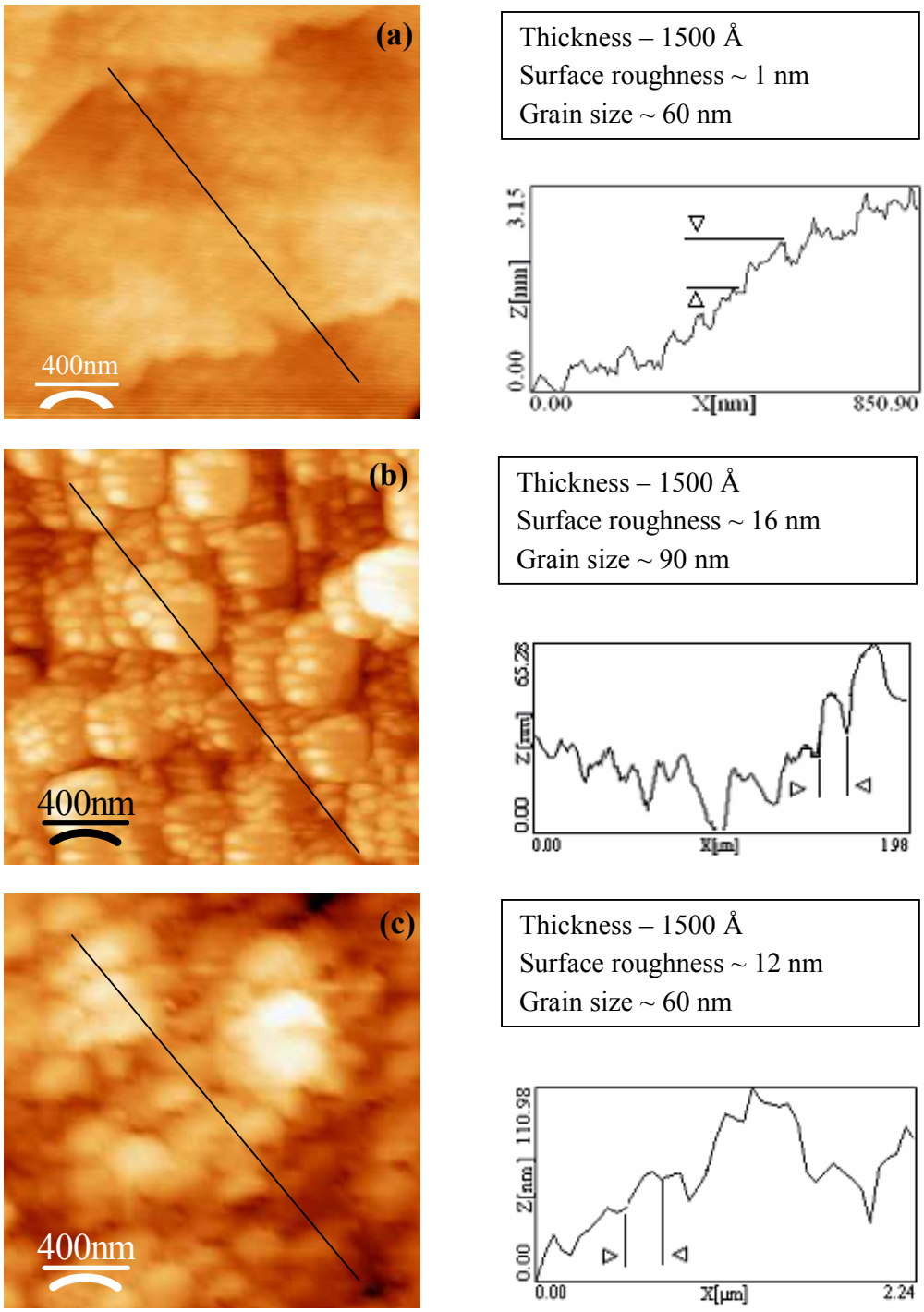

Figure 5.12: 2µm x 2µm AFM images of $La_{0.7}R_{0.3}MnO_3$ (LRMO) (R = Ca, Sr and Ba) films (a) LCMO, (b) LSMO and (c) LBMO with their respective surface roughness histogram. The two arrowheads define an atomic step.

LSMO and LBMO films respectively. The microstructure of LCMO film shows the step like grain growth which is characteristic of a highly oriented film where the strain is uniformly distributed over the film surface, while the LSMO and LBMO films show the island mode of grain growth. The line scan across the image is height vs. distance profile shown on the right side of fig.5.12. The estimated step heights are ~1.2nm, 15nm and 21nm for LCMO, LSMO and LBMO films respectively. The surface roughness analysis has been made using mean square average of these steps and the estimated values of surface roughness are ~1nm, 16nm and 12nm for LCMO, LSMO and LBMO films respectively. The grain size varies from 60 - 90nm in LRMO films.

5.2.3 Resistivity and MR studies

The temperature dependence of resistivity has been plotted for all the LRMO/LAO films grown by CSD method from 385K to 10K under 0 and 9T fields in fig.5.13. In zero applied field, the resistivity values at 10K [ρ_{10K}] and at T_P [ρ_P] are 0.32 mΩcm and 60 mΩcm (T_P ~ 248K) for LCMO , 1.5 mΩcm and 12.5 mΩcm (T_P ~ 362K) for LSMO and 31 mΩcm and 110 mΩcm (T_P ~ 330K) for LBMO respectively. It is interesting to note that, for the CSD grown LRMO films, values of resistivity and T_P are in good agreement with those reported for LRMO films prepared using PLD [20]. Further, sharpness in the electronic transition implies the absence of grain boundary contribution at low temperatures in LRMO films.

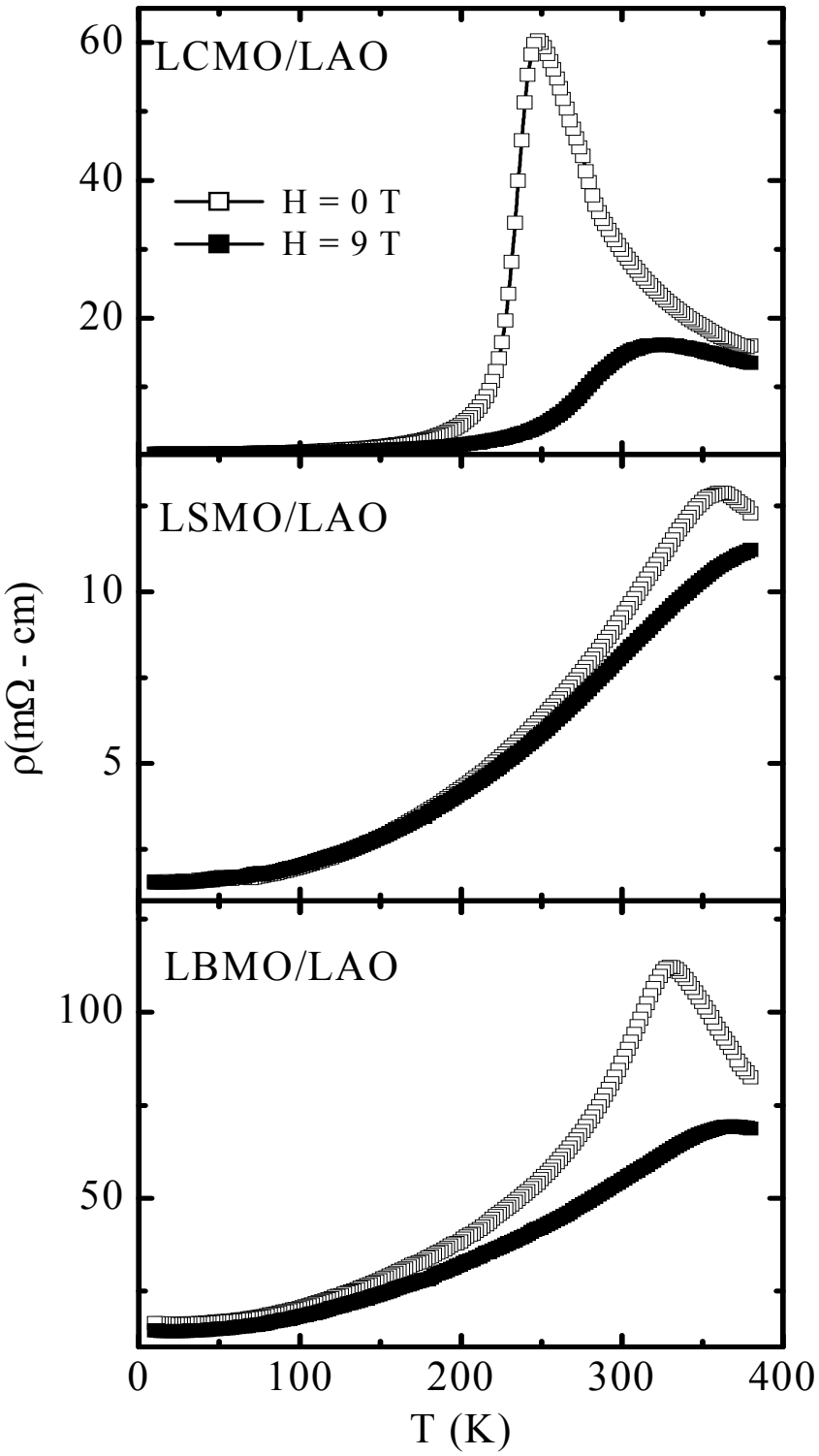

Figure 5.13: ρ – T plots for $La_{0.7}R_{0.3}MnO_3$ (LRMO) (R=Ca, Sr and Ba) films in H = 0 and 9T fields.

Magnetoresistance

The field dependence of MR measured at various temperatures (10-330K) for LRMO/LAO films is plotted in fig.5.14. All the LRMO films exhibit maximum MR in the vicinity of T_P and MR decreases with decrease in temperature. It is now well established fact that, in manganites, MR effect originates due to the two different kinds of reasons. Firstly, at very low temperature, LFMR effect mainly arises due to the spin dependent scattering process at insulating grain boundaries [16,18] while HFMR is associated with the increased connectivity between the grains owing to the reorientation of disordered spins at interface at high fields and reduction in pinning of Mn ions at grain surface [16,19]. Secondly, at T_P, CMR effect is ascribed to the field induced suppression in spin disorder at Mn-O-Mn coupling [16]. The low temperature MR behavior of CSD made LRMO films appears to be more interesting. At 10K, LCMO and LSMO films show almost negligible LFMR and HFMR, while LBMO film exhibits LFMR and HFMR ~ 5% and ~15% respectively. However, no steep rise in LFMR behavior has been observed at 10K with temperature clearly suggesting the absence of low temperature grain boundary effect in these highly epitaxial LRMO films. At intermediate temperatures (100-240K), the low field and high field MR increases progressively with applied fields and temperatures. The MR saturates and becomes maximum at T_P which is common behavior for all LRMO films.

Around T_P, the subsequent values of maximum LFMR and HFMR are ~ 50% and ~90% for LCMO (at 240K) and 5% and 47% for LBMO (at 330K) respectively, while near around RT (at 330K) LSMO exhibits MR ~5% and 27% corresponding to LFMR and HFMR values. The observed appreciable rise in MR at T_P in all the LRMO films may be attributed to the field induced delocalization of charge carriers due to the structural disorder at grain boundaries and at Mn-O-Mn bond angles [16].

Further, it has been observed from the resistivity and MR studies on LRMO films [Fig. 5.13 and 5.14] that, MR decreases while T_P enhances as R changes from Ca to Sr. The reduction in MR along with T_P enhancement can be ascribed to the increase in average A-site cationic radius, $<r_A>$, from Ca to Sr, which increases the Mn-O-Mn bond angle towards the 180º which in turn improves the matrix element responsible for

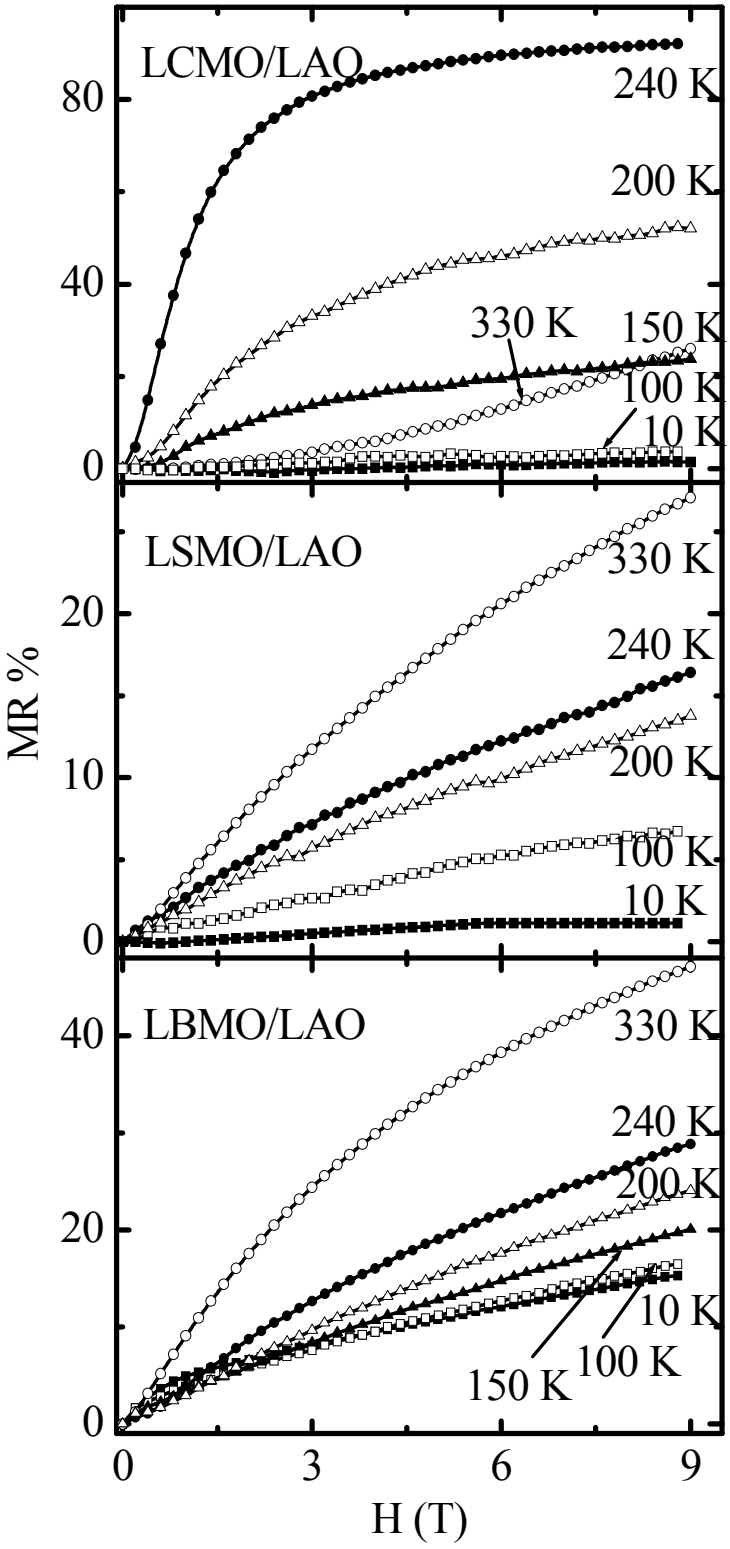

Figure 5.14: MR vs. H isotherms for $La_{0.7}R_{0.3}MnO_3$ (LRMO) (R=Ca, Sr and Ba) films.

electronic transport and T_P and hence large drop in MR [21]. Further increase in $<r_A>$ in LBMO films exerts a strain in the lattice which affects the Mn-O hybridization causing slight reduction in T_P and consequent enhancement in MR [21,22].

5.2.4 I-V studies

To understand the mechanism of electronic charge transport in LRMO thin films, current-voltage (I-V) characteristics at zero external field and at various temperatures in (82-300K) were determined by applying dc current and measuring the voltage developed in a four point contact geometry [23]. Figure 5.15 (a) shows applied current (I) vs. voltage (V) plots for LRMO films measured in current-in-plane (CIP) geometry. The maximum current applied to the film was 1mA. I-V measurements show similar behavior for forward and reverse applied current and hence I-V characteristics for positive bias current have been only displayed in fig.5.15(a). I-V behavior is slightly nonohmic in LBMO film which can be best fitted in power law of the form $I \propto V^{\alpha}$, where $\alpha = 1 - 2$ is temperature and field dependent parameter [24]. Nonlinearity increases slightly with temperature which is depicted from the fits with α - values increasing marginally from 1.005 to 1.142 for LCMO; 1.02 to 1.1 for LSMO and 1.002 to 1.4 for LBMO film from 82K to RT respectively. The nonlinear I-V behavior has its origin in electron tunneling process across the amorphous insulating grain interfaces [25].

To elucidate the effect of temperature, differential conductance (dI/dV) were calculated for LRMO films and plotted against the voltage (V) at various temperatures (82-300K) in fig.5.15(b). The parabolic nature of conductance versus voltage is the characteristic feature of electron tunneling process and has significant effect of temperature, which modifies its shape and slope. It can be seen from the plots that, conductance increases with applied voltages for all the temperatures which is attributed to the electron tunneling process suggested by Simmons model described as,

$$G(dI/dV) = a + bV^{n},$$

where a is the zero bias conductance, b is the co-efficient which is the function of potential barrier and n is the constant whose value predict the kind of electrical transport mechanism presents [25-27].

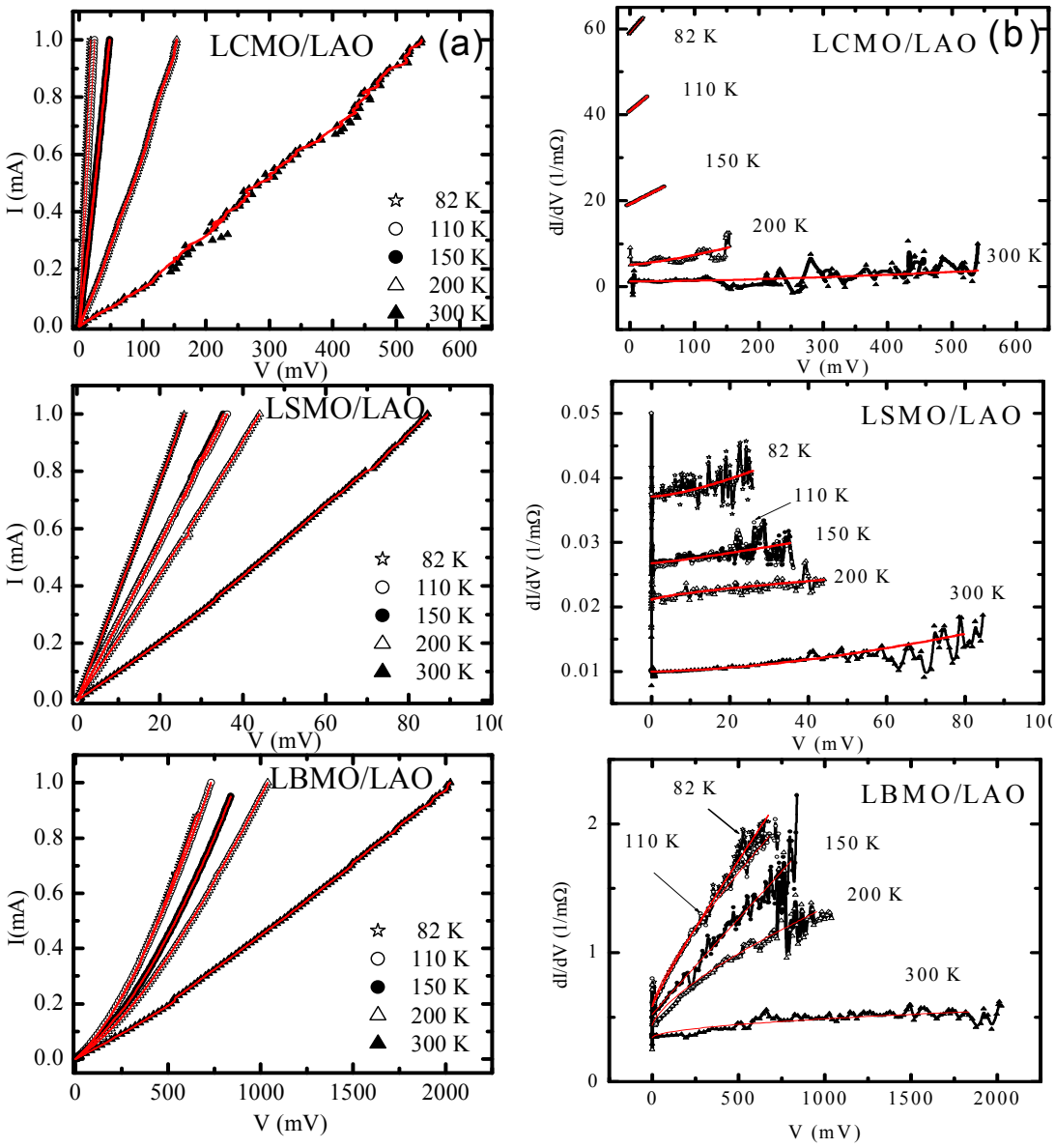

Figure 5.15: (a) Current vs. Voltage characteristics and (b) dI/dV vs. Voltage plots at various temperatures (82-300K) for $La_{0.7}R_{0.3}MnO_3$ (LRMO) (R=Ca, Sr and Ba) films. Solid lines show the fittings of I-V and conductance.

Table 5.3 summarizes the obtained values of fitting parameters. Based on the values of n, available from the reports, the possible tunneling mechanisms are: i) $n \geq 0.6$, indicates tunneling through disordered metallic oxide type; ii) n~1, quasiparticle tunneling via pairs of localized states; iii) $n > 1$, suggests spin-flip scattering at the grain boundary

Table 5.3: Various fitting parameters of Simmons model fits to the equation $G(dI/dV) = a + bV^n$,

.	Temperature (K)	a $(m\Omega)^{-1}$	b $(V\text{-}\Omega)^{-1}$	n
LCMO	82	57.248	372.587	1.10171
	110	41.598	221.123	1.11739
	150	19.084	192.258	1.25751
	200	5.6777	47.5646	1.31539
	300	1.2125	66.7892	1.5964
LSMO	82	0.0211	216.92	0.70339
	110	0.0268	46.36	1.18047
	150	0.0277	44.36	1.4509
	200	0.0371	35.73	1.65202
	300	0.00998	4.18	1.67102
LBMO	82	0.585	211.512	0.9070
	110	0.481	178.237	0.7968
	150	0.518	147.138	0.981
	200	0.415	91.305	0.768
	300	0.351	14.671	0.52

dominated and iv) $n \sim 2$, predicts the direct tunneling of charge carriers [28-30]. The values of $n > 1$ [from Table 5.3] implies the presence of spin flip scattering at the grain boundaries in presently studied CSD deposited LCMO and LSMO films whereas $n < 1$ suggests the tunneling through disorder grain interface for LBMO film.

In summary, the high quality LRMO manganite thin films were deposited using low cost and simple chemical route. The structural and microstructural properties revealed the epitaxial growth of the film along the c-direction having clear grain morphology and orientation. The peak resistivity and T_P values of the CSD grown LRMO films were equivalent to those of the PLD made thin films and have the same MR as the PLD grown films over the entire temperature range from 10 to 330K. MR and I-V studies indicate the dominant electronic transport in metallic regime via the spin flip scattering in LCMO and LSMO films and tunneling through disorder metallic interfaces in LBMO film.

5.3 Effect of SHI irradiation on LRMO manganite thin films

Swift Heavy Ion (SHI) irradiation is an efficient tool for creation of point defects, vacancies, columnar defects and localized strain in various materials (mainly thin films) which in turn affect their crystallographic, surface and physical properties [31-33]. SHI irradiation on manganite thin films mostly leads to detrimental effects on structural and transport properties. For instance, the irradiation results in enhancement of resistivity, suppression of T_p and MR, etc [31,34]. Though the deteriorated properties of the irradiated films have adverse effect with respect to their applications as data storage devices, there is an improvement in the application potential of such films in uncooled bolometers, magnetic field sensors, etc. [35]. However, till date, all the endeavors to control the physical properties of manganites by irradiation have been made on the thin films synthesized using either Pulsed Laser Deposition (PLD) or other physical methods. There have been no attempts to study the irradiation effects in manganite films synthesized by chemical methods. In this context, the results obtained from the studies on the effect of SHI irradiation on physical properties of $La_{0.7}R_{0.3}MnO_3$ (LRMO; R = Ca, Sr and Ba) thin films prepared using CSD route, have been presented.

Highly energetic charged particles while traversing through matter losses their energy mainly by two ways, first, the electronic energy loss [$(S_e)= dE_e/dx$] which is the inelastic collisions of charged particles with atomic electrons of the material while the second is nuclear energy loss [$(S_n)= dE_n/dx$] which is the elastic scattering of the charged particles from the atomic nuclei. For the high energetic charge (~ MeV), electronic energy loss is dominated. The values of electronic and nuclear energy loss, calculated using Stopping Range of Ion in Matter (SRIM) 2003 programme [36], for the presently studied LRMO films are ~12 keV/nm and ~33.6 eV/nm for LCMO, ~13.4 keV/nm and 37 eV/nm for LSMO and 13.2 keV/nm and 36.4 eV/nm for LBMO respectively. The projected range of SHI energetic ions in LRMO films is ~ 1μm which implies that almost all ions pass through the film thickness and hence the observed irradiation effects are to be analyzed as consequence of ion induced electronic energy transfer. The reported electronic energy threshold, calculated using Szenes thermal spike model, for LCMO is ~6.6 keV/nm [37] which is far lower than electronic energy loss (S_e) calculated for LRMO films studied, implying the possibilities of columnar like defects formation in these films. The selection

of highly energetic 200 MeV Ag^{+15} ions has been made in the present irradiation studies, since these ions can easily pass through the entire thickness of the thin film due to their higher mass resulting into creation of columnar tracks before striking the substrate. This results in a uniform distribution of strain in the film which is not the case with low energy ion implantation [34].

SHI irradiation was performed at Inter University Accelerator Centre (IUAC), New Delhi, India, using a 15 UD tandem accelerator using 200 MeV Ag^{+15} ion beam [38] with a beam current ~ 0.3 pnA [39] and in ion doses of 7.5×10^{10} and 1×10^{12} ions/cm^2. The irradiations were performed at an angle of 5°±1° away from the *c* axis to avoid channeling. The ion beam was focused on to a spot of 1mm×1mm and scanned over an area of 10mm×10mm using magnetic scanner to achieve dose uniformity across the sample area which was typically 2.5mm×2.5mm. The structural and microstructural properties of irradiated LRMO thin films were studied by XRD and AFM measurements. Using d.c. four probe resistivity technique, the electrical resistivity of all the films was measured i) as a function of temperature in the range of 5-385 K in zero-field and in an applied field of 9 T and ii) as a function of magnetic field (up to 9 Tesla) at various temperatures [PPMS, Quantum Design].

5.3.1 Structural studies

XRD studies

Typical indexed XRD patterns of pristine and irradiated LRMO films (R = Ca, Sr and Ba) on LAO (*h00*) single crystal substrates have been shown in figs.5.16 (a), (b) and (c). All the LRMO films are epitaxially c-axis (*00l*) oriented and are indexed using respective bulk cell parameters of LCMO, LSMO and LBMO. The values of FWHM for (*002*) peak, δ-mismatch and cubic lattice parameters obtained from XRD analysis of pristine and irradiated LRMO films are given in Table 5.4. It can be seen from fig.5.16 and Table 5.4 that, for LCMO and LSMO films, the intensity of the diffraction peaks decreases and the values of FWHM and δ increase monotonically with irradiation dose while exactly opposite trend is observed in LBMO films. For instance, the FWHM of (*002*) peak of the LCMO and LSMO increases from 0.534° and 0.121° for pristine to 0.677° and 0.396° for 1 x 10^{12} ions/cm^2 irradiated film,

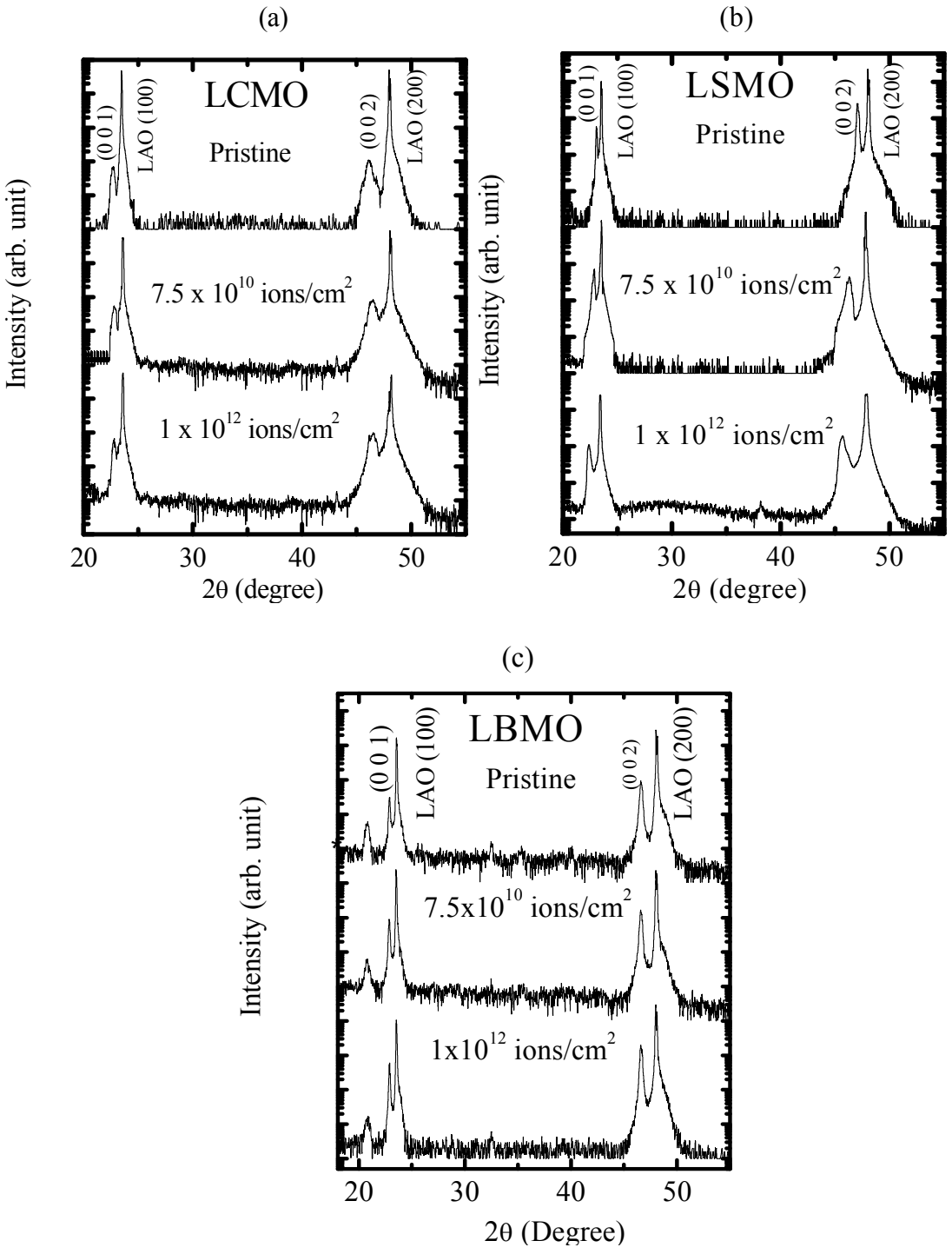

Figure 5.16: XRD patterns for pristine and irradiated $La_{0.7}R_{0.3}MnO_3$ (LRMO) (R = Ca, Sr and Ba (a) LCMO/LAO (b) LSMO/LAO and (c) LBMO/LAO films. The asterisk (*) denotes BaO impurity phase.

Table 5.4: Values of FWHM, lattice mismatch (δ%) and cubic cell parameter for pristine and irradiated LRMO/LAO thin films.

Sample		FWHM (*002*)	Mismatch (δ%)	Cubic lattice parameter (Å)
LCMO	Pristine	0.534º	-3.34	3.8597(3)
	$7.5x10^{10}$ ions/cm^2	0.660º	-3.36	3.8607(3)
	$1x10^{12}$ ions/cm^2	0.677º	-3.57	3.8629(3)
LSMO	Pristine	0.121º	-1.89	3.8779(2)
	$7.5x10^{10}$ ions/cm^2	0.392º	-2.93	3.8819(2)
	$1x10^{12}$ ions/cm^2	0.396º	-4.50	3.8859(2)
LBMO	Pristine	0.224°	-2.88	3.9091(3)
	$7.5x10^{10}$ ions/cm^2	0.212°	-2.8	3.9051(3)
	$1x10^{12}$ ions/cm^2	0.205°	-2.7	3.9140(3)

while its intensity decreases (by factor of 10 in case of LSMO) as compared to that of the pristine and film irradiated with 1 x 10^{12} ions/cm^2. Interestingly, the FWHM of (*002*) peak of the LBMO film decreases from 0.224º for pristine to 0.205º for 1×10^{12} ion/cm^2 irradiated film with subsequent increase in its peak intensity. The substrate-material mismatch (δ) values are found to increase on irradiation from -3.34% for pristine to -3.36% for 7.5 x 10^{10} ions/cm^2 and -3.57% for 1 x 10^{12} ions/cm^2 irradiated LCMO films while -1.89% for pristine to -2.93% and -4.5% for 7.5 x 10^{10} ions/cm^2 and 1 x 10^{12} ions/cm^2 dose irradiated LSMO films. In contrary to this, for LBMO films, the mismatch, δ, decreases from -2.88% for pristine to -2.8% and 2.7% for the films irradiated with irradiation dose of 7.5 x 10^{10} ions/cm^2 and 1 x 10^{12} ions/cm^2 respectively. The observed variation in the calculated cubic lattice parameters with irradiation has been listed in Table 5.4 for all the LRMO films. The significant enhancement in peak intensity and reduction in FWHM and δ mismatch, clearly suggest the irradiation induced improvement in crystalline order of the LBMO films whereas the crystallinity is adversely affected by the irradiation in LCMO and LSMO films.

Surface morphology

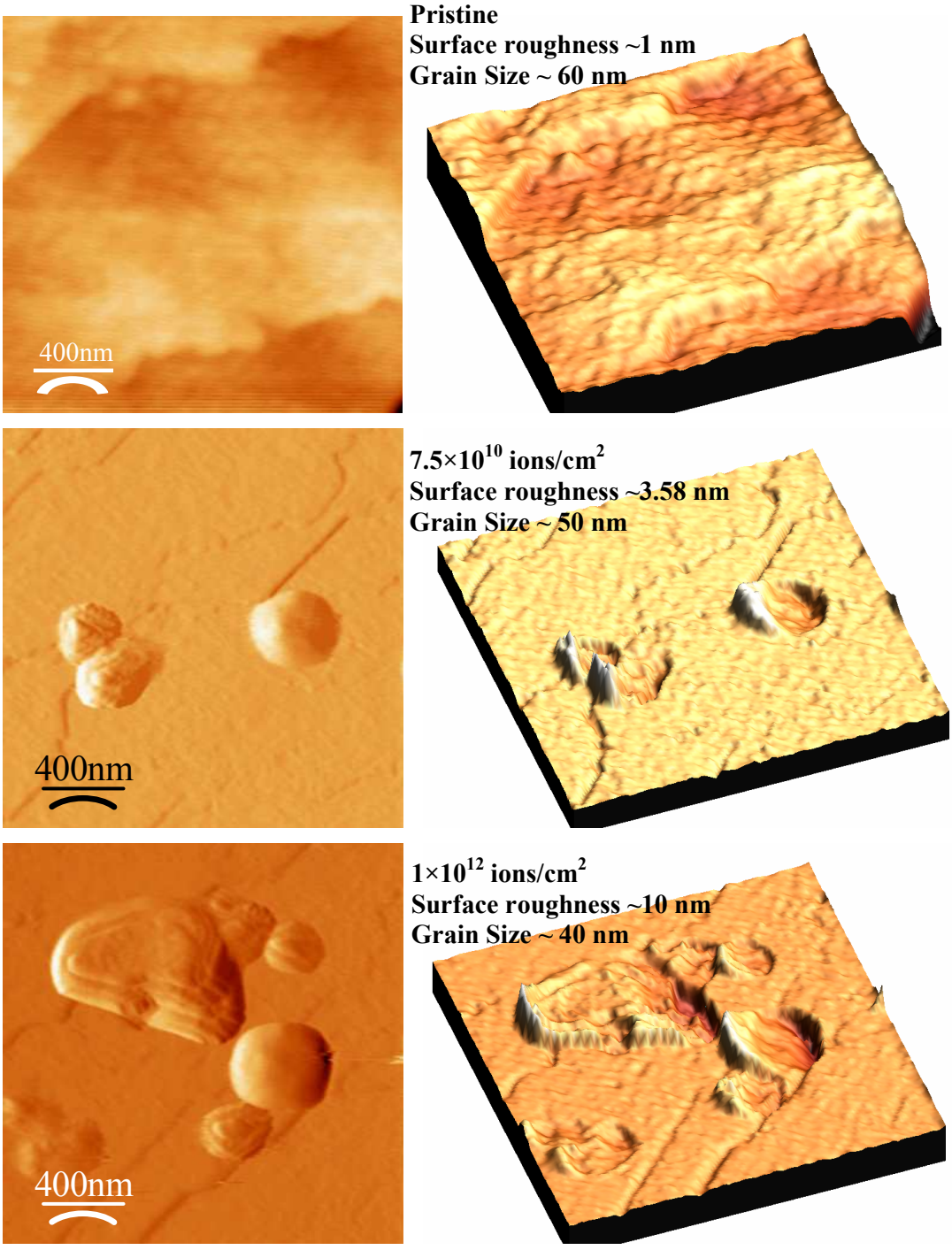

Figure 5.17(a): 2μ x 2μ AFM images of pristine (top), 7.5×10^{10} ions/cm^2 irradiated (middle) and 1×10^{12} ions/cm^2 irradiated (bottom) LCMO/LAO films with their respective 3D view.

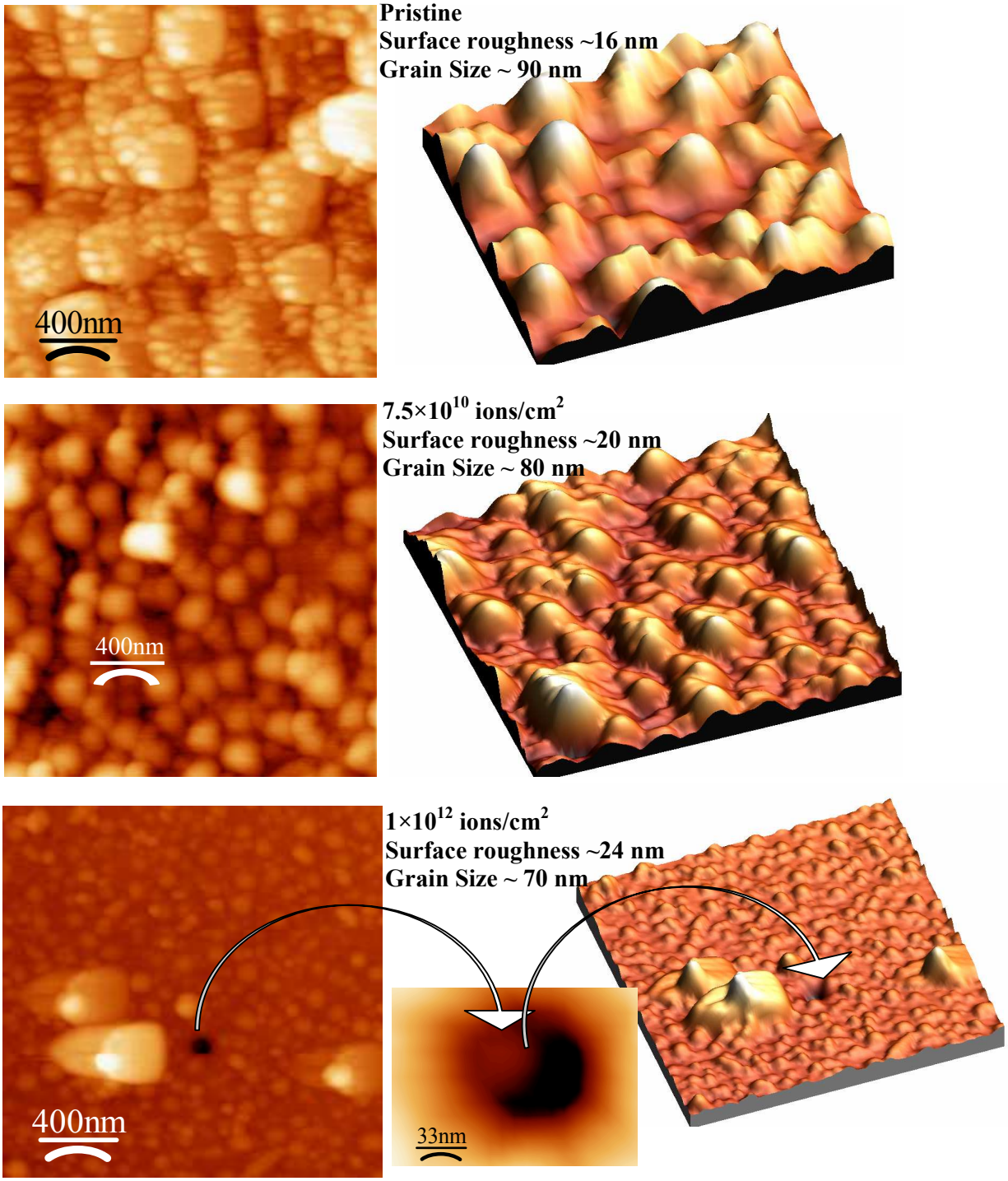

Figure 5.17(b): 2μ x 2μ AFM images of pristine (top), 7.5×10^{10} ions/cm^2 irradiated (middle) and 1×10^{12} ions/cm^2 irradiated (bottom) LSMO/LAO films with their respective 3D view.

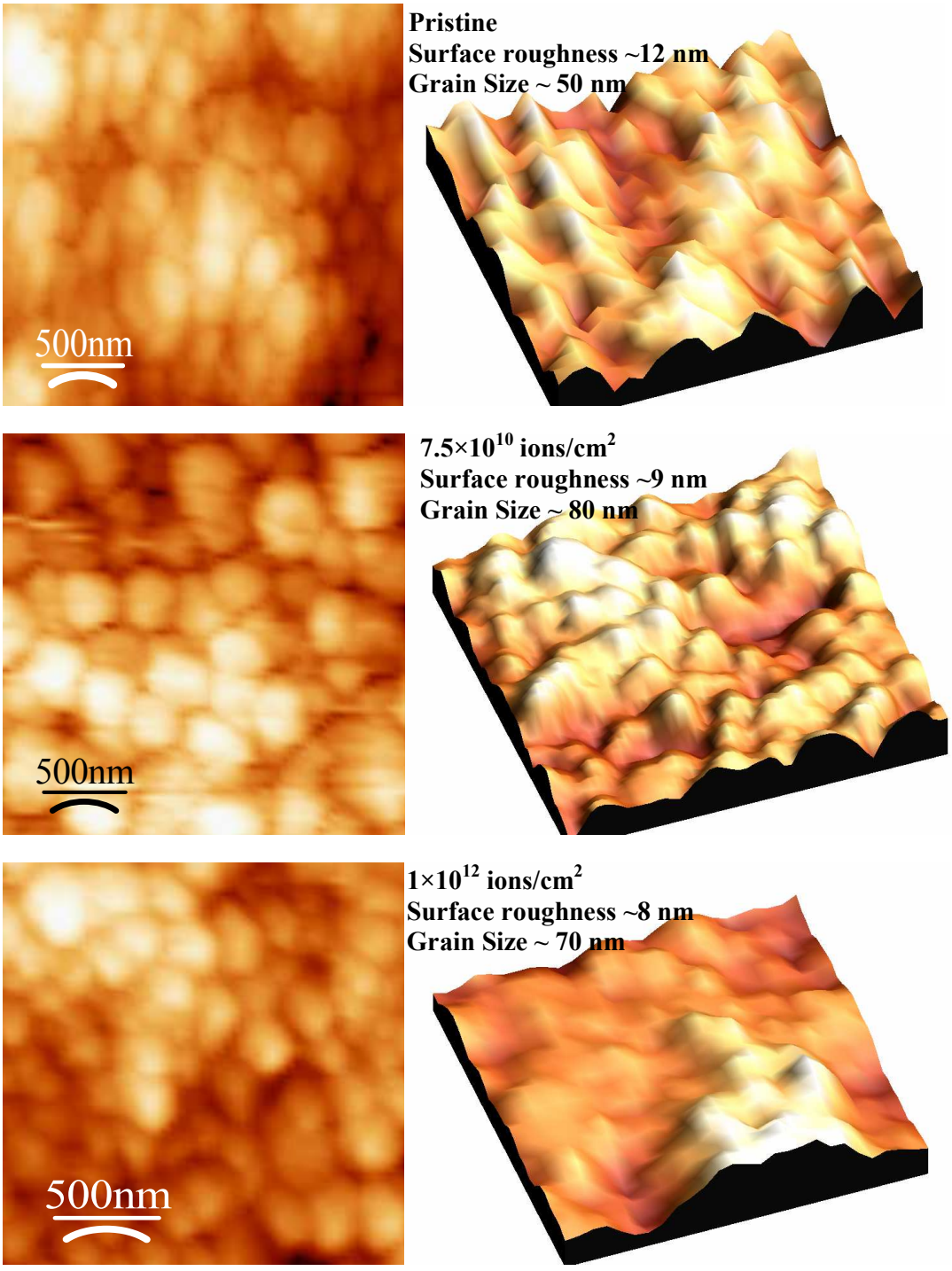

Figure 5.17(c): 2μ x 2μ AFM images of pristine (top), 7.5×10^{10} ions/cm^2 irradiated (middle) and 1×10^{12} ions/cm^2 irradiated (bottom) LBMO/LAO films with their respective 3D views.

Surface morphologies of various LRMO/LAO pristine and irradiated films studied using AFM are shown in figs.5.17(a), (b) and (c). It can be seen from the fig.5.17(a) and (b) that, irradiation with 200 MeV Ag^{+15} ions has adverse effect on the microstructure of the LCMO and LSMO thin films, while in case of LBMO, there is an improvement in the microstructure of the films with ion dose [Fig. 5.17(c)].

The irradiation induced surface modifications in LCMO films can be apparently seen from fig.5.17(a). The surface roughness increases from 1nm for pristine to 3.58nm and 10nm for the films irradiated with respective ion dose of 7.5×10^{10} ions/cm^2 and 1×10^{12} ions/cm^2 while, the grain size decreases to 50nm for 7.5×10^{10} ions/cm^2 and 40nm for 1×10^{12} ions/cm^2 from their pristine value of 60nm. Also, at some portions, surface swelling is observed in irradiated LCMO films which may be presumably due to the subsurface clustering of point defects created because of irradiation. This effect becomes more prominent with irradiation dose [40].

The AFM images for the pristine and irradiated LSMO films shown in fig.5.17(b) that, demonstrate the deterioration in surface morphology and grain structure due to the irradiation with 7.5×10^{10} and 1×10^{12} ions/cm^2. The observed surface roughness for the pristine film is ~16nm which becomes ~20nm for 7.5×10^{10} ion/cm^2 and ~24nm for 1×10^{12} ion/cm^2 irradiated films. The values of average grain size obtained from AFM pictures are 90nm, 80nm and 70nm for the pristine and 7.5×10^{10} and 1×10^{12} ions/cm^2 irradiated films, respectively. In case of LSMO film, irradiated with maximum ion dose of $1x10^{12}$ ios/cm^2, columnar defect formation having average radius ~ 5±0.5 nm. The arrow indicates the magnified portion of that column area [Fig. 5.17(b)].

The microstructures of pristine and irradiated LBMO films are shown in fig.5.17(c). Interestingly, in the LBMO films, the value of average grain size increases and surface roughness decreases with successive irradiation which is evident from fig.5.17(c). The observed surface roughness for the pristine film is ~12nm which reduces to 9nm for 7.5×10^{10} ion/cm^2 and 8nm for 1×10^{12} ion/cm^2 irradiated films. The values of average grain size obtained from AFM pictures are 50nm, 80nm and 70nm for the pristine film and for 7.5×10^{10} and 1×10^{12} ions/cm^2 irradiated films, respectively.

Apart from a moderate reduction in surface roughness which points towards better orientation, an enhancement in grain size with increasing irradiation in LBMO films, suggests a dominant possibility of conglomeration of two or more grains to form a bigger size grain. This would result in a decreased grain boundary region and, consequently, an improved electronic transport at the grain boundaries which accounts for irradiation induced reduction of resistivity in CSD grown LBMO thin films. While in LCMO and LSMO films, reduction of grain size and enhanced surface roughness along with the irradiation induced defects, surface swelling in LCMO and columnar defects in LSMO, would introduce the electronic and magnetic anisotropies which in turn leads to the considerable increment in resistivity and decrement in T_P and MR in these films after the irradiation [31,32,40].

5.3.2 Resistivity and magnetoresistance measurements

RT and Magneto RT

The $\rho - T$ measurements on pristine and irradiated LRMO thin films have been carried out in 0 and 9T field and are plotted in fig.5.18. The resistivity of LCMO and LSMO films is found to increase appreciably on irradiation as compared to their pristine counterparts with a concomitant suppression in T_P with increasing irradiation dose which is consistent with the reports available on irradiation studies of PLD grown manganite thin films [31-34]. In LCMO films, in zero applied field, peak resistivity (ρ_P) increases ~3 times and ~ 4 times at 10K for maximum irradiation dose of 1 x 10^{12} ions/cm^2, whereas in LSMO films, peak resistivity (ρ_P) increases ~ 10 times and ~ 20 times at 10K for maximum irradiation dose of 1 x 10^{12} ions/cm^2 [Table 5.5]. Also, it can be noted that, the sharp resistivity drop observed at T_P in pristine LSMO film disappears in successively irradiated LSMO films. The irradiated LSMO films exhibit broad maxima in ρ-T curves around the T_P as well as at very low temperatures ≤ 50K.

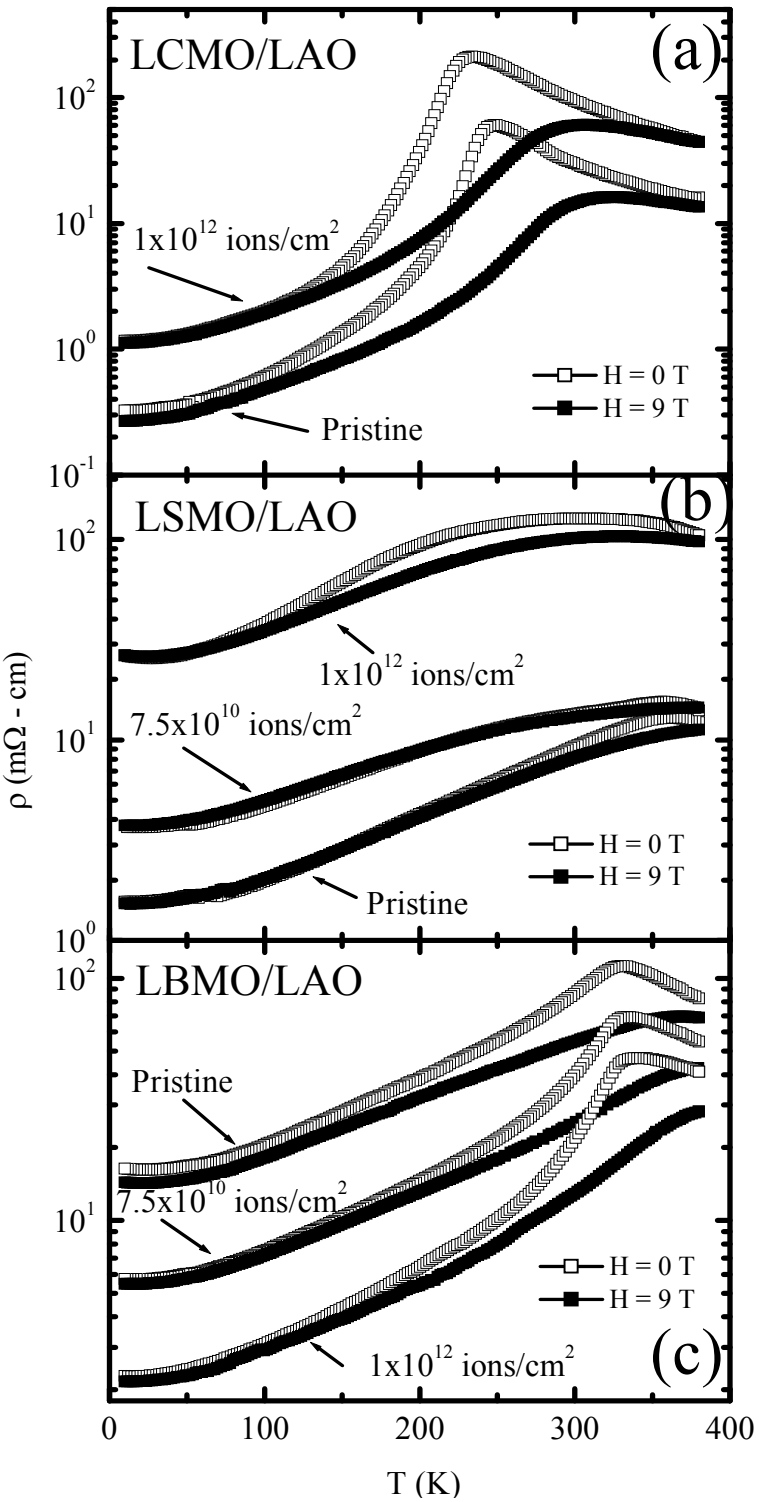

Figure 5.18: ρ – T plots for pristine and irradiated $La_{0.7}R_{0.3}MnO_3$ (LRMO) (R = Ca, Sr and Ba) (a) LCMO/LAO (b) LSMO/LAO and (c) LBMO/LAO films.

Table 5.5: Values of resistivity at 10K [ρ_{10K}], peak resistivity [ρ_P] and T_P for pristine and 7.5 x 10^{10} ions/cm^2 and 1 x 10^{12} ions/cm^2 irradiated LRMO/LAO thin films.

Sample		ρ_{10K} (mΩcm)	ρ_P (mΩcm)	T_P (K)
LCMO	Pristine	0.32	60	248
	1 x 10^{12} ions/cm^2	1.2	200	228
LSMO	Pristine	1.5	12.5	362
	7.5 x 10^{10} ions/cm^2	3.7	15	350
	1 x 10^{12} ions/cm^2	30	125	300
LBMO	Pristine	31	110	330
	7.5 x 10^{10} ions/cm^2	15	55	333
	1 x 10^{12} ions/cm^2	0.3	36	337

Interestingly, in the LBMO films, irradiation induces a significantly consistent suppression in resistivity over the whole temperature range investigated. For instance, the resistivity decreases by a factor of 2 and 4, respectively, at 330K and 10K with an ion dose of 7.5×10^{10} ions/cm^2, while it decreases by a factor of 3 and 10, respectively, at 330K and 10K with an ion dose of 1×10^{12} ions/cm^2 [Table 5.5]. Also, it is interesting to note that, for the LBMO case, with increasing irradiation, T_P remains nearly unaffected as it shifts slightly from 330K for pristine to 337K for 1×10^{12} ions/cm^2 irradiated film. This kind of irradiation induced suppression of resistivity, with T_P remaining unaffected in CSD grown LBMO films, is a unique observation vis-à-vis the irradiation induced enhancement of resistivity and suppression of T_P in LCMO and LSMO thin films grown using either PLD or CSD methods.

Magnetoresistance

To understand magnetotransport behavior of various pristine and irradiated LRMO films, MR vs. H isotherms have been plotted at various temperatures and are shown in figs.5.19(a), (b) and (c). All the films exhibit maximum MR in the vicinity of T_P which decreases with temperature [Fig.5.19]. The temperature dependence of MR behavior of all the films is discussed in the following paragraphs.

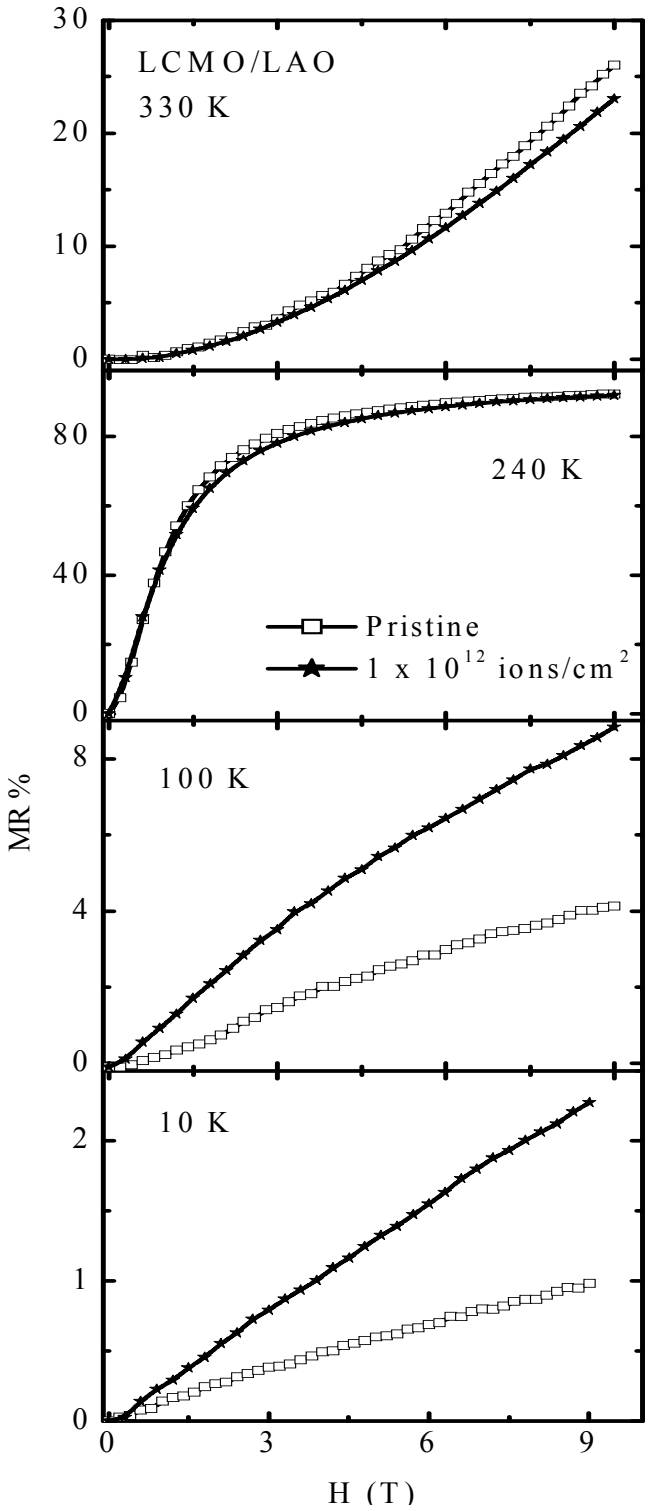

Figure 5.19(a): MR vs. H isotherms for pristine and 1×10^{12} ions/cm^2 irradiated LCMO/LAO films

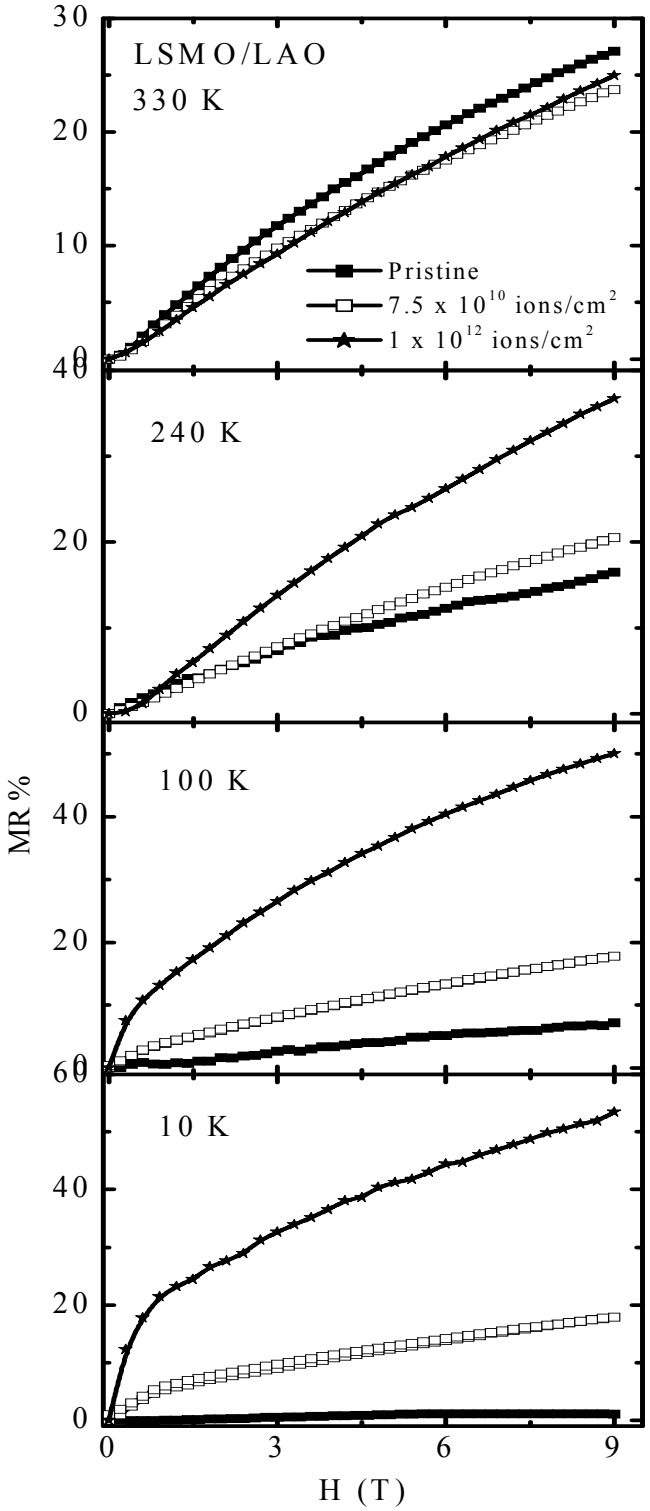

Figure 5.19(b): MR vs. H isotherms for pristine and 7.5 x 10^{10} ions/cm^2 irradiated and 1×10^{12} ions/cm^2 irradiated LSMO/LAO films.

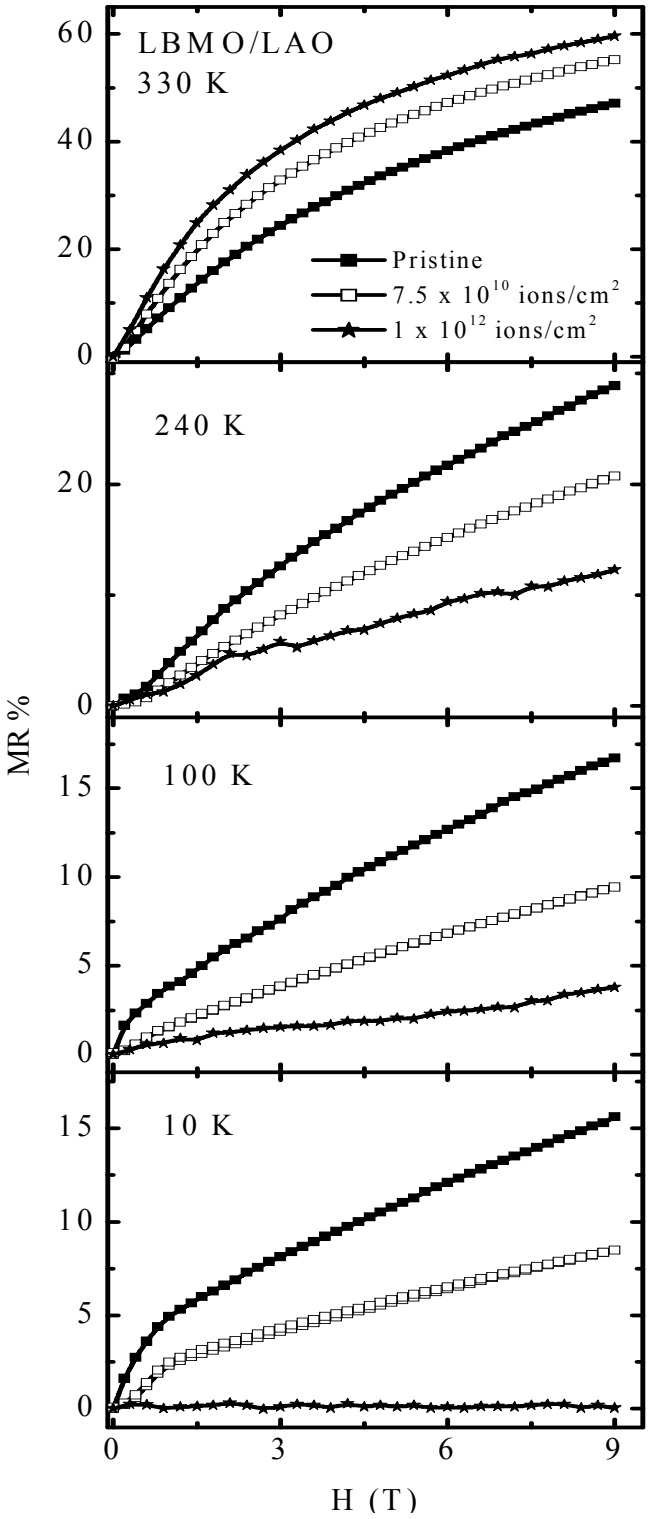

Figure 5.19(c): MR vs. H isotherms for pristine and 7.5 x 10^{10} ions/cm^2 irradiated and 1×10^{12} ions/cm^2 irradiated LBMO/LAO films.

Table 5.6: Values of LFMR and HFMR at different temperatures for pristine and 7.5 x 10^{10} ions/cm^2 and 1 x 10^{12} ions/cm^2 irradiated LRMO/LAO thin films.

		LCMO		
		Pristine		**1x10^{12} ions/cm^2**
10K	**LFMR (< 1T)**	Negligible		~ 0.4 %
	HFMR (~ 9T)	~ 1 %		~ 2.5%
100K	**LFMR (< 1T)**	~ 1 %		~ 2 %
	HFMR (~ 9T)	~ 4 %		~ 9 %
240K	**LFMR (< 1T)**	~ 50 %		~ 50 %
	HFMR (~ 9T)	~ 92 %		~ 92 %
330K	**LFMR (< 1T)**	Negligible		Negligible
	HFMR (~ 9T)	~ 26 %		~ 24 %
		LSMO		
		Pristine	**7.5x10^{10} ions/cm^2**	**1x10^{12} ions/cm^2**
10K	**LFMR (< 1T)**	Negligible	~ 8 %	~ 20 %
	HFMR (~ 9T)	Negligible	~ 18 %	~ 55 %
100K	**LFMR (< 1T)**	Negligible	~ 3 %	~ 13 %
	HFMR (~ 9T)	~ 8 %	~ 18 %	~ 50 %
240K	**LFMR (< 1T)**	~ 4 %	~ 4 %	~ 4 %
	HFMR (~ 9T)	~ 17 %	~ 20 %	~ 38 %
330K	**LFMR (< 1T)**	~ 4 %	~ 4 %	~ 4 %
	HFMR (~ 9T)	~ 26 %	~ 24 %	~ 25 %
		LBMO		
		Pristine	**7.5x10^{10} ions/cm^2**	**1x10^{12} ions/cm^2**
10K	**LFMR (< 1T)**	~ 5 %	~ 2-3 %	Negligible
	HFMR (~ 9T)	~ 15 %	~ 8 %	Negligible
100K	**LFMR (< 1T)**	~ 3 %	Negligible	Negligible
	HFMR (~ 9T)	~ 17 %	~ 10 %	~ 5 %
240K	**LFMR (< 1T)**	~ 3 %	Negligible	Negligible
	HFMR (~ 9T)	~ 30 %	~ 20 %	~ 10 %
330K	**LFMR (< 1T)**	~ 8 %	~ 12 %	~ 18 %
	HFMR (~ 9T)	~ 48 %	~ 55 %	~ 60 %

LCMO

At a low temperature (10K), the pristine LCMO film exhibits almost negligible LFMR (in a field of < 1T) and HFMR ~1%. The values of LFMR and HFMR for the 1 x 10^{12} ions/cm^2 ion irradiated LCMO film are ~0.4% and 2.5% respectively [Fig. 5.19(a), Table 5.6].

At intermediate temperature of 100K, the values of LFMR are 1% and 2% while HFMR 4% and 9% for pristine and 1 x 10^{12} ions/cm^2 irradiated LCMO films respectively [Table 5.6]. In irradiated LCMO films, an appreciable increase of LFMR and HFMR at low temperatures (up to 100K) can be attributed to the irradiation induced enhanced structural disorder, scattering centers, pinning of Mn spins at the grain surface and increased strain field which introduces electronic and magnetic field anisotropies. These implications further supported by the XRD data [increases of mismatch and suppression of peak intensity with irradiation (Fig.5.16 (a))] and AFM studies [reduction in grain size and increase in surface roughness with irradiation (Fig. 5.17 (a))].

At 240K (~T_P), LFMR and HFMR ~50% and 92% are exhibited by pristine and irradiated LCMO films which can be attributed to reduction in spin disorder at Mn-O-Mn bond angle due to applied field.

LSMO

The field dependence of MR in pristine and 7.5 x 10^{10} ions/cm^2 and 1 x 10^{12} ions/cm^2 ion irradiated LSMO thin films are plotted at different temperatures in fig.5.19(b). The observed MR behavior exhibited by pristine LSMO is similar to the one for high quality epitaxial films [17,20]. However, the MR vs. H behavior of the films irradiated with 7.5 x 10^{10} ions/cm^2 and 1 x 10^{12} ions/cm^2 shows completely different features at low temperatures (below 240K). In the temperature range 10-240K, the observed MR behavior of irradiated LSMO films is nearly independent of temperature.

At low temperature (10K), pristine LSMO film exhibits almost negligible LFMR and HFMR which becomes unusually large ~8% and 18% for the7.5 x 10^{10} ions/cm^2 and ~20% and 55% for 1 x 10^{12} ions/cm^2 ion irradiated films [Table 5.6]. The enhancement in HFMR seems to be more pronounced for the film irradiated with maximum irradiation dose of 1 x 10^{12} ions/cm^2.

At intermediate temperature of 100K, the values of LFMR and HFMR are negligible and 8% for pristine, 3% and 18% for 7.5 x 10^{10} ions/cm^2 and 13% and 50% for 1 x 10^{12} ions/cm^2 ion irradiated LSMO films respectively, while at 240K, these values of LFMR and HFMR become 4% and 17% for pristine, 4% and 20% for 7.5 x 10^{10} ions/cm^2 irradiated and 4% and 38% for 1 x 10^{12} ions/cm^2 irradiated film respectively [Table 5.6].

At 330K, the pristine film exhibits slightly higher HFMR ~26% as compared to irradiated LSMO films and there is no effect irradiation dose on the MR behavior [Table 5.6].

To understand the observed unusual low temperature MR behavior of irradiated CSD grown LSMO films, it is necessary to account for the effect of swift heavy ions interaction with material. When 200 MeV Ag^{+15} ions pass through the LSMO films, calculated electronic and nuclear energy losses ~13.4 keV/nm (S_e) and 37 eV/nm (S_n) respectively, suggests that, the entire process is dominated by the electronic energy loss. It is reported that, for the creation of continuous amorphous columnar tracks in the material, the required energy threshold is ~6.7 keV/nm which is much lower than the observed S_e. This is evident from the observed modifications in the surface morphologies of irradiated LSMO films [Fig 5.17 (b)]. Within the regions of defect formed on irradiation, the behavior of material is highly chaotic and the physical properties within these regions are entirely different from those of the pristine. The possible reason for the enhancement of MR at low temperatures (18% for 7.5 x 10^{10} and 55% for 1 x 10^{12} ions/cm^2 irradiated films) may be the strain field developed by the lattice distortions at the peripheries of the individual columnar defects. This inference is supported by the appreciable decrease in intensity of XRD peaks and the significant enhancement in lattice mismatch for the irradiated films [Fig.5.16(b), Table 5.4]. The increase in strain field created on irradiation affects the Mn-O hybridization which in turn is responsible for the charge localization at low temperatures.

LBMO

Figure 1.19(c) shows the MR vs. H isotherms for pristine and irradiated LBMO thin films which can be understood as follows,

At a low temperature of 10K, the pristine LBMO film exhibits low field LFMR ~5% (in a field of < 1T). This uncharacteristic MR behavior of an oriented thin film partially resembles the LFMR behavior of polycrystalline samples, the origin of which is attributed to the intergrain spin polarized tunneling (SPT) of charge carriers [16]. It is interesting to note that, the LFMR for the irradiated films at 10K decreases to ~2-3% and to zero for respective ion doses of 7.5×10^{10} ions/cm^2 and 1×10^{12} ions/cm^2. Also, the high field MR (HFMR) (in a field >1T) at 10K decreases from ~15% for the pristine film to nearly zero for the film irradiated with 1×10^{12} ions/cm^2. This points towards irradiation induced enhancement in connectivity between the grains, reduction in pinning of Mn-ion spins at grain boundaries, etc.

At an intermediate temperature of 100K, pristine film shows LFMR ~3% which is nearly zero in irradiated films while the values of HFMR are17%, 10% and 5% for pristine, 7.5 x 10^{10} ions/cm^2 and 1 x 10^{12} ions/cm^2 irradiated films respectively. At 240K, the pristine film shows LFMR < 3% and irradiated films show almost negligible MR. The HFMR is nearly 30% for pristine film which reduces to 20% and 10%, respectively, for the films irradiated with 7.5×10^{10} ions/cm^2 and 1×10^{12} ions/cm^2.

In the vicinity of T_P, at 330K, the LFMR of ~8%, 12% and 18% is observed for the pristine, 7.5×10^{10} and 1×10^{12} ions/cm^2 irradiated films, respectively. The HFMR observed for the pristine film is ~48%, while successive irradiation doses of 7.5×10^{10} and 1×10^{12} ions/cm^2 increases the HFMR to ~55% and 60%, respectively. Such an irradiation induced enhancement in MR at T_P may be attributed to the field induced delocalization of charge carriers due to the structural disorder at grain boundaries and at Mn-O-Mn bond angles [16,18,19].

In LBMO films, the above-mentioned results, depicting an irradiation induced suppression in MR at low temperatures and an enhancement of MR at high temperatures around T_P, underline the importance of deteriorating grain boundary contribution to MR. Moreover, the irradiation induced suppression of LFMR indicates further the improvement

in crystallographic orientation and parallel alignment of magnetic domains. This inference is supported by increasing line intensity in XRD patterns [Fig.5.16(c)]. At low temperatures, HFMR arises due to poor connectivity between grains, pinning of Mn spin at grains boundaries, etc. [18,19]. The suppression of HFMR at 10K indicates irradiation induced enhancement in grain connectivity. Such granular contribution is also evident from the MR behavior at T_P; the enhancement in MR with increasing ion dose at 330K implies that the magnetic order at the grain boundaries improves, thus, allowing a better electronic transport.

It is evident from the MR studies on pristine and irradiated LRMO thin films that, in LCMO and LSMO films, an enhancement in MR at low temperature is due to the increase in structural disorder, scattering, pinning centers and strain fields due to the creation of surface swellings and columnar defects introduced by the SHI irradiation. On the other hand, in LBMO films, the improved crystallinity and grain morphologies in the ion irradiated films results into the considerable reduction in MR at low temperatures and enhancement of MR at RT.

5.3.3 TCR and FCR studies

To evaluate the effect of irradiation on the application potential of these CSD grown films, the temperature and the field sensitivity of resistivity have been calculated. These parameters, quantified as the temperature coefficient of resistance [TCR% = (1/R×dR/dT)×100] and the field coefficient of resistance [FCR%=(1/R×dR/dH)×100], and were determined from ρ - T and ρ - H data and are plotted for all LRMO films in figs.5.19(a) and (b) respectively. In the irradiated LCMO and LSMO films, the electronic and magnetic anisotropies, induced due to the defects created, result in the reduction of temperature and magnetic field sensitivities as compared to their pristine counterparts, while in LBMO films, there is a significant net positive enhancement in TCR value (3.5% at 330K) and a net increase in the value of negative FCR (3.7% at 330K and <0.5T) at T_P (330K) (slightly above room temperature).

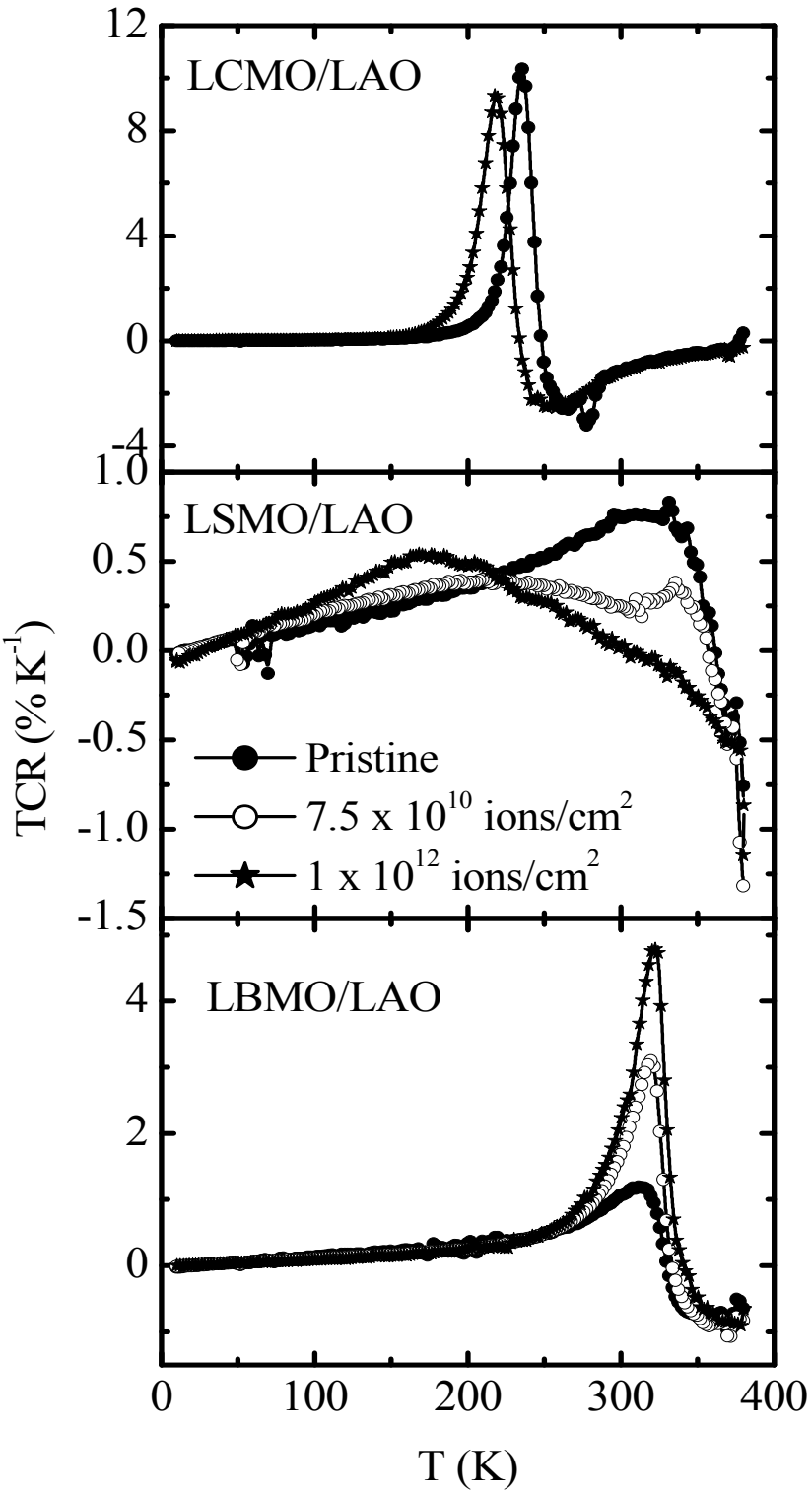

Figure 5.20(a): TCR vs. T plots for pristine and irradiated LRMO/LAO (R = Ca, Sr and Ba) films.

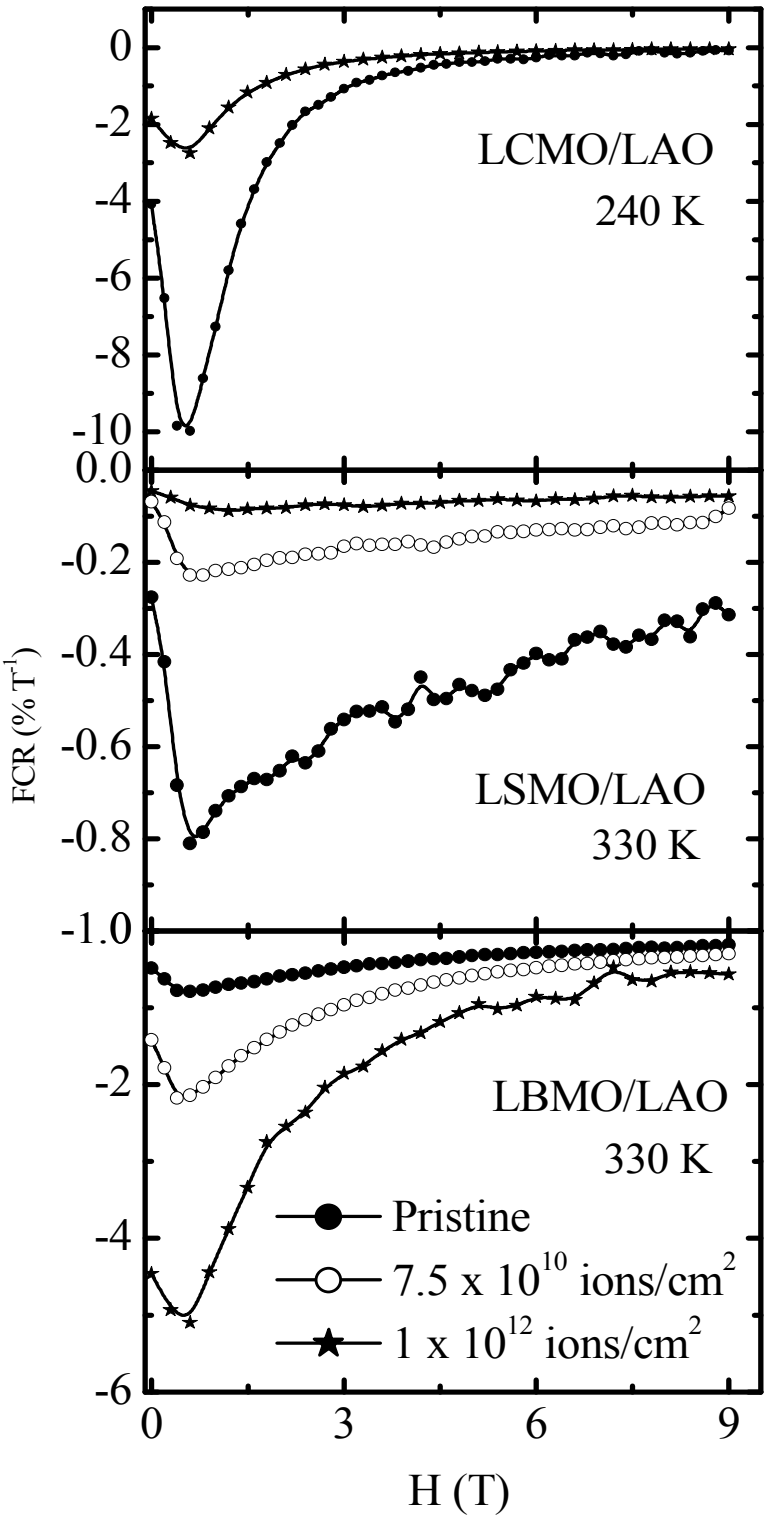

Figure 5.20(b): FCR vs. H plots for pristine and irradiated LRMO/LAO (R = Ca, Sr and Ba) films.

To sum up, the swift ion irradiation effects on microstructural, electronic and magnetotransport properties of LRMO films grown by CSD method have been investigated. The structural, transport and MR properties of irradiated LBMO films are opposite to those observed for the LCMO and LSMO films. Irradiation has deteriorating effect on structural and transport properties of LCMO and LSMO films where in there is an increase in resistivity with suppression in MR as compared to their pristine counterparts. In LBMO films, the SHI irradiation induced suppression in resistivity and enhancement of MR, makes them useful for temperature and field sensor application.

Conclusions

In summary, the studies on $La_{0.7}R_{0.3}MnO_3$ (LRMO) (R = Ca, Sr and Ba) nanostructured manganite thin films synthesized using novel chemical solution deposition route have been presented. The important conclusions derived from the above studies are summarized as follows

Firstly, the dependence of structural, microstructural, electronic and magnetotransport properties of CSD grown LSMO films on the growth parameters, annealing temperature and time have been discussed. Increase in annealing temperature and time period resulted in an increase in average grain size from 50nm to 90nm. The reduction in film resistivity and enhancement in T_P can be correlated to the increase in grain size and hence better electronic transport at grain boundaries. It is evident from the MR vs. H isotherms of all the LSMO films that, at RT, the LFMR and HFMR increases progressively with reduction in grain size.

Secondly, a comparative study of the various physical properties of CSD grown LRMO (R = Ca, Sr and Ba) films in the light of their structural, transport and magnetotransport behavior has been made. It is observed that, the CSD method yields good quality epitaxial films with reproducible results which are comparable with the reported PLD grown LRMO films.

Finally, the effect of SHI irradiation on the chemically prepared LRMO thin films has been explored. Irradiation has adverse effect on the structural, transport and MR properties of LCMO and LSMO films while in LBMO films, the SHI irradiation results in the suppression in resistivity (consistent with improved crystallinity, microstructure and

variations in MR) which opens up new avenue for engineering, the electronic and magnetotransport properties of manganites for applications employing swift heavy ion irradiation.

References

1. R. Von Helmolt, J. Weeker, B. Holzapfel, L. Schultz, and K. Samwer, Phys. Rev. Lett. 71, 2331 (1993)
2. S. Jin, T. H. Tiefel, M. McCromack, R. A. Fastnacht, R. Ramesh, and L. H. Chen, Science, 264, 413 (1994)
3. S. Pignard, K. Yu. Zhang, Y. Leprince, Wang K. Han, H. Vincent, J. P. Senateur, Thin Solid Films, 391, 21 (2001)
4. Y. Q. Li, J. Zhang, S. Pombrik, S. DiMascio, W. Stevens, Y. F. Yan and N. P. Ong, J. Mater, Res. 10, 2166 (1995)
5. G. J. Snyder , R. Hiskes, S. DiCarolis, M. R. Beasley and T. H. Geballe, Phys. Rev. B, 53, 14434 (1996)
6. Brian L. Cushing, Vladimir L. Kolesnichenko, and Charles J. O'Connor, Chem. Rev. 104, 3893 (2004)
7. A. M. Haghiri Gosnet and J. P. Renard, J. Phys. D: Appl. Phys. 36, 127 (2003)
8. U. Hasenkox, C. Mitze and R. Waser, J. Am. Ceram. Soc. 80, 2709 (1997)
9. K. Tanaka, S. Okamura and T. Shiosaki, Jpn. J. Appl. Phys. 40, 6821 (2001)
10. Seung Young Bae and Shan Xiang Wang, J. Mater, Res. 13, 3234 (1998)
11. A. D. Palli, F. F. Lange, M. Ahlskog, Reghu Menon and A. K. Cheetham, J. Mater, Res. 14, 1337 (1999)
12. X. Zhu, Y. Sun, J. Dai and W. Song, J. Phys. D: Appl. Phys. 39, 2654 (2006)
13. D. C. Worledge, G. Jeffrey Snyder, M. R. Beasley, T. H. Geballe, Ron Hiskes and Steve DiCarolis, J. Appl. Phys. 80, 5158 (1996)
14. E. Rozenberg and M. Auslender, J. Phys.: Condens. Matter. 14, 8755 (2002)
15. Y. Xu , J. Zhang, G. Cao, C. Jing and S. Cao., Phys. Rev. B, 73, 224410 (2006)
16. H. Y. Hwang, S. W Cheong, N. P. Ong and B. Batlogg, Phys. Rev. Lett. 77, 2041 (1996)

17. X. W. Li, A. Gupta, G. Xiao, and G. Q. Gong, Appl. Phys. Lett. 71, 1124 (1997)

18. A. de Andres, M. Garcia-Hernandez, J. L. Martinez, Phys. Rev. B 60, 7328 (1999)

19. L. Balcells, J. Fontcuberta, B. Martinez, and X. Obradors, Phys. Rev. B, 58, 14697 (1998)

20. J. M. D. Coey, M. Viret and L. Ranno, Phys. Rev. Lett. 75, 3910 (1995)

21. H.Y Hwang, S.W. Cheong, N.P.Ong and B. Batlogg, Phys. Rev. Lett. 75, 914 (1995)

22. P. G. Radaelli and G. Iannone, M. Marezio, H. Y. Hwang and S. W. Cheong, J. D. Jorgensen and D. N. Argyriou, Phy. Rev. B, 56, 8265 (1997)

23. R. Gunnarsson, A. Kadigrobov and Z. Ivanov, Phys. Rev. B, 66, 024404 (2002)

24. M. Ziese, S. Sena, C. Shearwood, H. J. Blythe, M. R. J. Gibbs and G. A. Gehring, Phys. Rev. B, 57, 2963 (1998)

25. N.D.Mathur, S.P.Isaac, G.Burnell, B.-S. Teo, L. F. Cohen, J. L. MacManus-Driscoll, J. E. Evetts, and M. G. Blamire, Nature, 387, 266 (1997)

26. J. G. Simmons. J. Appl. Phys.,34, 1793 (1963)

27. M. G. Blamire, C. W. Schneider, G. Hammerl and J. Mannhart, Appl. Phys. Lett. 82, 2670 (2003)

28. A. K. Raychaudhuri, Adv. Phy. 44, 21 (1995)

29. L. I. Glazman and A. K. Matveev, Sov. Phys. JEPT 67, 1276 (1998); Zh. Eksp. Teor. Fiz 94, 332 (1988)

30. F. Guinea, Phys. Rev. B, 58, 9212 (1998)

31. C. H. Chen, V. Talyansky, C. Kwon, M. Rajeswari, R. P. Sharma, R. Ramesh, T. Venkatesan, J. Melngailis, Z. Zhang and W. K. Chu, Appl. Phys. Lett. 69, 3089 (1996)

32. S.B.Ogale, Y.H. Li, M. Rajeswari, L.S.Riba, R. Ramesh, T. Venkatesan, A. J. Millis, Ravi Kumar, G. K. Mehta, Ravi Bathe and S. I. Patil, J. Appl. Phys. 87, 4210 (2000)

33. J. H. Markna, R. N. Parmar, D. G. Kuberkar, Ravi Kumar, D. S. Rana and S. K. Malik, Appl. Phys. Lett. 88, 152503 (2006)

34. B.L.Belevtsev, V.B. Krasovitsky, V. V. Bobkov, D. G. Naugle, K. D. D. Rathnayaka and A. Parasiris, Eur. Phys. J. B, 15, 461 (2001)

35. A. Goyal, M. Rajeswari, R. Shreekala, S. E. Lofland, S. M. Bhagat, T. Boettcher, C. Kwon, R. Ramesh, and T. Venkatesan, Appl. Phys. Lett. 71, 17 (1997)

36. Program SRIM (2003) by J. F. Ziegler and J. P. Biersack, http://www.srim.org

37. G. Szenes, Phys. Rev. B. 51, 8026 (1995)

38. To generate 200 MeV Ag ion beam using pelletron accelerator, first negatively charged Ag ions are produced and accelerated with the chosen terminal potential (V). To further accelerate the ions, charge stripping of the ions is performed to convert the Ag ions to higher charge state, e.g. +15, by passing the ion through a stripper foil (carbon foil). This high charge state ion is further accelerated by the same potential to carry higher energy. Charge state q of the ion depends purely on the requirement of the energy of the beam and can be calculated using the formula, E = (1+q)V. With E=200Mev, V~ 12.5 MV, the value of q is 15. The charge state is merely used to achieve the desired energy of 200 MeV energy

39. pnA stand for particle nanoampere current. In the case of ion irradiation, the unit for the current is particle Ampere. In the present experiment, the beam current is ~ 4.5 nA. To calculate pnA, the current is divided by the charge state which means that each particle/ion carries electronic charge equivalent to its charge state.

40. S. B. Ogale, K. Ghosh, J. Y. Gu, R. Shreekala, S. R. Shinde, M. Downes, M. Rajeswari, R. P. Sharma, R. L. Greene, T. Venkatesan, R. Ramesh, Ravi Bathe, S.I. Patil, Ravi Kumar, S. K. Arora, and G. K. Mehta, J. Appl. Phys. 84, 6255 (1998)

41. R. N. Parmar, J. H. Markna, D. G. Kuberkar, Ravi Kumar, D. S. Rana, Vivas C. Bagve and S. K. Malik, Appl. Phys. Lett. 89, 202506 (2006)

Scope for the future work

During the course of present work, an effort has been made to synthesize and characterize some new mixed oxide manganites using a novel CSD technique and PLD method of film deposition. An interesting phenomenon of low temperature resistivity minima has been observed in LPBMO manganites. The effect of SHI irradiation of the manganite thin films has been studied in the present work. In addition, detailed temperature dependent neutron diffraction studies on the La based mixed oxide superconductors of the type $\mathbf{La_{2-x}Dy_XCa_{2x}Ba_2Cu_{4+2x}O_z}$ **(x = 0.3, 0.5) (**La2125) were carried out to understand the effect of bond length variations and average Cu valences on the superconductivity in these compounds.

Some of the aspects related to the present findings on these materials need further investigations. To list few of them –

- It would be interesting to study the effect of Ca & Cu addition on the critical current density of La-2125 mixed oxide superconductors, as; these compounds possess stable tetragonal structure having more oxygen stability as compared to 123 superconductors.
- Also, detailed analysis of the local structure calculations on the La-2125 samples, based on the Rietveld refined ND data at low temperatures will help to throw some light on the fluctuated nature of Cu valence in these compounds.
- Also, it would be a good effort to synthesize few La(Nd/Gd/Sm)PrBaMO type of manganites and study their transport behavior for the observation of low temperature minima and to understand the cause for it.
- Regarding the synthesis of thin films using cost effective and novel CSD route, it will prove to be highly useful, if one can deposit the manganite thin films of LSMO compounds having transition temperature above RT and comparatively higher MR effect in them.

List of Publications in International/National Journals/symposia/conferences

1. **Neutron Diffraction studies on $La_{2-x}Dy_XCa_{2x}Ba_2Cu_{4+2x}O_z$ superconductors**
   S. Rayaprol**, Rohini Parmar,** D. G. Kuberkar, Keka Chakravorty, P. S. R.Krishna and M. Ramanadham
   ***Pramana* J. of Physics 63, 213 (2004)**

2. **Low Temperature Neutron Diffraction Studies on Superconductors of the type $La_{2-x}Dy_xCa_{2x}Ba_2Cu_{4+2x}O_z$**
   Rohini N. Parmar, J. H. Markna, D. S. Rana, C.M.Thakar, N.A.Shah, S.Rayaprol, D. G. Kuberkar, Keka R. Chakraborty, P. S. R. Krishna and M. Ramnadham
   Solid State Physics (India), 49, 822 (2004)

3. **Resistivity minimum at low temperature in the manganite compound $(La_{0.5}Pr_{0.2})Ba_{0.3}MnO_3$**
   J. H. Markna, D. S. Rana, **R. N. Parmar**, C. M. Thaker, , J. A. Bhalodia, D. G. Kuberkar, P. Raychaudhuri, J. John and S. K. Malik
   Solid State Physics (India), 49, 824 (2004)

4. **Low temperature transport anomaly in the magnetoresistive compound $(La_{0.5}Pr_{0.2})Ba_{0.3}MnO_3$**
   D. S. Rana, J. H. Markna, **R. N. Parmar**, D. G. Kuberkar, P. Raychaudhuri, J. John and S. K. Malik
   Phys. Rev. B, 71, 212404 (2005)

5. **Electronic transport and magnetism in $(La_{0.7-2x}Eu_x)(Ca_{0.3}Sr_x)MnO_3$ compounds**
   D. S. Rana, C. M. Thaker, K. R. Mavani, J.H. Markna, **R. N. Parmar**, N.A.Shah, D. G. Kuberkar and S.K. Malik
   Hyperfine Interactions, 10, 1007 (2005)

6. **Growth-parameter-dependent magnetoresistance in pulsed-laser-deposited $(La_{0.5}Pr_{0.2})Ba_{0.3}MnO_3$ thin films**
   K. R. Mavani, D. S. Rana J. H. Markna, **R. N. Parmar**, and D. G. Kuberkar P. Misra, L. M. Kukreja, D. C. Kundaliya and S. K. Malik
   J. Appl. Phys. 98, 086111 (2005)

7. **I-V studies on $La_{0.7}(Ca/Sr)_{0.3}MnO_3$ manganite thin films grown by Chemical Solution Deposition (CSD) method**
   P. S. Vachhani, **R. N. Parmar,** P. S. Solanki, J. Raval, J. H. Markna, N. A. Shah, J. A. Bhalodia, D. S. Rana[†] and D.G.Kuberkar
   Solid State Physics (India), 50, 517 (2005)

8. **Low Temperature Bond Valence Sum study of $La_{1.7}Dy_{0.3}Ca_{0.6}Ba_2Cu_{4.6}O_z$ oxide superconductors**
R. N. Parmar, J. H. Markana, C. M. Thakar, S. Rayaprol, J.A.Bhalodia, N.A. Shah, D. G. Kuberkar, Keka R. Chakraborty, P. S. R. Krishna and M. Ramnadham
Solid State Phenomena, 111, 163 (2006)

9. **Thickness dependent Shift Heavy Ion Irradiation effect on Electronic Transport of $(La_{0.5}Pr_{0.2})Ba_{0.3}MnO_3$ Thin Films**
J. H. Markna, **R. N. Parmar**, and D. G. Kuberkar, Ravi Kumar, D. S. Rana and S. K. Malik
Appl. Phys. Lett. 88, 152503 (2006)

10. **Swift heavy ion irradiation induced enhancement in resistivity of $La_{0.7}Ba_{0.3}MnO_3$ thin films synthesized by chemical solution deposition**
R. N. Parmar, J. H. Markana, D. S. Rana, Vivas G. Bagve, D. G. Kuberkar, Ravi Kumar and S. K. Malik
Appl. Phys. Lett. 89, 202506 (2006)

11. **Effects of Swift Heavy Ions Irradiation on Epitaxial $La_{0.5}Pr_{0.2}Sr_{0.3}MnO_3$ Thin Films grown by Pulsed Laser Deposition**
J. H. Markna, **R. N. Parmar**, D. G. Kuberkar, Ravi Kumar, P. Misra, L.M. Kukreja, D. S. Rana and S.K. Malik
NIMB B 2006 (Under revision)

12. **200 MeV Ag^{+15} ion irradiation created columnar defects and enhanced critical current density of La-2125 type superconducting thin films**
K. R. Mavani, D. S. Rana, **R. N. Parmar**, S. Rayaprol, D. G. Kuberkar, Ravi Kumar, M. Tonouchi, J. John and R. Nagarajan
Solid State Communication 2006 (Under revision)

13. **Enhancement in TCR of $La_{0.5}Pr_{0.2}Ba_{0.3}MnO_3$ manganite thin film by Swift heavy ion irradiation**
P.S. Vachhani, R.R. Doshi, R.N. Parmar, J.H. Markna, J.A. Bhalodia, Ravi Kumar and D.G. Kuberkar
Solid State Physics (India), accepted (2006)

14. **Grain size dependent transport and magnetoresistance behavior of CSD grown nanostructured $La_{0.7}Sr_{0.3}MnO_3$ manganite films**
R. N. Parmar, J. H. Markna, P. S. Solanki, P. S. Vachhani and D. G. Kuberkar
Communicated to J. Nanoscience & Nanotechnology 2006

15. **Strain induced non-linear conduction in epitaxial $La_{0.7}A_{0.3}MnO_3$ manganite thin films**
P. S. Vachhani, P. S. Solanki, J. H. Markna, **R. N. Parmar**, J. A. Bhalodia and D. G. Kuberkar
Communicated to Indian Journal of Engineering and Materials Science 2006

16. **Role of structural displacements in $La_{2-x}Dy_XCa_{2x}Ba_2Cu_{4+2x}O_z$ (x = 0.3, 0.5) Superconductor: A temperature dependent Neutron Diffraction study**
R. N. Parmar, J. H. Markana, S. Rayaprol, D. G. Kuberkar,
Keka R. Chakraborty, P. S. R. Krishna and M. Ramnadham
To be communicated

17. **Electronic transport and magnetotransport properties of LPSMO/Al_2O_3/LPSMO Multilayer**
J. H. Markna, P. S. Vachhani, **R. N. Parmar**, D. G. Kuberkar, Ravi Kumar,
P. Misra, L. M. Kukreja, D. S. Rana and S.K. Malik
To be communicated

Schools, Workshops, Seminars, Symposia, Meetings & Conferences attended:

1. National workshop on **"Functional Oxide Materials"** organized by IUAC at IUAC, New Delhi, September 25-26, 2006

2. 3rd National Symposium on **"Pulsed Laser Deposition of Thin Films and Nano-structured materials"** (PLD-2005) organized by DAE-BRNS at Tirupati, October 7-9, 2005

3. National workshop on **"Neutrons as Probes of Condensed Matter"** organized by UGC-DAE CSR and SSPD, BARC, Mumbai, February 24-25, 2006

4. National workshop on **"Nanotechnology: Challenges & Opportunities",** at Saurashtra University, Rajkot, October 17, 2005

5. **"3rd International Conference on Materials for Advanced Technologies"** (ICMAT- 2005)" to be held at Suntech, Singapore. July 3-8, 2005

6. One day seminar on **"Current Trends in Materials Research"** organized under UGC- SAP program at Department of Physics, Saurashtra University, Rajkot, February 28, 2005

7. **"DAE Solid State Physics Symposia"** organized by Department of Atomic Energy, BARC, Mumbai at Amritsar, December 26 - 30, 2004

8. **"National Workshop on Thin film Technologies & Applications"** (NAWOTTA) organized by PSG arts & Science College association with MRSI, at Coimbatore, July 9-12, 2004

9. **"International Workshop on Nanomaterials & Magnetic Semiconductors"** (IWNMS) organized by M.S. University, Baroda. February 8-12, 2004

10. **"3rd Gujarat Congress Research Student Meet"** (GCRSM) at Vallabh Vidhyanagar, January 1st, 2004

11. International **"Conference on Neutron Scattering"** (CNS-2004) organized by BRNS at BARC, Mumbai 400 085. January 2-4, 2004

12. "**National Workshops on Advanced Methods for Materials Characterization"** (NWMS) organized by Materials Research Society of India (MRSI) at BARC, Mumbai. October 11 - 15, 2004